Lanthanide-Doped Upconversion Materials: Synthesis, Surface Modification, and Sensing Applications

vorgelegt von

M. Sc.

Chunning Sun

ORCID: 0000-0003-0938-1631

an der Fakultät II - Mathematik und Naturwissenschaften
der Technischen Universität Berlin
zur Erlangung des akademischen Grades

Doktor der Naturwissenschaften
- Dr. rer. nat. -

genehmigte Dissertation

Promotionsausschuss:

Vorsitzender: Prof. Dr. Reinhard Schomäcker
Gutachter: Prof. Dr. Michael Gradzielski
Gutachter: Prof. Dr. Alexander Eychmüller (Technische Universität Dresden)

Tag der wissenschaftlichen Aussprache: 15. März 2021

Berlin 2021

Acknowledgments

First, I would like to express my sincere gratitude to my supervisor, Prof. Michael Gradzielski for guidance, motivation, and support during my Ph.D. study, and for always giving me the freedom to pursue my own ideas.

Next, I truly appreciate my colleagues, Petra Erdmann, Maria Bülth and Daniela Fliegner for all their generous help with unlimited patience. Jana Lutzki and Michaela Dzionara for providing assistance and convenience in the lab. Dr. René Straßnick for helping to build the fluorescence spectrophotometer with an IR laser. Monika Noji for help with computer problems. Bin Dai, Esra Oguztürk, Özge Azeri, Christoph Brückner, Kathrin Siegl, Eric Liberra, Tomas Omasta, Miriam Simon, Vivian Spiering, Albert Prause, Sarah Schatte, Sven Riemer, Anja Hörmann, Sebastian Bayer, Olga Kuzminskaya for their help, support, critique, discussions, and suggestions. Specifically, I am deeply grateful to Benjamin von Lospichl, a best friend for his sacrifice of time to help with a lot of paperwork (translations and writing letters), and for solving many problems I encountered.

I would like to acknowledge my collaborators, Prof. Michael Schäferling (Münster University of Applied Sciences) and Dr. Ute Resch-Genger (BAM) for the fluorescence measurement at the beginning and beneficial discussions of the results. I also thank members from ZELMI, Christoph Fahrenson and Ulrich Gernert for teaching me to use the SEM instrument, Jan Simke and Sören Selve for their assistance in TEM measurements.

I would also like to thank Dr. Wen Ju, Dr. Xingli Wang from Prof. Peter Strasser's group, and Dr. Guiyang Yao from Prof. Roderich Süssmuth's group for scientific discussions and supports for my research.

The greatest gratitude goes to my wife, Xurui Wei for her continued support in all these years and for taking good care of our beloved daughter, Mila. I also thank my parents and older sister for their supports and understanding.

Finally, I would like to acknowledge the China Scholarship Council (CSC) and TU Berlin for financial support and research opportunities.

Abstract

Lanthanide-doped upconversion materials have attracted considerable attention in recent years for their potential applications in a wide range of fields including in imaging, sensing, thermodynamic therapy, anti-counterfeiting, solar cells, and full color volumetric three-dimensional displays, owing to their capability of converting near-infrared light to visible and ultraviolet light. Specifically, this dissertation focused on the preparation of upconversion materials by wet chemistry methods, surface modification, and sensing applications of upconversion-based nanosystems.

The first research part focused on the direct synthesis of hydrophilic lanthanide-doped upconversion nano-/microcrystals *via* a one-pot solvothermal method. To prepare upconversion crystals in a well-controlled way, different parameters were investigated, such as types of dopant ions (Er^{3+}, Tm^{3+}, Ho^{3+}, and Gd^{3+}), volume ratios between H_2O and organic co-solvent (ethylene glycol, polyethylene glycols, and propylene glycols), and molar ratios between the fluoride ion and lanthanide ions. By careful control of the solvothermal conditions, upconversion crystals with various sizes and morphologies can be obtained, including nanospheres, nano-/microprisms, and microrods. Moreover, based on the temporal particle evolution during the solvothermal process, a possible formation mechanism for the growth and the morphological changes of the crystals was proposed.

Next, hydrophobic upconversion nanoparticles (NPs) and nanorods were prepared at high temperature using oleic acid as the ligand in the synthetic process, and an easy-to-process method was developed for the fast and efficient hydrophobic-to-hydrophilic conversion of upconversion NPs in either biphasic solvent systems or single hydrophobic media without any noticeable detrimental effects on size, shape, and phase of crystals during the ligand removal process. Additionally, this method can be applied to small-sized upconversion NPs with a diameter of *ca.* 20 nm and HCl-sensitive upconversion host material ($NaLaF_4$). Furthermore, the obtained ligand-free upconversion NPs can be readily transferred into the aqueous solution and further modified with water-soluble capping molecules by sequential surface functionalization.

Finally, different upconversion-based systems were explored for fluorescence sensing applications where upconversion nanoparticles served as the energy donor. By assembling organic dye molecules and Au NPs with upconversion nanoparticles,

fluorescence turn-off sensing of Cu^{2+} and turn-on sensing of CN^- were achieved based on the fluorescence resonance energy transfer (FRET) process. The limit of detection for Cu^{2+} and CN^- was 9.42 μM and 1.53 μM, respectively. Moreover, a non-contact upconversion nanosystem based on the excitation energy attenuation (EEA) effect and a conventional upconversion nanosystem based on the joint effect of EEA and FRET were developed for the fluorescence sensing of H_2O_2, where MoO_{3-x} nanosheets act as the energy acceptor in both systems. Additionally, the non-contact strategy can be applied to the sensing of pH, showing a broad pH-responsive property.

In this dissertation, hydrophilic upconversion materials were prepared *via* either the solvothermal method using a water-soluble ligand or surface modification of as-prepared hydrophobic upconversion crystals. Moreover, conventional upconversion-based nanocomposites and non-contact upconversion nanosystems were developed for the sensing of analytes, such as Cu^{2+}, CN^-, pH, and H_2O_2.

Zusammenfassung

Lanthanid-dotierte Hochkonversionsmaterialien haben aufgrund ihrer Fähigkeit Licht aus dem nahinfrarotem Bereich in sichtbares bzw. ultraviolettes Licht umzuwandeln in den letzten Jahren aufgrund ihrer potenziellen Anwendungen in einer Vielzahl von Bereichen, einschließlich Bildgebung, Sensorik, thermodynamischer Therapie, Fälschungssicherheit, Solarzellen und volumetrischen dreidimensionalen Vollfarbdisplays, beträchtliche Aufmerksamkeit auf. Diese Dissertation konzentriert sich insbesondere auf die Herstellung von Hochkonversionsmaterialien durch nasschemische Methoden und Oberflächenmodifikation sowie die Anwendung dieser Materialen in Form von nanostrukturierten Systemen im Bereich der Sensoranwendung.

Der erste Teil der Forschungsarbeit konzentrierte sich auf die direkte Synthese von hydrophilen Lanthanid-dotierten Hochkonversionsnano- bzw. mikrokristallen über eine Eintopf-Solvothermalmethode. Um die Hochkonversionskristalle gut kontrolliert herzustellen zu können, wurden verschiedene Parameter untersucht, wie z. B. Arten von Dotierstoffionen (Er^{3+}, Tm^{3+}, Ho^{3+}, und Gd^{3+}), Volumenverhältnisse zwischen H_2O und einem zweiten organischem Lösungsmittel (Ethylenglykol, Polyethylenglykole und Propylenglykole) und Molverhältnisse zwischen dem Fluoridion und den Lanthanoidionen. Durch eine sorgfältige Kontrolle der Solvothermalbedingungen ist es möglich Hochkonversionskristalle mit verschiedenen Größen und Formen zu erhalten, einschließlich Nanokugeln, Nano-/Mikroprismen und Mikroruten. Darüber hinaus wurde, basierend auf der zeitlichen Partikelentwicklung während des Solvothermalprozesses, ein möglicher Bildungsmechanismus für das Wachstum und die morphologischen Veränderungen der Kristalle vorgeschlagen.

Als nächstes wurden hydrophobe Hochkonversions-Nanopartikel (NPs) und Nanostäbe bei hoher Temperatur unter Verwendung von Ölsäure als Ligand im Syntheseverfahren hergestellt. Des Weiteren wurde ein einfach zu implementierendes Verfahren für die schnelle und effiziente Umwandlung von Hochkonversions-NPs von hydrophob zu hydrophil entwickelt. Dies geschieht entweder in zweiphasigen Lösungsmittelsystemen oder in einzelnen hydrophoben Medien ohne merkliche nachteilige Auswirkungen auf Größe, Form und Phase der Kristalle während des Ligandenentfernungsprozesses. Zusätzlich kann dieses Verfahren auf kleine Hochkonversions-NPs mit einem Durchmesser von etwa 20 nm und HCl-sensitives

Hochkonversions-Wirtsmaterial ($NaLaF_4$) angewendet werden. Darüber hinaus können die erhaltenen ligandenfreien Hochkonversions-NPs leicht in eine wässrige Lösung übertragen und durch sequentielle Oberflächenfunktionalisierung mit wasserlöslichen Verkappungsmolekülen weiter modifiziert werden.

Schließlich wurden verschiedene auf Hochkonversion basierende Systeme für Fluoreszenzsensoranwendungen untersucht, bei denen Hochkonversions-Nanopartikel als Energiedonor dienten. Durch ein Zusammensetzen von organischen Farbstoffmolekülen und Au-NPs mit Hochkonversions-Nanopartikeln wurde eine Aktivierung der Fluoreszenz von Cu^{2+} und eine Deaktivierung der Fluoreszenz von CN^- auf der Grundlage des Fluoreszenzresonanzenergietransferprozesses (FRET) erreicht. Die Nachweisgrenze für Cu^{2+} und CN^- betrug 9.42 uM bzw. 1.53 uM. Darüber hinaus wurden ein berührungsloses Hochkonversionsnanosystem basierend auf dem Effekt der Anregungsenergiedämpfung (EEA) und ein herkömmliches Hochkonversionsnanosystem basierend auf dem gemeinsamen Effekt von EEA und FRET für die Fluoreszenzmessung von H_2O_2 entwickelt, wobei MoO_{3-x}-Nanoblättchen als Energieakzeptoren in beiden Systemen fungieren. Zusätzlich kann die berührungslose Strategie auf die Erfassung des pH-Werts angewendet werden, wobei sich eine breite pH-abhängige Eigenschaft zeigt.

In dieser Dissertation wurden hydrophile Hochkonversionsmaterialien entweder über das Solvothermalverfahren unter Verwendung eines wasserlöslichen Liganden oder durch Oberflächenmodifizierung der auf diese Art hergestellten hydrophoben Hochkonversionskristalle untersucht und hergestellt. Darüber hinaus wurden konventionelle Nanokomposite auf Hochkonversionsbasis und berührungslose Hochkonversionsnanosysteme für die Erfassung von Analyten wie Cu^{2+}, CN^-, pH und H_2O_2 entwickelt.

List of Abbreviations

Abbreviation	Expansion
Ln	lanthanide
RE	rare-earth
UV	ultraviolet
UVB	ultraviolet B
NIR	near-infrared
UCL	upconversion luminescence
CW	continuous-wave
CIE	Commission Internationale de l'Eclairage
R/G	red-to-green ratio
NP	nanoparticle
NR	nanorod
NS	nanosheet
3D	three-dimensional
r.p.m	round per minute
ppm	parts-per-million
ESA	excited-state absorption
ETU	energy transfer upconversion
PA	photon avalanche
CSU	cooperative sensitization upconversion
EMU	energy migration upconversion
GSA	ground-state absorption
SEM	scanning electron microscopy
TEM	transmission electron microscopy
HR-TEM	high-resolution transmission electron microscopy
EDS	energy-dispersive X-ray spectroscopic
XRD	powder X-ray diffraction
^{1}H NMR	proton nuclear magnetic resonance
FT-IR	Fourier transform infrared
TGA	thermogravimetric analysis
LSS	liquid-solid-solution
LOD	limit of detection
FRET	fluorescence resonance energy transfer
EEA	excitation energy attenuation

UCNP	$NaYF_4$:Yb,Er nanoparticle
OA-UCNP	oleate-capped $NaYF_4$:Yb,Er nanoparticle
OA-csUCNP	oleate-capped $NaYF_4$:Yb,Er@$NaYF_4$:Yb nanoparticle
OA	oleic acid
OM	oleylamine
ODE	1-octadecene
EG	ethylene glycol
DEG	diethylene glycol
PEG	polyethylene glycol
PPG	polypropylene glycol
DSNTA	disodium nitrilotriacetate
PVP	polyvinyl pyrrolidone
PEI	polyethylenimine
PAA	poly(acrylic acid)
FA	formic acid
LA	lactic acid
AA	acetic acid
DMF	N,N-dimethylformamide
DMSO	dimethyl sulfoxide
ACN	acetonitrile
MeOH	methanol
FAM	formamide
NMP	N-methyl-2-pyrrolidone
Cys	cysteine
Gln	glutamine
Gly	glycine
Leu	leucine
Pro	proline
Ser	serine
Thr	threonine
Val	valine
EBT	Eriochrome Black T
THPC	tetrakis(hydroxymethyl)phosphonium chloride
BRB	Britton Robinson buffer

Table of Contents

Chapter 1: Introduction

1.1 Ln and Their Properties

1.1.1 Electron Configurations of Ln

The Ln family, ranging from lanthanum to lutetium, together with the other two chemically similar elements (scandium and yttrium), are generally called RE elements[1]. The Ln elements show similar chemical and physical properties owing to their similarities in electron configurations ([Xe] $4f^{n-1}$ $5d^{0-1}$ $6s^2$). The Ln series commonly exists as its trivalent cation with the electronic configuration of [Xe] $4f^n$, where n varies from 0 (La^{3+}) to 14 (Lu^{3+}). In addition to the trivalent states, some of them also have oxidation states of +2 or +4, like Eu^{2+}, Yb^{2+}, Ce^{4+}, and Tb^{4+}. A summary of electron configurations of the Ln elements and their common ions is shown in table 1.1.

Table 1.1 Electron configurations of the Ln and their common ions

Atomic number	Symbol	Atom	Ln^{3+}	Ln^{2+}	Ln^{4+}
57	La	[Xe] $5d^1$ $6s^2$	[Xe]		
58	Ce	[Xe] $4f^1$ $5d^1$ $6s^2$	[Xe] $4f^1$		[Xe]
59	Pr	[Xe] $4f^3$ $6s^2$	[Xe] $4f^2$		[Xe] $4f^1$
60	Nd	[Xe] $4f^4$ $6s^2$	[Xe] $4f^3$	[Xe] $4f^4$	[Xe] $4f^2$
61	Pm	[Xe] $4f^5$ $6s^2$	[Xe] $4f^4$		
62	Sm	[Xe] $4f^6$ $6s^2$	[Xe] $4f^5$	[Xe] $4f^6$	
63	Eu	[Xe] $4f^7$ $6s^2$	[Xe] $4f^6$	[Xe] $4f^7$	
64	Gd	[Xe] $4f^7$ $5d^1$ $6s^2$	[Xe] $4f^7$		
65	Tb	[Xe] $4f^9$ $6s^2$	[Xe] $4f^8$		[Xe] $4f^7$
66	Dy	[Xe] $4f^{10}$ $6s^2$	[Xe] $4f^9$	[Xe] $4f^{10}$	[Xe] $4f^8$
67	Ho	[Xe] $4f^{11}$ $6s^2$	[Xe] $4f^{10}$		
68	Er	[Xe] $4f^{12}$ $6s^2$	[Xe] $4f^{11}$		
69	Tm	[Xe] $4f^{13}$ $6s^2$	[Xe] $4f^{12}$	[Xe] $4f^{13}$	
70	Yb	[Xe] $4f^{14}$ $6s^2$	[Xe] $4f^{13}$	[Xe] $4f^{14}$	
71	Lu	[Xe] $4f^{14}$ $5d^1$ $6s^2$	[Xe] $4f^{14}$		

1.1.2 Optical Properties of Ln

All Ln elements, except lutetium (d-block), belong to f-block elements. The primary feature of Ln ions originates from the different numbers of electrons filled in the 4f electron shell. The energy levels from the 4f electron configuration are abundant, resulting in many intraconfigurational transitions (Fig. 1.1)[2]. Since the 4f electrons of Ln ions are well shielded by the outer $5s^25p^6$ subshells, the electronic transitions within the 4f orbitals are barely affected by their microsurroundings[3]. The transitions of the 4f electrons are responsible for the interesting photophysical properties of the Ln ions, such as excellent photostability, a large anti-Stokes shift, long luminescence lifetime, and sharp-band emission. The luminescence emission colors of the Ln ions arise from their intra f-f transitions and the promotion of 4f electrons into the 5d subshell (f-d transitions), ranging from UV to visible light, and even NIR region. Energy transitions and major emissions of Ln ions are summarized in Table 1.2. Owing to their abundant energy levels and intraconfigurational transitions, Ln ions are considered as promising luminescent centers.

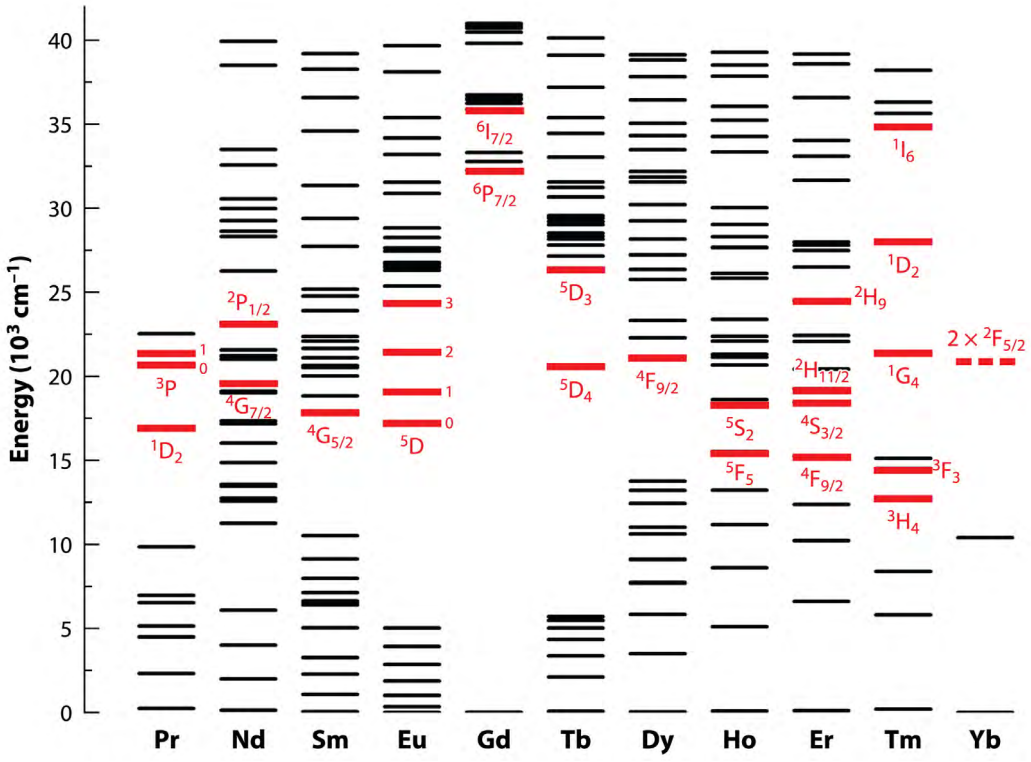

Fig. 1.1 Energy-level diagrams of Ln ions. The main levels that can generate luminescence are marked in red. Reproduced with permission from ref. [2]. Copyright 2015 Annual Reviews.

Table 1.2 Energy transitions and major emissions of Ln ions

Ln ions	Energy transitions	Primary emissions (nm)
Pr^{3+}	$^3P_0 \rightarrow {}^3H_4$, $^1I_6 \rightarrow {}^3H_5$, $^3P_0 \rightarrow {}^3H_5$, $^3P_0 \rightarrow {}^3H_6$, $^3P_0 \rightarrow {}^3F_2$, $^3P_1 \rightarrow {}^3F_3$, $^3P_0 \rightarrow {}^3F_4$, $^1I_6 \rightarrow {}^1G_4$	489, 526, 548, 618, 652, 670, 732, 860
Nd^{3+}	$^2P_{1/2} \rightarrow {}^4I_{9/2}$, $^2P_{1/2} \rightarrow {}^4I_{11/2}$, $^2P_{1/2} \rightarrow {}^4I_{13/2}$, $^4G_{7/2} \rightarrow {}^4I_{9/2}$, $^2P_{1/2} \rightarrow {}^4I_{15/2}$, $^4G_{7/2} \rightarrow {}^4I_{11/2}$, $^2G_{7/2} \rightarrow {}^4I_{9/2}$, $^4G_{7/2} \rightarrow {}^4I_{13/2}$, $^4G_{7/2} \rightarrow {}^4I_{15/2}$	430, 482, 525, 535, 580, 600, 664, 766
Sm^{3+}	$^4G_{5/2} \rightarrow {}^6H_{5/2}$, $^4G_{5/2} \rightarrow {}^6H_{7/2}$	555, 590
Eu^{3+}	$^5D_0 \rightarrow {}^7F_1$, $^5D_0 \rightarrow {}^7F_2$, $^5D_0 \rightarrow {}^7F_4$	590, 615, 690
Gd^{3+}	$^6G_{7/2} \rightarrow {}^8S_{7/2}$, $^6D_{9/2} \rightarrow {}^8S_{7/2}$, $^6I_J \rightarrow {}^8S_{7/2}$, $^6P_{5/2} \rightarrow {}^8S_{7/2}$, $^6P_{7/2} \rightarrow {}^8S_{7/2}$	204, 254, 278, 306, 312
Tb^{3+}	$^5D_4 \rightarrow {}^7F_6$, $^5D_4 \rightarrow {}^7F_5$, $^5D_4 \rightarrow {}^7F_4$, $^5D_4 \rightarrow {}^7F_3$	490, 540, 580, 615
Dy^{3+}	$^4F_{9/2} \rightarrow {}^6H_{13/2}$	570
Ho^{3+}	$^5S_2 \rightarrow {}^5I_8$, $^5F_5 \rightarrow {}^5I_8$	542, 645, 658
Er^{3+}	$^2H_{9/2} \rightarrow {}^4I_{15/2}$, $^2H_{11/2} \rightarrow {}^4I_{15/2}$, $^4S_{3/2} \rightarrow {}^4I_{15/2}$, $^4F_{9/2} \rightarrow {}^4I_{15/2}$	411, 523, 542, 656
Tm^{3+}	$^1I_6 \rightarrow {}^3H_6$, $^1I_6 \rightarrow {}^3F_4$, $^1D_2 \rightarrow {}^3H_6$, $^1D_2 \rightarrow {}^3F_4$, $^1G_4 \rightarrow {}^3H_6$, $^1G_4 \rightarrow {}^3F_4$, $^3F_3 \rightarrow {}^3H_6$, $^3H_4 \rightarrow {}^3H_6$	294, 345, 368, 450, 475, 650, 700, 800

1.2 Ln-based Upconversion Materials

Upconversion, an anti-Stokes process, refers to nonlinear optical processes characterized by the continuous absorption of two or more low-energy photons, resulting in the emission of the high-energy light. Since Bloembergen[4] investigated the upconversion phenomenon with an infrared quantum counter device in 1959, many efforts have been contributed to enlarge the family of upconversion materials. In stark contrast to second harmonic generation and simultaneous two-photon absorption, the upconversion photophysical process is realized *via* long-lived intermediate energy levels, realizing efficient upconversion emissions by a CW laser with a relatively low power density (1-10^3 W/cm^3).

A Ln-doped upconversion phosphor commonly consists of an optically transparent and chemically inert inorganic host of low phonon energy, sensitizer ions with a relatively high absorption cross-section, and emissive activator ions. Although upconversion can be expected in principle from most Ln-doped host materials, to achieve efficient UCL, elaborate consideration of the choice of the host material, the selection and concentration of doped sensitizer and activator ions are required.

1.2.1 Host Materials

The selection of appropriate host materials is of great importance in the synthesis of nanocrystals with high upconversion efficiency and controllable emissive luminescence. An optimal host matrix should exhibit low lattice phonon energies in order to minimize non-radiative energy losses during the upconversion process and maximize the luminescence quantum yield, high transparency for free migration of the excitation and emission photons, and excellent chemical and thermal stabilities to retain the original crystal structures. Heavy halides like chlorides, bromides, and iodides typically exhibit low phonon energies (<300 cm^{-1}). Nonetheless, their hygroscopic nature and poor chemical stability inhibit their application. Oxides exhibit high chemical stability, while their phonon energies (generally larger than 500 cm^{-1}) will increase the non-radiative loss, lower the luminescence quantum yield, and lessen the radiative emission. In contrast, fluoride-based lattice such as YF_3 and LaF_3[5, 6] usually exhibits relatively low phonon energies (~350 cm^{-1}) and high chemical stability, ensuring high luminescence efficiency. Since all RE ions exhibit similar ionic radii and chemical properties, their fluoride compounds are ideal host lattices for Ln-doped upconversion materials. Moreover, for the purpose of prevention to form crystal defects and lattice stresses, the host material based on cations usually requires the ionic radii closely matches to dopant ions, like Na^+, Ca^{2+}, and Y^{3+}, and therefore Na^+, Ca^{2+}, and Y^{3+} fluoride-based materials are the superior lattice choices for the preparation of high-quality upconversion phosphors[7, 8]. Additionally, more efficient UCL is always found in host materials with low symmetry compared to those with host lattices of high symmetry. For instance, the upconversion efficiency of the green emission in hexagonal $NaYF_4$:Yb,Er is about 10 times higher than that of in cubic $NaYF_4$:Yb,Er[9]. Hitherto, hexagonal $NaYF_4$-based crystals have been used as the most prominent host matrix for upconversion materials.

1.2.2 Activator

Since inorganic host materials do not participate in the upconversion process, luminescent ions, also known as activators, are used to dope the host matrix to obtain specific emissions. Most Ln ions can theoretically be applied to produce UCL as they have more than one excited 4f energy level, but the most efficient Ln ions used as activators were limited to Er^{3+}, Ho^{3+}, and Tm^{3+} ions at the beginning[10-13], owing to their long-lived metastable excited states, as well as the ladder-like arrangement of

intermediate energy levels with multiple and equal spaces. To date, activator ions have been expanded to Gd^{3+}, Ce^{3+}, Eu^{3+}, Tb^{3+}, Dy^{3+}, and Sm^{3+} ions in well-designed core-shell upconversion nanocrystals since the discovery of the energy migration upconversion process[14].

The multiphonon relaxation rate constant (k_{nr}) for 4f levels is described as[15]

$$k_{nr} \propto \exp\left(-\beta \frac{\Delta E}{\hbar\omega_{max}}\right) \quad (1)$$

where β is an empirical constant that relies on the host material, ΔE represents the energy gap between the populated level and the next lower-lying energy level of an Ln ion, and $\hbar\omega_{max}$ is the highest energy vibrational mode of the host lattice. The energy gap law implies that the multiphonon relaxation rate constant decreases exponentially with an increase in the energy gap of the activator ion. In accordance with the energy gap law, the most efficient upconversion nanocrystals are observed with Er^{3+} and Tm^{3+} as the activators.

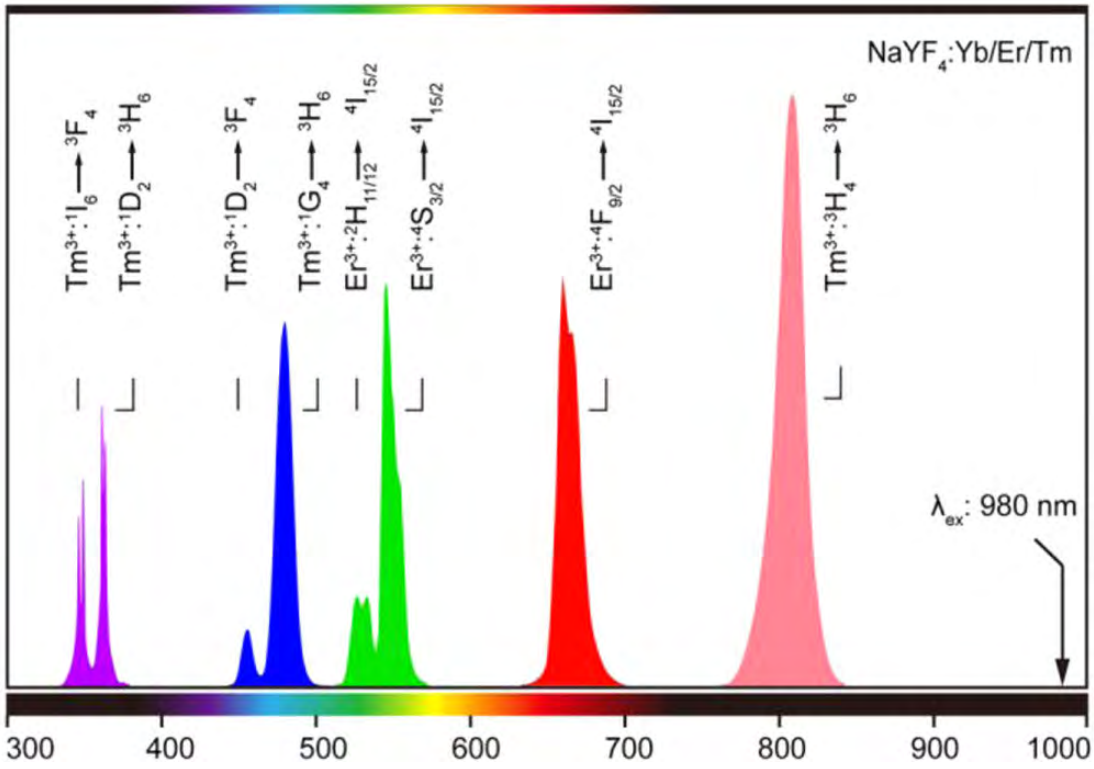

Fig. 1.2 Typical upconversion emissions, ranging from the UV to NIR regions, from Yb/Er and Yb/Tm co-doped upconversion materials under 980 nm excitation. Reproduced with permission from ref. [17]. Copyright 2016 American Chemical Society.

In principle, the upconversion efficiency can be improved by simply increasing the dopant concentration in the particle. However, the ion-to-ion distance of dopants in the host lattice would decrease, resulting in an increased probability for non-radiation cross-relaxation. Moreover, upon Ln-doping in the nanocrystal, crystal defects such as interstitial anions form, and cation vacancies are generated to maintain charge neutrality, leading to a further lowering of the upconversion efficiency. To obtain efficient luminescence in Ln-doped upconversion NPs, the activator dopant concentration must be stringently controlled. Generally, activator dopant concentrations in upconversion NPs for efficient luminescence is limited to up to 0.5% for Tm^{3+} and 3% for Er^{3+}[10, 16, 17]. Typical UCL from Yb/Er and Yb/Tm co-doped upconversion materials under 980 nm excitation are shown in Fig. 1.2.

1.2.3 Sensitizer

Since the activator dopant concentration is kept to a low degree, it results in a relatively low overall upconversion efficiency in singly doped NPs. To enhance the upconversion efficiency, a sensitizer is usually co-doped in typical upconversion NPs to increase the NIR absorption and eliminate the relatively weak absorptivity of activator ions, which is attributed to its capability of transferring the absorbed energy to the neighboring activator in the crystal lattice and maintaining the ion-to-ion distance between the dopants to minimize cross-relaxation quenching effects.

With respect to Ln-based upconversion systems with Er^{3+}, Ho^{3+}, or Tm^{3+} as activator ions, the Yb^{3+} is the most commonly used sensitizer ion[9, 18], as the trivalent Yb ion possesses a simple energy level diagram with only one excited state of $^2F_{5/2}$. A broad absorption cross-section of Yb^{3+} ion locates at around 980 nm due to the $^2F_{7/2}$ - $^2F_{5/2}$ transition, which is larger than that of other Ln ions. Additionally, the $^2F_{7/2}$ - $^2F_{5/2}$ transition of Yb^{3+} overlaps well with f-f transitions of typical activator ions (Er^{3+}, Ho^{3+}, or Tm^{3+}), thus permitting efficient energy transfer from the sensitizer to other ions. To enhance upconversion efficiencies, the sensitizer content doped in the host lattice is usually kept at higher molar concentrations (~20 mol%)[19].

Despite the excellent upconversion efficiency obtained by the use of Yb^{3+} ion as a sensitizer, applications of these Yb-doped NPs in biological systems are limited due to the 980 nm excitation radiation overlaps with the absorption band of water molecules. Therefore, when passing through biological samples, a significant attenuation of excitation radiation accompanied by overheating of the samples is observed, ultimately

leading to the damage of biological samples. Recently, Nd^{3+} has been investigated as a substitute sensitizer, allowing photon upconversion using suitable excitation wavelengths within the "biological window" (800 nm excitation)[20], circumventing the limitations of Yb-based upconversion NPs and expanding the applicability in bio-applications[21].

In addition to the use of Ln dopants as sensitizers, organic dyes have emerged as a new kind of sensitizers for upconversion NPs ascribing to their intense and broadband absorption. The organic dyes are applied as antennas and donate the absorbed energy from dye ligands to Ln dopants *via* the FRET process, resulting in the efficient production of photon upconversion[22-29].

1.3 Mechanisms of Upconversion Process

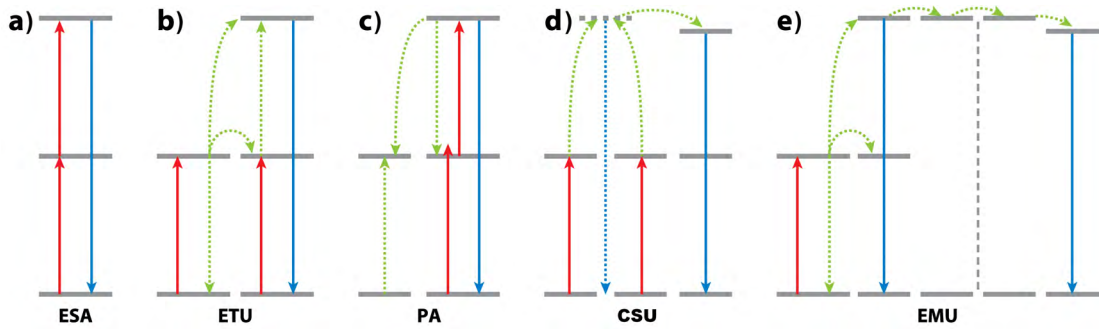

Fig. 1.3 energy transfer mechanisms of upconversion emissions: (a) ESA, (b) ETU, (c) PA, (d) CSU, and (e) EMU. The gray dashed line in panel e represents the core/shell interface. Reproduced with permission from ref. [2]. Copyright 2015 Annual Reviews.

In contrast to the conventional luminescence process (a Stokes process), which is realized by the promotion of electrons in the ground state to the excited state through the absorption of a high-energy photon, the upconversion process depends on the accumulation of low-energy photons through long-lived multiple excited states, which is referred to an anti-Stokes process. Some essential prerequisites are required for the upconversion process, such as the long lifetime of the excited-state and the ladder-like energy level structure[30, 31].

Upconversion was first proposed by Bloembergen in 1959[4], and the process was first observed by Auzel in 1966[32]. Five different mechanisms have been developed to explain the upconversion process, including ESA, ETU, PA, CSU, and EMU, which is depicted in Fig. 1.3.

1.3.1 ESA

The ESA is an upconversion process by successive absorption of at least two photons by a single Ln ion, and the energy transfer process is presented in Fig. 1.3a. The electrons of the Ln ion are primarily placed in the ground state. The absorption occurs when incident light with suitable energy excites, followed by the promotion of the ground state electron to the excited state, which is referred to as GSA. The electron is populated to a higher excited state by further absorption of a second photon, which is referred to as ESA. The excited electrons go back to the ground state with a release of a higher energy photon *via* radiative relaxation. Although the ESA process simply takes place in a single Ln ion, like Er^{3+} ion[33], the weak absorption caused by parity-forbidden intra-4f transitions strongly suppresses the efficiency.

1.3.2 ETU

Unlike ESA, the ETU process, which is the most efficient upconversion process, involves two types of luminescent centers, namely a sensitizer and an activator. The absorption cross-section of the sensitizer usually is larger than that of the activator. The process is shown in Fig. 1.3b. Two neighboring ions can be promoted to the metastable excited state upon excitation with low-energy photons, and the excited activator can then be excited to a higher excited state, which is realized by non-radiative energy transfer from the neighboring sensitizer through dipole-dipole resonant interaction. As electrons drop back to the ground state, high-energy emission light is generated from the activator.

In contrast to the ESA process, the upconversion efficiency of the ETU process is sensitive to the distance between the neighboring sensitizer and activator, which is determined by the concentrations of dopants. Ln ions with multiple excited states provide great advantages for the ETU process. Moreover, the energy-level matching of the sensitizer and the activator strongly influences the efficiency of the ETU process.

1.3.3 PA

The PA process was first discovered by Chivian et al. in Pr-based infrared quantum counters in 1979[34], which is shown in Fig. 1.3c. The PA process initiates with a non-resonant weak GSA process, promoting electrons to an excited state, and further

elevate to a higher excited state (superexcited) by resonant ESA process. Then cross-relaxation occurs between the superexcited ion and a neighboring ground-state ion resonantly, resulting in the occupation of the intermediate states of both ions. Resonant ESA process by incident radiation brings these excited electrons back up to the superexcited state. The repeating of the cross-relaxation populates the intermediate states exponentially, along with excitation above the threshold. Thus, PA-induced upconversion emissions readily occur as long as the consumption of superexcited ions is less than that of the ground state ions.

The PA mechanism of the upconversion process is the most complicated process and is found only in a few reports. For instance, Jin et al. found a photon avalanche effect in upconversion NPs with highly doped Tm^{3+} ion (8%)[35], realizing a super-resolution imaging with a low laser power down to 0.19 mW/cm^2.

1.3.4 CSU

The CUC process (Fig. 1.3d), similar to ETU, usually involves two types of luminescent centers, i.e., a cooperative sensitizer and activator[36]. The sensitizers are first promoted to the excited state *via* absorption of excitation photons, and both excited sensitizer ions can interact with the adjacent activator ion, the electrons of activator ion by to a higher state through cooperative energy transfer. Finally, the excited activator can relax to the ground state with upconversion emissions. The feature of the activator is the lack of adequate long-lived intermediate energy levels, which is the main difference between the two processes. The efficiency of CSU is approximately three orders of magnitude lower than the ETU process, and thus hinder their potential bio-applications.

1.3.5 EMU

The EMU pathway was first proposed by Liu and co-workers[14] in well-designed core-shell ($NaGdF_4$:Yb,Tm@$NaGdF_4$:Ln (Ln = Dy, Eu, Tb, or Sm)) nanostructures in 2011 (Fig. 1.3e), which is involved in four types of luminescent centers, namely a sensitizer, accumulator, migrator, and activator. The low-energy pump photons are firstly harvested by a sensitizer (Yb^{3+}) *via* GSA process, and the ETU process subsequently occurs by transferring the energy to a neighboring accumulator (Tm^{3+}), promoting the electrons of the accumulator to higher excited states, followed by the energy extraction

from the accumulator to a migrator (Gd^{3+}), where the energy is randomly hopped through the migrator ion sublattice until trapped by an activator ion. Upconversion emissions generate when electrons drop back to the ground state. Meanwhile, upconversion emissions from the accumulator ions can also occur. A key feature of the EMU process is that the energy absorbed by the sensitizer can be stored within the accumulator and then transfer to the activator. The stringent selection of activators thus can be primarily exempted. Moreover, luminescence quenching, owing to the activator composition and concentration, is minimized, benefiting from the core-shell layout. As a consequence, multicolor upconversion emissions can be realized by activators that barely have long-lived intermediate energy levels.

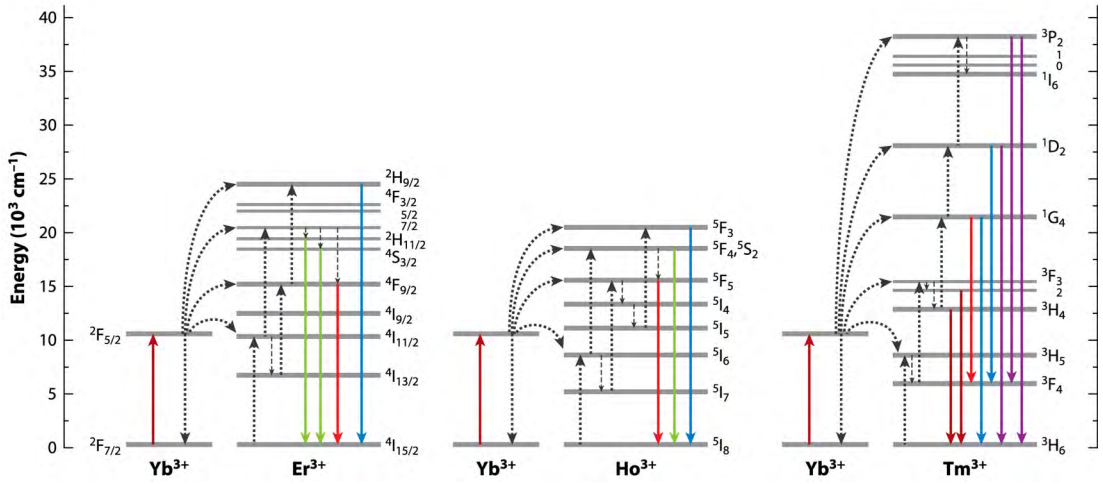

Fig. 1.4 Energy-level diagrams and proposed UC energy transfer pathways in the Yb/Er, Yb/Ho, and Yb/Tm pairs. Reproduced with permission from ref. [2]. Copyright 2015 Annual Reviews.

These mechanisms described above can operate alone or in combination, and efficient photon UC has been observed to occur primarily in the Ln elements, while the highest UC efficiency at low excitation power is realized only for a few Ln^{3+} ions, like Er^{3+}, Ho^{3+}, and Tm^{3+}. The proposed UC energy transfer pathways with the Yb^{3+} as the sensitizer, Er^{3+}, Ho^{3+}, or Tm^{3+} as the activator is shown in Fig. 1.4.

1.4 Synthetic Methods for Upconversion Materials

As the host, dopant, phase, size, and shape of NPs play important roles in the chemical and optical properties of upconversion NPs, it is essential to develop facile and efficient synthetic strategies in a highly controlled manner. Wet chemical synthetic methods with flexibly adjusted parameters, such as reaction temperature, time, the concentration of precursors and ligands, have been explored to prepare upconversion

NPs. To date, hydro/solvothermal synthesis, thermal decomposition and coprecipitation method are the most commonly used approaches for preparing high-quality upconversion NPs with highly crystallinity, controllable structure, and well-defined morphology.

1.4.1 Hydro/Solvothermal Method

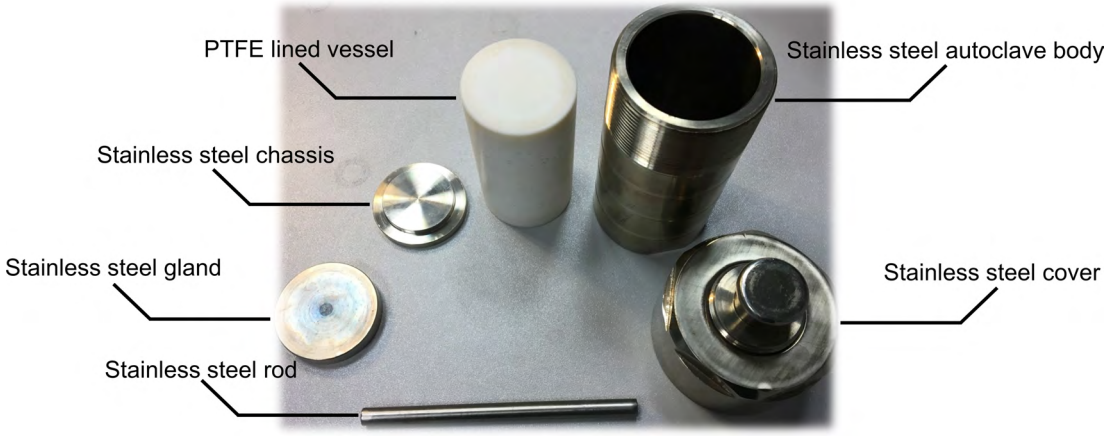

Fig. 1.5 Illustration of Teflon Lined Autoclave Reactor.

The hydro/solvothermal method describes any heterogeneous chemical reactions in the presence of a solvent above the room temperature and at a pressure greater than one atmosphere in a closed system. The term “hydrothermal” is applied when water is used as the solvent. Otherwise, the term “solvothermal” is used. Generally, the reaction is performed in a specialized vessel known as a Teflon-lined autoclave, and the typical structure of an autoclave is shown in Fig. 1.5. The reaction temperature is usually above the critical point of the solvent with a concomitant high-pressure environment generated in the sealed autoclave, whereas traditional solvent-based routes are limited by the boiling point. The high temperature and pressure increase the solubility of reactants and speed up reactions that cannot or hardly occurred at atmospheric conditions. These essential features make the hydro/solvothermal method an effective and convenient process in preparing various inorganic materials with diverse controllable morphologies and architectures in terms of cost and potential for large-scale production.

In 2005, Li’s group developed a LSS strategy to synthesize many different monodispersed inorganic NPs *via* a solvothermal route with OA as the capping agent[37]. A phase transfer and separation mechanism occur at the interfaces of the liquid, solid, and solution phases. Metal ions can react with other anions after the

transfer from the aqueous solution to the solid phase (Fig. 1.6a). Employing the LSS solvothermal method with a slight modification, a variety of LnF_3 and $NaLnF_4$ nanocrystals with controllable crystal size, phase, and morphology were prepared (Fig. 1.6b)[38].

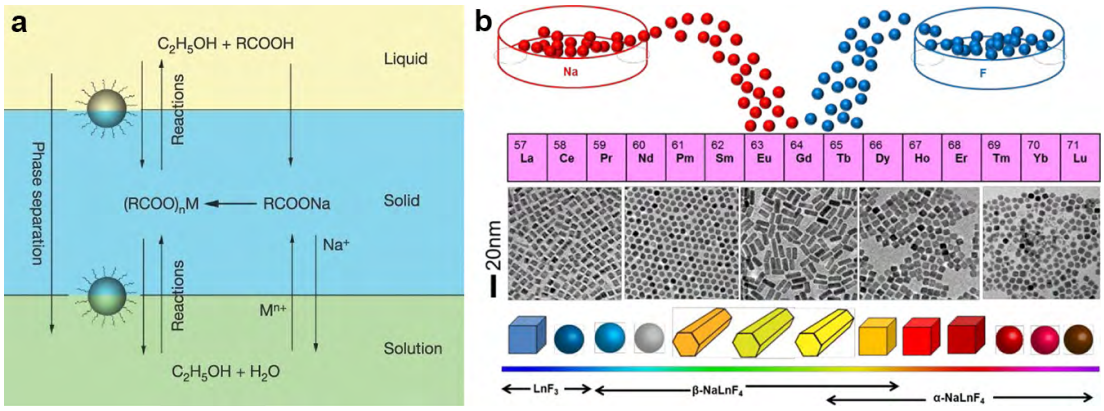

Fig. 1.6 (a) Scheme of LSS phase transfer synthetic strategy. (b) Schematic illustration of the syntheses of Ln series based $NaLnF_4$ nanocrystals. TEM images of the representative samples from left to the right are CeF_3, β-$NaPrF_4$, β-$NaGdF_4$, α-$NaDyF_4$, and α-$NaYbF_4$. A phase transition along with shape evolution from LnF_3 (nanocubes) to hexagonal β- (spherical dots and NRs) and cubic α-$NaLnF_4$ (nanocubes and spherical dots) was observed. Reproduced with permission from ref. [37, 38]. Copyrights 2005 Nature Publishing Group, 2015 American Chemical Society.

Recently, Liu's group developed a novel Gd^{3+}-doping strategy to control the crystal size, phase, and optical properties of $NaYF_4$ nanocrystals simultaneously with the help of the LSS solvothermal method (Fig. 1.7)[39]. They disclosed that the Gd^{3+} doping at precisely defined concentrations in the reaction solution can not only result in a rapid cubic-to-hexagonal phase transformation within two hours in the solvothermal process but also lead to a remarkable decrease in the reaction temperature to as low as 230 °C for the formation of ultrasmall hexagonal upconversion NPs, which is inaccessible by other methods with such low reaction temperature. Gd^{3+} impurity doping induced the change of size and morphology, and phase transformation was further verified when $NaLuF_4$ was used as the host matrix[40]. Zhao's group report another significant progress by using a modified LSS solvothermal method to generate well-defined nanoarrays of tubes and rods of upconversion NPs under different reaction conditions[41]. In addition to the aforementioned upconversion NPs, other fluoride-based matrixes like CaF_2[8], SrF_2[42], and BaF_2[43] can also be readily obtained *via* the modified LSS solvothermal method.

Apart from the preparation of hydrophobic upconversion NPs using OA as the capping

agent, hydrophilic upconversion NPs can be obtained directly in the presence of hydrophilic ligands *via* the simple one-pot hydro/solvothermal synthesis strategy. Sodium citrate[44], ethylenediaminetetraacetic acid[45], PVP[46], cetyltrimethylammonium bromide[47], PEI [19], PAA[46], and 2-aminoethyl dihydrogen phosphate [48] have been applied as hydrophilic ligands to prepare nano-/micro-sized upconversion NPs.

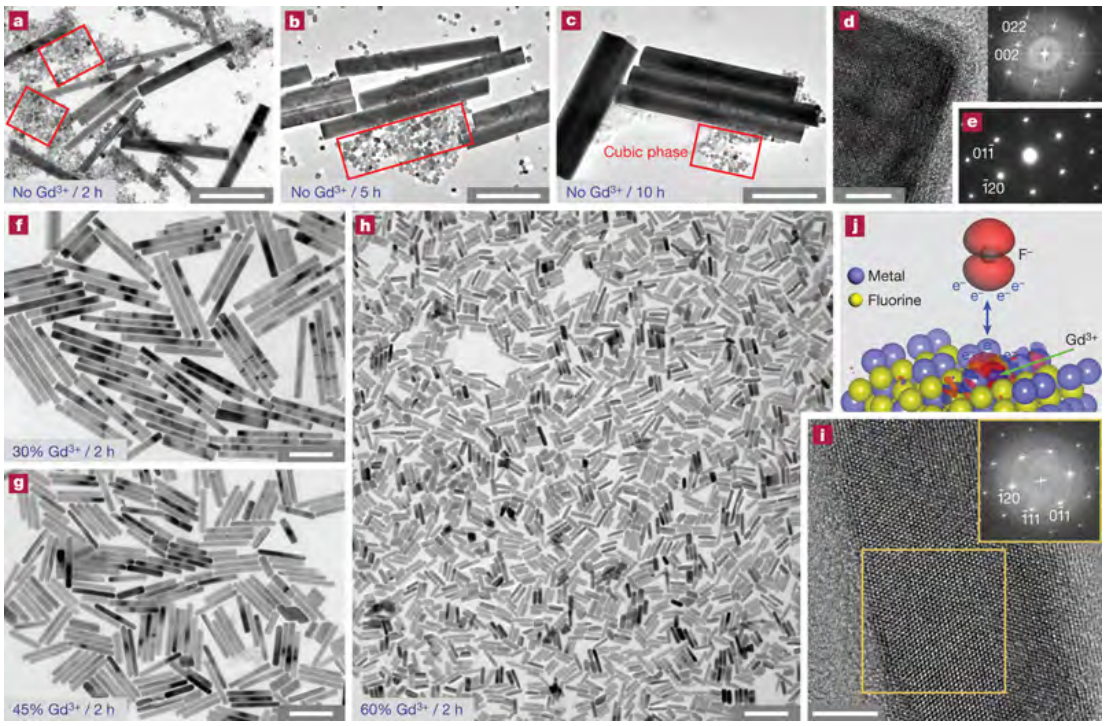

Fig. 1.7 (a)-(c) TEM images of $NaYF_4$:Yb,Er products obtained after heating for 2, 5, and 10 h in the absence of Gd^{3+} dopant ions. HR-TEM image (d) and selected area electron diffraction pattern (e) of the nanocube. (f)-(h) TEM images of the $NaYF_4$:Yb,Er products obtained after heating for 2 h in the presence of 30, 45, and 60 mol% Gd^{3+} dopant ions, respectively. (i) HR-TEM image of the NRs. (j) DFT calculation. Scale bars are 500 nm for panels (a)-(c), 200 nm for panels (f)-(h) and 5 nm for panels d and i. Reproduced with permission from ref. [39]. Copyright 2010 Nature Publishing Group.

1.4.2 Thermal Decomposition

The thermal decomposition strategy usually involves the heat-induced chemical decomposition of organometallic precursors in high-boiling-point organic solvents at elevated temperatures in an oxygen-free environment. For the typical synthesis of fluoride-based upconversion NPs, metal trifluoroacetate is generally used as a precursor, OA, OM, ODE, and tri-n-octylphosphine oxide are commonly used as the organic solvents. By precisely tailoring the experimental parameters, like the choice of the solvents, the concentration of metal precursors, reaction time and temperature, high-quality upconversion NPs with good crystallinity, narrow size distribution and

excellent optical properties can be readily obtained.

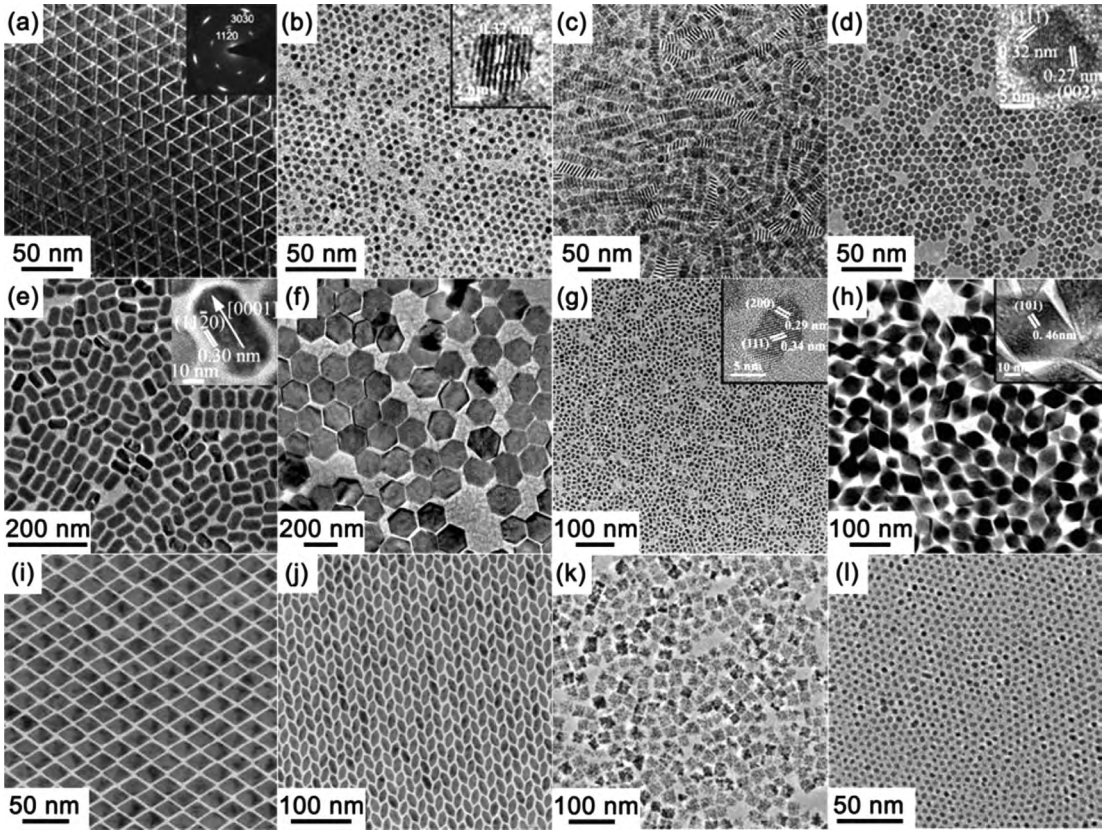

Fig. 1.8 TEM images of LaF_3 (a), LaOF:Eu (b), LaOCl (c), cubic phased $NaYF_4$ (d), hexagonal phased $NaYF_4$ (e), hexagonal phased $NaYF_4$:Yb,Er (f), $KPrF_4$ (g), $LiErF_4$ (h), DyF_3 (i), TbF_3 (j), CeO_2 (k), and CeO_2 (l) NPs synthesized from thermal decomposition. Reproduced with permission from ref. [49-56]. Copyrights 2005, 2008, 2009, and 2012 American Chemical Society, 2009 Royal Society of Chemistry, 2008 John Wiley and Sons, 2013 Nature Publishing Group.

In 2005, Yan's group firstly reported the thermal decomposition synthesis of LaF_3 triangular nanoplates with the $La(CF_3COO)_3$ as a single-source precursor and OA/ODE as the organic solvents[49]. Chow et al. adopted this method to synthesize ultrasmall upconversion NPs for bioapplications with the employment of OM as the reaction solvent and as the surface ligand[57]. By manipulating the reaction time and the ratio of sodium to lanthanide trifluoroacetates dissolved in a mixed solution of OA and ODE, the upconversion NPs can be rationally tuned to morphologies from spherical NPs to NRs, hexagonal nanoprisms, and nanoplates[58]. Monodispersed LnOF[50], LaOCl nanoplates[51], Ln-doped $NaYF_4$ nanocrystals[52], $KLnF_4$ (Ln = Pr to Gd, Y) nanopolyhedra, $LiLnF_4$ (Ln = Tb to Lu, Y) rhombic nanoplates[53], high-quality LnF_3 nanoplates[54], and uniform CeO_2 NPs with controlled morphology[55, 56] can be prepared when appropriate precursors and solvents are used (Fig. 1.8).

Despite the recent progress, the most significant limitation of the decomposition of trifluoroacetates is the production of various deleterious fluorinated and oxyfluorinated carbon gases (including trifluoroacetic anhydride, carbonyl difluoride, trifluoroacetyl fluoride, and tetrafluoroethylene), and thus all the experiments must be carefully carried out in well-ventilated hoods, and great care should be taken so as not to inhale any of the evolved gases. Obviously, the thermal decomposition of the trifluoroacetate is not green for the environment and bioapplications.

1.4.3 High-Temperature Coprecipitation

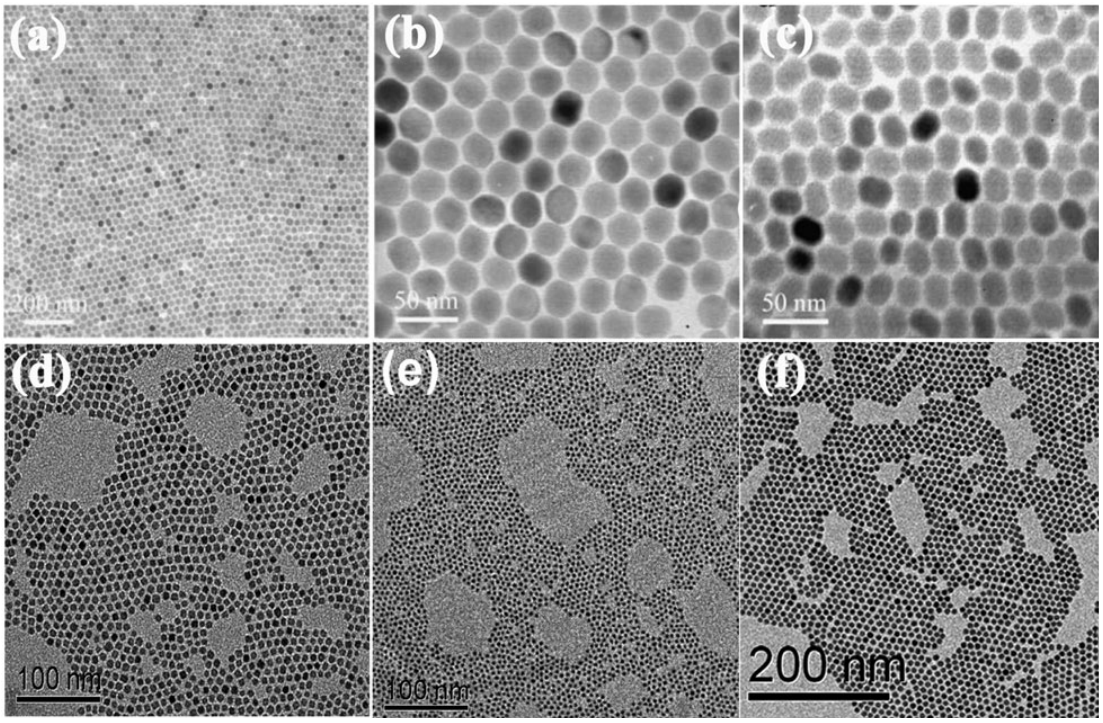

Fig. 1.9 TEM images of Ln-doped β-$NaYF_4$ (a-c), ultrasmall CaF_2 (d, e), and $NaGdF_4$ NPs (f). Reproduced with permission from ref. [59-61]. Copyrights 2008 IOP Publishing, 2010 and 2013 John Wiley and Sons.

In contrast to the other two techniques above, specialized reaction vessels, stringent reaction conditions, complex synthetic procedures, and long reaction times are not required for high-temperature coprecipitation. It is also considered to be one of the most efficient methods to prepare ultrasmall upconversion NPs. The pioneering work was done by van Veggel and co-workers, who employed the coprecipitation method to fabricate Ln-doped LaF_3 NPs[6]. Chow and co-workers reported a refined coprecipitation method to synthesize small Ln-doped LaF_3 NPs with narrow size distribution[12]. The di-n-octadecyldithiophosphate was used as the stabilizing agent to control the particle growth in both cases. In 2004, Haase's group first reported the

synthesis of 5-30 nm cubic phase Ln-doped $NaYF_4$ NPs in the presence of the high-boiling solvent (N-(2-hydroxyethyl)ethylenediamine) *via* the coprecipitation method[7].

In an attempt to generate high uniform hexagonal-phased upconversion NPs with narrower size distributions and higher luminescence efficiencies than those produced by conventional coprecipitation methods, Zhang's group developed a user-friendly high-temperature coprecipitation method with ODE as the solvent and OA as the capping agent[59]. Small amorphous $NaYF_4$ coprecipitates were first formed at room temperature, and uniform nanocrystals were then generated *via* an Ostwald ripening mechanism at elevated temperatures (300 °C). By changing the surfactant concentration, nanosphere, nanoplate, and nanoellipse shaped Ln-doped $NaYF_4$ NPs can be produced (Fig. 1.9a-c). Since then, this method has been adopted to prepare monodisperse Ln-doped $NaLuF_4$[62], $NaScF_4$, $NaTbF_4$, and LaF_3[63] NPs. Moreover, monodisperse and uniform Ln-doped upconversion NPs with ultrasmall sizes (<10 nm) can also be obtained through this method (Fig. 1.9d-f)[60, 61]. Another significant demonstration was reported by Liu and co-workers[64]. They were able to fabricate a diverse library of monodisperse sub-50 nm upconversion NPs with 3D nano-architectures through the high-temperature coprecipitation method. The scope of this synthetic method was further expanded in the preparation of high-quality core-shell-structured upconversion NPs[65, 66].

1.5 Strategies for Enhancing UCL

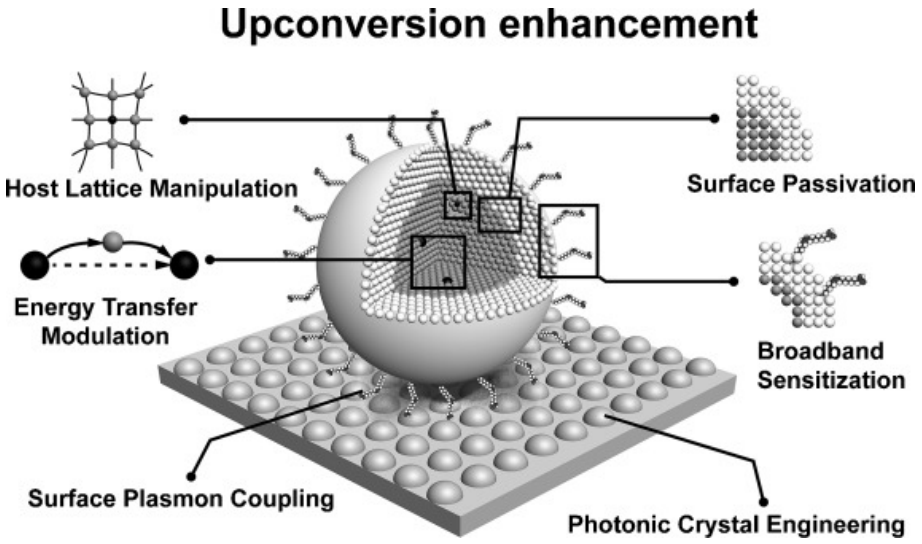

Fig. 1.10 Schematic illustration of the main strategies for enhancing luminescence in Ln-doped upconversion NPs. Reproduced with permission from ref. [67]. Copyright 2014 John Wiley and Sons.

Despite significant progress achieved with the precise control over shape, size, and emission profile of Ln-doped upconversion NPs, the inherent low upconversion efficiency of upconversion NPs still significantly limits their practical applications. Up to now, a range of approaches including host lattice manipulation, energy transfer modulation, surface passivation, surface plasmon coupling, broadband sensitization, and photonic crystals engineering have been proposed for enhancing the UCL (Fig. 1.10).

1.5.1 Host Lattice Manipulation

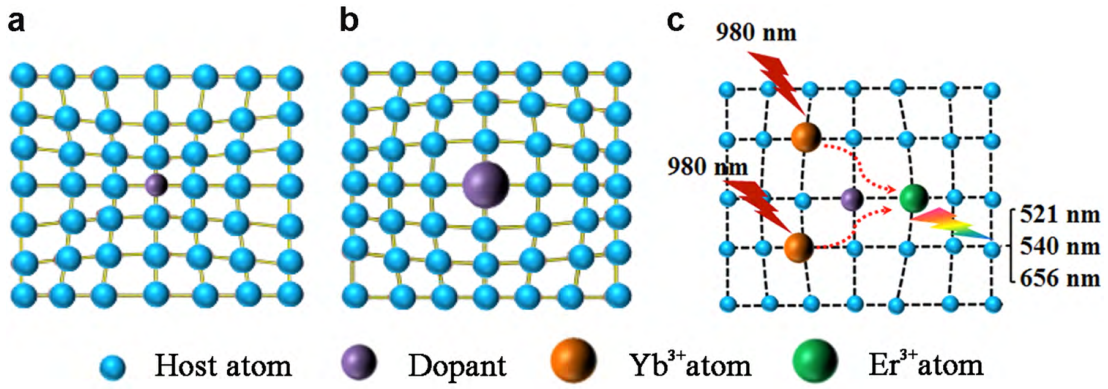

Fig. 1.11 Crystal lattice contraction (a) and expansion (b) as a result of the substitution of a host atom with a dopant of varied size. (c) Illustration of Yb^{3+} and Er^{3+} doped upconversion crystal. Reproduced with permission from ref. [68]. Copyright 2018 Nature Publishing Group.

The UCL of Ln-doped upconversion materials mainly derives from intra f-f electronic transitions, which can be manipulated by adjusting the local crystal field. Lower symmetry of the host lattice by tailoring the crystal structure will make a contribution to the enhancement of the UCL intensity, which can be modified simply by ion doping (Fig. 1.11)[68]. The asymmetric change in the crystal field will promote the intermixing of the 4f energy levels with the high electronic configuration in Ln ions, resulting in the UCL enhancement. Early studies had focused on the lithium doping approach to increase the UCL, as the metallic lithium-ion possesses the smallest ionic radius and can be easily incorporated into the host lattice. By incorporation Li^+ in upconversion NPs, Wang and Nann realized a 30-fold increase in the UCL intensity[69]. Eight-fold enhancement of blue emission was observed in the Li^+ ion doped $NaYF_4$:Yb,Tm NPs by Zhang's group in 2013[70]. Moreover, an enhancement of the red emission was found in gadolinium-based upconversion NPs[71]. Apart from Li^+ ion doping, some other transition metal ions, like Sc^{3+}[72], Zn^{2+}[73], Bi^{3+}[74], and Fe^{3+}[75], had been successfully doped into the host matrix, leading to an enhancement in photon upconversion.

1.5.2 Energy Transfer Modulation

Energy transfer modulation is another commonly adopted approach to enhance the UCL. The upconversion process of upconversion NPs is largely based on the energy transfer mechanism, which usually involves radiative energy transfer between the sensitizer and the activator.

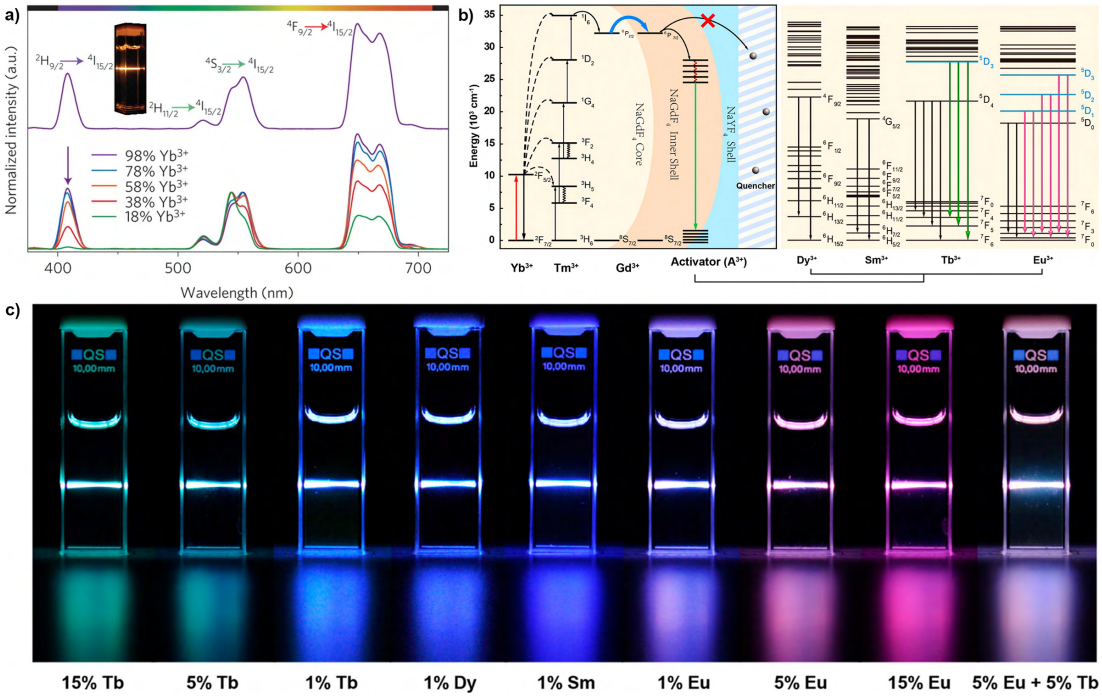

Fig. 1.12 (a) The upconversion emission spectra of KYb_2F_7:Er (2 mol%) (top) and KYb_2F_7:Er,Lu (2/0-80 mol%) (bottom) NPs obtained under a 980 nm laser excitation. Inset: a typical photograph of KYb_2F_7:Er nanocrystals. (b) Proposed energy-transfer mechanisms in the multi-layered NPs. (c) Luminescence photographs of representative samples with extra $NaYF_4$ layer under irradiation of a 980 nm laser. Reproduced with permission from ref. [76, 77]. Copyrights 2014 Nature Publishing Group, 2012 American Chemical Society.

In general, a high doping level of activator ions (Er^{3+}, Ho^{3+}, or Tm^{3+}) in Ln-doped upconversion NPs had been proposed to maximize the excitation energy transfer absorbed by the Yb^{3+} sensitizer. However, a high concentration of the activator may also induce an increase in non-radiation cross-relaxation, leading to the self-quenching of the UCL. To address this issue, Jin's group reported designed upconversion NPs with high Tm^{3+} dopant concentration[78]. High-powered excitation irradiation, which could alleviate the cross-relaxation quenching effect by the high activator concentration, was used to achieve a 70-fold enhancement in UCL. Another strategy is to increase the sensitizer dopant concentration to efficiently utilize excitation energy. However, immense quenching of luminescence will occur with high doping levels of

Yb^{3+} in conventional upconversion NPs, owing to the increased probability of random energy migration to lattice or surface defects. Liu's group proposed A new class of orthorhombic KYb_2F_7:Er nanocrystals with a high doping concentration of the sensitizer (Yb^{3+})[76]. Owing to the unique lattice arrangement, which can effectively lower the migration-involved energy loss even at a high dopant concentration of Yb^{3+}, an efficient improvement of the UCL was achieved (Fig. 1.12a).

In addition, the excitation energy can be exchanged between the host matrices and the dopants, thus, the UCL could be increased at a specific wavelength. Earlier studies had proved the strong interaction between Mn^{2+} and Er^{3+} ions in MnF_2:Yb,Er NPs[79], resulting in intensity ratio enhancement of red-to-green emission. Similar studies also displayed the single-band emission in $KMnF_3$[80], $NaMnF_3$[81], and $NaYF_4$[82] as host lattices. Another case that can realize the excitation energy with the dopants is the gadolinium-based host material. In favor of the energy transfer process, fast rates of energy migration over a long distance can be realized through the Gd^{3+} sublattice. Liu's group designed a core-shell structure with various Ln ions incorporated into different layers with defined concentrations, realizing efficient UCL for a large array of Ln activators (Eu^{3+}, Dy^{3+}, Tb^{3+}, and Sm^{3+}) without long-lived intermediate energy states[14]. To prevent the surface quenching of the migrating energy, a core-shell-shell structure with a $NaYF_4$ layer grown onto the $NaGdF_4$:Yb,Tm@$NaGdF_4$:A (A = activator ion) NP was further developed (Fig. 1.12b, c)[77]. Very recently, Wang's group realized enhanced multiphoton upconversion through spatial confinement of energy migration by constructing $NaYF_4$@$NaYbF_4$:Tm@$NaYF_4$ core-shell-shell nanostructure[83].

1.5.3 Surface Passivation

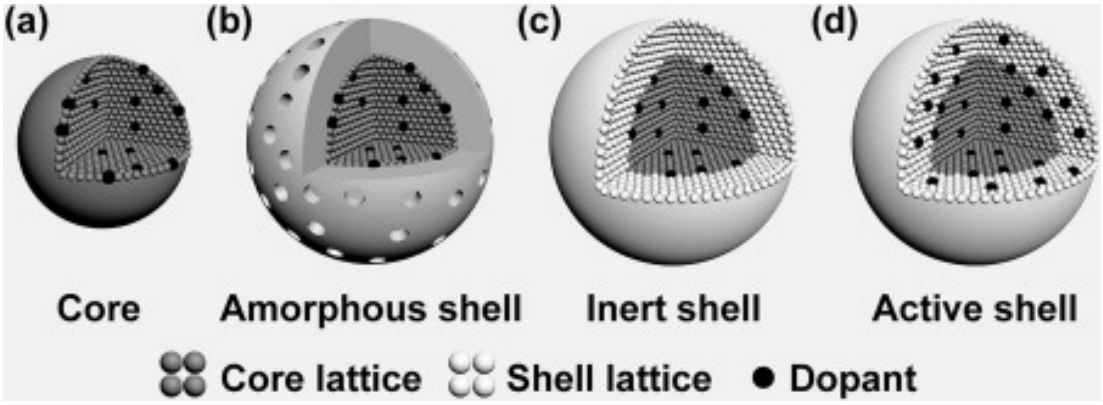

Fig. 1.13 Schematic illustrations of different types of core-shell structure for enhanced UCL. (a) Core NP. (b) Amorphous shell coating. (c) Inert crystalline shell coating. (d) Active-shell coating. Reproduced with permission from ref. [67]. Copyright 2014 John Wiley and Sons.

Compared with bulk upconversion materials, Ln-doped upconversion NPs exhibit lower luminescence due to surface quenching caused by their high surface-to-volume ratio. A large portion of dopant ions will be trapped on the outermost surface of the NPs after the doping processes. Therefore, the UCL can be readily affected by surface impurities, ligands, and solvent molecules through multi-phonon relaxation processes. A shell deposition including amorphous, inert, and active shell (Fig. 1.13), provides another strategy to enhance the UCL by eliminating the surface defect, and spatially confined dopant ions in the interior core.

Silica is the most common material to be used as an amorphous shell[84]. Zhang's group developed a microemulsion method to coat silica onto hydrophobic upconversion NPs[85], the silica shell thickness can be precisely controlled from 20 to 100 nm by tuning the addition amount of tetraethyl orthosilicate. In addition, the utilization of the same composition as the host lattice as an optically inactive shell not only provides a strong crystal field but also effectively prevents the transfer of energy to the particle surface. Yi and Chow first reported approximately 30-fold improvement in the UCL with a 1.5 nm-thick $NaYF_4$ shell coated on $NaYF_4$:Yb,Er/Tm nanocrystals[86]. This approach was further extended to other host materials, such as $NaGdF_4$[87] and KYF_4[88]. Moreover, the different chemical composition can also be constructed as an inert-shell significantly enhance the UCL[89]. In 2009, Capobianco and co-workers reported an enhancement of the UCL in $NaGdF_4$:Yb,Er NPs coated with a thin $NaGdF_4$:Yb active shell[90]. The sensitizer modified shell allows efficient energy transfer to the activators confined in the core and prevents the transfer of excitation energy to the particle surface. Apart from the sensitizer-involved shell, the activator-modified shell can also be applied to enhance the UCL. Zhang and co-workers reported a remarkable enhancement in the emission intensity through a designed $NaYF_4$@$NaYF_4$ core-shell structure with Yb/Tm doped in the core and Yb/Er doped in the shell[91]. Based on the same method, various core-shell materials with enhanced luminescence could be constructed[60, 92, 93].

1.5.4 Surface Plasmon Coupling

Surface plasmon coupling is another effective approach to improve the UCL. surface plasmon resonance, known as the collective oscillation of electrons on the metal surface, are able to propagate along a metallic surface and generate intense local electromagnetic fields in the vicinity of metal nanostructures. Consequently, metal NPs,

capable of coupling with upconversion NPs, have been regarded as effective light-trapping units to boost the efficiency of the upconversion process. The surface plasmon can considerably affect the luminescence of upconversion NPs by enhancing the absorption of the sensitizer through the electric-field coupling, improving the radiative decay rate of the activator, and increasing energy transfer from the sensitizer to the activator. However, the surface plasmon resonance greatly depends on the geometric configuration of the metal NPs. Therefore, it is important to optimize the plasmonic structure to enhance the UCL.

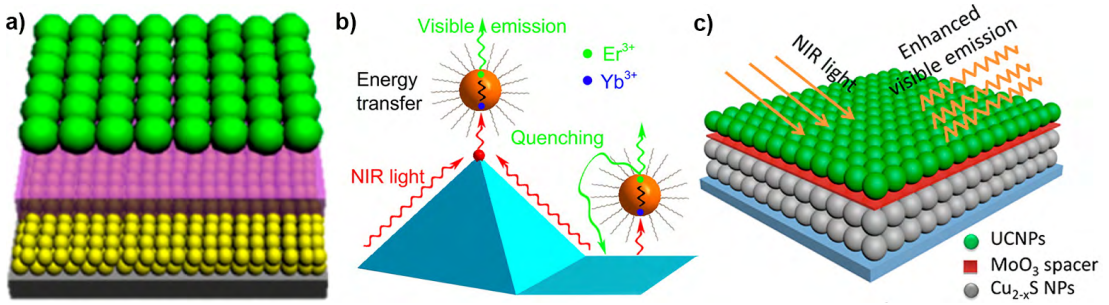

Fig. 1.14 (a) Schematic structure of a layer of Au or Ag NPs, a thin Al_2O_3 layer, and a monolayer of upconversion NPs. (b) Schematic of the energy transfer, upconversion, and quenching processes on the top and bottom of the gold pyramid substrate. (c) Schematic illustration of the $Cu_{2-x}S/MoO_3/NaYF_4$ hybrid structure. Reproduced with permission from ref. [94-96]. Copyrights 2012, 2014, and 2016 American Chemical Society.

In 2012, Saboktakin et al. fabricated a noble metal/Al_2O_3/upconversion multi-layered structure to enhance the UCL (Fig. 1.14a)[94]. They found that the luminescent improvement was dependent on the thickness of the oxide spacer layer and the type of noble metal NPs. the largest enhancement in luminescence was found to be 5.2-fold for Au NPs with a spacer thickness of 5 nm and 45-fold for Ag NPs with a spacer thickness of 10 nm. Zhang and co-workers designed a 3D plasmonic nanoantenna architecture consisting of liftable SiO_2 pillars encapsulated with different types of Au nanostructures[97], and the plasma frequency could be adjusted by the height of SiO_2 pillars. A significant 310-fold enhancement of UCL was observed when the resonant-absorption peak was adjusted to approximately 920 nm with a pillar height of 75 nm. Moreover, Kang and co-workers synthesized hybrid plasmonic upconversion nanocomposites consisting of $Au@SiO_2$ coupled with $NaGdF_4$:Yb,Nd@$NaGdF_4$:Yb,Er@$NaGdF_4$[98], realizing an enhancement of the UCL up to 20 folds, and precise emission color tuning upon excitation at 808 nm *via* the adjustment of the SiO_2 spacer thickness. To increase the energy transfer from the sensitizer to the activator, Sun and co-workers reported a 6-fold rate increase in the

resonant energy transfer from Yb^{3+} to Er^{3+} by resonant surface plasmon polaritons waves using gold pyramid arrays (Fig. 1.14b)[95]. Meanwhile, they also observed the strong metal-mediated quenching of the green fluorescence on flat gold surfaces. In addition to using noble metals as surface plasmon materials, heavily doped semiconductor NPs, which are able to generate surface plasmon resonances, can also be used to enhance the UCL. $Cu_{2-x}S$ (Fig. 1.14c)[96] was used to substantially improve the UCL intensity of upconversion NPs, and upconversion NPs/WO_{3-x} hybrids exhibited a 500-fold enhancement at 521 nm emission[99].

1.5.5 Broadband Sensitization

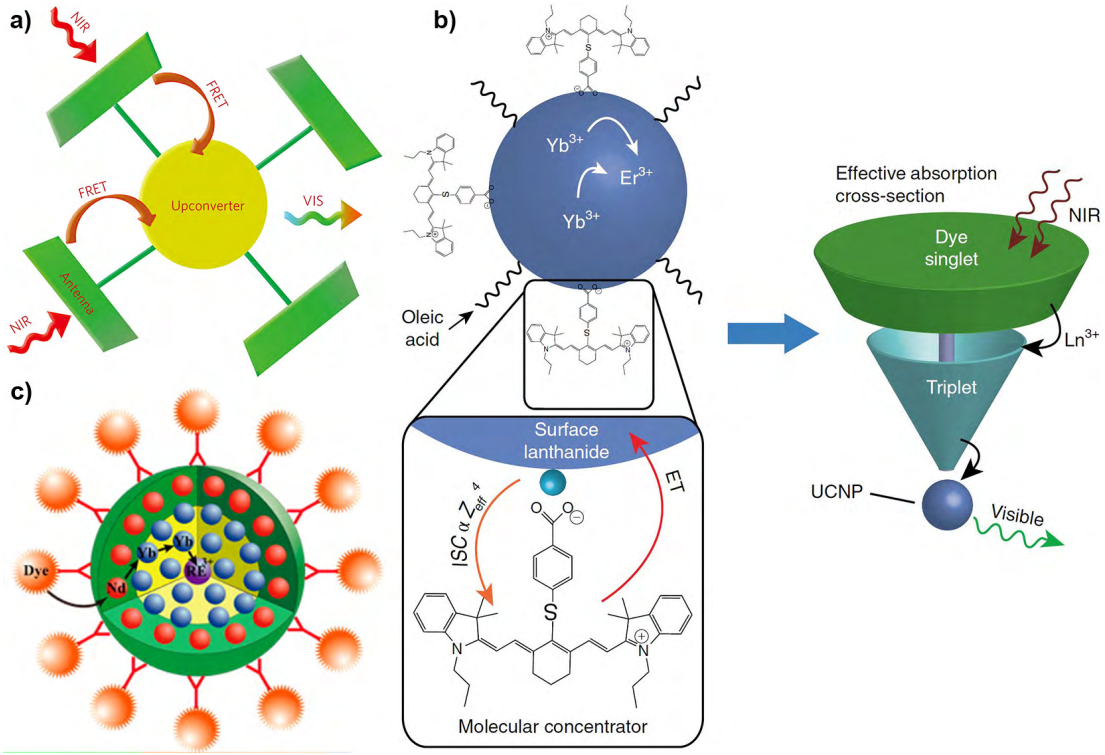

Fig. 1.15 (a) Principal concept of the dye-sensitized NP. (b) Depiction of the antenna-like nature of IR806 in sensitizing the upconversion NPs, conveying the much larger absorption cross-section of IR806 relative to upconversion NPs. (c) Energy-cascaded upconversion in dye-sensitized core/shell nanocrystals. Reproduced with permission from ref. [22, 23, 28]. Copyrights 2012 and 2018 Nature Publishing Group, 2015 American Chemical Society.

The intrinsic limitation of Ln ions with weak and narrow-band absorption influences their light-harvesting ability and restrict the UCL. To address this problem, organic dyes with large absorption cross-sections have been proposed as broadband sensitizers to couple with upconversion NPs to improve upconversion efficiency, where this improvement derives from their large absorption cross-sections, high light absorption

capacity, and tunable excitation wavelength[100]. In general, organic dyes act as antennas to absorb NIR light in a strong and broad manner and transfer their energy to the Ln sensitizers in upconversion NPs.

By applying this strategy, Zou and co-workers first reported the IR-806-sensitized $NaYF_4$:Yb/Er NPs with a broadband wavelength absorption (Fig. 1.15a)[22]. The dye-sensitized upconversion NPs achieved a remarkable 3,300-fold increase in luminescence intensity owing to increased absorptivity and broadened absorption spectrum. Moreover, David and co-workers designed dye/upconversion NPs hybrids with a 33,000-fold increase in brightness and a 100-fold increase in upconversion efficiency[23], and discovered the critical mechanisms of improved upconversion performance by NIR dye antennas mediated upconversion NPs (Fig. 1.15b). In addition, NIR dye-sensitized core/shell upconversion nanocomposites were produced to eliminate the surface-related luminescence quenching. In 2015, Prasad's group introduced a new concept of energy-cascaded upconversion using NIR dye-sensitized $NaYbF_4$:Tm@$NaYF_4$:Nd core/shell NPs (Fig. 1.15c)[28], realizing a broad spectral range of infrared excitation and high upconversion quantum efficiency. To date, various organic dyes were applied to broaden the light absorption range and boost the upconversion efficiency[24-27, 101-103].

1.5.6 Other Strategies

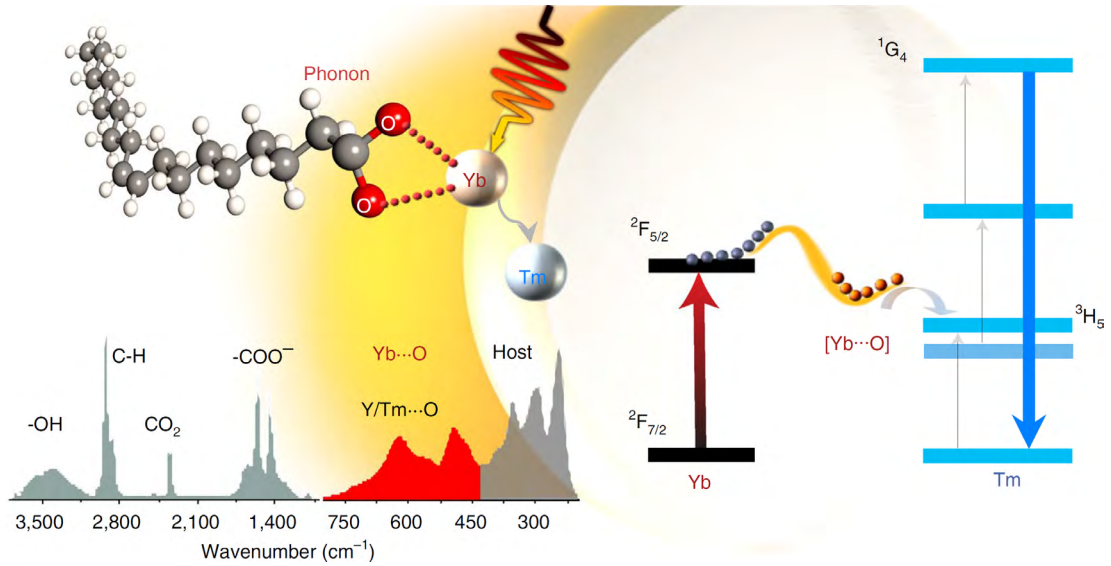

Fig. 1.16 Schematic illustration of the surface-phonon-enhanced upconversion process. Reproduced with permission from ref. [104]. Copyright 2018 Nature Publishing Group.

Apart from the above-mentioned methods, some other strategies were proposed to

improve the UCL. Very recently, Jin's group built a high-efficiency upconversion system with heat-favorable phonons existing at the surface[104]. The Yb-O chelating, which acts as surface phonons, promotes the energy transfer from the sensitizers to the activator, achieving 2,000-fold enhancement in blue emission for Yb,Tm-doped upconversion NPs at an elevated temperature (Fig. 1.16). Other feasible strategies, including photonic crystal engineering and super-high-power excitation, had also been proposed and validated for improving upconversion efficiency[78, 105].

1.6 Emerging Applications

In stark contrast to semiconductor quantum dots and organic dyes, upconversion NPs feature excellent chemical and optical properties, including large anti-Stokes shifts, long fluorescence lifetimes, sharp multicolor emissions, low cytotoxicity, as well as high chemical- and photo-stability. Based on these outstanding merits, upconversion NPs are regarded as promising luminescent materials for applications in the optical field.

1.6.1 Bioimaging and Biosensing

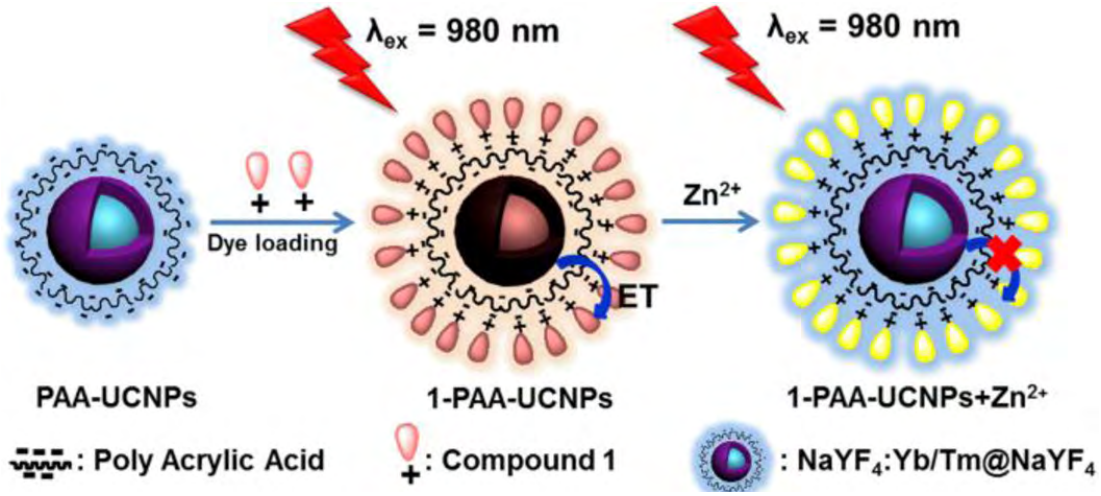

Fig. 1.17 Schematic illustration of the synthesis of chromophore-assembled upconversion NPs and their response to Zn^{2+}. Reproduced with permission from ref. [106]. Copyright 2015 American Chemical Society.

Zhang's group reported a general approach to prepare single-band upconversion NPs with different colors[107]. When conjugated with the antibody, multiplexed simultaneous in situ detection of tumor biomarkers in breast cancer cells and tissue specimens. Compared with classical technology, it provides more accurate results for the quantification of proteins at low levels.

Peng and co-workers designed chromophore-assembled upconversion NPs nanoprobes with the ability of selective sensing of Zn^{2+}[106]. The FRET process occurred between the chromophores and upconversion NPs, inducing the effective UCL quenching. Upon the addition of Zn^{2+}, the UCL subsequently recovered, thus allowing for the detection of Zn^{2+} (Fig. 1.17). The hybrid nanoprobes were also able to be applied for in vitro and in vivo Zn^{2+} sensing in the zebrafish.

1.6.2 Therapeutic Applications

Light, a noninvasive stimulus with tunable wavelength, power, spot size, and irradiation time, has been considered as the most promising medium for responsive therapeutic applications. Photo-triggered theranostics with improved efficiency and minimized side effects possess highly temporal and spatial precision. Photo-sensitive materials are commonly sensitive to visible and UV light. However, UV or visible light featured high energy will lead to serious phototoxicity and low tissue penetration depth. Therefore, upconversion NPs open the door for realizing NIR-controlled theranostics due to their unique optical properties.

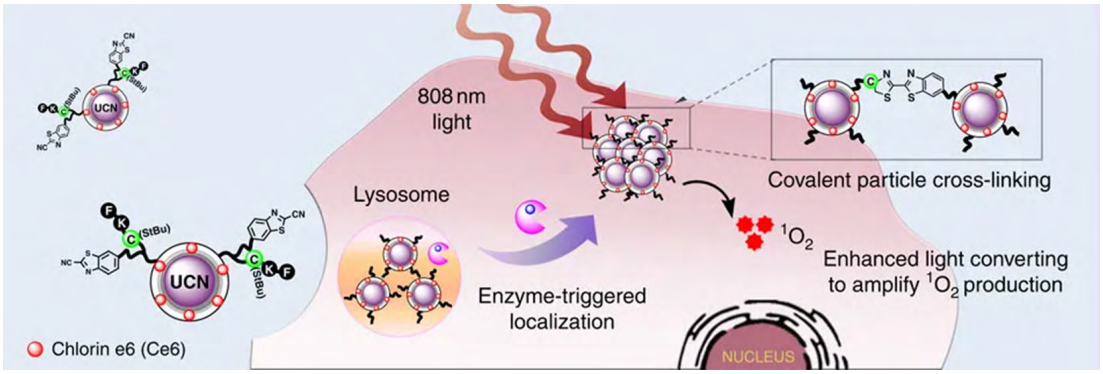

Fig. 1.18 Illustration of the microenvironment-sensitive strategy for covalent cross-linking of peptide-premodified UCNs in tumor areas. Reproduced with permission from ref. [108]. Copyright 2016 Nature Publishing Group.

Ai and co-workers designed a tumor microenvironment-responsive strategy for covalent cross-linking of peptide-modified upconversion NPs (Fig. 1.18)[108], leading to the accumulation of upconversion NPs. Thus, enzyme-triggered accumulated upconversion NPs significantly magnified the UCL upon 808 nm irradiation, and further amplifies the singlet oxygen production from the photosensitizers on upconversion NPs for the photodynamic therapy against malignant tumors in vitro and in vivo, realizing outstanding tumor inhibition. In 2019, Liu and co-workers designed a

mitochondria-specific, NIR light-triggered photodynamic therapy nanoplatform with Janus nanostructures consisting of Nd^{3+}-sensitized upconversion NPs and porphyrinic-based metal-organic frameworks[109]. By virtue of the efficient upconversion process and energy transfer from upconversion NPs to the metal-organic framework domain in the Janus structure, the hybrid nanoplatform allows for the generation of $^1O_2$ under irritation with 808 nm NIR laser, which effectively minimize the laser irradiation-induced overheating effect. Furthermore, mitochondria-mediated photodynamic therapy initiated the intrinsic apoptotic pathway, leading to an excellent therapeutic effect over nontargeted therapy.

1.6.3 Upconversion Optogenetics

Optogenetics, a revolutionary biological technique, involves the use of light to precisely control photo-responsive ion channels in neurons[110-112]. Channelrhodopsin-2, a commonly used light-sensitive ion channel protein, can be stimulated by visible light (~470 nm) to open ion pores on the cellular membrane, leading to the penetration of Ca^{2+} and Na^+ into the cytoplasm. However, direct visible light excitation will lead to either low stimulation efficiency or high tissue damage. Compared with visible light, NIR irradiation with high tissue penetration offers an alternative option to manipulate the neural activity. Therefore, upconversion-guided optogenetics becomes feasible in the manipulation of neural tissues.

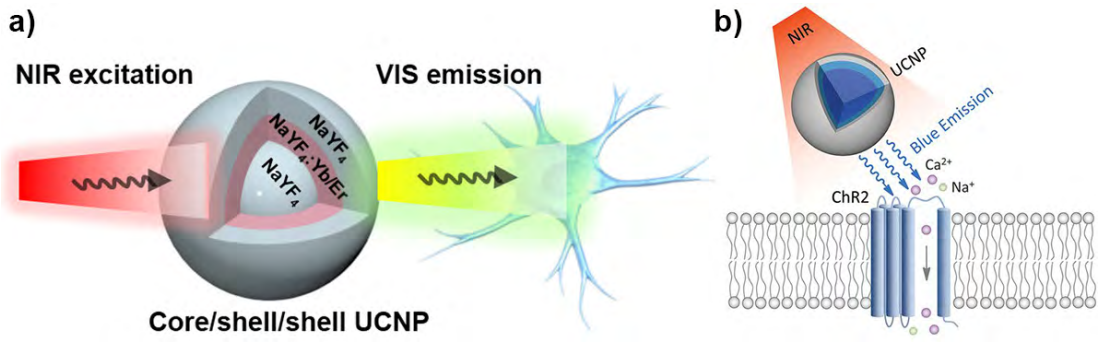

Fig. 1.19 (a) Schematic of using $NaYF_4$@$NaYF_4$:Yb,Er@$NaYF_4$ core-shell-shell upconversion NPs as a transducer to convert NIR irradiation into visible light for inhibiting the activities of neurons expressing eNpHR proteins. (b) Schematic principle of upconversion NP-mediated NIR upconversion optogenetics. Reproduced with permission from ref. [113, 114]. Copyrights 2017 American Chemical Society, 2018 Science Publishing Group.

Shi and colleagues synthesized core-shell-shell upconversion NPs with optimized Yb^{3+} content (Fig. 1.19a)[113], realizing the inhabitation of the electrical activity of the neurons

with NIR irradiation in the targeted sites of the deep rat brain. Very recently, Chen and co-workers demonstrated molecularly tailored upconversion NPs as optogenetic actuators to simulate labeled neurons in the deep brain with a less-invasive optical neuronal activity (Fig. 1.19b)[114]. This effective approach held great potential for neurological disorder therapies and deep brain stimulation.

1.6.4 Upconversion Lasing

Lasing, particularly in the region of deep UV with high photon energy and high beam quality, has broad applications in photonics, physics, and biology. With the advance in crystal technology for the emission wavelengths covering the near-UV, visible, and NIR ranges, various solid-state lasers have been successfully developed as replacements for traditional gas- and liquid-phase lasers. Upconversion-mediated lasers with efficient optical gain media are notably attractive, empowering high efficiency lasing in the near-/deep-UV region.

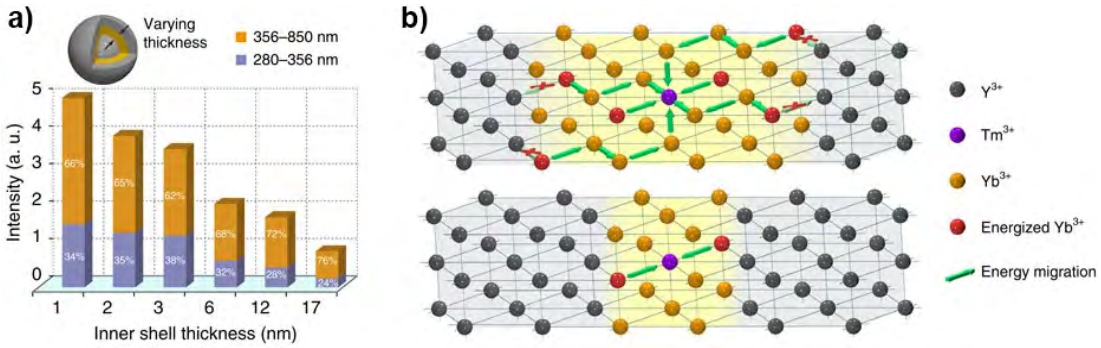

Fig. 1.20 (a) Upconversion emission intensity versus inner shell thickness (1-17 nm). (b) Schematic illustration showing proposed energy transfer from Yb^{3+} to Tm^{3+} in Yb-sublattice of varying dimensions. Reproduced with permission from ref. [83]. Copyright 2016 Nature Publishing Group.

Wang's group designed $NaYF_4$@$NaYbF_4$:Tm@$NaYF_4$ core-shell-shell upconversion NPs with enhanced multiphoton upconversion harnessed by spatial confinement of energy migration in the nanosized structure (Fig. 1.20)[83], realizing efficient five-photon upconverted emission of Tm^{3+}. The designed upconversion NPs were further applied as diode-pumped deep UV lasing. Later on, Jin and co-workers synthesized double-shelled $LiYbF_4$:Tm@$LiYbF_4$@$LiLuF_4$ upconversion NPs, fabricating mass-manufactural UVB microlasers with high optical gain, strong light confinements, and good device repeatability[115].

1.6.5 Anti-Counterfeiting

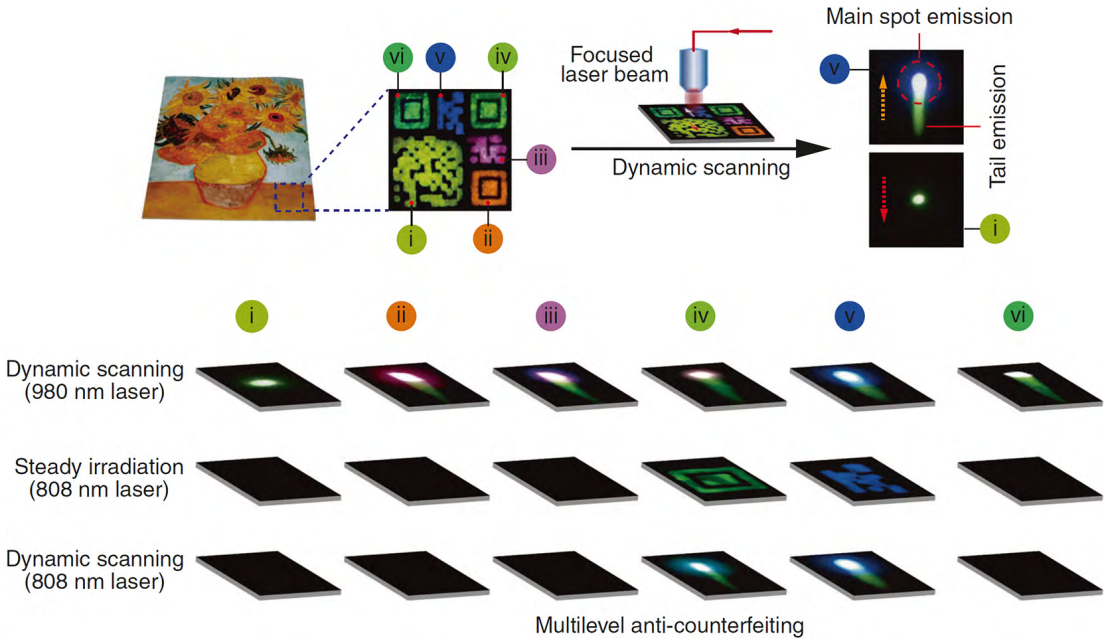

Fig. 1.21 Multilevel anti-counterfeiting application with Mn^{2+}-activated core-shell NPs. Reproduced with permission from ref. [117]. Copyright 2017 Nature Publishing Group.

In contrast to organic dye fluorescence, which is easy to fake and duplicate, Ln-doped upconversion NPs, featuring high chemical- and photo-stability, tunable and multicolor emission wavelength, are favorable for anti-counterfeiting applications.

In 2013, Jin's group reported different lifetime decay rates (from μs to ms) of $NaYF_4$:Yb,Tm nanocrystals under a single-wavelength excitation[116], demonstrating a new approach to multiplexing in the time domain, unlocking a great potential of luminescent upconversion NPs as a powerful analytical technique to manage the complex challenges in life sciences. Very recently, Liu's group designed a particulate platform with the integration of long-lived Mn^{2+}-doped upconversion emission and short-lived Ln-doped upconversion emission[117], allowing feasible excitation at 808 nm and 980 nm irradiation by the precise manipulation of the NP's structure. This platform allows the production of binary temporal codes for efficient data encoding, and making multilevel anti-counterfeiting possible at a single-particle level without the need for time-gated set-up to separate and decode security data (Fig. 1.21).

1.7 Objectives and Outline of Thesis

1.7.1 Research Objectives

Despite the progress that has been made in the field of Ln-doped upconversion materials research including preparation, mechanism, and applications, there is still ample space for improvement in this field. First, upconversion crystals are usually prepared by using OA as the ligand, leading to the hydrophobic nature of the as-made crystals, and postmodifications are necessary prior to most real applications. Therefore, direct preparation of hydrophilic upconversion materials with controllable size and morphology is of great importance. Second, several strategies have been developed to modify the surface property of oleate-capped upconversion materials. However, there still lacks a general method to realize the hydrophobic-to-hydrophilic transition of the upconversion nanocrystals. Third, as the mechanism for sensing applications of upconversion-based materials mainly depends on the FRET process, it is interesting to develop new upconversion-based systems for analytes using other mechanisms, thereby broadening the scientific spectrum of upconversion NPs.

The specific objectives of this thesis were to

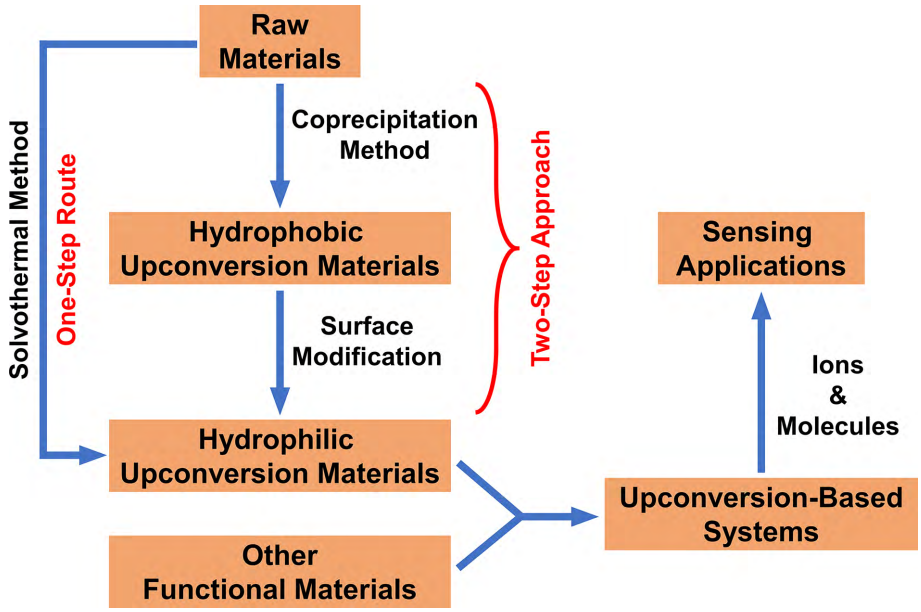

1) Prepare hydrophilic upconversion crystals with controllable size and morphology *via* direct one-pot synthesis, and determine the mechanism of crystal evolution.

2) Develop a fast and efficient approach to realize the conversion of hydrophobic upconversion nanocrystals to hydrophilic ones.

3) Construct new upconversion-based nanosystems for sensing applications by coupling them with other new functional materials.

4) Use a different mechanism for fluorescence sensing of analytes other than simply depend on the FRET process between upconversion materials and analytes.

1.7.2 Thesis Outline

The outline of the thesis is as follows:

In Chapter 1, I have presented a brief introduction of the Ln-doped upconversion materials including criteria for the host, sensitizer and activator selection, mechanisms, synthetic methods and general applications.

In Chapter 2, I will discuss the solvothermal method to prepare Ln-doped upconversion nano-/microparticles with controllable size and shape by changing reaction parameters, such as the dopant, the volume ratio between mixture solvent and the molar ratio between reactants. The results of this chapter have been published in the journal of ChemNanoMat (*ChemNanoMat*, **2021**, 7, 174-183. DOI: 10.1002/cnma.202000564).

In Chapter 3, I will describe an easy-to-process approach to remove the ligand from the surface of oleate-stabilized upconversion NPs using short-chain acids as stripping agents, realizing fast and efficient hydrophobic-to-hydrophilic transition of upconversion NPs. The results of this chapter have been published in the journal of Materials Advances (*Mater. Adv.*, **2020**, 1, 1602-1607. DOI: 10.1039/D0MA00411A).

In Chapter 4, I will demonstrate the integration of upconversion NPs with functional nanomaterials to construct upconversion-based nanocomposites for fluorescence turn-on/off sensing of ions based on the FRET process. The results of this chapter have been published in the journals of Materials Advances (*Mater. Adv.*, **2020**, 1, 1602-1607) and Analyst (*Analyst*, **2021**, DOI: 10.1039/D0AN01954B).

In Chapter 5, I will introduce a non-contact upconversion nanosystem based on the

EEA effect for the fluorescence sensing of H_2O_2 and pH. The results of this chapter have been published in the journal of Nanoscale Advances (*Nanoscale Adv.*, **2021**, DOI: 10.1039/D0NA01045F).

In Chapter 6, I will highlight the conclusions of this thesis and suggest some future directions for Ln-doped upconversion materials.

1.8 References

[1] J.-C.G. Bünzli, Benefiting from the unique properties of lanthanide ions, *Acc. Chem. Res.*, **2006**, 39, 53-61.

[2] L.-D. Sun, H. Dong, P.-Z. Zhang, and C.-H. Yan, Upconversion of rare earth nanomaterials, *Annu. Rev. Phys. Chem.*, **2015**, 66, 619-642.

[3] X. Li, F. Zhang, and D. Zhao, Lab on upconversion nanoparticles: optical properties and applications engineering *via* designed nanostructure, *Chem. Soc. Rev.*, **2015**, 44, 1346-1378.

[4] N. Bloembergen, Solid state infrared quantum counters, *Phys. Rev. Lett.*, **1959**, 2, 84-85.

[5] R.X. Yan, and Y.D. Li, Down/up conversion in Ln^{3+}-doped YF_3 nanocrystals, *Adv. Funct. Mater.*, **2005**, 15, 763-770.

[6] J.W. Stouwdam, and F.C.J.M. van Veggel, Near-infrared emission of redispersible Er^{3+}, Nd^{3+}, and Ho^{3+} doped LaF_3 nanoparticles, *Nano Lett.*, **2002**, 2, 733-737.

[7] S. Heer, K. Kömpe, H.U. Güdel, and M. Haase, Highly efficient multicolour upconversion emission in transparent colloids of lanthanide-doped $NaYF_4$ nanocrystals, *Adv. Mater.*, **2004**, 16, 2102-2105.

[8] G. Wang, Q. Peng, and Y. Li, Upconversion luminescence of monodisperse CaF_2:Yb^{3+}/Er^{3+} nanocrystals, *J. Am. Chem. Soc.*, **2009**, 131, 14200-14201.

[9] K.W. Krämer, D. Biner, G. Frei, H.U. Güdel, M.P. Hehlen, and S.R. Lüthi, Hexagonal sodium yttrium fluoride based green and blue emitting upconversion phosphors, *Chem. Mater.*, **2004**, 16, 1244-1251.

[10] J.-C. Boyer, F. Vetrone, L.A. Cuccia, and J.A. Capobianco, Synthesis of colloidal upconverting $NaYF_4$ nanocrystals doped with Er^{3+}, Yb^{3+} and Tm^{3+}, Yb^{3+} *via* thermal decomposition of lanthanide trifluoroacetate precursors, *J. Am. Chem. Soc.*, **2006**, 128, 7444-7445.

[11] O. Ehlert, R. Thomann, M. Darbandi, and T. Nann, A four-color colloidal multiplexing nanoparticle system, *ACS Nano*, **2008**, 2, 120-124.

[12] G.-S. Yi, and G.-M. Chow, Colloidal LaF_3:Yb,Er, LaF_3:Yb,Ho and LaF_3:Yb,Tm nanocrystals with multicolor upconversion fluorescence, *J. Mater. Chem.*, **2005**, 15, 4460-4464.

[13] J.-C. Boyer, L.A. Cuccia, and J.A. Capobianco, Synthesis of colloidal upconverting $NaYF_4$:Er^{3+}/Yb^{3+} and Tm^{3+}/Yb^{3+} monodisperse nanocrystals, *Nano Lett.*, **2007**, 7, 847-852.

[14] F. Wang, R. Deng, J. Wang, Q. Wang, Y. Han, H. Zhu, X. Chen, and X. Liu, Tuning upconversion through energy migration in core-shell nanoparticles, *Nat. Mater.*, **2011**, 10, 968-973.

[15] J.M.F. van Dijk, and M.F.H. Schuurmans, On the nonradiative and radiative decay rates and a modified exponential energy gap law for 4f-4f transitions in rare-earth ions, *J. Chem. Phys.*, **1983**, 78, 5317-5323.

[16] A.D. Ostrowski, E.M. Chan, D.J. Gargas, E.M. Katz, G. Han, P.J. Schuck, D.J. Milliron, and B.E. Cohen, Controlled synthesis and single-particle imaging of bright, sub-10 nm lanthanide-doped upconverting nanocrystals, *ACS Nano*, **2012**, 6, 2686-2692.

[17] Q. Su, W. Feng, D. Yang, and F. Li, Resonance energy transfer in upconversion nanoplatforms for selective biodetection, *Acc. Chem. Res.*, **2017**, 50, 32-40.

[18] L. Wang, and Y. Li, Green upconversion nanocrystals for DNA detection, *Chem. Commun.*, **2006**, 24, 2557-2559.

[19] F. Wang, and X. Liu, Upconversion multicolor fine-tuning: visible to near-infrared emission from lanthanide-doped $NaYF_4$ nanoparticles, *J. Am. Chem. Soc.*, **2008**, 130, 5642-5643.

[20] X. Xie, N. Gao, R. Deng, Q. Sun, Q.-H. Xu, and X. Liu, Mechanistic investigation of photon upconversion in Nd^{3+}-sensitized core-shell nanoparticles, *J. Am. Chem. Soc.*, **2013**, 135, 12608-12611.

[21] B. Liu, C. Li, P. Yang, Z. Hou, and J. Lin, 808-nm-light-excited lanthanide-doped nanoparticles: rational design, luminescence control and theranostic applications, *Adv. Mater.*, **2017**, 29, 1605434.

[22] W. Zou, C. Visser, J.A. Maduro, M.S. Pshenichnikov, and J.C. Hummelen, Broadband dye-sensitized upconversion of near-infrared light, *Nat. Photonics*, **2012**, 6, 560-564.

[23] D.J. Garfield, N.J. Borys, S.M. Hamed, N.A. Torquato, C.A. Tajon, B. Tian, B. Shevitski, E.S. Barnard, Y.D. Suh, S. Aloni, J.B. Neaton, E.M. Chan, B.E. Cohen, and P.J. Schuck, Enrichment of molecular antenna triplets amplifies upconverting nanoparticle emission, *Nat. Photonics*, **2018**, 12, 402-407.

[24] G. Chen, W. Shao, R.R. Valiev, T.Y. Ohulchanskyy, G.S. He, H. Ågren, and P.N. Prasad, Efficient broadband upconversion of near-infrared light in dye-sensitized core/shell nanocrystals, *Adv. Opt. Mater.*, **2016**, 4, 1760-1766.

[25] S. Hao, Y. Shang, D. Li, H. Agren, C.-H. Yang, and G. Chen, Enhancing dye-sensitized solar cell efficiency through broadband near-infrared upconverting nanoparticles, *Nanoscale*, **2017**, 9, 6711-6715.

[26] X. Wu, H. Lee, O. Bilsel, Y. Zhang, Z. Li, T. Chen, Y. Liu, C. Duan, J. Shen, A. Punjabi, and G. Han, Tailoring dye-sensitized upconversion nanoparticle excitation bands towards excitation wavelength selective imaging, *Nanoscale*, **2015**, 7, 18424-18428 .

[27] J. Xu, P. Yang, M. Sun, H. Bi, B. Liu, D. Yang, S. Gai, F. He, and J. Lin, Highly emissive dye-sensitized upconversion nanostructure for dual-photosensitizer photodynamic therapy and bioimaging, *ACS Nano*, **2017**, 11, 4133-4144.

[28] G. Chen, J. Damasco, H. Qiu, W. Shao, T.Y. Ohulchanskyy, R.R. Valiev, X. Wu, G. Han, Y. Wang, C. Yang, H. Ågren, and P.N. Prasad, Energy-cascaded upconversion in an organic dye-sensitized core/shell fluoride nanocrystal, *Nano Lett.*, **2015**, 15, 7400-7407.

[29] W. Shao, G. Chen, A. Kuzmin, H.L. Kutscher, A. Pliss, T.Y. Ohulchanskyy, and P.N. Prasad, Tunable narrow band emissions from dye-sensitized core/shell/shell nanocrystals in the second near-infrared biological window, *J. Am. Chem. Soc.*, **2016**, 138, 16192-16195.

[30] F. Auzel, Upconversion and anti-stokes processes with f and d ions in solids, *Chem. Rev.*, **2004**, 104, 139-174.

[31] H. Dong, L.-D. Sun, and C.-H. Yan, Basic understanding of the lanthanide related upconversion emissions, *Nanoscale*, **2013**, 5, 5703-5714.

[32] F. Auzel, Compteur quantique par transfert d'energie entre deux ions de terres rares dans un tungstate mixte et dans un verre, *C. R. Acad. Sci. Paris B*, **1966**, 262, 1016.

[33] G. Chen, T.Y. Ohulchanskyy, A. Kachynski, H. Ågren, and P.N. Prasad, Intense visible and near-infrared upconversion photoluminescence in colloidal $LiYF_4:Er^{3+}$ nanocrystals under excitation at 1490 nm, *ACS Nano*, **2011**, 5, 4981-4986.

[34] J.S. Chivian, W.E. Case, and D.D. Eden, The photon avalanche: a new phenomenon in Pr^{3+}-based infrared quantum counters, *Appl. Phys. Lett.*, **1979**, 35, 124-125.

[35] Y. Liu, Y. Lu, X. Yang, X. Zheng, S. Wen, F. Wang, X. Vidal, J. Zhao, D. Liu, Z. Zhou, C. Ma, J. Zhou, J.A. Piper, P. Xi, and D. Jin, Amplified stimulated emission in upconversion nanoparticles for super-resolution nanoscopy, *Nature*, **2017**, 543, 229-233.

[36] W. Strek, P. Deren, and A. Bednarkiewicz, Cooperative processes in $KYb(WO_4)_2$ crystal doped with Eu^{3+} and Tb^{3+} ions, *J. Lumin.*, **2000**, 87-89, 999-1001.

[37] X. Wang, J. Zhuang, Q. Peng, and Y. Li, A general strategy for nanocrystal synthesis, *Nature*, **2005**, 437, 121-124.

[38] J. Ren, G. Jia, Y. Guo, A. Wang, and S. Xu, Unraveling morphology and phase control of $NaLnF_4$ upconverting nanocrystals, *J. Phys. Chem. C*, **2016**, 120, 1342-1351.

[39] F. Wang, Y. Han, C.S. Lim, Y. Lu, J. Wang, J. Xu, H. Chen, C. Zhang, M. Hong, and X. Liu, Simultaneous phase and size control of upconversion nanocrystals through lanthanide doping, *Nature*, **2010**, 463, 1061-1065.

[40] S. Zeng, J. Xiao, Q. Yang, and J. Hao, Bi-functional $NaLuF_4:Gd^{3+}/Yb^{3+}/Tm^{3+}$ nanocrystals: structure controlled synthesis, near-infrared upconversion emission and tunable magnetic properties, *J. Mater. Chem.*, **2012**, 22, 9870-9874.

[41] F. Zhang, Y. Wan, T. Yu, F. Zhang, Y. Shi, S. Xie, Y. Li, L. Xu, B. Tu, and D. Zhao, Uniform nanostructured arrays of sodium rare-earth fluorides for highly efficient multicolor upconversion luminescence, *Angew. Chem. Int. Edit.*, **2007**, 46, 7976-7979.

[42] D. Chen, Y. Yu, F. Huang, P. Huang, A. Yang, and Y. Wang, Modifying the size and shape of monodisperse bifunctional alkaline-earth fluoride nanocrystals through lanthanide doping, *J. Am. Chem. Soc.*, **2010**, 132, 9976-9978.

[43] T. Xie, S. Li, Q. Peng, and Y. Li, Monodisperse BaF_2 nanocrystals: phases, size transitions, and self-assembly, *Angew. Chem. Int. Edit.*, **2009**, 48, 196-200.

[44] C. Li, J. Yang, Z. Quan, P. Yang, D. Kong, and J. Lin, Different microstructures of β-$NaYF_4$ fabricated by hydrothermal process: effects of ph values and fluoride sources, *Chem. Mater.*, **2007**, 19, 4933-4942.

[45] J. Liu, L. Wang, X. Sun, and X. Zhu, Cerium vanadate nanorod arrays from ionic chelator-mediated self-assembly, *Angew. Chem. Int. Edit.*, **2010**, 49, 3492-3495.

[46] C. Zhang, Y. Yuan, S. Zhang, Y. Wang, and Z. Liu, Biosensing platform based on fluorescence resonance energy transfer from upconverting nanocrystals to graphene oxide, *Angew. Chem. Int. Edit.*, **2011**, 50, 6851-6854.

[47] J.H. Zeng, J. Su, Z.H. Li, R.X. Yan, and Y.D. Li, Synthesis and upconversion luminescence of hexagonal-phase $NaYF_4$:Yb,Er^{3+} phosphors of controlled size and morphology, *Adv. Mater.*, **2005**, 17, 2119-2123.

[48] D. Tu, L. Liu, Q. Ju, Y. Liu, H. Zhu, R. Li, and X. Chen, Time-resolved FRET biosensor based on amine-functionalized lanthanide-doped $NaYF_4$ nanocrystals, *Angew. Chem. Int. Edit.*, **2011**, 50, 6306-6310.

[49] Y.-W. Zhang, X. Sun, R. Si, L.-P. You, and C.-H. Yan, Single-crystalline and monodisperse LaF_3 triangular nanoplates from a single-source precursor, *J. Am. Chem. Soc.*, **2005**, 127, 3260-3261.

[50] Y.-P. Du, Y.-W. Zhang, L.-D. Sun, and C.-H. Yan, Luminescent monodisperse nanocrystals of lanthanide oxyfluorides synthesized from trifluoroacetate precursors in high-boiling solvents, *J. Phys. Chem. C*, **2008**, 112, 405-415.

[51] Y.-P. Du, Y.-W. Zhang, L.-D. Sun, and C.-H. Yan, Atomically efficient synthesis of self-assembled monodisperse and ultrathin lanthanide oxychloride nanoplates, *J. Am. Chem. Soc.*, **2009**, 131, 3162-3163.

[52] H.-X. Mai, Y.-W. Zhang, R. Si, Z.-G. Yan, L.-d. Sun, L.-P. You, and C.-H. Yan, High-quality sodium rare-earth fluoride nanocrystals: controlled synthesis and optical properties, *J. Am. Chem. Soc.*, **2006**, 128, 6426-6436.

[53] Y.-P. Du, Y.-W. Zhang, L.-D. Sun, and C.-H. Yan, Optically active uniform potassium and lithium rare earth fluoride nanocrystals derived from metal trifluroacetate precursors, *Dalton Trans.*, **2009**, 40, 8574-8581.

[54] X. Ye, J. Chen, M. Engel, J.A. Millan, W. Li, L. Qi, G. Xing, J.E. Collins, C.R. Kagan, J. Li, S.C. Glotzer, and C.B. Murray, Competition of shape and interaction patchiness for self-assembling nanoplates, *Nat. Chem.*, **2013**, 5, 466-473.

[55] H.-P. Zhou, Y.-W. Zhang, H.-X. Mai, X. Sun, Q. Liu, W.-G. Song, and C.-H. Yan, Spontaneous organization of uniform CeO_2 nanoflowers by 3D oriented attachment in hot surfactant solutions monitored with an in situ electrical conductance technique,

Chem. Eur. J., **2008**, 14, 3380-3390.

[56] S.S. Lee, H. Zhu, E.Q. Contreras, A. Prakash, H.L. Puppala, and V.L. Colvin, High temperature decomposition of cerium precursors to form ceria nanocrystal libraries for biological applications, *Chem. Mater.*, **2012**, 24, 424-432.

[57] G.S. Yi, and G.M. Chow, Synthesis of hexagonal-phase $NaYF_4$:Yb,Er and $NaYF_4$:Yb,Tm nanocrystals with efficient up-conversion fluorescence, *Adv. Funct. Mater.*, **2006**, 16, 2324-2329.

[58] X. Ye, J.E. Collins, Y. Kang, J. Chen, D.T.N. Chen, A.G. Yodh, and C.B. Murray, Morphologically controlled synthesis of colloidal upconversion nanophosphors and their shape-directed self-assembly, *Proc. Natl. Acad. Sci.*, **2010**, 107, 22430-22435.

[59] Z. Li, and Y. Zhang, An efficient and user-friendly method for the synthesis of hexagonal-phase $NaYF_4$:Yb,Er/Tm nanocrystals with controllable shape and upconversion fluorescence, *Nanotechnology*, **2008**, 19, 345606.

[60] Y. Liu, D. Tu, H. Zhu, R. Li, W. Luo, and X. Chen, A strategy to achieve efficient dual-mode luminescence of Eu^{3+} in lanthanides doped multifunctional $NaGdF_4$ nanocrystals, *Adv. Mater.*, **2010**, 22, 3266-3271.

[61] W. Zheng, S. Zhou, Z. Chen, P. Hu, Y. Liu, D. Tu, H. Zhu, R. Li, M. Huang, and X. Chen, Sub-10 nm lanthanide-doped CaF_2 nanoprobes for time-resolved luminescent biodetection, *Angew. Chem. Int. Edit.*, **2013**, 52, 6671-6676.

[62] K. Zheng, G. He, W. Song, X. Bi, and W. Qin, A strategy for enhancing the sensitivity of optical thermometers in β-$NaLuF_4$:Yb^{3+}/Er^{3+} nanocrystals, *J. Mater. Chem. C*, **2015**, 3, 11589-11594.

[63] S. Gai, G. Yang, X. Li, C. Li, Y. Dai, F. He, and P. Yang, Facile synthesis and up-conversion properties of monodisperse rare earth fluoride nanocrystals, *Dalton Trans.*, **2012**, 41, 11716-11724.

[64] D. Liu, X. Xu, Y. Du, X. Qin, Y. Zhang, C. Ma, S. Wen, W. Ren, E.M. Goldys, J.A. Piper, S. Dou, X. Liu, and D. Jin, Three-dimensional controlled growth of monodisperse sub-50 nm heterogeneous nanocrystals, *Nat. Commun.*, **2016**, 7, 10254.

[65] Z. Li, Y. Zhang, and S. Jiang, Multicolor core/shell-structured upconversion fluorescent nanoparticles, *Adv. Mater.*, **2008**, 20, 4765-4769.

[66] R. Deng, F. Qin, R. Chen, W. Huang, M. Hong, and X. Liu, Temporal full-colour tuning through non-steady-state upconversion, *Nat. Nanotechnol.*, **2015**, 10, 237-242.

[67] S. Han, R. Deng, X. Xie, and X. Liu, Enhancing luminescence in lanthanide-doped upconversion nanoparticles, *Angew. Chem. Int. Edit.*, **2014**, 53, 11702-11715.

[68] L. Lyu, H. Cheong, X. Ai, W. Zhang, J. Li, H. Yang, J. Lin, and B. Xing, Near-infrared light-mediated rare-earth nanocrystals: recent advances in improving photon conversion and alleviating the thermal effect, *NPG Asia Mater.*, **2018**, 10, 685-702.

[69] H.-Q. Wang, and T. Nann, Monodisperse upconverting nanocrystals by microwave-assisted synthesis, *ACS Nano*, **2009**, 3, 3804-3808.

[70] C. Zhao, X. Kong, X. Liu, L. Tu, F. Wu, Y. Zhang, K. Liu, Q. Zeng, and H. Zhang, Li^+ ion

doping: an approach for improving the crystallinity and upconversion emissions of $NaYF_4:Yb^{3+},Tm^{3+}$ nanoparticles, *Nanoscale*, **2013**, 5, 8084-8089.

[71] W. Yin, L. Zhao, L. Zhou , Z. Gu, X. Liu, G. Tian , S. Jin , L. Yan, W. Ren, G. Xing, and Y. Zhao, Enhanced red emission from $GdF_3:Yb^{3+},Er^{3+}$ upconversion nanocrystals by Li^+ doping and their application for bioimaging, *Chem. Eur. J.*, **2012**, 18, 9239-9245.

[72] Q. Huang, J. Yu, E. Ma, and K. Lin, Synthesis and characterization of highly efficient near-infrared upconversion $Sc^{3+}/Er^{3+}/Yb^{3+}$ tridoped $NaYF_4$, *J. Phys. Chem. C*, **2010**, 114, 4719-4724.

[73] H. Liang, Y. Zheng, G. Chen, L. Wu, Z. Zhang, and W. Cao, Enhancement of upconversion luminescence of $Y_2O_3:Er^{3+}$ nanocrystals by codoping Li^+-Zn^{2+}, *J. Alloys Compd.*, **2011**, 509, 409-413.

[74] N. Niu, F. He, S. Gai, C. Li, X. Zhang, S. Huang, and P. Yang, Rapid microwave reflux process for the synthesis of pure hexagonal $NaYF_4:Yb^{3+},Ln^{3+},Bi^{3+}$ (Ln^{3+} = Er^{3+}, Tm^{3+}, Ho^{3+}) and its enhanced UC luminescence, *J. Mater. Chem.*, **2012**, 22, 21613-21623.

[75] P. Ramasamy, P. Chandra, S.W. Rhee, and J. Kim, Enhanced upconversion luminescence in $NaGdF_4$:Yb,Er nanocrystals by Fe^{3+} doping and their application in bioimaging, *Nanoscale*, **2013**, 5, 8711-8717.

[76] J. Wang, R. Deng, M.A. MacDonald, B. Chen, J. Yuan, F. Wang, D. Chi, T.S. Andy Hor, P. Zhang, G. Liu, Y. Han, and X. Liu, Enhancing multiphoton upconversion through energy clustering at sublattice level, *Nat. Mater.*, **2014**, 13, 157-162.

[77] Q. Su, S. Han, X. Xie, H. Zhu, H. Chen, C.-K. Chen, R.-S. Liu, X. Chen, F. Wang, and X. Liu, The effect of surface coating on energy migration-mediated upconversion, *J. Am. Chem. Soc.*, **2012**, 134, 20849-20857.

[78] J. Zhao, D. Jin, E.P. Schartner, Y. Lu, Y. Liu, A.V. Zvyagin, L. Zhang, J.M. Dawes, P. Xi, J.A. Piper, E.M. Goldys, and T.M. Monro, Single-nanocrystal sensitivity achieved by enhanced upconversion luminescence, *Nat. Nanotechnol.*, **2013**, 8, 729-734.

[79] M.-Y. Xie, X.-N. Peng, X.-F. Fu, J.-J. Zhang, G.-L. Li, and X.-F. Yu, Synthesis of Yb^{3+}/Er^{3+} co-doped MnF_2 nanocrystals with bright red up-converted fluorescence, *Scr. Mater.*, **2009**, 60, 190-193.

[80] J. Wang, F. Wang, C. Wang, Z. Liu, and X. Liu, Single-band upconversion emission in lanthanide-doped $KMnF_3$ nanocrystals, *Angew. Chem. Int. Edit.*, **2011**, 50, 10369-10372.

[81] Y. Zhang, J.D. Lin, V. Vijayaragavan, K.K. Bhakoo, and T.T.Y. Tan, Tuning sub-10 nm single-phase $NaMnF_3$ nanocrystals as ultrasensitive hosts for pure intense fluorescence and excellent T1 magnetic resonance imaging, *Chem. Commun.*, **2012**, 48, 10322-10324.

[82] G. Tian, Z. Gu, L. Zhou, W. Yin, X. Liu, L. Yan, S. Jin, W. Ren, G. Xing, S. Li, and Y. Zhao, Mn^{2+} dopant-controlled synthesis of $NaYF_4$:Yb/Er upconversion nanoparticles for in vivo imaging and drug delivery, *Adv. Mater.*, **2012**, 24, 1226-1231.

[83] X. Chen, L. Jin, W. Kong, T. Sun, W. Zhang, X. Liu, J. Fan, S.F. Yu, and F. Wang, Confining energy migration in upconversion nanoparticles towards deep ultraviolet

lasing, *Nat. Commun.*, **2016**, 7, 10304.

[84] J.-N. Liu, W.-B. Bu, and J.-L. Shi, Silica coated upconversion nanoparticles: a versatile platform for the development of efficient theranostics, *Acc. Chem. Res.*, **2015**, 48, 1797-1805.

[85] R. Abdul Jalil, and Y. Zhang, Biocompatibility of silica coated $NaYF_4$ upconversion fluorescent nanocrystals, *Biomaterials*, **2008**, 29, 4122-4128.

[86] G.-S. Yi, and G.-M. Chow, Water-soluble $NaYF_4$:Yb,Er(Tm)/$NaYF_4$/polymer core/shell/shell nanoparticles with significant enhancement of upconversion fluorescence, *Chem. Mater.*, **2007**, 19, 341-343.

[87] F. Wang, J. Wang, and X. Liu, Direct evidence of a surface quenching effect on size-dependent luminescence of upconversion nanoparticles, *Angew. Chem. Int. Edit.*, **2010**, 49, 7456-7460.

[88] H. Schäfer, P. Ptacek, O. Zerzouf, and M. Haase, Synthesis and optical properties of KYF_4/Yb,Er nanocrystals, and their surface modification with undoped KYF_4, *Adv. Funct. Mater.*, **2008**, 18, 2913-2918.

[89] C. Dong, A. Korinek, B. Blasiak, B. Tomanek, and F.C.J.M. van Veggel, Cation exchange: a facile method to make $NaYF_4$:Yb,Tm-$NaGdF_4$ core-shell nanoparticles with a thin, tunable, and uniform shell, *Chem. Mater.*, **2012**, 24, 1297-1305.

[90] F. Vetrone, R. Naccache, V. Mahalingam, C.G. Morgan, and J.A. Capobianco, The active-core/active-shell approach: a strategy to enhance the upconversion luminescence in lanthanide-doped nanoparticles, *Adv. Funct. Mater.*, **2009**, 19, 2924-2929.

[91] H.-S. Qian, and Y. Zhang, Synthesis of hexagonal-phase core-shell $NaYF_4$ nanocrystals with tunable upconversion fluorescence, *Langmuir*, **2008**, 24, 12123-12125.

[92] D. Yang, C. Li, G. Li, M. Shang, X. Kang, and J. Lin, Colloidal synthesis and remarkable enhancement of the upconversion luminescence of $BaGdF_5$:Yb^{3+}/Er^{3+} nanoparticles by active-shell modification, *J. Mater. Chem.*, **2011**, 21, 5923-5927.

[93] D. Chen, Y. Yu, F. Huang, H. Lin, P. Huang, A. Yang, Z. Wang, and Y. Wang, Lanthanide dopant-induced formation of uniform sub-10 nm active-core/active-shell nanocrystals with near-infrared to near-infrared dual-modal luminescence, *J. Mater. Chem.*, **2012**, 22, 2632-2640.

[94] M. Saboktakin, X. Ye, S.J. Oh, S.-H. Hong, A.T. Fafarman, U.K. Chettiar, N. Engheta, C.B. Murray, and C.R. Kagan, Metal-enhanced upconversion luminescence tunable through metal nanoparticle-nanophosphor separation, *ACS Nano*, **2012**, 6, 8758-8766.

[95] Q.-C. Sun, H. Mundoor, J.C. Ribot, V. Singh, I.I. Smalyukh, and P. Nagpal, Plasmon-enhanced energy transfer for improved upconversion of infrared radiation in doped-lanthanide nanocrystals, *Nano Lett.*, **2014**, 14, 101-106.

[96] D. Zhou, D. Liu, W. Xu, Z. Yin, X. Chen, P. Zhou, S. Cui, Z. Chen, and H. Song, Observation of considerable upconversion enhancement induced by $Cu_{2-x}S$ plasmon nanoparticles, *ACS Nano*, **2016**, 10, 5169-5179.

[97] W. Zhang, F. Ding, and S.Y. Chou, Large enhancement of upconversion luminescence of $NaYF_4:Yb^{3+}/Er^{3+}$ nanocrystal by 3D plasmonic nano-antennas, *Adv. Mater.*, **2012**, 24, 236-241.

[98] F. Kang, J. He, T. Sun, Z.Y. Bao, F. Wang, and D.Y. Lei, Plasmonic dual-enhancement and precise color tuning of gold nanorod@SiO_2 coupled core-shell-shell upconversion nanocrystals, *Adv. Funct. Mater.*, **2017**, 27, 1701842.

[99] J. Li, W. Zhang, C. Lu, Z. Lou, and B. Li, Nonmetallic plasmon induced 500-fold enhancement in the upconversion emission of the UCNPs/WO_{3-x} hybrid, *Nanoscale Horiz.*, **2019**, 4, 999-1005.

[100] X. Wang, R.R. Valiev, T.Y. Ohulchanskyy, H. Agren, C. Yang, and G. Chen, Dye-sensitized lanthanide-doped upconversion nanoparticles, *Chem. Soc. Rev.*, **2017**, 46, 4150-4167.

[101] X. Zou, M. Xu, W. Yuan, Q. Wang, Y. Shi, W. Feng, and F. Li, A water-dispersible dye-sensitized upconversion nanocomposite modified with phosphatidylcholine for lymphatic imaging, *Chem. Commun.*, **2016**, 52, 13389-13392.

[102] X. Wu, Y. Zhang, K. Takle, O. Bilsel, Z. Li, H. Lee, Z. Zhang, D. Li, W. Fan, C. Duan, E.M. Chan, C. Lois, Y. Xiang, and G. Han, Dye-sensitized core/active shell upconversion nanoparticles for optogenetics and bioimaging applications, *ACS Nano*, **2016**, 10, 1060-1066.

[103] J. Lee, B. Yoo, H. Lee, G.D. Cha, H.-S. Lee, Y. Cho, S.Y. Kim, H. Seo, W. Lee, D. Son, M. Kang, H.M. Kim, Y.I. Park, T. Hyeon, and D.-H. Kim, Ultra-wideband multi-dye-sensitized upconverting nanoparticles for information security application, *Adv. Mater.*, **2016**, 29, 1603169.

[104] J. Zhou, S. Wen, J. Liao, C. Clarke, S.A. Tawfik, W. Ren, C. Mi, F. Wang, and D. Jin, Activation of the surface dark-layer to enhance upconversion in a thermal field, *Nat. Photonics*, **2018**, 12, 154-158.

[105] Z. Yin, H. Li, W. Xu, S. Cui, D. Zhou, X. Chen, Y. Zhu, G. Qin, and H. Song, Local field modulation induced three-order upconversion enhancement: combining surface plasmon effect and photonic crystal effect, *Adv. Mater.*, **2016**, 28, 2518-2525.

[106] J. Peng, W. Xu, C.L. Teoh, S. Han, B. Kim, A. Samanta, J.C. Er, L. Wang, L. Yuan, X. Liu, and Y.-T. Chang, High-efficiency in vitro and in vivo detection of Zn^{2+} by dye-assembled upconversion nanoparticles, *J. Am. Chem. Soc.*, **2015**, 137, 2336-2342.

[107] L. Zhou, R. Wang, C. Yao, X. Li, C. Wang, X. Zhang, C. Xu, A. Zeng, D. Zhao, and F. Zhang, Single-band upconversion nanoprobes for multiplexed simultaneous in situ molecular mapping of cancer biomarkers, *Nat. Commun.*, **2015**, 6, 6938.

[108] X. Ai, C.J.H. Ho, J. Aw, A.B.E. Attia, J. Mu, Y. Wang, X. Wang, Y. Wang, X. Liu, H. Chen, M. Gao, X. Chen, E.K.L. Yeow, G. Liu, M. Olivo, and B. Xing, In vivo covalent cross-linking of photon-converted rare-earth nanostructures for tumour localization and theranostics, *Nat. Commun.*, **2016**, 7, 10432.

[109] C. Liu, B. Liu, J. Zhao, Z. Di, D. Chen, Z. Gu, L. Li, and Y. Zhao, Nd^{3+}-sensitized

upconversion metal-organic frameworks for mitochondria-targeted amplified photodynamic therapy, *Angew. Chem. Int. Edit.*, **2020**, 59, 2634-2638.

[110] P. Hegemann, and A. Möglich, Channelrhodopsin engineering and exploration of new optogenetic tools, *Nat. Methods*, **2011**, 8, 39-42

[111] A. Berndt, S. Y. Lee, J. Wietek, C. Ramakrishnan, E. E. Steinberg, A. J. Rashid, H. Kim, S. Park, A. Santoro, P. W. Frankland, S. M. Iyer, S. Pak, S. Ährlund-Richter, S. L. Delp, R. C. Malenka, S. A. Josselyn, M. Carlén, P. Hegemann, and K. Deisseroth, Structural foundations of optogenetics: determinants of channelrhodopsin ion selectivity, *Proc. Natl. Acad. Sci.*, **2016**, 113, 822-829

[112] B. R. Rost, F. Schneider-Warme, D. Schmitz, and P. Hegemann, Optogenetic tools for subcellular applications in neuroscience, *Neuron*, **2017**, 96, 572-603.

[113] X. Lin, X. Chen, W. Zhang, T. Sun, P. Fang, Q. Liao, X. Chen, J. He, M. Liu, F. Wang, and P. Shi, Core-shell-shell upconversion nanoparticles with enhanced emission for wireless optogenetic inhibition, *Nano Lett.*, **2018**, 18, 948-956.

[114] S. Chen, A.Z. Weitemier, X. Zeng, L. He, X. Wang, Y. Tao, A.J.Y. Huang, Y. Hashimotodani, M. Kano, H. Iwasaki, L.K. Parajuli, S. Okabe, D.B.L. Teh, A.H. All, I. Tsutsui-Kimura, K.F. Tanaka, X. Liu, and T.J. McHugh, Near-infrared deep brain stimulation *via* upconversion nanoparticle-mediated optogenetics, *Science*, **2018**, 359, 679-684.

[115] L. Jin, Y. Wu, Y. Wang, S. Liu, Y. Zhang, Z. Li, X. Chen, W. Zhang, S. Xiao, and Q. Song, Mass-manufactural lanthanide-based ultraviolet B microlasers, *Adv. Mater.*, **2018**, 31, 1807079.

[116] Y. Lu, J. Zhao, R. Zhang, Y. Liu, D. Liu, E.M. Goldys, X. Yang, P. Xi, A. Sunna, J. Lu, Y. Shi, R.C. Leif, Y. Huo, J. Shen, J.A. Piper, J.P. Robinson, and D. Jin, Tunable lifetime multiplexing using luminescent nanocrystals, *Nat. Photonics*, **2014**, 8, 32-36.

[117] X. Liu, Y. Wang, X. Li, Z. Yi, R. Deng, L. Liang, X. Xie, D.T.B. Loong, S. Song, D. Fan, A.H. All, H. Zhang, L. Huang, and X. Liu, Binary temporal upconversion codes of Mn^{2+}-activated nanoparticles for multilevel anti-counterfeiting, *Nat. Commun.*, **2017**, 8, 899.

Chapter 2: Synthesis of Hydrophilic Upconversion Nano-/Microcrystals: A One-Step Route

Chapter 2 is based on the following article

> Chunning Sun, Michael Schäferling, Ute Resch-Genger, Michael Gradzielski, "Solvothermal synthesis of lanthanide-doped $NaYF_4$ upconversion crystals with size and shape control: particle properties and growth mechanism", *ChemNanoMat*, **2021**, 7, 174-183 (DOI: 10.1002/cnma.202000564).

C. Sun and M. Gradzielski conceived and designed the experiments. C. Sun performed the experiments and analyzed the data. M. Schäferling conducted the fluorescence measurements. M. Schäferling and U. Resch-Genger contributed to the discussion of fluorescence data. C. Sun and M. Gradzielski co-wrote the manuscript. All authors discussed the results and commented on the manuscript.

2.1 Introduction

Ln-doped upconversion materials commonly consist of an optically transparent and chemically inert inorganic host of low phonon energy, sensitizer ions that have a relatively high absorption cross-section like Yb^{3+}, and emissive activator ions such as Er^{3+}, Tm^{3+}, and Ho^{3+} ions. To date, RE-based oxides[1], oxysulfides[2], oxyfluorides[3], phosphates[4], vanadates[5] and fluorides[6] have been widely investigated as host matrices. For constructing upconversion materials, a proper host material is carefully chosen in order to dilute the activators and sensitizers to minimize cross-relaxation. Optimal host materials should possess the properties of low lattice phonon energies, high transparency in the excitation and emission wavelength, and excellent chemical stability. Heavy halides like chlorides, bromides, and iodides typically exhibit low phonon energies (<300 cm^{-1}). Nonetheless, their hygroscopic nature inhibits their application. Oxides exhibit high chemical stability, while their phonon energies are generally larger than 500 cm^{-1}, which will increase the non-radiative loss and lessen the radiative emission. In contrast, fluorides usually exhibit relatively low phonon energies (~350 cm^{-1}) and high chemical stability. Therefore, fluorides, like $NaYF_4$, are the most frequently used host materials[7, 8]. To minimize energy loss processes due

to cross-relaxation, typically a relatively high amount of the sensitizer, commonly Yb^{3+} with its simple two energy-level structure in a concentration of about 20 mol%, and a relatively low amount of the activator, normally less than 2 mol%, are used.

For the synthesis of upconversion nano- and microcrystals, several synthetic approaches have been used, including the thermal decomposition method[9-12], hydro/solvothermal method[13, 14], and coprecipitation method[15-17]. The hydro/solvothermal synthesis utilizes a solvent under high pressures and mild temperatures to speed up reactions between solids. This presents an effective and convenient process in preparing various inorganic materials with diverse controllable morphologies and architectures in terms of cost and potential for large-scale production. Li's group[18] developed a LSS strategy to prepare upconversion nanocrystals *via* the solvothermal method using OA as a stabilizer. Well-defined upconversion crystals with tunable size can also be prepared *via* the LSS method by changing experimental parameters, like ligand amount, F^- concentration, and impurity doping[7, 19]. While these upconversion crystals are hydrophobic, post-modification is required prior to practical applications. Polymers and small molecules have been used as hydrophilic ligands for the synthesis of upconversion crystals under the hydro/solvothermal method. Zhang's group[20, 21] developed a simple solvothermal method to prepare PEI-capped upconversion NPs with an average size of 50 nm. PVP was applied as well to synthesize hydrophilic upconversion NPs[22]. Lin's group[23-26] used sodium citrate as a chelating agent, studied several factors, like the amount of ligand, reaction temperature, pH value, and fluoride source, in tailoring the phases, shapes, and sizes of upconversion crystals. Moreover, Yang's group[27] studied different surfactants (disodium ethylenediaminetetraacetate, sodium dodecyl sulfate, sodium tartrate, and PVP) to control the crystal size and morphology of upconversion crystals. Zhao's group[28] used different binary acids to prepare carboxyl-functionalized upconversion phosphors with controlled phase, shape, and size *via* a one-step hydrothermal method. These hydrophilic ligands may coordinate with metal ions to adjust the concentration of free ions, thereby affecting the growth kinetics. Additionally, the ligands can selectively absorb on different facets of crystallites, which could modulate the morphology and size of crystals. Nitrilotriacetic acid and its salts are useful compounds as chelating agents. They are considered as excellent ligands to coordinate with many metal ions, such as Fe, Co, and Ni[29-31], ascribing to their diversity of coordination mode (tetradentate ligand: three carboxyl groups and one nitrogen). However, the synthesis of upconversion crystals with the help of these

ligands hasn't been investigated yet.

In this chapter, the synthesis of Ln-doped $NaYF_4$ crystals *via* the solvothermal method was described using disodium nitrilotriacetate as a ligand in the absence of a surfactant and their subsequent characterization with respect to structure and optical performance. Thereby we could identify the volume ratio of EG and water and the content of NH_4F as essential parameters for the control of the crystalline phase. The various dopant concentration of Gd^{3+} ion, different organic co-solvents, and the reaction time have profound effects on the control of crystalline morphology and size, which have been investigated in detail. Based on the experimental results, a feasible mechanism of morphological evolution and crystal growth is proposed. Additionally, the photoluminescence properties of the crystals were studied for particles differing in crystal phase, size, and chemical composition.

2.2 Materials and Methods

2.2.1 Reagents

$YCl_3 \cdot 6H_2O$ (99.9%), $YbCl_3 \cdot 6H_2O$ (99.9%), $ErCl_3 \cdot 6H_2O$ (99.9%), $HoCl_3 \cdot 6H_2O$ (99.9%), $TmCl_3$ (99.9%), $GdCl_3$ (99.9%), DSNTA (99%), NH_4F(≥98%), EG (99.9%), DEG (99%), PEG 200, PEG 400, PPG 400, and PPG 1000 were purchased from Sigma-Aldrich. All the chemicals were used as received without further purification. Milli-Q water (18.2 MΩ·cm at 25 ºC) was used in all experiments.

2.2.2 Instruments

XRD spectra were obtained using Philips X'Pert MPD Pro X-ray diffractometer at a scanning rate of 4° min^{-1} in the 2θ range from 10° to 90° with Cu Kα radiation (λ = 0.15406 nm). SEM and EDS were measured using a field emission electron microscope (FE-SEM, S4000, Hitachi). TEM, HR-TEM, and EDS mapping were performed by FEI Tecnai G2 20 S-TWIN with a LaB6 cathode operating at 200 kV. UCL spectra were recorded on a calibrated Edinburgh Instruments FSP 920 spectrometer equipped with a 2 W, 976 nm diode laser in Division Biophotonics. The photoluminescence of the crystals was measured with a concentration of 1 mg/mL in ethanol after 10 min ultrasonication, and the measurements were performed at room temperature.

2.2.3 Preparation

In a typical procedure used for the preparation of $NaYF_4$:Yb,Er (20/2 mol%) crystals, 2 mL of a 0.5 mol/L $RECl_3$ (RE = Y, Yb, and Er) solution were added to a solution of 30 mL EG and H_2O (of varying ratio) containing 2 mmol of DSNTA to form metal-ligand complexes (the molar ratio of DSNTA to $RECl_3$ is 2:1). After vigorous stirring at room temperature for 60 min, 7 mmol of NH_4F was added, and the reaction mixture was stirred for another 60 min. Then the reaction mixture was transferred into a 50 mL Teflon bottle held in a stainless-steel autoclave, which was sealed and maintained at 190 ºC for 12 h. Afterwards, the autoclave was cooled to room temperature by simply placing it under ambient conditions. The white precipitate was collected by centrifugation and washed once with the ethanol and twice with the water, and then dried in air at 70 ºC for 12 h. Other samples, like $NaYF_4$:Yb,Ho (Yb/Ho = 20/2 mol%) and $NaYF_4$:Yb,Tm (Yb/Tm = 20/2 mol%) were synthesized in the same manner as described above for the $NaYF_4$:Yb,Er (Yb/Er = 20/2 mol%) sample. Additionally, different volume ratios of EG/H_2O (1/4, 1/3, 1/2, 1/1, 2/1, 3/1), different molar ratios of NH_4F/RE^{3+} (4/1, 6/1, 7/1, 8/1, 12/1, 16/1), different dopant concentrations of Gd^{3+} ion (0 ~ 60 mol%) and solvothermal treatment times (2 h, 4 h, 6 h, 12 h) were employed to systematically investigate their impact on the morphological evolution and structural properties of the resulting particles.

2.3 Results and Discussion

Synthetic parameters will influence the phase structure, morphology, and size of Ln-doped $NaYF_4$ crystals, and further affect the optical properties of the products. The effect of the type of activator dopant ion, the volume ratio of EG/H_2O, the molar ratio of NH_4F/RE^{3+}, the Gd^{3+} ion content, and the type of organic co-solvent on the crystal phase, structure, morphology, size, and optical performance of upconversion materials were investigated in detail. The aim of this work was to establish systematic relations between the structure of the crystals formed and their photophysical properties. The synthetic process and resulting crystals obtained with different parameters are shown in Scheme 2.1.

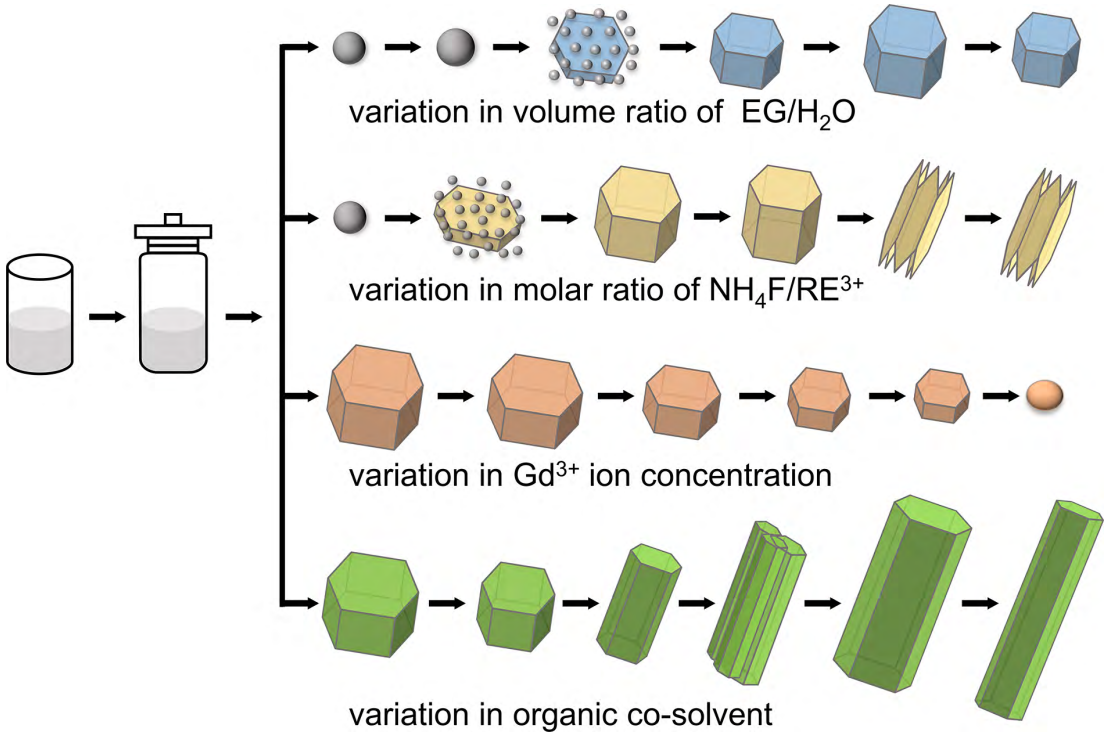

Scheme 2.1 Schematic illustration for the parameters on the final upconversion crystals.

2.3.1 Controlled Synthesis of Ln-Doped $NaYF_4$ Crystals

Synthetic conditions were investigated systematically to determine how these parameters affect the microscopic crystallinity as well as the mesoscopic/colloidal structure of the formed nano- and microcrystals.

2.3.2 Structure and Morphology of Initial System

The type of crystal and its phase purity for the samples with different doped activator ions are firstly examined by XRD. The XRD patterns of the as-obtained $NaYF_4$:Yb,Ln (Ln = Er, Ho, or Tm) particles are shown in Fig. 2.1a. All samples show the peaks of pure crystalline hexagonal β-$NaYF_4$, which are in good accordance with the standard XRD pattern of hexagonal $NaYF_4$ (JCPDS No. 28-1192). It should be noted that no second phase is observed in the XRD patterns, implying that the crystalline phase hasn't been influenced when the Y^{3+} ion is substituted by Er^{3+}, $Ho^{3+,}$ or Tm^{3+} ion, owing to the approximately equal radius of these Ln ions. As an example of Er^{3+} ion doping, Fig. 2.1b shows the EDS pattern of the crystals, which reveals the presence of Na, Y, F, Yb, and a small amount of Er element. It confirms the successful synthesis of $NaYF_4$:Yb,Er crystals. Moreover, EDS mappings indicate that these component atoms were homogeneously distributed in the crystals (Fig. 2h-l).

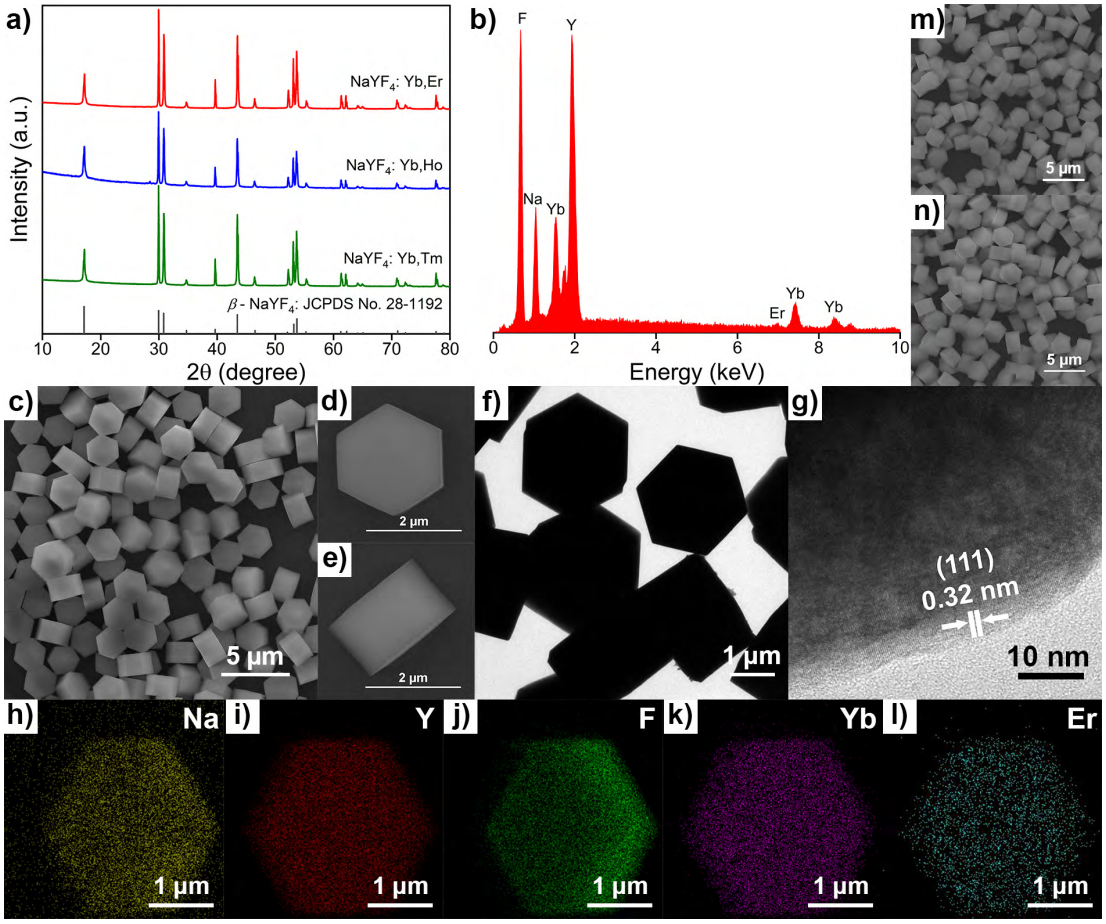

Fig. 2.1 (a) XRD patterns of $NaYF_4$:Yb,Ln and the standard data of hexagonal $NaYF_4$ (JCPDS No. 28-1192). (b) EDS analysis of $NaYF_4$:Yb,Er microprisms. (c) SEM images of $NaYF_4$:Yb,Er crystals, (d) top and (e) side view of $NaYF_4$:Yb,Er microcrystal. (f) TEM and (g) HR-TEM images of $NaYF_4$:Yb,Er crystals. EDS elemental mapping for (h) Na, (i) Y, (j) F, (k) Yb, and (l) Er of a single $NaYF_4$:Yb,Er microparticle. SEM images of (m) $NaYF_4$:Yb,Ho and (n) $NaYF_4$:Yb,Tm crystals.

As can be seen from SEM and TEM images of β-$NaYF_4$:Yb,Er (Fig. 2.1c and f), the as-prepared sample contains fairly uniform hexagonal microprisms with excellent monodispersity and clear-cut crystallographic facets. These hexagonal microprisms possess an average size with a diameter of about 2.54 μm and length of about 1.50 μm (aspect ratio of 0.59). The lattice fringes on the individual crystal are clearly distinguished in the HR-TEM image (Figure 1d), indicating the high crystallinity of the prepared microcrystals. The distance between the lattice fringes is measured to be about 0.32 nm, corresponding to the d-spacing for the (111) lattice planes of the hexagonal $NaYF_4$ structure. In addition, the higher magnification SEM images (Fig. 2.1d and e) present ultra-smooth planes at both top and side surfaces without apparent defects and small particles attached on them. The average diameter and length change very little when the Ho^{3+} or Tm^{3+} ion takes the place of the Er^{3+} ion as the dopant ion (Fig. 2.1m and n). It is worth mentioning that the general morphologies and

sizes of the as-obtained products are independent of the doped activator ions in β-$NaYF_4$. In addition, as can be concluded from the sharpness of the diffraction peaks in XRD patterns and SEM images, highly crystalline microprisms can be synthesized at a relatively low temperature, which is essential for phosphors with fewer traps and stronger luminescence. It is worth mentioning that the general morphology and size of the as-obtained products are independent of the doped activator ions in β-$NaYF_4$, which are depicted in Table 2.1.

Table 2.1 Summary of samples prepared with different activator dopant ions

Dopant ions[a]	Morphology	Structure	Average diameter (μm)	Average length (μm)	Aspect ratio
Yb & Er	microprism	hexagonal	2.54	1.50	0.59
Yb & Ho	microprism	hexagonal	2.36	1.40	0.59
Yb & Tm	microprism	hexagonal	2.43	1.39	0.57

[a] other synthetic parameters: EG/H_2O = 2/1, NH_4F/RE^{3+} = 7/1, reaction time: 12h.

2.3.3 Effect of Mixing Ratio of EG and H_2O

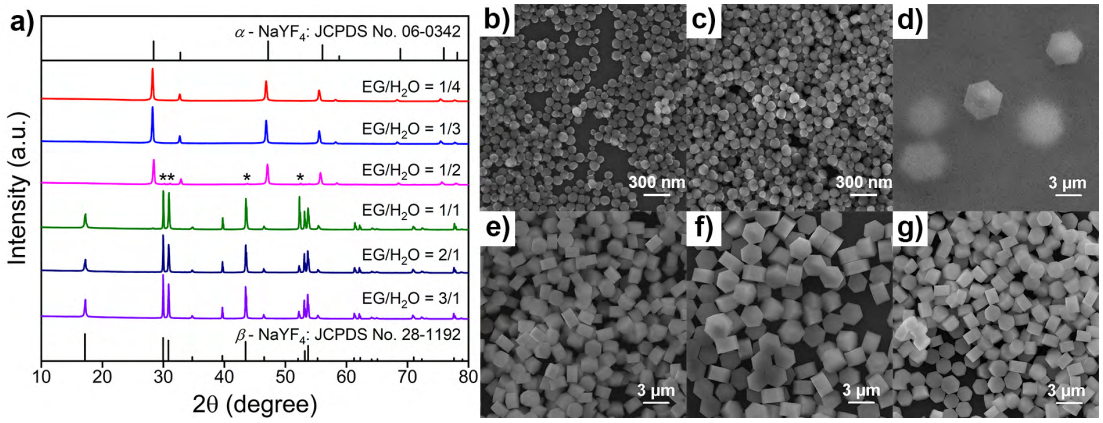

Fig. 2.2 (a) XRD patterns of crystals prepared under different volume ratios of EG/H_2O and the standard data of cubic (JCPDS No. 06-0342) and hexagonal $NaYF_4$ (JCPDS No. 28-1192). SEM images of $NaYF_4$:Yb,Er prepared at different volume ratios of EG/H_2O. (b) 1/4, (c) 1/3, (d) 1/2, (e) 1/1, (f) 2/1, (g) 3/1.

When the hydro/solvothermal method is applied for the synthesis of nano-/microcrystals, the selected solvent can influence the solubility, diffusion, and reactivity of the reagents during the crystallization and particles with different morphology and size can be obtained. For instance, Song et al.[32] showed that Gd_2O_2S:Eu spheres with tunable size were prepared by adjusting the volume ratio of EG/ethanol to change the diffusion rate of ions in the solution. Hence, the choice of solvent should be important,

and for that reason, we investigated systematically the solvent mixture of EG and H_2O.

For that purpose, $NaYF_4$:Yb,Er samples were fabricated by applying the same principal procedure, but varying the volume ratios of EG/H_2O. The XRD patterns of products with different EG/H_2O volume ratios, as well as standard data of cubic and hexagonal $NaYF_4$ are shown in Fig. 2.2a. One observes that when the volume ratio of EG/H_2O is lower than 1/3, the diffraction patterns of the obtained crystals match well with the corresponding standard data of cubic $NaYF_4$ (JCPDS No. 06-0342) when the value reaches 1/2, some other peaks start to appear, in addition to the characteristic peaks of the cubic phase, which can be indexed to the hexagonal $NaYF_4$ (JCPDS No. 28-1192). This indicates that the final system consists of both cubic and hexagonal phases of $NaYF_4$. As the volume ratio of EG/H_2O further increases, the XRD results are well consistent with the standard hexagonal $NaYF_4$ XRD patterns, and no other impurity peaks are observed, implying the formation of pure crystalline β-$NaYF_4$:Yb,Er in the obtained products.

Fig. 2.2b-g shows representative SEM images of $NaYF_4$:Yb,Er crystals prepared by using the mixed solvents with different volume ratios. At a low EG/H_2O volume ratio, the sample is made up of spherical NPs with an average diameter of 102 nm (EG/H_2O = 1/4) and 121 nm (EG/H_2O = 1/3), respectively (Fig. 2.2b and c). As the ratio of EG/H_2O increases to 1/2, microsheets with a mean diameter of about 4.43 μm can be observed (Fig. 2d), the mixture of NPs and microsheets in the system is consistent with the XRD result, where one observes cubic and hexagonal crystallites present. As the volume ratio increases to 1, microprisms with a diameter of 1.92 μm and length of 1.06 μm are obtained, while the NPs disappear entirely (Fig. 2.2e). When the volume ratio of EG/H_2O rises to 2, the SEM image (Fig. 2.2f) exhibits regular and uniform hexagonal-shaped morphology with a smooth surface. The size of the obtained crystals is 2.54 μm in diameter and 1.50 μm in height (aspect ratio of 0.59). Further increasing the volume ratio of EG/H_2O, the morphology remains unchanged, but the average diameter and height of prepared crystals tend to decrease (Fig. 2.2g), the surface of the as-made crystals, however, appears to be coarser compared with those obtained under the volume ratio of 2.

On the basis of the above results, it can be concluded that the volume ratio of EG/H_2O plays a dominant role in controlling the morphology and crystallinity of the final products. For optimizing the content of hexagonal $NaYF_4$:Yb,Er and having a high

degree of monodispersity, as well as well-defined crystallographic facets, the optimal volume ratio of EG/H_2O was found to be 2. The final morphologies and sizes of the as-synthesized products are summarized in Table 2.2.

Table 2.2 Summary of $NaYF_4$:Yb,Er crystals prepared with different volume ratios of EG/H_2O

EG/H_2O[b]	Morphology	Structure	Average diameter (μm)	Average length (μm)	Aspect ratio
1/4	nanosphere	cubic	0.10	-	-
1/3	nanosphere	cubic	0.12	-	-
1/2	nanosphere & microsheet	cubic & hexagonal	0.05 (nanosphere) & 4.43 (microsheet)	-	-
1/1	microprism	hexagonal	1.92	1.06	0.55
2/1	microprism	hexagonal	2.54	1.50	0.59
3/1	microprism	hexagonal	1.88	1.09	0.58

[b] other synthetic parameters: NH_4F/RE^{3+} = 7/1, reaction time: 12h.

2.3.4 Effect of Molar Ratio Between Fluoride NH_4F and RE^{3+}

Xu and co-workers[33] have shown that different molar ratios of NaF/RE^{3+} can strongly influence the final morphology of the product. Various morphologies of micro-sized $NaYF_4$:Yb,Er crystals could be controlled by simply adjusting the molar ratios of NaF/RE^{3+}. This parameter affects the growth and morphology evolution during crystal formation.

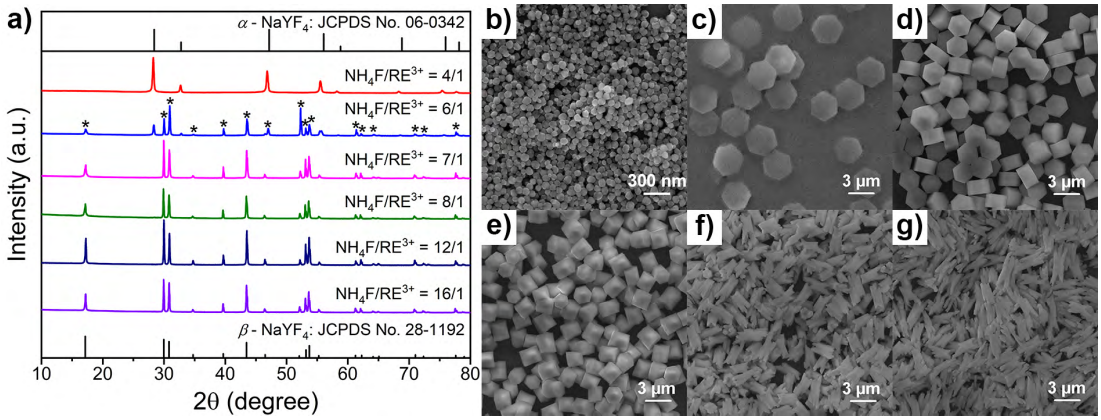

Fig. 2.3 (a) XRD patterns of products prepared under different molar ratios of NH_4F/RE^{3+} and the standard data of cubic $NaYF_4$ (JCPDS No. 06-0342) and hexagonal $NaYF_4$ (JCPDS No. 28-1192). SEM images of $NaYF_4$:Yb,Er prepared at different molar ratios of NH_4F/RE^{3+}. (b) 4, (c) 6, (d) 7, (e) 8, (f) 12, (g) 16.

To investigate the effect of the molar ratio of NH_4F/RE^{3+} on the structure and

morphology of our $NaYF_4$:Yb,Er crystals, a series of control experiments were carried out with various molar ratios of NH_4F/RE^{3+} while the other experimental parameters remained constant. The corresponding XRD patterns of the final products are shown in Fig. 2.3a. The as-prepared samples under different molar ratios of NH_4F/RE^{3+} exhibit quite different XRD patterns, the sample obtained at a low molar ratio (NH_4F/RE^{3+} = 4) is consistent with the standard data of cubic $NaYF_4$ (JCPDS No. 06-0342). As the molar ratio increases to 6, the characteristic peaks of the obtained XRD show the coexistence of the standard cubic and hexagonal phase of $NaYF_4$, implying that a new hexagonal phase appears in the final product. At the same time, the intensity of the peaks of the cubic phase decreases compared with those obtained at the low molar ratio. When the molar ratio is further increased (NH_4F/RE^{3+} >7), the XRD patterns are in excellent agreement with the standard data of the hexagonal $NaYF_4$ phase (JCPDS No. 28-1192), no other impurity peaks are detected, indicating the presence of pure β-$NaYF_4$:Yb,Er.

Fig. 2.3b-g shows typical SEM images of the samples prepared with different molar ratios of NH_4F/RE^{3+}. As observed in Fig. 2.3b, NPs with a mean diameter of 83 nm are obtained at a lower molar ratio (NH_4F/RE^{3+}= 4), these NPs are of cubic structure, as ascertained by the XRD analysis. When the experiment is conducted at NH_4F/RE^{3+} = 6, as shown in Fig. 2.3c, the product is composed of nano-sized α-$NaYF_4$:Yb,Er spheres and micro-sized β-$NaYF_4$:Yb,Er sheets with an average diameter of 3.54 μm. As the molar ratio of NH_4F/RE^{3+} increases to 7, NPs are no longer observed, and only hexagonal microprisms with an average size of 2.54 μm in diameter and 1.50 μm in length are obtained, which present ultra-smooth planes at both ends and side surfaces, excellent uniformity and monodispersity (Fig. 2.3d). With the molar ratio slightly increasing to 8, the morphology is also hexagonal (Fig. 2.3e), but the mean diameter of the crystals decreases to 1.93 μm, while the mean length increases to 1.76 μm, and the corresponding aspect ratio is slightly increasing. As the molar ratio further increases, irregular structured hexagonal $NaYF_4$:Yb,Er crystals of increasing length are obtained (Fig. 2.3f and g).

From the abovementioned analysis, it can be concluded that the NH_4F content has a significant influence on the morphologies of the products, and the optimal molar ratio of NH_4F/RE^{3+} is 7, which allows the forming of micro-sized β-$NaYF_4$:Yb,Er particles. Obviously, the molar ratio of NH_4F/RE^{3+} has a remarkable influence on the structure and morphology of the final products. The corresponding morphologies and

dimensions, as well as aspect ratios of the products, are summarized in Table 2.3.

Table 2.3 Summary of $NaYF_4$:Yb,Er crystals prepared with different NH_4F/ RE^{3+} molar ratios

NH_4F/RE^{3+}[c]	Morphology	Structure	Average diameter (μm)	Average length (μm)	Aspect ratio
4	nanosphere	cubic	0.08	-	-
6	nanosphere & michrosheet	cubic & hexagonal	0.04 (nanosphere) & 3.54 (microsheet)	-	-
7	microprism	hexagonal	2.54	1.50	0.59
8	microprism	hexagonal	1.93	1.76	0.91
12	irregular microrod	hexagonal	1.06	2.27	2.14
16	irregular microrod	hexagonal	1.02	3.12	3.06

[c] other synthetic parameters: EG/H_2O = 2/1, reaction time: 12h.

2.3.5 Effect of Gd^{3+} Ion Content

Liu and co-workers[19] have shown that the increasing Gd^{3+} ion dopant slows the diffusion of F^- ions to the surface, inducing a reduction of the $NaYF_4$ nanocrystal in size by increasing the electron charge density on the surface of crystals, and a similar result was also observed with a $NaYbF_4$ host matrix[34]. Herein, different contents of Gd^{3+} ion were applied to explore their effect on the morphology and size evolution of resultant crystals prepared by the solvothermal method.

To determine the crystallinity of the as-prepared $NaYF_4$:Yb,Er,Gd (20/2/x mol%, x = 0 ~ 60) with varying Gd^{3+} ion dopant concentrations, they were examined by XRD patterns. The products show well-defined peaks for a Gd^{3+} ion content in the range of 0% to 40%, confirming their good crystallinity, and the XRD patterns of these products coincide well with the standard hexagonal $NaYF_4$ pattern of JCPDS No. 28-1192, indicating that the pure hexagonal phase structure of the Ln-doped $NaYF_4$ is formed when the Gd^{3+} ion dopant concentration is less than 40%. As the Gd^{3+} ion dopant concentrations further increase, the relative intensity of the characteristic peaks, as shown in Fig. 2.4a, is lower compared with those prepared with lower Gd^{3+} content, while those characteristic peaks still agree well with the standard XRD pattern of hexagonal $NaYF_4$. As the Gd^{3+} ion content increases, the diffraction peaks shown in XRD patterns broaden, and no extra diffraction peaks were observed, implying the formation of a homogeneous Y-Gd solid solution, because of the small structural

difference between the hexagonal phases of $NaGdF_4$ and $NaYF_4$. In addition, owing to the gradual replacement of Y^{3+} ion by larger Gd^{3+} ion in the host, the volume of the unit-cell expands, resulting in the slight shift of the peaks toward lower diffraction angles in the XRD patterns.

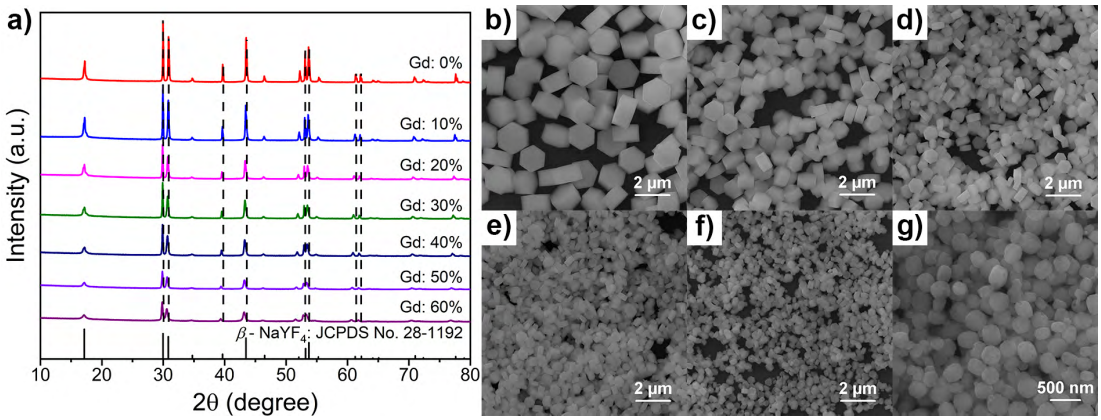

Fig. 2.4 (a) XRD patterns of products prepared with different content of Gd^{3+} ion and the standard data of hexagonal $NaYF_4$ (JCPDS No. 28-1192). SEM images of products obtained with the different content of Gd^{3+} ion. (b) 10%, (c) 20%, (d) 30%, (e) 40%, (f) 50%, (g) 60%.

Fig. 2.4b-g shows representative SEM images of the samples obtained with different Gd^{3+} ion dopant concentrations under the same synthetic condition. Fig. 2.2f, Fig. 2.4b and c reveal an inverse relationship between the amount of Gd^{3+} ion and the resulting size of the crystals when the Gd^{3+} ion dopant content increases from 0% to 20%, while the hexagonal structure remains unchanged. The average diameter and height dramatically decrease to 1.70 μm and 0.87 μm with the Gd^{3+} content of 10%, and further reduce to 1.13 μm and 0.52 μm when the dopant content reaches 20%, whereas the aspect ratio presents a slightly descending trend, declining from 0.59 to 0.46. When the dopant content varies in the range of 30% to 50%, the diameter and height, as shown in Fig. 2.4d-f, continuously decrease to nanoscale, the as-synthesized products are composed of uneven hexagonal prisms in size, and the crystal morphology of the obtained products is also hexagonal. Further increasing the content of Gd^{3+} ion to 60% (Fig. 2.4g), the product tends to grow into spherical NPs with coarse surfaces instead of well-defined hexagonal prisms. The abovementioned XRD results with the widening trend of the peaks also prove the reduction of the average crystalline size with increasing Gd^{3+} content. It should be noted that the content of the Gd^{3+} ion not only evidently decreases the size of the products but also remarkably affects the crystal formation and growth. The structural information of the as-prepared samples is listed in Table 2.4.

Table 2.4 Summary of $NaYF_4$:Yb,Er crystals prepared with different Gd^{3+} dopant content

Gd^{3+} content (mol%)[d]	Morphology	Structure	Average diameter (μm)	Average length (μm)	Aspect ratio
0	microprism	hexagonal	2.54	1.50	0.59
10%	microprism	hexagonal	1.70	0.87	0.51
20%	microprism	hexagonal	1.13	0.52	0.46
30%	nanoprism	hexagonal	0.72	0.31	0.43
40%	nanoprism	hexagonal	0.49	0.22	0.45
50%	nanoprism	hexagonal	0.32	0.18	0.56
60%	nanosphere	hexagonal	0.26	-	-

[d] other synthetic parameters: EG/H_2O = 2/1, NH_4F/RE^{3+} = 7/1, reaction time: 12h.

2.3.6 Effect of Different Organic Co-Solvents

Having seen the importance of the solvent on the outcome of particle formation, we now also explored the effect of substituting the low molecular weight solvent (EG) by higher molecular weight oligo ethylene (PEG) and PPGs.

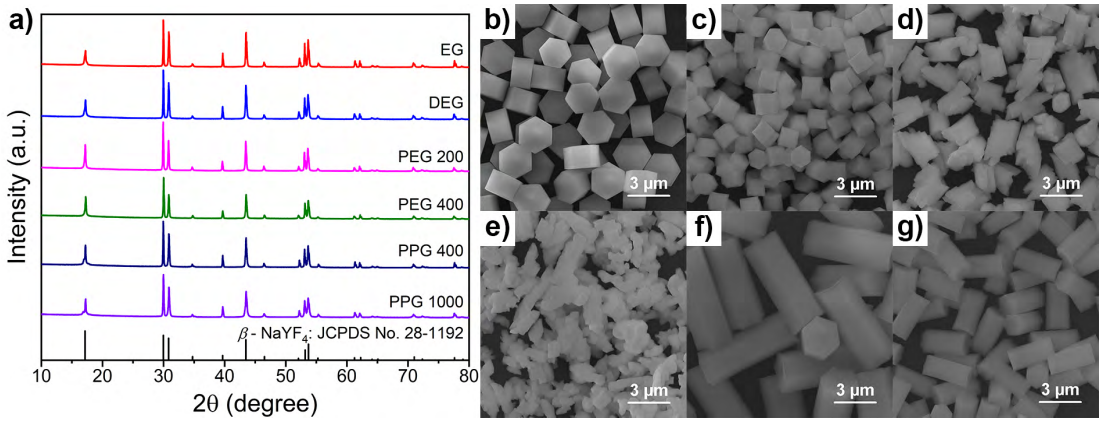

Fig. 2.5 (a) XRD patterns of products prepared with different organic co-solvents and the standard data of hexagonal $NaYF_4$ (JCPDS No. 28-1192). SEM images of products obtained with different organic co-solvents. (b) EG, (c) DEG, (d) PEG 200, (e) PEG 400, (f) PPG 400, (g) PPG 1000.

For that purpose, a series of experiments were conducted with various organic co-solvents substituting the EG but otherwise retaining the reaction conditions. Fig. 2.5a shows the XRD patterns of as-made crystals with the different organic co-solvents as well as standard data of the hexagonal $NaYF_4$ phase. The XRD results reveal that all crystals show conformity to the standard pattern of hexagonal $NaYF_4$ (JCPDS No. 28-1192).

Typical SEM images are shown in Fig. 2.5b-g. As can be seen from the SEM images, the crystals tend to grow into an irregular shape for using PEG 200 and PEG 400 (Fig. 2.5d and e). Apparently, for EG, well-defined crystals can only be formed at a low molecular weight (Fig. 2.5b and c). However, when PPGs are employed, uniform hexagonal microrods with excellent monodispersity and clear-cut crystallographic facets are obtained. When the molecular weight of the PPG rises from 400 to 1000, the mean diameter decreases from 2.85 μm to 1.67 μm, and the length is reduced from 6.32 μm to 3.03 μm. In addition, a reduction in aspect ratio takes place (Fig. 2.5f and g). It is interesting to note that the methyl branching of the organic co-solvent apparently favors the formation of crystals with well-defined crystallographic facets, and apparently, this small modification in the chain of the second solvent component has a substantial effect on the formed crystals. The corresponding features of the products are summarized in Table 2.5.

Table 2.5 Summary of $NaYF_4$:Yb,Er crystals prepared with different organic co-solvents

Organic co-solvent[e]	Morphology	Structure	Average Diameter (μm)	Average Length (μm)	Aspect ratio
EG	microprism	hexagonal	2.54	1.50	0.59
DEG	microprism	hexagonal	1.45	1.22	0.84
PEG 200	irregular microrod	hexagonal	1.50	2.36	1.57
PEG 400	irregular microrod	hexagonal	-	3.38	-
PPG 400	microrod	hexagonal	2.85	6.32	2.22
PPG 1000	microrod	hexagonal	1.67	3.03	1.81

[e] other synthetic parameters: organic co-solvent/H_2O = 2/1, NH_4F/RE^{3+} = 7/1, reaction time: 12h.

2.4 Crystal Growth and Formation Mechanisms

In order to obtain insights into the formation processes of the Ln-doped $NaYF_4$ crystals with different morphologies, β-$NaYF_4$:Yb,Er microprisms were used as a representative case to study the morphological evolution and crystal growth as a function of time by taking samples after different reaction times. Fig. 2.6a presents XRD patterns of the crystallinity and phase transformation of $NaYF_4$:Yb,Er at different reaction times, which show a marked evolution with the elapsed reaction time. The diffraction peaks of the sample after 2 h coincide with those of a pure cubic $NaYF_4$ phase (JCPDS No. 06-0342). As the time increases to 4 h, the XRD shows additional

peaks characteristic for the hexagonal phase of $NaYF_4$. This indicates that the initially present cubic crystals are converted into a newly developing hexagonal phase, which then is also present in the final product. Upon increasing the reaction time to 6 h and further to 12 h, XRD patterns are in excellent agreement with the standard data of the hexagonal $NaYF_4$ phase (JCPDS No. 28-1192), implying a complete disappearance of the cubic phase and one has now a pure hexagonal phase. Furthermore, the intensity of the diffraction peaks of the hexagonal phase increases as the reaction proceeds, signaling that the crystallinity is growing with the reaction time.

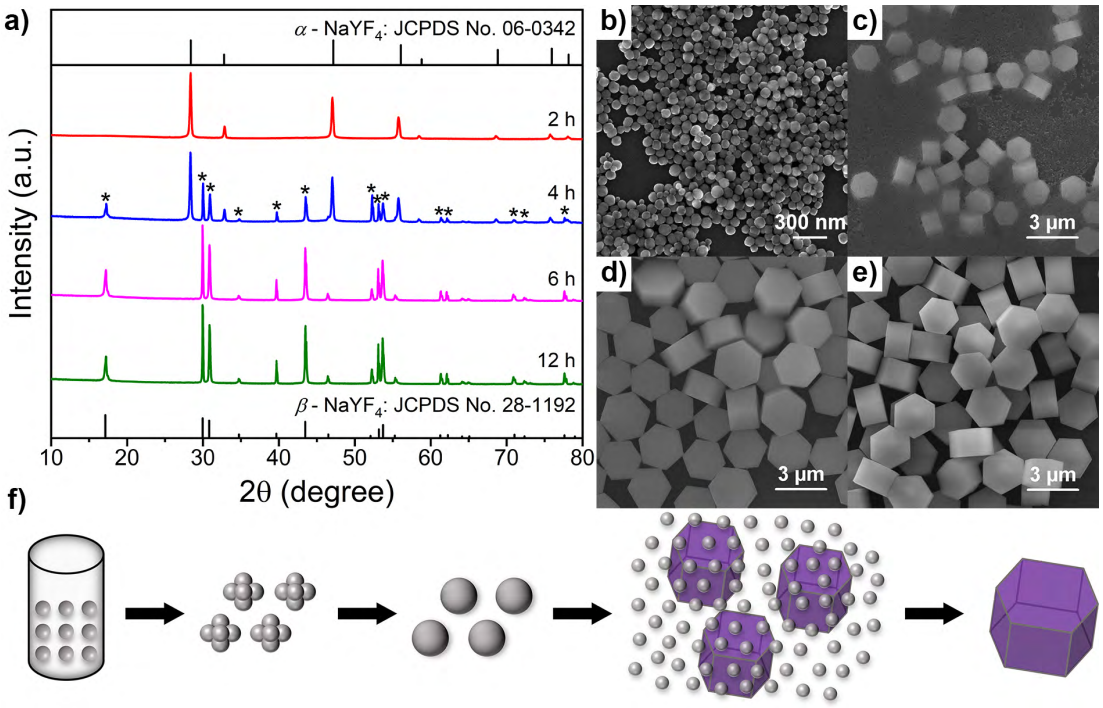

Fig. 2.6 (a) XRD patterns of $NaYF_4$:Yb,Er samples obtained after different reaction times, and the standard data of cubic $NaYF_4$ (JCPDS No. 06-0342) and hexagonal $NaYF_4$ (JCPDS No. 28-1192). SEM images of products obtained after different times. (b) 2 h, (c) 4 h, (d) 6 h, (e) 12 h. (EG/H_2O = 2/1, NH_4F/RE^{3+} = 7/1). (f) The possible formation mechanism of upconversion crystals. The morphological evolution experiences small nuclei as the intermediate, then to the mixture of nano and microparticles, and finally grows to micro-sized $NaYF_4$:Yb,Er crystals.

In parallel, the morphological evolution of the $NaYF_4$:Yb,Er particles was examined after different reaction times by SEM. The SEM images of Fig. 2.6a-d show different particle morphologies as a function of reaction times. In the early stage, the DSNTA was introduced into the solution to form Ln-ligand complexes through coordination interaction. After the reaction temperature reaches 190 ºC, the Ln ions would be released gradually as the complexes are weakened at high temperature and pressure. Then, Na^+ and F^- ions react with RE^{3+} to generate small nuclei, and these small nuclei

grow into cubic $NaYF_4$:Yb,Er nanocrystals within a short period of ~2 h. Fig. 2.6b shows that the sample prepared after 2 h consists of spherical NPs with a mean diameter of 88 nm, and the crystal form of the NPs is purely cubic (XRD analysis). The α-$NaYF_4$:Yb,Er NPs then further serve as seeds for the growth of β-$NaYF_4$:Yb,Er as the reaction proceeds. As shown in Fig. 2.6c, when the reaction time increases to 4 h, a coexistence of hexagonal microprisms and spherical NPs is observed, indicating the transition of NPs into microprisms. As the reaction proceeds up to 6 h and further to 12 h (Fig. 2.6d and e), the spherical NPs have disappeared, and only microprisms with an average diameter of 2.54 μm and a height of 1.50 μm are present, implying the complete transformation from spherical α-$NaYF_4$:Yb,Er nanocrystals into β-$NaYF_4$:Yb,Er microprisms. It is evident that the phase transition from cubic to hexagonal is directly related to the morphological change of the $NaYF_4$ crystals, which may be related to the different characteristic unit cell structures. Based on the above observations, the assumed formation mechanism of $NaYF_4$:Yb,Er microcrystals is illustrated in Fig. 2.6f.

2.5 Upconversion Photoluminescence Properties

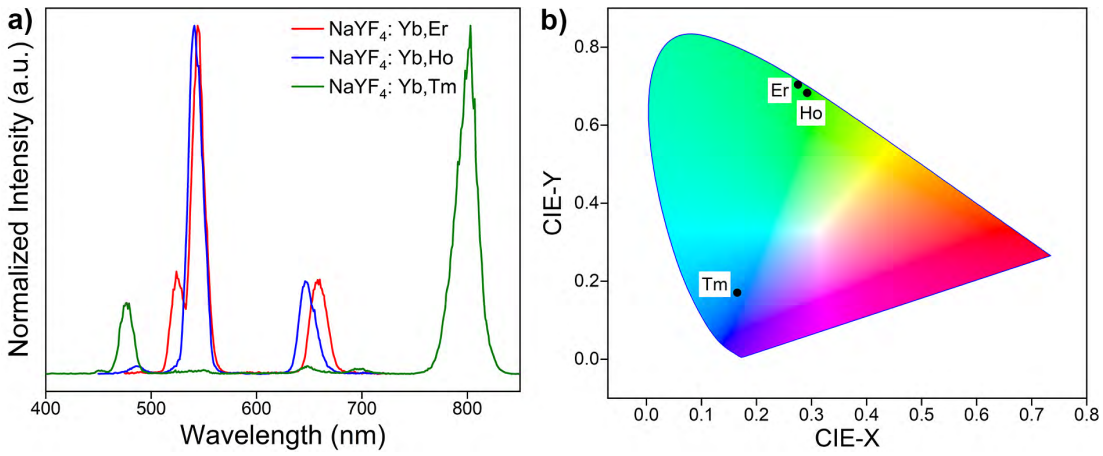

Fig. 2.7 (a) Normalized UCL spectra and (b) CIE chromaticity diagram of $NaYF_4$:Yb,Ln under 976 nm excitation (molar ratio Yb/Ln of 20/2 mol%).

Finally, we measured the UCL of the different UC particles. First, we investigated the UCL properties of $NaYF_4$ doped with Yb/Er, Yb/Ho, or Yb/Tm. The corresponding UCL spectra of β-$NaYF_4$:Yb,Ln are shown in Fig. 2.7a. All compounds show the typically spectral behavior of such co-doped upconversion materials revealing emission bands determined by the respective activator dopant ions. The UCL spectrum of the β-$NaYF_4$:Yb,Er particles contain emissions bands centered at 524 nm, 544 nm, and 658 nm, which can be assigned to $^2H_{11/2} \rightarrow {}^4I_{15/2}$, $^4S_{3/2} \rightarrow {}^4I_{15/2}$ and $^4F_{9/2} \rightarrow {}^4I_{15/2}$ transitions

of Er^{3+}, respectively. The spectrum of the β-$NaYF_4$:Yb,Ho sample exhibits an intense emission at 541 nm and a relatively weak emission at 645 nm originating from $^5S_2 \rightarrow {}^5I_8$ and $^5F_5 \rightarrow {}^5I_8$ transitions of Ho^{3+}. In the case of the Yb and Tm doped particles, two strong emission bands at 475 nm ($^1G_4 \rightarrow {}^3H_6$) and 800 nm ($^5F_5 \rightarrow {}^5I_8$), three weak emission bands at 450 nm ($^1D_2 \rightarrow {}^3F_4$), 648 nm ($^1G_4 \rightarrow {}^3F_4$), and 700 nm ($^3F_3 \rightarrow {}^3H_6$) occur. In general, it can be stated that the photoluminescent properties are relatively similar for crystals doped with Er^{3+} ion and Ho^{3+} ion, while for Tm^{3+} ion, the primary signal appears at 800 nm. As a result, the crystals with different activator dopant ions exhibit different emission intensities and colors. In order to quantify the overall color output of the different UC particles, chromaticity coordinates of β-$NaYF_4$:Yb,Ln were calculated according to the CIE chromaticity diagram, based on the corresponding UCL under 976 nm excitation. The results are plotted in Fig. 2.7b, and show the similarity of the Yb/Er and Yb/Ho doping, the CIE color coordinates of β-$NaYF_4$:Yb,Er (x= 0.2754, y = 0.7040) and β-$NaYF_4$:Yb,Ho (x = 0.2920, y = 0.6828) are located in the green region, while the Yb/Tm system has a very different color output with β-$NaYF_4$:Yb,Tm (x = 0.1651, y = 0.1707) being located in the blue region.

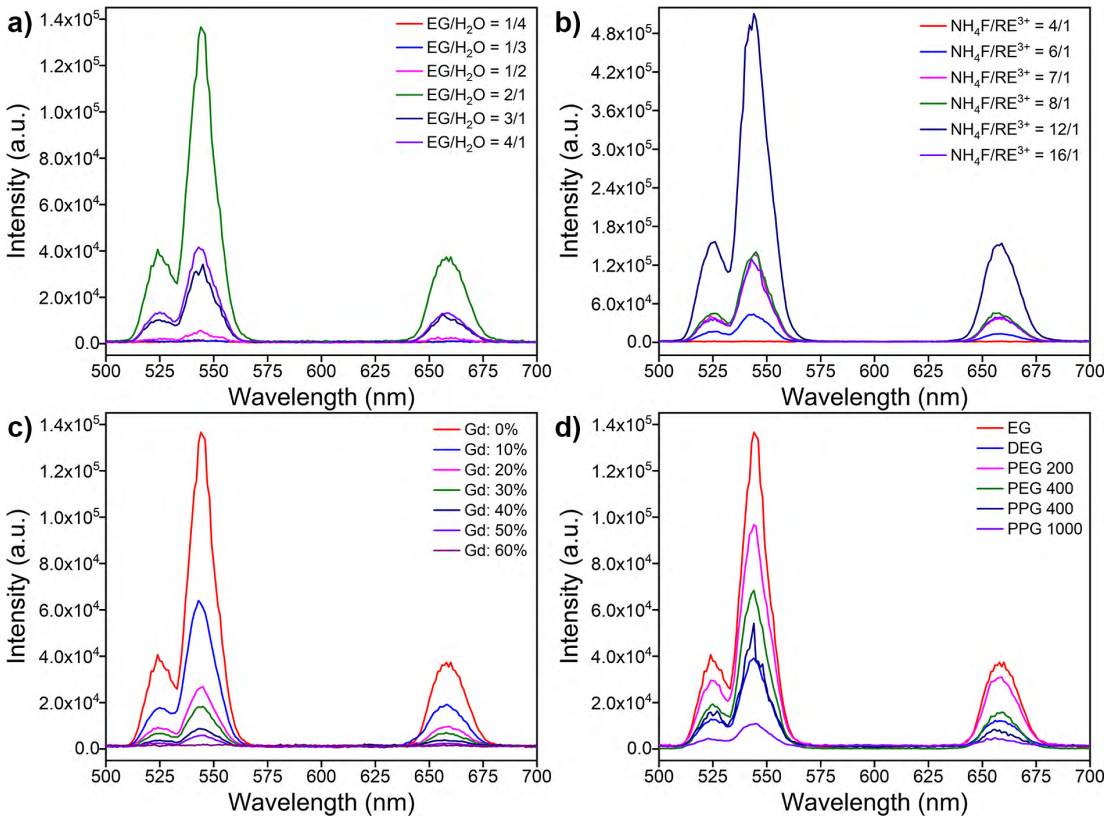

Fig. 2.8 UCL spectra of $NaYF_4$:Yb,Er prepared under (a) different volume ratios of EG/H_2O, (b) different molar ratios of NH_4F/RE^{3+}, (c) different Gd^{3+} dopant ion contents and (d) different organic co-solvents.

Subsequently, we focused on Er^{3+} based systems and studied the effect of different

synthetic parameters previously described in 2.3.3-2.3.6 on the UCL of the resulting particles. The results are summarized in Fig. 2.8. As can be seen from Fig. 2.8a-d, the α-$NaYF_4$:Yb,Er crystals, formed at a low EG/H_2O volume ratio and NH_4F/RE^{3+} molar ratio, are barely emissive. The green and red emissions appear once β-$NaYF_4$:Yb,Er is present. Since the morphologies and sizes of all these samples are different, the UCL intensity will be influence by affecting the scattering and absorption of the incident light. However, based on the UCL obtained with the same excitation condition, it can be concluded that intense UCL is achieved by the formation of well-defined crystals with a hexagonal β-$NaYF_4$ structure. This is in good agreement with previous studies[35].

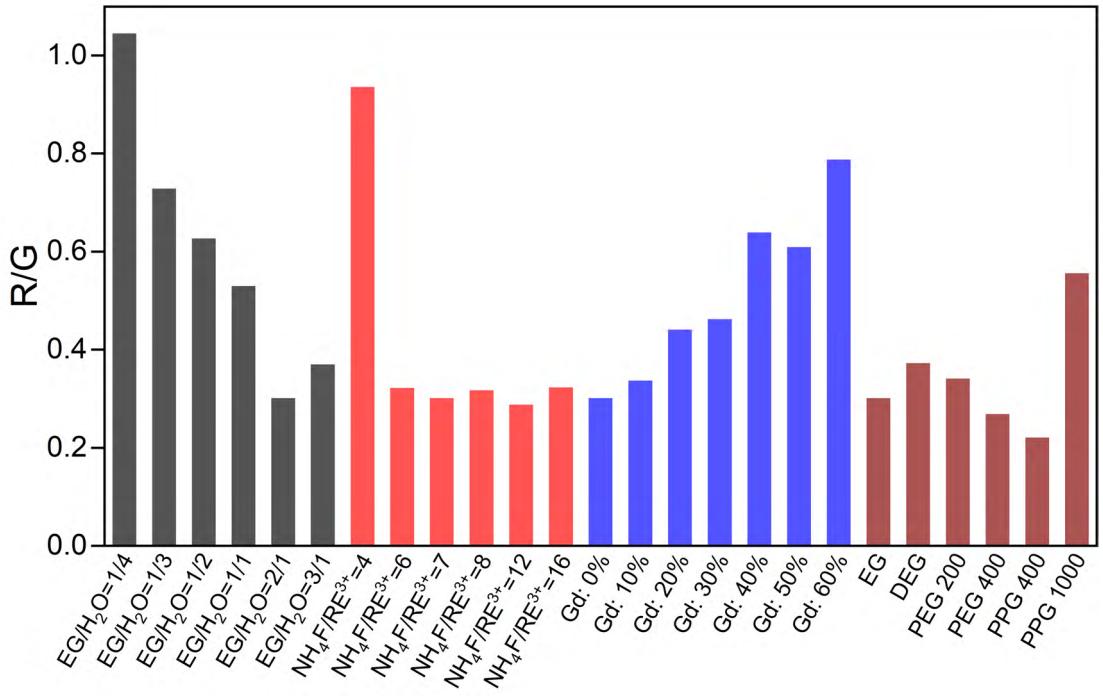

Fig. 2.9 Corresponding R/G ratio of upconversion crystals prepared with varying synthetic parameters.

The R/G of emission intensity is utilized to explain the luminescence changes of upconversion crystals prepared with various parameters, which is depicted in Fig. 2.9. The R/G value decreases from 1.04 to 0.30 with the increasing EG/H_2O volume ratio from 1/4 to 2/1, and a slight increase occurs with a further increase in EG/H_2O volume ratio. The R/G stabilizes at about 0.30 when the upconversion crystals are prepared with the NH_4F/RE^{3+} molar ratio above 6, except for the ones obtained at a low NH_4F/RE^{3+} molar ratio. A similar trend is observed with the crystals obtained in low molecular weight of organic co-solvent, and a significant increase in R/G when PPG1000 was used as the co-solvent. In addition, it is evident that the R/G is sensitive to the concentration of Gd^{3+} dopant ion. It can be found that the R/G increases with increasing the Gd^{3+} dopant ion concentration. The remarkable difference in the R/G

ratios of $NaYF_4$:Yb,Er,Gd may be attributed to the loss of crystallinity and the reduction of crystal size. Moreover, it is worth mentioning that the tunable emission color of upconversion samples can be obtained by varying synthetic parameters, as evidenced in Fig. 2.10.

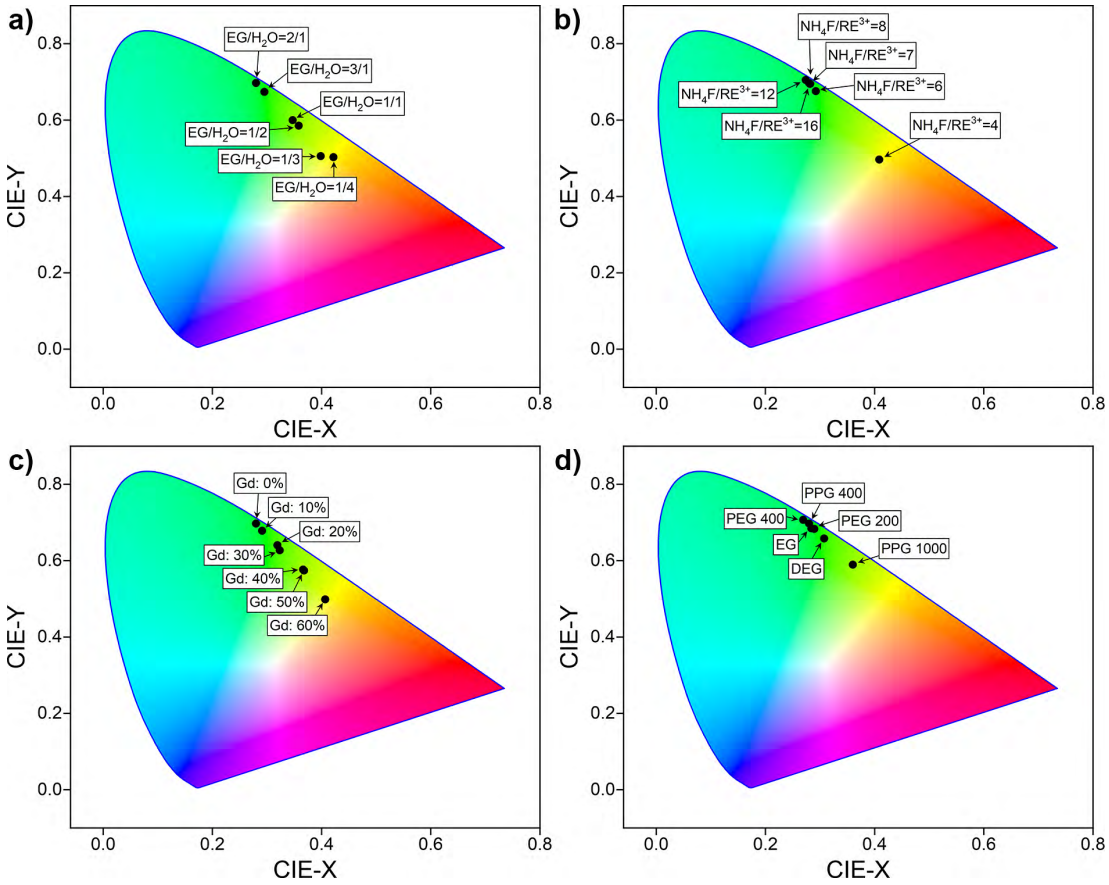

Fig. 2.10 CIE chromaticity diagrams of upconversion crystals prepared with varying (a) EG/H_2O volume ratio, (b) NH_4F/RE^{3+} molar ratio, (c) Gd^{3+} dopant ion concentration and (d) organic co-solvent.

2.6 Conclusion

In summary, Ln-doped $NaYF_4$ nano- and micro-sized upconversion crystals with diverse morphologies were successfully prepared *via* the solvothermal method using disodium nitrilotriacetate as the capping agent. The influence of the volume ratio of EG/H_2O, the molar ratio of NH_4F/RE^{3+}, the Gd^{3+} ion dopant concentration, type of activator dopant ions, using different organic co-solvents was systematically studied. As a result, the morphology of crystals can be well manipulated from NPs *via* nano/microprisms to microrods with high uniformity and monodispersity by carefully controlling the abovementioned experimental factors.

It was found that the crystal phase transition from cubic to hexagonal phase mainly depends on the volume ratio of EG/H_2O and the molar ratio of NH_4F/RE^{3+}, while the morphology is readily tuned by the change of organic co-solvents. Furthermore, the reaction time has to be large enough as apparently initially always cubic α-$NaYF_4$ is formed, which then under appropriate conditions is converted into hexagonal β-$NaYF_4$ during the further growth process. The particle size could be regulated by the doping with Gd^{3+} ions, while the crystal structure and morphology are independent of activator dopant ions. It is interesting to note that adding PPG as the co-solvent apparently favors the formation of microrods with well-defined crystallographic facets.

In addition, as the most interesting property of these crystalline particles, their upconversion photoluminescence properties under 976 nm excitation were proven to be strongly associated with their composition, phase structure, and morphology of synthesized crystals. By appropriately choosing the preparation conditions, one can then optimize the luminescence performance of these particles by having control over their microscopic and mesoscopic structure. Such optimized crystals with adjustable features and unique optical properties may find potential applications in the fields of lighting and display.

2.7 References

[1] L. Zong, P. Xu, Y. Ding, K. Zhao, Z. Wang, X. Yan, R. Yu, J. Chen, and X. Xing, $Y_2O_3:Yb^{3+}/Er^{3+}$ hollow spheres with controlled inner structures and enhanced upconverted photoluminescence, *Small*, **2015**, 11, 2768-2773.

[2] R. Martín-Rodríguez, S. Fischer, A. Ivaturi, B. Froehlich, K. W. Krämer, J. C. Goldschmidt, B. S. Richards, and A. Meijerink, Highly efficient IR to NIR upconversion in $Gd_2O_2S:Er^{3+}$ for photovoltaic applications, *Chem. Mater.*, **2013**, 25, 1912-1921.

[3] Y. Zhu, W. Xu, S. Cui, M. Liu, C. Lu, H. Song, and D. Kim, Controlled size and morphology, and phase transition of $YF_3:Yb^{3+},Er^{3+}$ and $YOF:Yb^{3+},Er^{3+}$ nanocrystals for fine color tuning, *J. Mater. Chem. C*, **2016**, 4, 331-339.

[4] C. Li, Z. Hou, C. Zhang, P. Yang, G. Li, Z. Xu, Y. Fan, and J. Lin, Controlled synthesis of Ln^{3+} (Ln = Tb, Eu, Dy) and V^{5+} ion-doped YPO_4 nano-/microstructures with tunable luminescent colors, *Chem. Mater.*, **2009**, 21, 4598-4607.

[5] F. Wang, X. Xue, and X. Liu, Multicolor tuning of (Ln, P)-doped YVO_4 nanoparticles by single-wavelength excitation, *Angew. Chem. Int. Edit.*, **2008**, 47, 906-909.

[6] H. Qiu, G. Chen, R. Fan, L. Yang, C. Liu, S. Hao, M. Sailor, H. Gren, C. Yang, and P. Prasad, Intense ultraviolet upconversion emission from water-dispersed colloidal $YF_3:Yb^{3+}/Tm^{3+}$ rhombic nanodisks, *Nanoscale*, **2014**, 6, 753-757.

[7] F. Zhang, Y. Wan, T. Yu, F. Zhang, Y. Shi, S. Xie, Y. Li, L. Xu, B. Tu, and D. Zhao, Uniform nanostructured arrays of sodium rare-earth fluorides for highly efficient multicolor upconversion luminescence, *Angew. Chem. Int. Edit.*, **2007**, 46, 7976-7979.

[8] F. Wang, and X. Liu, Upconversion multicolor fine-tuning: visible to near-infrared emission from lanthanide-doped $NaYF_4$ nanoparticles, *J. Am. Chem. Soc.*, **2008**, 130, 5642-5643.

[9] N. Johnson, A. Korinek, C. Dong, and F. van Veggel, Self-focusing by Ostwald ripening: a strategy for layer-by-layer epitaxial growth on upconverting nanocrystals, *J. Am. Chem. Soc.*, **2012**, 134, 11068-11071.

[10] J. Boyer, F. Vetrone, L. Cuccia, and J. Capobianco, Synthesis of colloidal upconverting $NaYF_4$ nanocrystals doped with Er^{3+}, Yb^{3+} and Tm^{3+}, Yb^{3+} *via* thermal decomposition of lanthanide trifluoroacetate precursors, *J. Am. Chem. Soc.*, **2006**, 128, 7444-7445.

[11] A. Pilch, C. Würth, M. Kaiser, D. Wawrzyńczyk, M. Kurnatowska, S. Arabasz, K. Prorok, M. Samoć, W. Strek, U. Resch-Genger, and A. Bednarkiewicz, Shaping luminescent properties of Yb^{3+} and Ho^{3+} co-doped upconverting core-shell β-$NaYF_4$ nanoparticles by dopant distribution and spacing, *Small*, **2017**, 13, 1701635.

[12] Y. Zhang, X. Sun, R. Si, L. You, and C. Yan, Single-crystalline and monodisperse LaF_3 triangular nanoplates from a single-source precursor, *J. Am. Chem. Soc.*, **2005**, 127, 3260-3261.

[13] N. Dyck, F. van Veggel, and G. Demopoulos, Size-dependent maximization of upconversion efficiency of citrate-stabilized β-phase $NaYF_4$:Yb^{3+},Er^{3+} crystals *via* annealing, *ACS Appl. Mater. Interfaces*, **2013**, 5, 11661-11667.

[14] J. Li, Z. Hao, X. Zhang, Y. Luo, J. Zhao, S. Lv, J. Cao, and J. Zhang, Hydrothermal synthesis and upconversion luminescence properties of β-$NaGdF_4$:Yb^{3+}/Tm^{3+} and β-$NaGdF_4$:Yb^{3+}/Ho^{3+} submicron crystals with regular morphologies, *J. Colloid. Interf. Sci.*, **2013**, 392, 206-212.

[15] Z. Li, and Y. Zhang, An efficient and user-friendly method for the synthesis of hexagonal-phase $NaYF_4$:Yb,Er/Tm nanocrystals with controllable shape and upconversion fluorescence, *Nanotechnology*, **2008**, 19, 345606.

[16] X. Teng, Y. Zhu, W. Wei, S. Wang, J. Huang, R. Naccache, W. Hu, A. Tok, Y. Han, Q. Zhang, Q. Fan, W. Huang, J. Capobianco, and L. Huang, Lanthanide-doped Na_xScF_{3+x} nanocrystals: crystal structure evolution and multicolor tuning, *J. Am. Chem. Soc.*, **2012**, 134, 8340-8343.

[17] H. Schäfer, P. Ptacek, H. Eickmeier, and M. Haase, Synthesis of hexagonal Yb^{3+},Er^{3+}-doped $NaYF_4$ nanocrystals at low temperature, *Adv. Funct. Mater.*, **2009**, 19, 3091-3097.

[18] X. Wang, J. Zhuang, Q. Peng, and Y. Li, A general strategy for nanocrystal synthesis, *Nature*, **2005**, 437, 121-124.

[19] F. Wang, Y. Han, C. Lim, Y. Lu, J. Wang, J. Xu, H. Chen, C. Zhang, M. Hong, and X. Liu, Simultaneous phase and size control of upconversion nanocrystals through lanthanide doping, *Nature*, **2010**, 463, 1061-1065.

[20] F. Wang, D. Chatterjee, Z. Li, Y. Zhang, X. Fan, and M. Wang, Synthesis of polyethylenimine/$NaYF_4$ nanoparticles with upconversion fluorescence, *Nanotechnology*, **2006**, 17, 5786.

[21] D. Chatterjee, A. Rufaihah, and Y. Zhang, Upconversion fluorescence imaging of cells and small animals using lanthanide doped nanocrystals, *Biomaterials*, **2008**, 29, 937-943.

[22] Z. Li, and Y. Zhang, Monodisperse silica-coated polyvinylpyrrolidone/$NaYF_4$ nanocrystals with multicolor upconversion fluorescence emission, *Angew. Chem. Int. Edit.*, **2006**, 45, 7732-7735.

[23] C. Li, Z. Quan, J. Yang, P. Yang, and J. Lin, Highly uniform and monodisperse β-$NaYF_4$:Ln^{3+} (Ln = Eu, Tb, Yb/Er, and Yb/Tm) hexagonal microprism crystals: hydrothermal synthesis and luminescent properties, *Inorg. Chem.*, **2007**, 46, 6329-6337.

[24] C. Li, C. Zhang, Z. Hou, L. Wang, Z. Quan, H. Lian, and J. Lin, β-$NaYF_4$ and β-$NaYF_4$:Eu^{3+} microstructures: morphology control and tunable luminescence properties, *J. Phys. Chem. C*, **2009**, 113, 2332-2339.

[25] C. Li, J. Yang, Z. Quan, P. Yang, D. Kong, and J. Lin, Different microstructures of β-$NaYF_4$ fabricated by hydrothermal process: effects of pH values and fluoride sources, *Chem. Mater.*, **2007**, 19, 4933-4942.

[26] C. Li, Z. Quan, P. Yang, S. Huang, H. Lian, and J. Lin, Shape-controllable synthesis and upconversion properties of lutetium fluoride (doped with Yb^{3+}/Er^{3+}) microcrystals by hydrothermal process, *J. Phys. Chem. C*, **2008**, 112, 13395-13404.

[27] F. He, N. Niu, L. Wang, J. Xu, Y. Wang, G. Yang, S. Gai, and P. Yang, Influence of surfactants on the morphology, upconversion emission, and magnetic properties of β-$NaGdF_4$:Yb^{3+},Ln^{3+} (Ln = Er, Tm, Ho), *Dalton Trans.*, **2013**, 42, 10019-10028.

[28] J. Yang, D. Shen, X. Li, W. Li, Y. Fang, Y. Wei, C. Yao, B. Tu, F. Zhang, and D. Zhao, One-step hydrothermal synthesis of carboxyl-functionalized upconversion phosphors for bioapplications, *Chem. Eur. J.*, **2012**, 18, 13642-13650.

[29] C. Li, X. Yin, L. Chen, Q. Li, and T. Wang, Synthesis of cobalt ion-based coordination polymer nanowires and their conversion into porous Co_3O_4 nanowires with good lithium storage properties, *Chem. Eur. J.*, **2010**, 16, 5215-5221.

[30] G. Wang, X. Gou, J. Horvat, and J. Park, Facile synthesis and characterization of iron oxide semiconductor nanowires for gas sensing application, *J. Phys. Chem. C*, **2008**, 112, 15220-15225.

[31] C. An, G. Liu, Y. Wang, L. Li, F. Qiu, Y. Xu, C. Xu, Y. Wang, L. Jiao, and H. Yuan, Porous nickel cobaltite nanorods: desired morphology inherited from coordination precursors and improved supercapacitive properties, *RSC Adv.*, **2013**, 3, 15382-15388.

[32] Y. Song, H. You, Y. Huang, M. Yang, Y. Zheng, L. Zhang, and N. Guo, Highly uniform and monodisperse Gd_2O_2S:Ln^{3+} (Ln = Eu, Tb) submicrospheres: solvothermal synthesis and luminescence properties, *Inorg. Chem.*, **2010**, 49, 11499-11504.

[33] M. Ding, C. Lu, L. Cao, Y. Ni, and Z. Xu, Controllable synthesis, formation mechanism and upconversion luminescence of β-$NaYF_4$:Yb^{3+}/Er^{3+} microcrystals by hydrothermal process, *CrystEngComm*, **2013**, 15, 8366-8373.

[34] J. Damasco, G. Chen, W. Shao, H. Ågren, H. Huang, W. Song, J. Lovell, and P. Prasad, Size-tunable and monodisperse Tm^{3+}/Gd^{3+}-doped hexagonal $NaYbF_4$ nanoparticles with engineered efficient near infrared-to-near infrared upconversion for in vivo imaging, *ACS Appl. Mater. Interfaces*, **2014**, 6, 13884-13893.

[35] G. Yi, and G. Chow, Synthesis of hexagonal-phase $NaYF_4$:Yb,Er and $NaYF_4$:Yb,Tm nanocrystals with efficient up-conversion fluorescence, *Adv. Funct. Mater.*, **2006**, 16, 2324-2329.

Chapter 3: Synthesis of Hydrophilic Upconversion Nanocrystals: A Two-Step Approach

Chapter 3 is based on the following article

> Chunning Sun, Jan Ron Justin Simke, Michael Gradzielski, "An efficient synthetic strategy for ligand-free upconversion nanoparticles", *Mater. Adv.*, **2020**, 1, 1602-1607 (DOI: 10.1039/D0MA00411A).

with the permission from Materials Advances. Copyright of the Royal Society of Chemistry (2020).

C. Sun and M. Gradzielski conceived and designed the experiments. C. Sun performed the experiments and analyzed the data. J. R. J. Simke conducted the TEM measurements. C. Sun and M. Gradzielski co-wrote the manuscript. All authors discussed the results and commented on the manuscript.

3.1 Introduction

High-quality upconversion NPs with precisely tuned size, composition, shape, as well as well-designed architecture are generally synthesized by applying the long-chain hydrocarbon OA as the ligand in the synthetic process[1-6]. The sterically stabilized oleate-capped upconversion NPs are prone to disperse in nonpolar and hydrophobic solvents, while most applications of upconversion NPs require the particles to be readily dispersed in hydrophilic media. To address this problem, postsynthetic surface modifications are essential for rendering upconversion NPs dispersible in the aqueous solution or polar organic media prior to subsequent practical applications. Heretofore, surface post-modifications of oleate-capped upconversion NPs including ligand exchange[7-12], oxidation[13-15], and removal[16, 17], amphiphilic polymer deposition[18-22], and silica coating[23, 24] have been applied. However, these existing methods involve either laborious procedures or time-consuming reactions. A generalized, fast, and efficient strategy for the hydrophobic-to-hydrophilic transition of upconversion NPs is largely missing.

Up to now, the ligand removal strategy is considered as a versatile approach to prepare hydrophilic upconversion NPs, as it provides more possibilities for further

functionalization of upconversion NPs. For instance, $NOBF_4$ was employed to replace the oleate ligand to prepare hydrophilic NPs, which were partially capped by the BF_4^- anion, and the quasi-ligand-free NPs were further functionalized by grafting different capping molecules on the surface. However, the air-sensitive and oxidative stripping reagent limits its application[16]. Another strategy was to use HCl solution (pH 4) to obtain ligand-free upconversion NPs from oleate-capped upconversion NPs based on an acid-base reaction. However, the stripping process occurred between solid oleate-capped upconversion NPs and acidic aqueous solution in a solid-liquid system, which lowered the removal efficiency of the oleate ligand from the surface of NPs and took hours of reaction time for complete ligand exfoliation[17].

To produce ligand-free upconversion NPs in a simple fashion, a fast, highly efficient, and easy-to-process approach was developed using short-chain acids including FA, AA, and LA as stripping agents by a simple vortexing method. Furthermore, biphasic and single solvent systems are introduced to allow for the ligand removal from the surface of oleate-stabilized upconversion NPs on the second time scales. More importantly, the resulting ligand-free upconversion NPs can be readily transferred to the aqueous solution and further functionalized by water-soluble capping molecules.

3.2 Materials and Methods

3.2.1 Reagents

Yttrium(III) acetate tetrahydrate (99.9%), ytterbium(III) acetate hydrate (99.9%), erbium(III) acetate hydrate (99.9%), Lanthanum(III) acetate hydrate (99.9%) were purchased from Alfa Aesar, OA (90%), ODE (90%), sodium acetate (CH_3COONa, 99%), cesium acetate (CH_3COOCs, 99.9%), NH_4F (≥98%), NaOH (≥98%), MeOH (99.8%), ethanol (≥99.8%), cyclohexane (99.5%), chloroform (≥99%), toluene (99.9%), DMF (99.8%), DMSO (≥99.5%), ACN (99.8%), NMP (99.5%), FAM (≥99%), FA (≥98%), AA (>99.5%), LA (~90%), PEI (branched, Mw ~25,000), PAA (50 wt. % in H_2O, Mw ~5,000), PVP (Mw ~10,000) were purchased from Sigma-Aldrich. All the commercial chemicals were used as received. Milli-Q water (18.2 MΩ·cm at 25 °C) was used in all experiments.

3.2.2 Instruments

FT-IR spectra were acquired on a Thermo Scientific Nicolet iS5 FT-IR spectrometer using the KBr method. The spectra were recorded in transmission mode with the wavenumber range from 4000-500 cm^{-1}. ^1H NMR spectra were collected by using a Bruker Advance II 500 MHz NMR spectrometer. UV-Vis absorption spectra were obtained by using a CARY 50 spectrophotometer. TEM and HR-TEM images were obtained by FEI Tecnai G^2 20 S-TWIN with a LaB_6 cathode operating at 200 kV. XRD spectra were obtained by using Philips X'Pert MPD Pro X-ray diffractometer at a scanning rate of 4°/min in the 2θ range from 10° to 90° with Cu Kα radiation (λ = 0.15406 nm). ζ-potential measurements were carried out with an Anton Paar Litesizer™ 500. TGA was performed with a Mettler Toledo TGA/DSC1 Star System analyzer under N_2 atmosphere flow at a ramp rate of 10 ºC/min. UCL emission spectra were collected at room temperature with a fiber-coupled spectrometer (Ocean HDX, Ocean Optics) equipped with an external 980 nm CW laser (Roithner Lasertechnik GmbH) with tunable power from 0 to 5 W.

3.2.3 Synthesis of OA-UCNPs

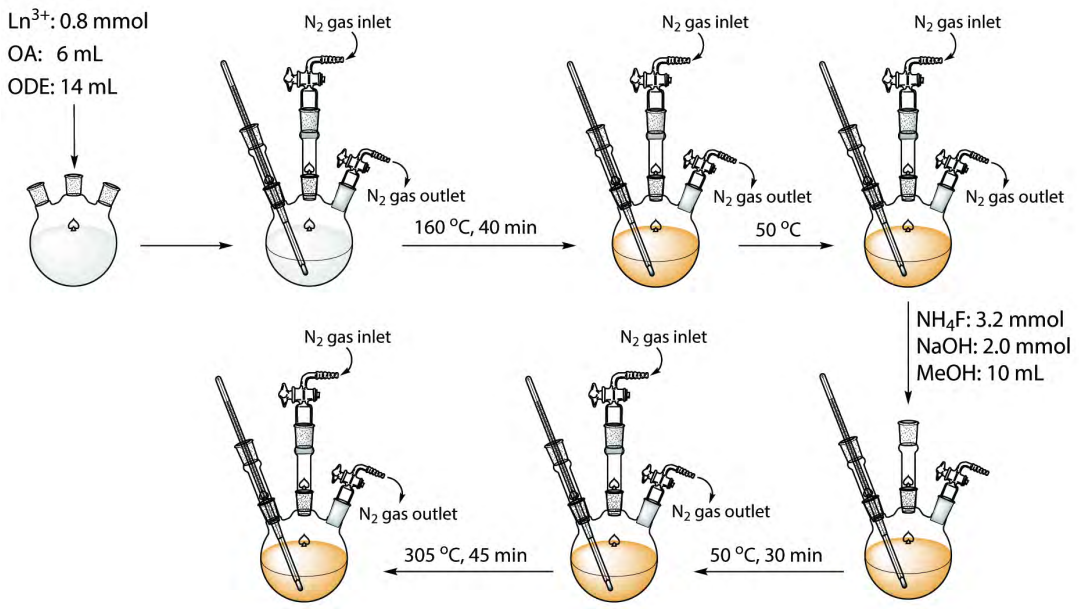

Fig. 3.1 Schematic diagram of the synthesis of upconversion NPs by the high-temperature coprecipitation method.

A schematic diagram of the synthesis of OA-UCNPs by the high-temperature coprecipitation method is shown in Fig. 3.1. Typically, 3.12 mL $Y(CH_3COO)_3$ (0.2 M),

0.8 mL $Yb(CH_3COO)_3$ (0.2 M) and 0.8 mL $Er(CH_3COO)_3$ (0.02 M) were added to a three-neck flask containing 6 mL OA and 14 mL ODE at room temperature. The mixed solution was heated to 110 ºC for 30 min to remove the water, followed by heating to 160 ºC for 40 min to form Ln-oleate complexes and then cooled down to 50 ºC. A MeOH solution (10 mL) containing NH_4F (3.2 mmol) and NaOH (2.0 mmol) was added afterward and stirred at 50 ºC for 30 min. After evaporating the MeOH, the mixed solution was heated to 305 ºC at a ramp rate of 10 °C/min and maintained at this temperature for a certain time under N_2 atmosphere. After cooling down to room temperature, OA-UCNPs were precipitated out by adding excess ethanol, collected by centrifugation at 6000 r.p.m for 5 min, repeatedly washed with ethanol, and finally redispersed in cyclohexane, chloroform, or toluene. The synthetic procedure of undoped oleate-capped $NaYF_4$ nanocrystals was similar to that of OA-UCNPs, except that 4 mL (0.2 M) was added to a mixture of OA (6 mL) and ODE (14 mL) in a three-necked flask. For the preparation of 35 nm OA-UCNPs, the reaction was maintained at 305 ºC for 45 min, and for 20 nm OA-UCNPs preparation, the reaction was maintained at 305 ºC for 35 min.

3.2.4 Synthesis of Oleate-Capped $NaLaF_4$ NRs

Typically, 4 mL $La(CH_3COO)_3$ (0.2 M), 4 mL CH_3COONa (0.2 M), and 6 mL CH_3COOCs (0.4 M) were added to a three-neck flask containing 6 mL OA and 14 mL ODE at room temperature. The mixed solution was heated to 110 °C for 30 min to remove the water, followed by heating to 170 °C for 30 min to form metal-oleate complexes and then cooled down to 45 °C. A MeOH solution (10 mL) containing NH_4F (4.8 mmol) was added afterward and stirred at 45 °C for 120 min. After evaporating the MeOH, the solution was heated to 310 °C at a ramp rate of 10 °C/min and maintained at this temperature for 60 min under N_2 atmosphere. After cooling down to room temperature, oleate-capped $NaLaF_4$ NRs were precipitated out by adding excess ethanol, collected by centrifugation at 6000 r.p.m for 5 min, repeatedly washed with ethanol, and finally redispersed in cyclohexane.

3.2.5 Ligand Removal in Single Solvent Systems

FA (5 mmol) was added to 2 mL cyclohexane, chloroform, or toluene solution containing OA-UCNPs (10 mg/mL) directly, the mixture was then shaken for 10 s at 3000 r.p.m on a vortex mixer, ligand-free UCNPs were precipitated out. The resultant

ligand-free UCNPs were obtained by centrifugation at 6000 r.p.m for 20 min, washed one time with ethanol and three times with water, and finally redispersed in water. Samples treated with FA in cyclohexane, chloroform, and toluene solution were labeled as FA-Cy, FA-Chl, and FA-Tol, respectively.

AA can also be used as the stripping agent, the procedure was similar to that of OA-UCNPs treated by FA, except that 10 mmol of AA was added. A homogeneous solution was finally obtained, ligand-free UCNPs were collected by centrifugation at 15000 r.p.m for 20 min, washed one time with ethanol and three times with water, and finally redispersed in water. Samples treated with AA in cyclohexane, chloroform, and toluene solution were labeled as AA-Cy, AA-Chl, and AA-Tol, respectively.

LA can be applied as the stripping agent as well, the procedure was similar to that of OA-UCNPs treated by FA, except for the use of chloroform as the dispersant. Ligand-free UCNPs were transferred to the LA layer and collected by centrifugation at 15000 r.p.m for 20 min, washed one time with ethanol and three times with water, and finally redispersed in water. Samples treated with LA in cyclohexane and toluene solution were labeled as LA-Cy and LA-Tol, respectively.

3.2.6 Ligand Removal in Biphasic Solvent Systems

FA (5 mmol) was initially dissolved in 2 mL polar solvents (ACN, DMF, DMSO, FAM, MeOH, or NMP), 2 mL cyclohexane solution containing OA-UCNPs (10 mg/mL) was added gently afterward to form a biphasic solvent system. After shaking for 10 s at 3000 r.p.m by simple vortexing, UCNPs were transferred from the upper cyclohexane layer to the bottom polar solvent. Ligand-free UCNPs were obtained by centrifugation at 15000 r.p.m for 20 min, washed one time with ethanol and three times with water, and finally redispersed in water. Ligand-free UCNPs prepared under FA treatment with different polar solvents were labeled as FA-Cy/ACN, FA-Cy/DMF, FA-Cy/DMSO, FA-Cy/FAM, FA-Cy/MeOH, and FA-Cy/NMP, respectively. AA (10 mmol) can also be used as the stripping agent, except for the use of ACN, DMSO, or FAM as the polar solvent. Oleate-free UCNPs prepared under AA treatment with different polar solvents were labeled as AA-Cy/DMF, AA-Cy/MeOH, and AA-Cy/NMP.

3.2.7 Ligand Removal *via* $NOBF_4$-Treatment

Typically, 2 mL of OA-UCNPs in cyclohexane (10 mg/mL) was combined with 2 mL of DMF containing $NOBF_4$ (0.01 M) at room temperature. The resulting mixture was shaken gently and then sonicated for 10 min. After centrifugation at 15000 r.p.m for 20 min to remove the supernatant, quasi-ligand-free UCNPs were obtained, which can be redispersed in water.

3.2.8 Ligand Removal *via* HCl-Treatment

Typically, OA-UCNPs powder (10 mg) were dispersed in 2 mL HCl aqueous solution (pH = 4) and sonicated until the solid was completely dissolved. The resultant ligand-free UCNPs were obtained by centrifugation at 15000 r.p.m for 20 min, washed one time with ethanol and three times with water, and finally redispersed in water.

3.2.9 Surface Functionalization of Ligand-Free UCNPs

Ligand-free UCNPs capped by other water-soluble capping molecules were prepared according to the previous work with some modifications[25]. Typically, 50 mg capping molecules (PVP, PAA, or PEI) were first dissolved in 5 mL H_2O, and the solution was adjusted to pH 8 with 50 mM NaOH (except for PEI). 5 mL bare UCNPs solution (5 mg/mL) were then added, followed by overnight stirring. The products were obtained *via* centrifugation at 15000 r.p.m for 20 min, washed three times with water, and finally redispersed in water with a concentration of 1 mg/mL.

3.3 Results and Discussion

3.3.1 Hydrophobic-to-Hydrophilic Transition of OA-UCNPs

Monodisperse hexagonal OA-UCNPs were synthesized by the coprecipitation method in a high-boiling-point solvent using OA as the capping ligand[6]. The resulting OA-UCNPs can be dispersed in nonpolar solvents (cyclohexane, chloroform, or toluene), owing to the presence of the oleate ligand on their surface. In order to render UCNPs hydrophilic, biphasic and single solvent systems are introduced to realize the ligand removal from the surface of OA-UCNPs. For the ligand removal occurs in biphasic solvent systems, a wide variety of polar solvents including ACN, DMF, DMSO, FAM,

MeOH, and NMP are employed to form liquid-liquid interfaces with cyclohexane, and the reaction is simply performed by a short contact of the organic dispersion of OA-UCNPs with immiscible polar solvents containing short-chain organic acids on a vortex mixer, leading to the in-solution transfer of UCNPs to the polar phase, a typical example is shown in Fig. 3.2a. In terms of single solvent systems, the ligand removal takes place when cyclohexane, chloroform, or toluene is adopted as the dispersant to stabilize OA-UCNPs. Ligand exfoliation is realized by direct addition of short-chain acids to a single solvent system, and ligand-free UCNPs are generated upon the sufficient interaction of the short-chain acids with the hydrophobic solvent through vigorous shaking in a short time, and a typical example is shown in Fig. 3.2b. More importantly, the ligand-free UCNPs obtained in the above-mentioned systems *via* the vortexing method can be easily transferred to the aqueous solution.

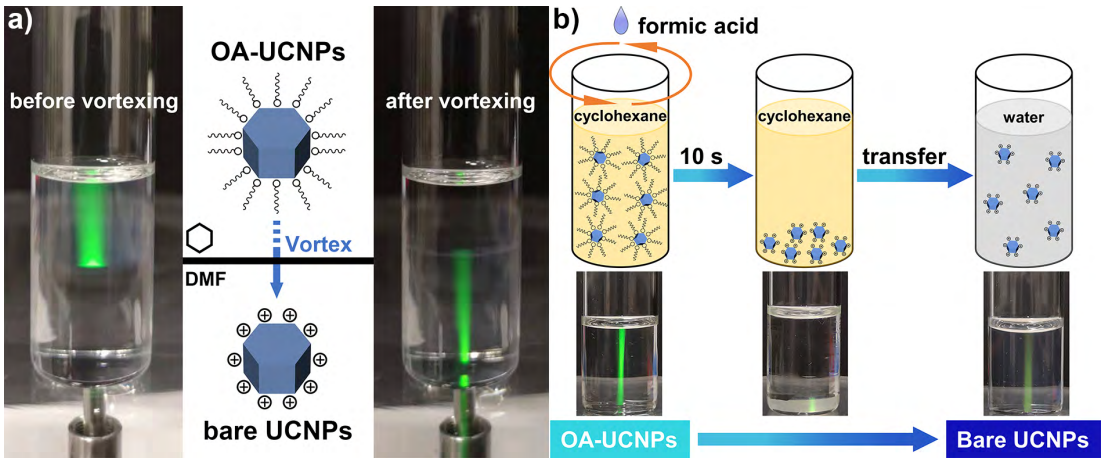

Fig. 3.2 (a) Illustration of the ligand removal process in a biphasic solvent system by the vortexing method. The emission light switches from the upper layer to the bottom layer along with the movement of UCNPs upon the activation of 980 nm laser. (b) Illustration of the ligand removal process of OA-UCNPs in cyclohexane with the direct addition of FA by the vortexing method in a single solvent system. (the luminescence light generated with the activation by a 980 nm laser that illuminates from the bottom)

Herein, a single hydrophobic solvent system, where FA is employed as the stripping agent and cyclohexane is used as the hydrophobic solvent for OA-UCNPs, is taken as a typical example (abbreviated as FA-Cy). Typically, 2 mL of cyclohexane solution containing OA-UCNPs (10 mg/mL) was first transferred to a glass vial, 0.5 mmol of FA was then added. After vigorous shaking at 3000 r.p.m for 10 s on a vortex mixer, ligand-free UCNPs were precipitated out from the cyclohexane, and the obtained bare UCNPs can be easily transferred to the aqueous solution. As shown in Fig. 3.2b, OA-UCNPs undergo effective collision with FA when the mixed solution is under vigorous shaking on a vortex mixer, and the acid-base reaction between FA and oleate ligand occurs

instantaneously, resulting in the formation of OA *via* protonation. The resultant OA releases from the surface of NPs and subsequently dissolves in cyclohexane solution. Moreover, the obtained ligand-free UCNPs cannot be dispersed in either cyclohexane or FA and thus are prone to precipitate out from the mixed solution. The fast acid-base reaction between FA and oleate ligand together with the spatial separation of the stripped OA and bare UCNPs enable efficient ligand removal in the FA-Cy system. The ligand removal process is tracked by FT-IR, ^{1}H NMR, TEM, XRD, TGA, and ζ-potential measurements.

3.3.2 Characterization of Oleate-Capped and Ligand-Free UCNPs

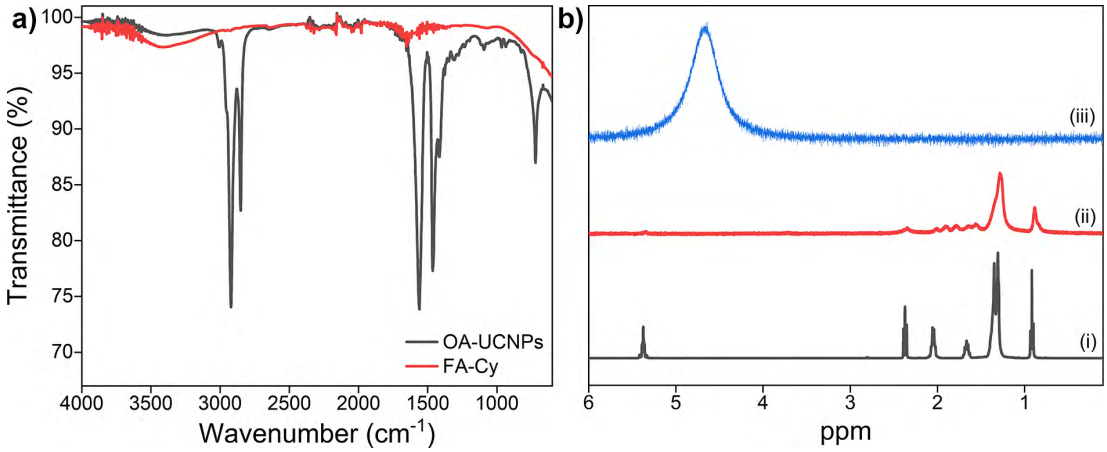

Fig. 3.3 (a) FT-IR spectra of OA-UCNPs and FA-treated OA-UCNPs. (b) ^{1}H NMR spectra of (i) OA dispersed in $CDCl_3$, (ii) OA-$NaYF_4$ NPs dispersed in $CDCl_3$, and (iii) FA-treated $NaYF_4$ NPs dispersed in D_2O. Chemical shifts are reported in ppm.

The successful removal of the oleate ligand from the surface of UCNPs is first confirmed by FT-IR (Fig. 3.3a). The transmission bands of as-synthesized OA-UCNPs at 2921 and 2851 cm^{-1} are attributed to asymmetric and symmetric stretching vibrations of methylene (-CH_2-) groups in the long alkyl chain of the oleate ligand. A weak peak at 3006 cm^{-1}, assigned to the =C-H stretching vibration, can be clearly observed in the FT-IR spectrum of the OA-UCNPs sample. Moreover, two peaks centered at 1560 and 1464 cm^{-1} can be assigned to the asymmetric and symmetric stretching vibrations of the carboxylate group. These characteristic peaks clearly prove the presence of oleate ligand on the surface of untreated OA-UCNPs. The disappearance of these characteristic peaks in the FA-Cy sample indicates the success in the ligand removal from the surface of OA-UCNPs after the acid treatment by the vortexing method. In addition, the broad band centered around 3500 cm^{-1} in the FA-Cy sample, assigning to the solvated water molecules, is consistent with the hydrophilic nature of ligand-free

UCNPs.

In order to further characterize the surface ligand of (un)treated NPs, ^{1}H NMR measurements are performed. To exclude disturbances of the Ln dopants (Yb^{3+} and Er^{3+}) on the ^{1}H NMR signal, resulting primarily from intrinsic paramagnetic properties of the dopants, undoped $NaYF_4$ NPs are applied instead for the ^{1}H NMR study. As seen in Fig. 3.3b, ^{1}H NMR signals of OA-$NaYF_4$ NPs dispersed in $CDCl_3$ locate at 5.3-5.5 ppm, 2.0-2.4 ppm,1.2-1.4 ppm, and 0.8-1.0 ppm, which can be assigned to -HC=CH-, -CH_2-, -$(CH_2)_6$-, and -CH_3 respectively. The result reveals the characteristic bands of OA with broadened signals compared with the spectrum of pure OA in $CDCl_3$. The line broadening originates from the inhomogeneous chemical environment and restricted rotational freedom of the oleate ligand anchored on the surface of NPs, which has been observed in previous studies[1-3]. After the vortex treatment with the FA, no signal is detected in the ^{1}H NMR spectrum of the FA-Cy sample dispersed in D_2O, except the solvent residual signal (4.67 ppm). The vanished characteristic bands in the ^{1}H NMR spectra corroborate the efficient ligand removal from the surface of OA-UCNPs and obtained ligand-free UCNPs.

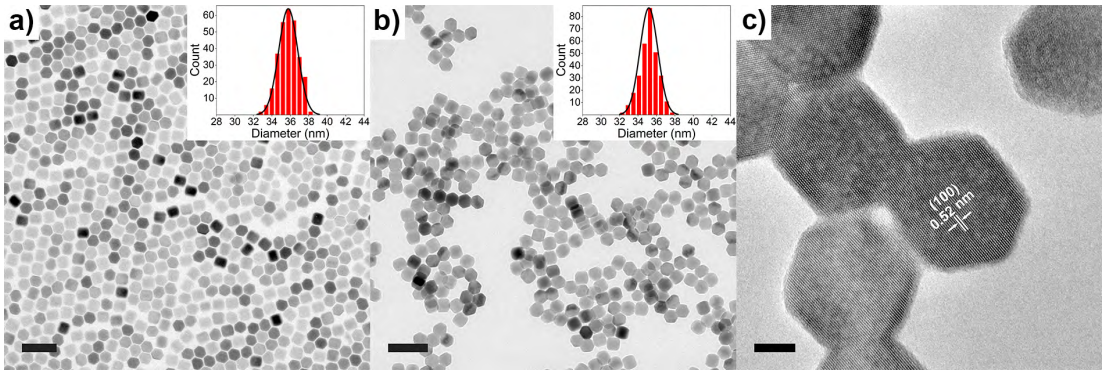

Fig. 3.4 TEM images of (a) OA-UCNPs and (b) ligand-free UCNPs obtained in the FA-Cy system. Insets: corresponding size histograms. Scale bars: 100 nm. Average particle sizes: (a) 35.8 ± 1.1 nm, (b) 35.2 ± 1.0 nm. (c) HR-TEM of OA-UCNPs. Scale bar: 10 nm.

The morphology and structure of as-synthesized and acid-treated OA-UCNPs are characterized by TEM and XRD. TEM images present that both as-prepared and acid-treated OA-UCNPs have a highly uniform hexagonal morphology. A particle analysis (at least 300 particles), performed from many such TEM images obtained from different regions of samples, confirms the maintained particle size with both original and acid-treated OA-UCNPs and demonstrates monodisperse oleate-capped and oleate-free UCNPs with a mean diameter of *ca.* 35 nm (Fig. 3.4a, b). TEM images and size distributions of other bare UCNPs obtained in different systems show almost identical

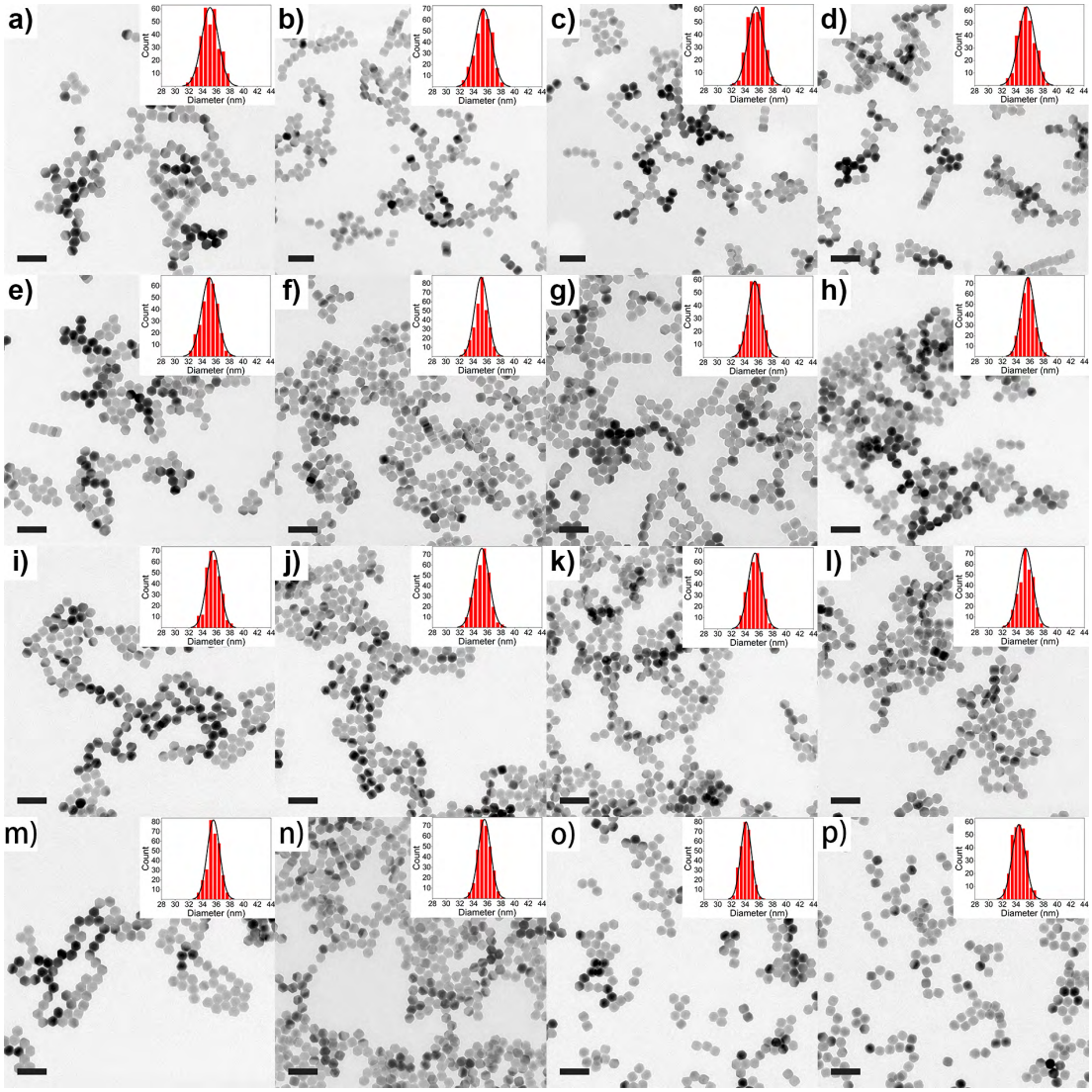

Fig. 3.5 TEM images of ligand-free UCNPs prepared in different systems. (a) FA-Cy/ACN, (b) FA-Cy/DMF, (c) FA-Cy/DMSO, (d) FA-Cy/FAM, (e) FA-Cy/MeOH, (f) FA-Cy/NMP, (g) FA-Chl, (h) FA-Tol, (i) AA-Cy/DMF, (j) AA-Cy/MeOH, (k) AA-Cy/NMP, (l) AA-Cy, (m) AA-Chl, (n) AA-Tol, (o) LA-Cy, (p) LA-Tol. Insets: corresponding size histograms. Scale bars: 100 nm. Average particle sizes: (a) 35.1 ± 1.2 nm, (b) 35.3 ± 1.1 nm, (c) 35.4 ± 1.3 nm, (d) 35.5 ± 1.2 nm, (e) 35.6 ± 1.2 nm, (f) 35.1 ± 1.2 nm, (g) 35.5 ± 1.0 nm, (h) 35.7 ± 0.9 nm, (i) 35.6 ± 1.0 nm, (j) 35.2 ± 1.1 nm, (k) 35.5 ± 1.0 nm, (l) 35.3 ± 1.0 nm, (m) 35.6 ± 0.9 nm, (n) 35.6 ± 1.0 nm, (o) 34.2 ± 0.8 nm, (p) 34.4 ± 1.0 nm.

results (Fig. 3.5), confirming the generality of this approach. Moreover, small-sized OA-UCNPs (*ca.* 20 nm) can be applied to the fast ligand removal as well when treated by FA in cyclohexane, and the TEM results reveal the maintained size and morphology after ligand exfoliation (Fig. 3.6). To further determine the crystallinity of (un)treated UCNPs, XRD measurements of both samples are performed. As shown in Fig. 3.7a, the well-defined diffraction peaks, both before and after acid treatment, confirm their well-defined crystallinity, and all the positions of the characteristic peaks can be well-indexed to a pure hexagonal phase, which are in good accordance with the standard

data of hexagonal $NaYF_4$ structure (JCPDS No. 28-1192). In addition, the lattice fringes on the individual NP are clearly distinguished in the HR-TEM image (Fig. 3.4c), indicating the high crystallinity of the prepared NPs. The distance between the lattice fringes is measured to be about 0.52 nm, corresponding to the d-spacing for the (100) lattice planes of the hexagonal $NaYF_4$ structure.

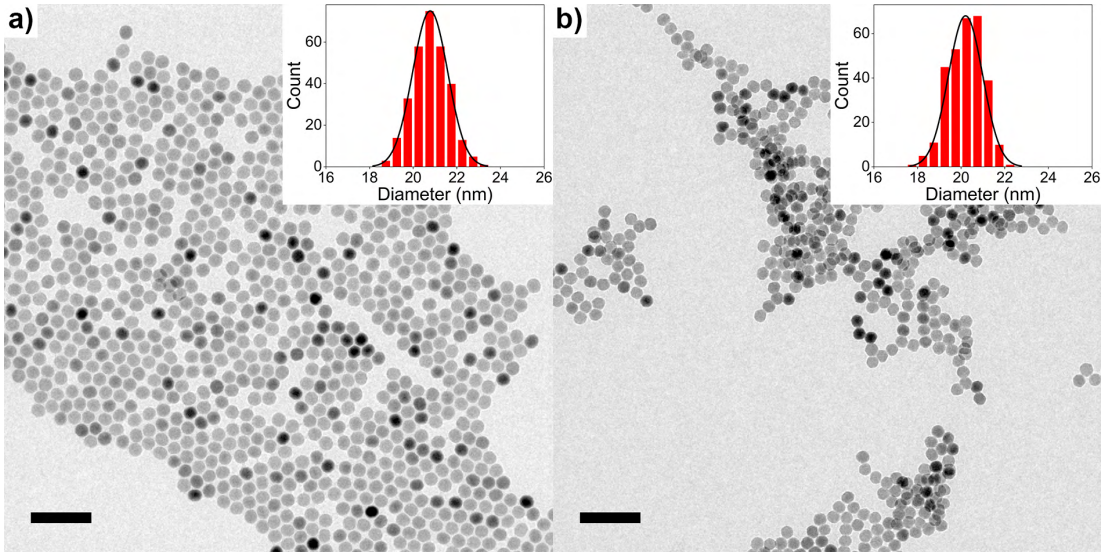

Fig. 3.6 TEM images of small-sized (a) OA-UCNPs and (b) ligand-free UCNPs obtained in the FA-Cy system. Insets: corresponding size histograms. Scale bars: 100 nm. Average particle sizes: (a) 20.8 ± 0.8 nm, (b) 20.2 ± 0.8 nm.

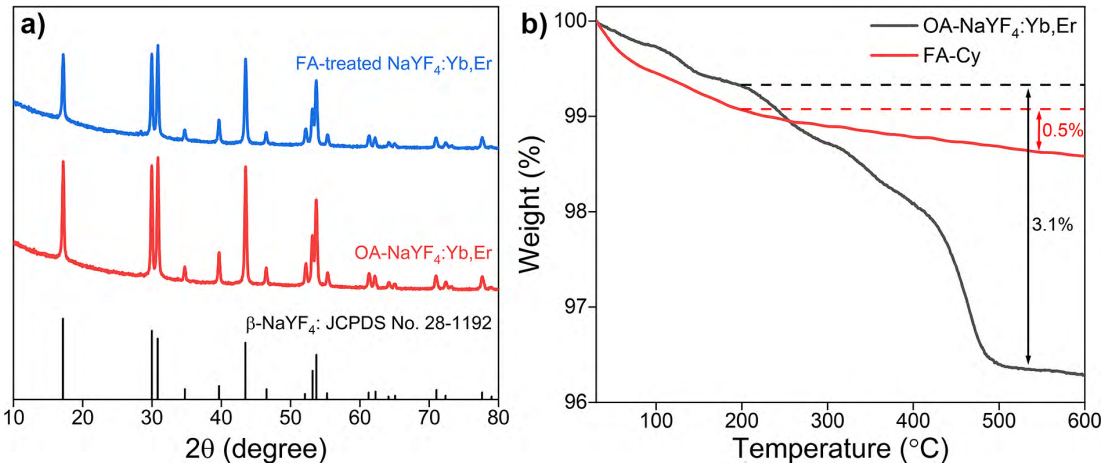

Fig. 3.7 (a) XRD patterns of original and acid-treated OA-UCNPs, and the standard data of hexagonal $NaYF_4$ (JCPDS No. 28-1192). (b) TGA curves of OA- and ligand-free UCNPs.

TGA is conducted to evaluate the amount of ligand on both as-synthesized and acid-treated UCNPs (Fig. 3.7b). The surface coverage of the oleate on the surface of OA-UCNPs, known as ligand density (φ, molecules/nm^2), is then calculated from the weight loss fraction of ligand by TGA using Equation (2)

$$\varphi = \frac{N_{OA}}{S} \quad (2)$$

Where N_{OA} is the number of OA, S is the total surface area of OA-UCNPs.

$$N_{OA} = n_{OA} \cdot N_A \quad (3)$$

$$n_{OA} = \frac{m_{OA}}{M_{OA}} \quad (4)$$

Where n_{OA} is the amount of OA, m_{OA} is the weight of OA, which is determined by TGA, N_A is the Avogadro constant; N_A = 6.02×10^{23} mol^{-1}, M_{OA} is the molar mass of OA ions, M_{OA} = 281.45 g/mol.

$$S = N_{UC} \cdot S_{UC} \quad (5)$$

$$N_{UC} = \frac{m_t}{m_{UC}} \quad (6)$$

$$m_{UC} = \rho_{UC} \cdot V_{UC} \quad (7)$$

$$V_{UC} = \frac{4}{3}\pi r_{UC}^3 \quad (8)$$

$$S_{UC} = 4\pi r_{UC}^2 \quad (9)$$

Where N_{UC} is the number of upconversion NPs, S_{UC} is the surface area of a single upconversion NP, m_t is the net weight of upconversion NPs, which is determined by TGA, m_{UC} is the weight of a single upconversion NP, ρ_{UC} is the density of single upconversion NP, ρ_{UC} = 4.31×10^{-21} g/nm^3, V_{UC} is the volume of a single upconversion NP, r_{UC} is the radius of a single upconversion NP, The prepared uniform UCNPs show a low aspect ratio (ca. 1.04), therefore, we approximate their shape as spheres for the ligand density calculation. By applying Equation (3)-(9) to Equation (2), the ligand density can be described as:

$$\varphi = \frac{\rho_{UC} r_{UC} m_{OA} N_A}{3(1-m_{OA}) M_{OA}} \quad (10)$$

The curve of OA-UCNPs shows a total weight loss of about 3.1% above 200 ºC, and according to Equation (10), the ligand density is calculated to be 1.8 OA/nm^2. However, compared with that of OA-UCNPs, the TGA curve of acid-treated NPs show a much lower total weight loss above 200 ºC (~0.5%) with an entirely different weight loss behavior. Thus, the TGA results further prove the successful ligand removal after acid treatment.

The ζ-potential is also investigated to estimate the effects of the ligand exfoliation process. Upon treatment with FA, bare UCNPs can be dissolved in water easily, and the ζ-potential of obtained bare UCNPs is determined to be 36.3 mV (pH ~5.5). The positive charge, ascribed to the uncoordinated metal cations, arises from the removal of the oleate ligand by protonation[17]. This indicates the conversion of hydrophobic OA-UCNPs into stable hydrophilic colloids. Furthermore, a similar behavior occurred in other acid-treated OA-UCNPs systems (Fig. 3.8).

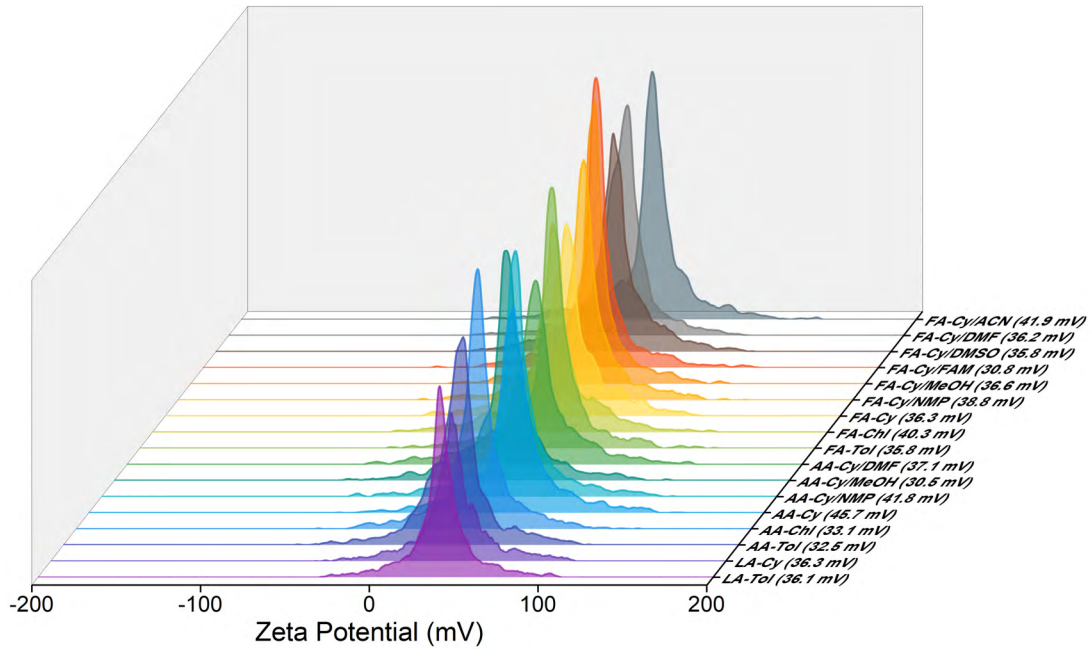

Fig. 3.8 ζ-potential of ligand-free UCNPs prepared under different conditions (measured at pH ~5.5).

In the light of the above-described FT-IR, ^{1}H NMR, TEM, XRD, TGA, and ζ-potential results, it can be concluded that the oleate ligand is completely removed by the treatment with short-chain acids under vortexing in a short time. At the same time, the acid treatment process has no noticeable adverse effects on the size, shape, and phase of the resulting bare UCNPs.

To investigate the optical property of UCNPs before and after ligand removal, UCL

spectra are carried out on OA-UCNPs and ligand-free UCNPs dispersed in hydrophobic solvents and water, respectively. As presented in Fig. 3.9, UCNPs generate green and red UCL emissions under 980 nm laser excitation, originating from $^2H_{11/2} \rightarrow {}^4I_{15/2}$, $^4S_{3/2} \rightarrow {}^4I_{15/2}$, and $^4F_{9/2} \rightarrow {}^4I_{15/2}$ transitions of the Er^{3+} ion. UCL intensities of OA-UCNPs show no significate differences in green and red regions when dissolved in different hydrophobic solvents, whereas UCL intensities of bare UCNPs dispersed in water reduce by almost a factor of 10 compared with those of OA-UCNPs dissolved in hydrophobic media.

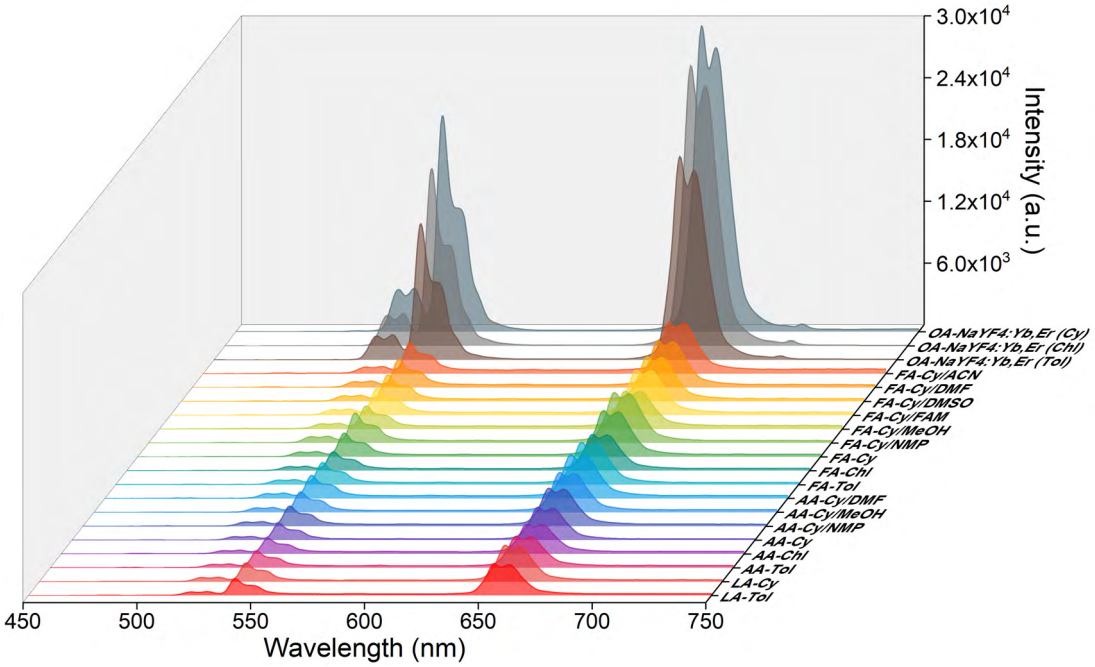

Fig. 3.9 UCL spectra of OA-UCNPs dissolved in different nonpolar solvents (1 mg/mL) and ligand-free UCNPs prepared in various systems dissolved in water (1 mg/mL) with excitation at 3W 980 nm CW laser.

This phenomenon is mainly caused by two factors. The first reason is due to the strong absorption of water in the NIR region, especially above 900 nm, while the excitation wavelength for the Yb^{3+} sensitized UCNPs is around 980 nm, and the incident light intensity attenuates by the water molecules, which will lead to the reduction of UCL emission. According to the Lambert-Beer law, the intensity of light falls off steadily with distance from the surface when electromagnetic radiation passes through a medium. Thus, the decrease rate in the light intensity with distance is proportional to the concentration (c) of the absorbing material and to the local intensity of the light at that position, $I(x)$.

$$\frac{d}{dx}I(x) = -\alpha c I(x) \tag{11}$$

Where α is the absorption coefficient of water at a specific wavelength, α = 0.43 cm^{-1} at 980 nm. Integration of the equation leads to

$$\frac{I}{I_0} = e^{-\alpha L} \tag{12}$$

Where I is the intensity of the transmitted light, I_0 is the intensity of the incident light, and L is the optical path length.

The attenuation is calculated to be 34.9% when the 980 nm light passes through a quartz cuvette with a 10 mm light path. More importantly, this phenomenon is primarily due to the presence of high energy OH-vibrations in water, that will increase the nonradiative relaxation of the excited states, induce the multiphonon deactivation of sensitizer ions, affect the multiphonon relaxation of activator ions, and thus quench the luminescence[26, 27].

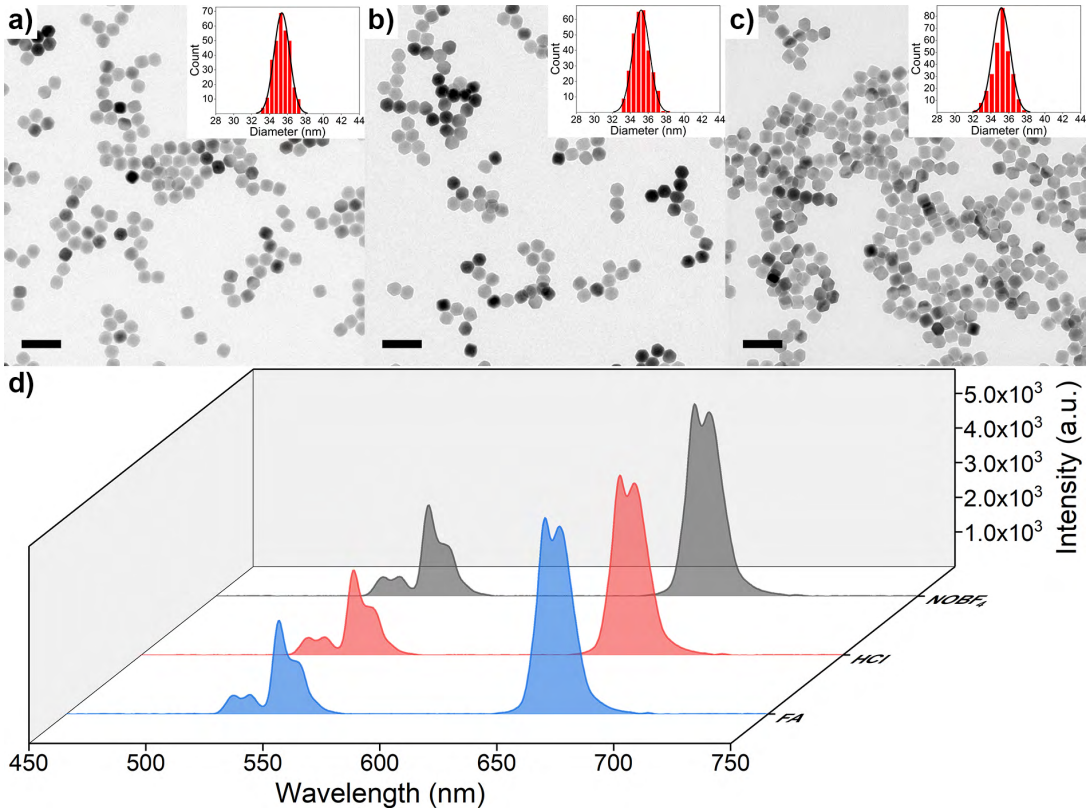

Fig. 3.10 TEM images of ligand-free UCNPs obtained by the treatment with (a) $NOBF_4$, (b) HCl, and (c) FA. Insets: corresponding size histograms. Scale bars: 100 nm. Average particle sizes: (a) 35.4 ± 0.8 nm, (b) 35.2 ± 0.9 nm (c) 35.2 ± 1.0 nm. (d) UCL spectra of bare UCNPs after treatment by $NOBF_4$, HCl, and FA under the excitation with a 3 W 980 nm CW laser (the concentration of UCNPs in water was fixed at 1 mg/mL).

To elucidate the efficiency of ligand removal by the here described method, ligand-free

UCNPs are prepared by other reported methods. Compared with previous methods, prepared *via* the treatment with either $NOBF_4$[16] or HCl[17], ligand-free UCNPs prepared by the here proposed method show similar results in the particle size and morphology, as well as the UCL upon 980 nm excitation (Fig. 3.10). However, the here developed method is much faster and reaction conditions are milder. In addition, various stripping agents and solvents can be employed for the ligand removal of OA-UCNPs. More importantly, the proposed method can be applied to HCl-sensitive materials, such as $NaLaF_4$[28]. As shown in Fig. 3.11, the morphology remains unchanged after the acid treatment of oleate-capped $NaLaF_4$ in the FA-NMP/Cy system.

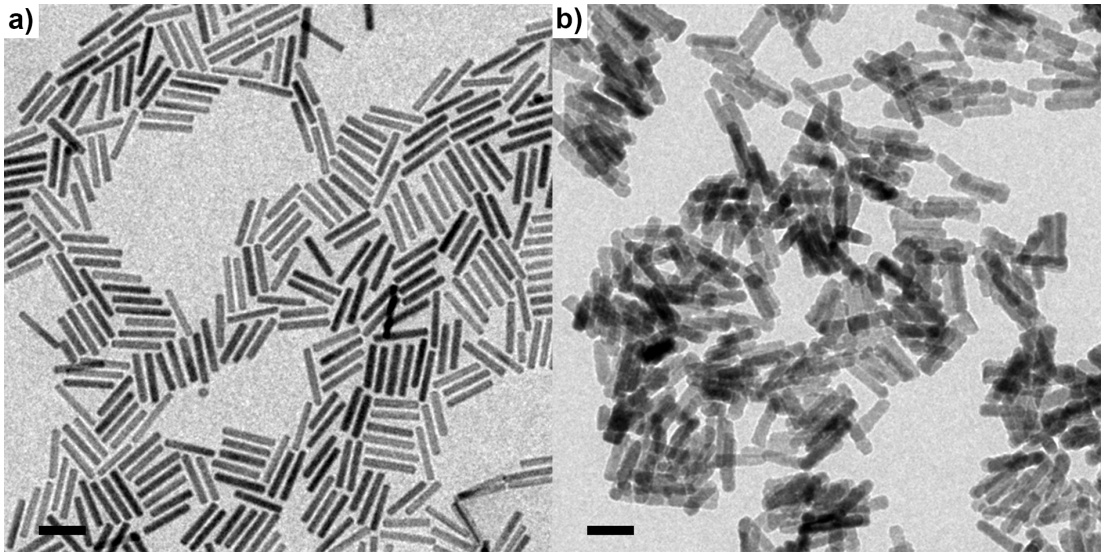

Fig. 3.11 TEM images of (a) oleate-capped $NaLaF_4$ NRs and (b) acid-treated oleate-capped $NaLaF_4$ NRs in the FA-NMP/Cy system. Scale bars: 50 nm.

3.3.2 Surface Modification of Ligand-Free UCNPs

The treatment of OA-UCNPs with FA makes the ligand-free UCNPs dispersible in water and positively charged bare UCNPs generate, favoring the attachment of water-soluble capping molecules by sequential surface functionalization. PAA, PVP, and PEI are applied as water-soluble capping molecules to modify the bare UCNPs. Different water-soluble capping molecules modified UCNPs are characterized by TEM, FT-IR, TGA, and UCL measurements.

The success in secondary surface modification by water-soluble polymers is first confirmed by FT-IR (Fig. 3.12d). All the transmission bands of polymers modified UCNPs show peaks centered around 2920 and 2856 cm^{-1} in the FT-IR spectrum, which are attributed to asymmetric and symmetric stretching vibrations of methylene ($-CH_2-$)

groups in polymers. Moreover, two typical peaks centered at 1553 and 1458 cm^{-1}, assigning to the asymmetric and symmetric stretching vibrations of the carboxylate group, confirm the presence of PAA on the surface. The peak centered at 1652 cm^{-1} can be assigned to the stretching vibration of the carbonyl (C=O) group, and the other two peaks centered at 1210 cm^{-1} and 1155 cm^{-1} can be attributed to the stretching vibrations of the C-N group, all these typical transition bands validate the presence of PVP on the surface. The strong transition band centered at 1560 cm^{-1} can be attributed to the N-H bending mode of the amino group ($-NH_2$) and another transition peak at 1170 cm^{-1} can be attributed to the stretching vibration of the C-N bond, these two characteristic peaks verify the presence of PEI on the surface. Additionally, all the transition bands of polymers modified UNCPs in the FT-IR spectrum show a broad peak centered at around 3500 cm^{-1}, which is due to the adsorbed water molecules, proving the hydrophilic nature of PAA-, PVP-, and PEI-UCNPs. After the transfer of polymer-modified UCNPs to the aqueous solution, the ζ-potential of PAA-, PVP-, and PEI-UCNPs are determined to be -20.6 mV, 26.9 mV, and 30.6 mV at pH 6, respectively, indicating stable hydrophilic colloidal NPs formed in water after surface modification of bare UCNPs by water-soluble polymers. TGA is then conducted to evaluate the amount of the polymers attached on the surface-modified UCNPs. As shown in Fig. 3.12e, the total weight loss of PAA-, PVP- and PEI-UCNPs above 200 ºC are about 5.8%, 3.5%, and 5.1%, respectively.

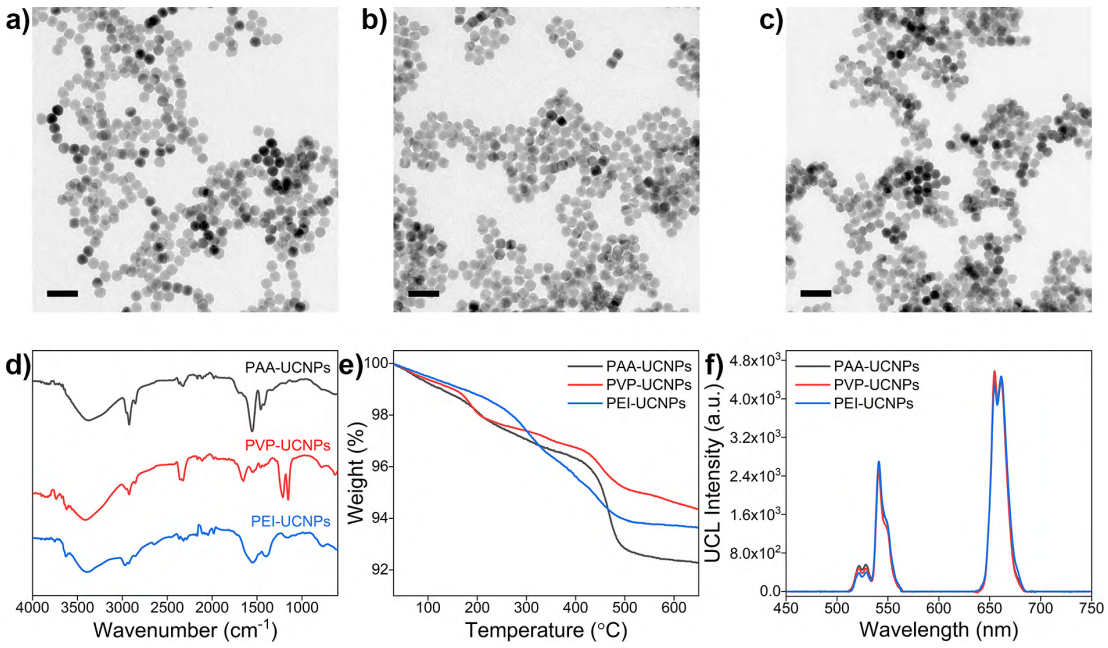

Fig. 3.12 TEM images of (a) PAA-UCNPs, (b) PVP-UCNPs, and (c) PEI-UCNPs. Scale bars: 100 nm. (d) FT-IR, (e) TGA, and (f) UCL of surface-modified UCNPs.

Compared with ligand-free UCNPs, TEM images (Fig. 3.12a-c) confirm the maintained shape and size after surface functionalization by different water-soluble polymers, and there are no obvious aggregations after modification with different capping agents, validating the versatility of bare UCNPs and providing more possibilities for further functionalization. Moreover, there are no apparent differences in the position and intensity of UCL emissions among bare, PAA-, PVP-, and PEI-modified UCNPs, as shown in Fig. 3.12f.

3.4 Conclusion

In summary, by introducing biphasic and single solvent systems, we have developed an efficient synthetic strategy for transferring hydrophobic OA-UCNPs to ligand-free ones using short-chain acids as stripping agents by a simple vortexing method. A wide range of polar solvents can be applied to form biphasic interfaces with cyclohexane, facilitating in-solution ligand exfoliation and allowing the transfer of bare UCNPs from the hydrophobic phase to the polar phase. Moreover, short-chain acids can be added directly as well to remove the surface ligand when cyclohexane, chloroform, or toluene is adopted as the dispersant for OA-UCNPs. The here described method is simply performed at ambient conditions on the second time scales without affecting the size, shape, and phase of the crystals. Additionally, the here developed method can be applied to HCl-sensitive materials as well. More importantly, ligand-free UCNPs are readily functionalized by sequential surface functionalization with water-soluble capping molecules, proving the versatility of obtained bare UCNPs. It is rational to believe that this facile approach can be applied to other oleate-stabilized NPs, allowing for the effective and efficient hydrophobic-to-hydrophilic transition.

3.5 References

[1] G.S. Yi, and G.M. Chow, Synthesis of hexagonal-phase $NaYF_4$:Yb,Er and $NaYF_4$:Yb,Tm nanocrystals with efficient up-conversion fluorescence, *Adv. Funct. Mater.*, **2006**, 16, 2324-2329.

[2] J.-C. Boyer, F. Vetrone, L.A. Cuccia, and J.A. Capobianco, Synthesis of colloidal upconverting $NaYF_4$ nanocrystals doped with Er^{3+}, Yb^{3+} and Tm^{3+}, Yb^{3+} *via* thermal decomposition of lanthanide trifluoroacetate precursors, *J. Am. Chem. Soc.*, **2006**, 128, 7444-7445.

[3] H.-X. Mai, Y.-W. Zhang, R. Si, Z.-G. Yan, L.-d. Sun, L.-P. You, and C.-H. Yan, High-quality sodium rare-earth fluoride nanocrystals: controlled synthesis and optical

properties, *J. Am. Chem. Soc.*, **2006**, 128, 6426-6436.

[4] N.J.J. Johnson, A. Korinek, C. Dong, and F.C.J.M. van Veggel, Self-focusing by ostwald ripening: a strategy for layer-by-layer epitaxial growth on upconverting nanocrystals, *J. Am. Chem. Soc.*, **2012**, 134, 11068-11071.

[5] X. Wang, J. Zhuang, Q. Peng, and Y. Li, A general strategy for nanocrystal synthesis, *Nature*, **2005**, 437, 121-124.

[6] Z. Li, and Y. Zhang, An efficient and user-friendly method for the synthesis of hexagonal-phase $NaYF_4$:Yb,Er/Tm nanocrystals with controllable shape and upconversion fluorescence, *Nanotechnology*, **2008**, 19, 345606.

[7] J.-C. Boyer, M.-P. Manseau, J.I. Murray, and F.C.J.M. van Veggel, Surface modification of upconverting $NaYF_4$ nanoparticles with peg−phosphate ligands for NIR (800 nm) biolabeling within the biological window, *Langmuir*, **2010**, 26, 1157-1164.

[8] N.J.J. Johnson, N.M. Sangeetha, J.-C. Boyer, and F.C.J.M. van Veggel, Facile ligand-exchange with polyvinylpyrrolidone and subsequent silica coating of hydrophobic upconverting β-$NaYF_4$:Yb^{3+}/Er^{3+} nanoparticles, *Nanoscale*, **2010**, 2, 771-777.

[9] N. Bogdan, F. Vetrone, R. Roy, and J.A. Capobianco, Carbohydrate-coated lanthanide-doped upconverting nanoparticles for lectin recognition, *J. Mater. Chem.*, **2010**, 20, 7543-7550.

[10] G.-S. Yi, and G.-M. Chow, Water-soluble $NaYF_4$:Yb,Er(Tm)/$NaYF_4$/polymer core/shell/shell nanoparticles with significant enhancement of upconversion fluorescence, *Chem. Mater.*, **2007**, 19, 341-343.

[11] M. Nyk, R. Kumar, T.Y. Ohulchanskyy, E.J. Bergey, and P.N. Prasad, High contrast in vitro and in vivo photoluminescence bioimaging using near infrared to near infrared up-conversion in Tm^{3+} and Yb^{3+} doped fluoride nanophosphors, *Nano Lett.*, **2008**, 8, 3834-3838.

[12] W. Ren, S. Wen, S.A. Tawfik, Q.P. Su, G. Lin, L.A. Ju, M.J. Ford, H. Ghodke, A. van Oijen, and D. Jin, Anisotropic functionalization of upconversion nanoparticles, *Chem. Sci.*, **2018**, 9, 4352-4358.

[13] H. Hu, M. Yu, F. Li, Z. Chen, X. Gao, L. Xiong, and C. Huang, Facile epoxidation strategy for producing amphiphilic up-converting rare-earth nanophosphors as biological labels, *Chem. Mater.*, **2008**, 20, 7003-7009.

[14] H.-P. Zhou, C.-H. Xu, W. Sun, and C.-H. Yan, Clean and flexible modification strategy for carboxyl/aldehyde-functionalized upconversion nanoparticles and their optical applications, *Adv. Funct. Mater.*, **2009**, 19, 3892-3900.

[15] Z. Chen, H. Chen, H. Hu, M. Yu, F. Li, Q. Zhang, Z. Zhou, T. Yi, and C. Huang, Versatile synthesis strategy for carboxylic acid−functionalized upconverting nanophosphors as biological labels, *J. Am. Chem. Soc.*, **2008**, 130, 3023-3029.

[16] A. Dong, X. Ye, J. Chen, Y. Kang, T. Gordon, J.M. Kikkawa, and C.B. Murray, A generalized ligand-exchange strategy enabling sequential surface functionalization of colloidal nanocrystals, *J. Am. Chem. Soc.*, **2011**, 133, 998-1006.

[17] N. Bogdan, F. Vetrone, G.A. Ozin, and J.A. Capobianco, Synthesis of ligand-free colloidally stable water dispersible brightly luminescent lanthanide-doped upconverting nanoparticles, *Nano Lett.*, **2011**, 11, 835-840.

[18] C. Wang, H. Tao, L. Cheng, and Z. Liu, Near-infrared light induced in vivo photodynamic therapy of cancer based on upconversion nanoparticles, *Biomaterials*, **2011**, 32, 6145-6154.

[19] S. Cui, H. Chen, H. Zhu, J. Tian, X. Chi, Z. Qian, S. Achilefu, and Y. Gu, Amphiphilic chitosan modified upconversion nanoparticles for in vivo photodynamic therapy induced by near-infrared light, *J. Mater. Chem.*, **2012**, 22, 4861-4873.

[20] M. Deng, N. Tu, F. Bai, and L. Wang, Surface functionalization of hydrophobic nanocrystals with one particle per micelle for bioapplications, *Chem. Mater.*, **2012**, 24, 2592-2597.

[21] S.H. Nam, Y.M. Bae, Y.I. Park, J.H. Kim, H.M. Kim, J.S. Choi, K.T. Lee, T. Hyeon, and Y.D. Suh, Long-term real-time tracking of lanthanide ion doped upconverting nanoparticles in living cells, *Angew. Chem. Int. Ed.*, **2011**, 50, 6093-6097.

[22] L.-L. Li, R. Zhang, L. Yin, K. Zheng, W. Qin, P.R. Selvin, and Y. Lu, Biomimetic surface engineering of lanthanide-doped upconversion nanoparticles as versatile bioprobes, *Angew. Chem. Int. Ed.*, **2012**, 51, 6121-6125.

[23] R. Abdul Jalil, and Y. Zhang, Biocompatibility of silica coated $NaYF_4$ upconversion fluorescent nanocrystals, *Biomaterials*, **2008**, 29, 4122-4128.

[24] J.-N. Liu, W.-B. Bu, and J.-L. Shi, Silica coated upconversion nanoparticles: a versatile platform for the development of efficient theranostics, *Acc. Chem. Res.*, **2015**, 48, 1797-1805.

[25] W. Kong, T. Sun, B. Chen, X. Chen, F. Ai, X. Zhu, M. L, W. Zhang, G. Zhu and F. Wang, *Inorg. Chem.*, **2017**, 56, 872-877.

[26] R. Arppe, I. Hyppanen, N. Perala, R. Peltomaa, M. Kaiser, C. Wurth, S. Christ, U. Resch-Genger, M. Schaferling, and T. Soukka, Quenching of the upconversion luminescence of $NaYF_4:Yb^{3+},Er^{3+}$ and $NaYF_4:Yb^{3+},Tm^{3+}$ nanophosphors by water: the role of the sensitizer Yb^{3+} in non-radiative relaxation, *Nanoscale*, **2015**, 7, 11746-11757.

[27] F.T. Rabouw, P.T. Prins, P. Villanueva-Delgado, M. Castelijns, R.G. Geitenbeek, and A. Meijerink, Quenching pathways in $NaYF_4:Er^{3+},Yb^{3+}$ upconversion nanocrystals, *ACS Nano*, **2018**, 12, 4812-4823.

[28] B. Chen, B. Ren, and F. Wang, Cs^+-assisted synthesis of $NaLaF_4$ nanoparticles, *Chem. Mater.*, **2019**, 31, 9497-9503.

Chapter 4: Upconversion-Based Nanocomposites for Fluorescence Sensing of Ions

Chapter 4 is based on the following articles

> Chunning Sun, Jan Ron Justin Simke, Michael Gradzielski, "An efficient synthetic strategy for ligand-free upconversion nanoparticles", *Mater. Adv.*, **2020**, 1, 1602-1607 (DOI: 10.1039/D0MA00411A).

and

> Chunning Sun, Michael Gradzielski, "Fluorescence sensing of cyanide anions based on Au-modified upconversion nanoassemblies", *Analyst*, **2021**, 146, 2152-2159 (DOI: 10.1039/D0AN01954B).

with the permission from Materials Advances and Analyst. Copyright of the Royal Society of Chemistry (2020 & 2021).

For the first article, C. Sun and M. Gradzielski conceived and designed the experiments. C. Sun performed the experiments and analyzed the data. J. R. J. Simke conducted the TEM measurements. C. Sun and M. Gradzielski co-wrote the manuscript. All authors discussed the results and commented on the manuscript.

For the second article, C. Sun and M. Gradzielski conceived and designed the experiments. C. Sun performed the experiments and analyzed the data. Both authors discussed the results and jointly wrote the manuscript.

4.1 Introduction

Copper ion (Cu^{2+}), one of the important essential elements in humans, plays a key role in various metabolic processes of organisms[1], including cytochrome c oxidase, superoxide dismutase, and tyrosinase. The homeostasis of Cu^{2+} is essential for maintaining health. A deficiency of copper can lead to anemia or pancytopenia[2]. However, a high level of Cu^{2+} will lead to numerous neurodegenerative diseases[3, 4], such as Alzheimer's disease and Wilson disease. Additionally, due to its widespread use in many industrial processes, Cu^{2+} has become one of the major environmental pollutions[5]. Excessive Cu^{2+} will imperil the survival of fish, shellfish, and bacteria in aquatic organisms, which reduces the self-purification capacity of natural water

systems[6]. Considering the adverse effects induced by the high Cu^{2+} level, the United States Environmental Protection Agency limits the maximum level of Cu^{2+} up to 20 μM in drinking water[7].

Cyanide ion (CN^-), unlike toxic metal cations that cause severe damage by virtue of their accumulative feature in organs, is a well-known hazardous anionic species, which can strongly interact with cytochrome c oxidase, resulting in the failure of oxygen transport to mitochondria and leading to the death of human beings and aquatic life within minutes by affecting the central nervous system even at a low concentration[8]. Therefore, the World Health Organization limits the acceptable level of cyanide up to 1.9 μM in drinking water[9]. In spite of its highly lethal toxicity, nearly 1.4 million tons of cyanide are produced every year, as it is widely used in industry, such as polymer and fiber manufacturing, gold mining, electroplating, and metallurgy. In consequence, unexpected cyanide leakage will seriously contaminate the groundwater and drinking water[10].

Accordingly, sensitive and selective sensing of Cu^{2+} and CN^- is of great importance for the environment and human health.

4.2 Materials and Methods

4.2.1 Reagents

Yttrium(III) acetate tetrahydrate (99.9%), ytterbium(III) acetate hydrate (99.9%), erbium(III) acetate hydrate (99.9%) were purchased from Alfa Aesar, OA (90%), ODE (90%), NH_4F (≥98%), NaOH (≥98%), MeOH (99.8%), ethanol (≥99.8%), cyclohexane (99.5%), DMF (99.8%), FA (≥98%), phosphoric acid (H_3PO_4, ≥99%), boric acid (H_3BO_3, ≥99.5%), AA (>99.5%), PEI (branched, Mw ~25,000), EBT (indicator grade), tetrachloroauric(III) acid trihydrate ($HAuCl_4 \cdot 3H_2O$, ≥99.9%), THPC (80% in H_2O), NaCN (≥95%), $NaNO_3$ (≥99%), KNO_3 (≥99%), $Ca(NO_3)_2 \cdot 4H_2O$ (≥99%), $Mg(NO_3)_2 \cdot 6H_2O$ (99%), $Ni(NO_3)_2 \cdot 6H_2O$ (≥98%), $Co(NO_3)_2 \cdot 6H_2O$ (≥98%), $Zn(NO_3)_2 \cdot 6H_2O$ (≥99%), $Fe(NO_3)_3 \cdot 9H_2O$ (≥98%), $Cu(NO_3)_2 \cdot 3H_2O$ (≥99%), $Al(NO_3)_3 \cdot 9H_2O$ (≥98%), $Mn(NO_3)_2 \cdot 4H_2O$ (≥97%), $Cr(NO_3)_3 \cdot 9H_2O$ (99%), NaF (≥99%), NaCl (≥99.5%), NaBr (≥99%), NaI (≥99.5%), CH_3COONa (≥99%), Na_2CO_3 (≥99%), $NaNO_2$ (≥99%), Na_2SO_3 (≥98%), Na_2SO_4 (≥99%) were purchased from Sigma-Aldrich. BRB solution (100 mM, pH 3) was prepared by mixing with 100 mM H_3BO_3, 100 mM

H_3PO_4, and 100 mM AA, and then titrated to pH 3 with 5 M NaOH. All the commercial chemicals were used as received. Milli-Q water (18.2 MΩ·cm at 25 °C) was used in all experiments.

4.2.2 Instruments

FT-IR spectra were acquired on a Thermo Scientific Nicolet iS5 FT-IR spectrometer using the KBr method. The spectra were recorded in transmission mode with the wavenumber range from 4000-500 cm^{-1}. UV-Vis absorption spectra were obtained by using a CARY 50 spectrophotometer. TEM, HR-TEM, and EDS were performed by FEI Tecnai G^2 20 S-TWIN with a LaB_6 cathode operating at 200 kV. XRD spectra were obtained by using Philips X'Pert MPD Pro X-ray diffractometer at a scanning rate of 4°/min in the 2θ range from 10° to 90° with Cu Kα radiation (λ = 0.15406 nm). ζ-potential measurements were carried out with an Anton Paar Litesizer™ 500. UCL emission spectra were collected at room temperature with a fiber-coupled spectrometer (Ocean HDX, Ocean Optics) equipped with an external 980 nm CW laser (Roithner Lasertechnik GmbH) with tunable power from 0 to 5 W.

4.2.3 Synthesis of OA-UCNPs

OA-UCNPs were prepared as described in Chapter 3, and dispersed in cyclohexane.

4.2.4 Synthesis of OA-csUCNPs

OA-csUCNPs core-shell-structured upconversion NPs were prepared by coating a similar material on the core OA-UCNPs[11], as shown in Fig. 4.1. Typically, $Y(CH_3COO)_3$ (3.2 mL, 0.2 M) and $Yb(CH_3COO)_3$ (0.8 mL, 0.2 M) were added to a three-neck flask containing 6 mL OA and 14 mL ODE at room temperature. The mixed solution was heated to 110 ºC for 30 min to remove the water, followed by heating to 160 ºC for 40 min to form Ln-oleate complexes and then cooled down to room temperature. The as-synthesized OA-UCNPs core NPs dispersed in cyclohexane were added to the flask. The solution was heated to 110 ºC to remove the cyclohexane and then subsequently cooled down to room temperature. A MeOH solution (10 mL) containing NH_4F (3.2 mmol) and NaOH (2.0 mmol) was added afterward and stirred at 50 ºC for 30 min. After heating to 110 ºC to evaporate the MeOH, the solution was heated to 305 ºC at a ramp rate of 10 °C/min and maintained at that temperature for

40 min under N_2 atmosphere. After cooling down to room temperature naturally, OA-csUCNPs were precipitated out with the addition of excess ethanol, collected by centrifugation at 6000 r.p.m for 5 min, washed with ethanol several times, and finally redispersed in cyclohexane.

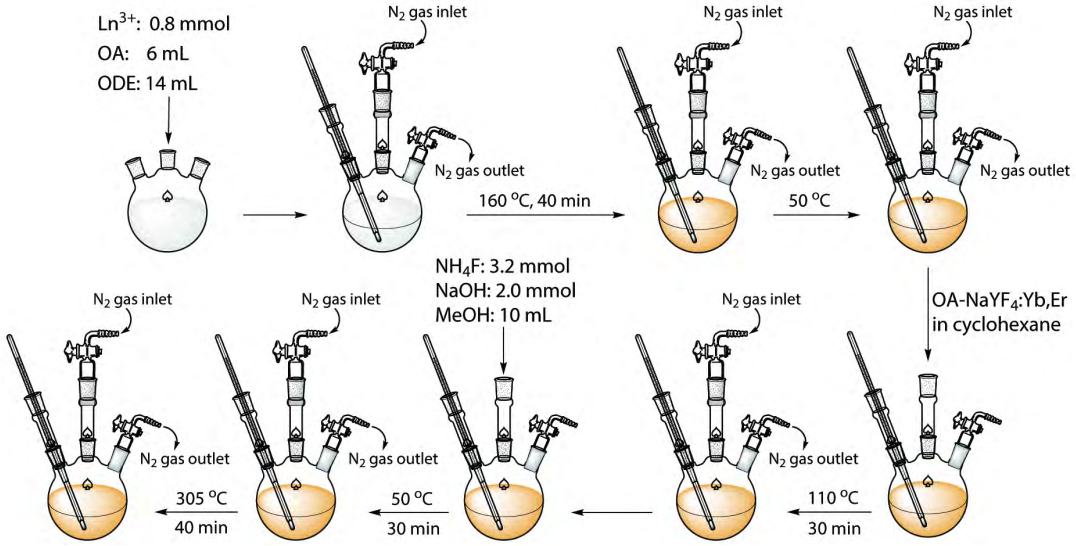

Fig. 4.1 Schematic diagram of the synthesis of core-shell upconversion NPs by co-precipitation method.

4.2.5 Synthesis of PEI-csUCNPs

To prepare PEI-csUCNPs, ligand-free csUCNPs were first prepared via the aforementioned vortexing method. Typically, 5 mmol FA were added to 2 mL cyclohexane solution containing OA-csUCNPs (10 mg/mL) directly, the mixture was then shaken for 10 s (3000 r.p.m) on a vortex mixer, ligand-free UCNPs were precipitated out. The resultant NPs were obtained by centrifugation at 6000 r.p.m for 20 min, washed one time with ethanol and three times with water, and finally redispersed in water. 40 mg PEI were then added to 4 mL bare csUCNPs solution (5 mg/mL), followed by overnight stirring. PEI-csUCNPs were obtained *via* centrifugation at 10,000 r.p.m for 20 min, washed three times with water, and finally redispersed in water.

4.2.6 Preparation of csUCNPs/EBT Nanocomposites

PEI-csUCNPs were prepared with the same procedure as described above and redispersed in water with a concentration of 1 mg/mL, EBT stock solution was prepared by dissolving EBT dye in water with a concentration of 2 mM. 0.5 mL of EBT solution

was mixed with 0.5 mL of PEI-csUCNPs solution, and the mixed solution was vortexed (3000 r.p.m) for 5 min. The precipitate was obtained by centrifugation at 15000 r.p.m for 20 min and repeatedly washed three times with water to remove excess EBT. Finally, the csUCNPs/EBT nanocomposites were redispersed in the BRB solution (100 mM, pH 3).

4.2.7 Procedures for Cu^{2+} Sensing

Stock solutions of nitrate salts including Na^{+}, K^{+}, Ca^{2+}, Mg^{2+}, Ni^{2+}, Co^{2+}, Zn^{2+}, Fe^{3+}, Cu^{2+}, Al^{3+}, Mn^{2+}, and Cr^{3+} (2 mM) were prepared in aqueous solution. The sensing of csUCNPs/EBT nanocomposites to Cu^{2+} was performed by adding different amount of Cu^{2+} stock solution to csUCNPs/EBT nanocomposites solution, the concentration of UCNPs was kept at 0.5 mg/mL, selectivity experiments were performed by adding appropriate amounts of other cations stock solution with a similar procedure. All UCL spectra were recorded under the excitation of a 980 nm CW laser with the pow of 3 W.

4.2.8 Preparation of csUCNPs/Au Nanocomposites

To prepare csUCNPs/Au nanocomposites, Au NPs were first synthesized as described previously[12]. Typically, 12 µL THPC and 0.25 mL NaOH (2.0 M) were added to 45 mL water, then the mixture was stirred vigorously for 5 min followed by a quick injection of 2 mL $HAuCl_4$ solution (1 wt%). The color changed to dark brown immediately. This solution was stored in a dark container and stirred overnight.

The csUCNPs/Au nanoassemblies were prepared by the addition of appropriate freshly prepared Au NPs to a solution containing PEI-csUCNPs (the content of csUCNPs was fixed at 0.5 mg/mL) and ultrasonicated for 10 min. Assuming the diameters of the Au NPs and the csUCNPs to be 1.7 and 43 nm, respectively, we can estimate that ~140 Au NPs are decorating one csUCNP for 0.10 mM Au content. The resulting csUCNPs/Au nanocomposites were then collected by centrifugation at 9000 r.p.m for 30 min, washed with water several times, and redispersed in DMF/H_2O (5/1, v/v). This solvent mixture was employed as in pure water the system becomes a bit turbid due to agglomeration processes.

4.2.9 Procedures for CN^- Sensing

Stock solutions of the anions (4 mM) including CN^-, F^-, Cl^-, Br^-, I^-, CH_3COO^-, CO_3^{2-}, NO_2^-, NO_3^-, SO_3^{2-}, and SO_4^{2-} were prepared in DMF/H_2O (5/1, v/v). The sensing of CN^- was performed by adding different amounts of CN^- stock solution to csUCNPs/Au nanocomposites in DMF/H_2O (5/1, v/v), the concentration of csUCNPs was kept at 0.5 mg/mL, and the concentration of the CN^- ranged from 0 to 280 μM. Selectivity experiments were performed by the addition of 2 mM other anions stock solution with a similar procedure. The UCL spectra of resulting samples were recorded under the excitation of a 980 nm laser with the power of 3 W.

4.3 Results and Discussion

4.3.1 Design Strategy of Upconversion-Based Nanoprobes for Cu^{2+}

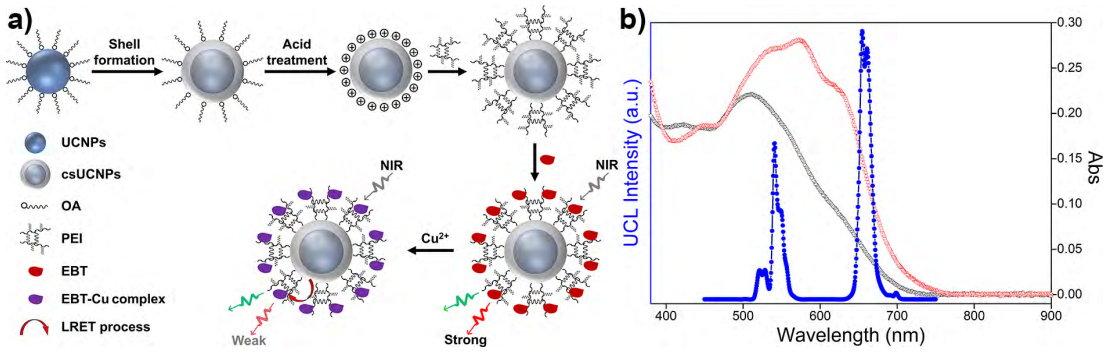

Fig. 4.2 (a) Schematic illustration of the synthesis of csUCNPs/EBT nanoprobes and their response to Cu^{2+}. (b) UV-vis spectra of csUCNPs/EBT in the absence (black) and presence (red) of Cu^{2+} in BRB solution (100 mM, pH 3), and UCL spectrum of PEI-csUCNPs (blue) in water.

The design strategy of csUCNPs/EBT nanocomposites for selective Cu^{2+} sensing relies on the FRET process, where csUCNPs are used as the energy donor and the EBT-Cu complex acts as the energy acceptor. As shown in Fig. 4.2a, OA-csUCNPs are firstly prepared through the previously reported high-temperature coprecipitation method, and ligand-free csUCNPs are then prepared by the removal of the oleate ligand through the treatment with FA, followed by modification of PEI to obtain PEI-csUCNPs. The EBT dye, a kind of sulfonate, can easily assemble on the positively charged PEI-csUCNPs through electrostatic interactions. Without modification, green and red UCL emissions will occur when csUCNPs are activated by 980 nm laser. Upon addition of Cu^{2+}, the EBT-Cu adducts exhibit an increased absorption intensity after 600 nm when compared with the EBT dye, revealing the enhanced spectral overlap

between the absorption of the metal-dye complex and red UCL emission of csUCNPs, indicating the possibility of an enhanced FRET process between csUCNPs and the metal-dye complex.

4.3.2 Characterization of csUCNPs/EBT Nanocomposites

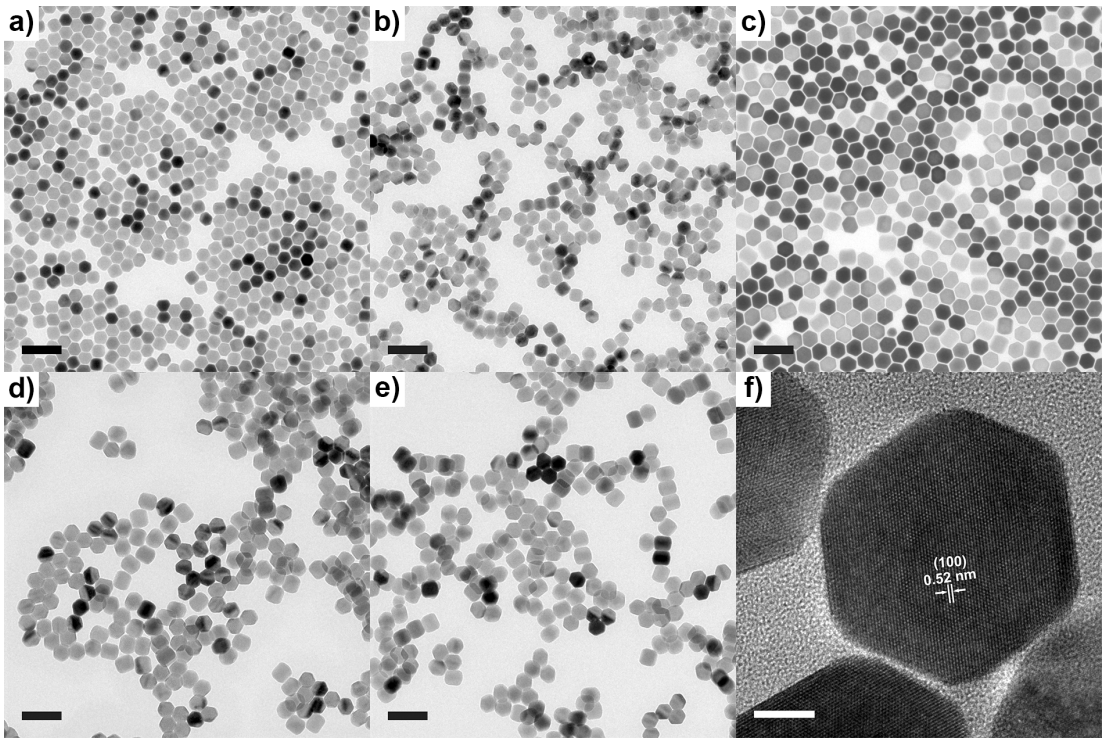

Fig. 4.3 TEM images of (a) OA-UCNPs, (b) ligand-free UCNPs, (c) OA-csUCNPs, (d) ligand-free csUCNPs, and (e) PEI-csUCNPs. Insets: corresponding size histogram. Scale bars: 100 nm. (f) HR-TEM image of OA-csUCNPs. Scale bar: 10 nm.

Hydrophobic core OA-UCNPs are first prepared by employing OA as the ligand *via* the high-temperature coprecipitation method[13]. TEM image exhibits that the core OA-UCNPs have a uniform hexagonal morphology, and the average diameter is measured to be about 35 nm (Fig. 4.3a). OA-csUCNPs core-shell-structured upconversion NPs are prepared by coating a similar material on the core OA-UCNPs, the average diameter of hexagonal-shaped OA-csUCNPs increases to approximately 43 nm with maintained uniformity, suggesting the successful growth of the shell on the core OA-UCNPs (Fig. 4.3c). Moreover, bare UCNPs and csUCNPs can be easily obtained by acid treatment of corresponding OA-capped upconversion NPs *via* the vortexing method, and TEM images show that the particle size and morphology remain unchanged after the ligand removal from the surface of NPs (Fig. 4.3b, d). Additionally, bare csUCNPs can be further functionalized by water-soluble PEI molecules *via*

secondary surface modification, and the TEM image of obtained PEI-csUCNPs shows unchanged size and morphology compared with ligand-free csUCNPs (Fig. 4.3e).

The crystal type and phase purity of core-only and core-shell upconversion NPs are examined by XRD. The XRD patterns of the core-only UCNPs and core-shell-structured csUCNPs (Fig. 4.4a), which are in excellent agreement with the pure hexagonal phase (JCPDS file number 28-1192), demonstrate high crystallinity with well-defined diffraction peaks. In addition, the lattice fringes on the individual core-shell upconversion are clearly distinguished in the HR-TEM image (Fig. 4.3f), confirming the high crystallinity of the prepared OA-csUCNPs. The distance between the lattice fringes is measured to be about 0.52 nm, corresponding to the d-spacing for the (100) lattice planes of the hexagonal $NaYF_4$ structure.

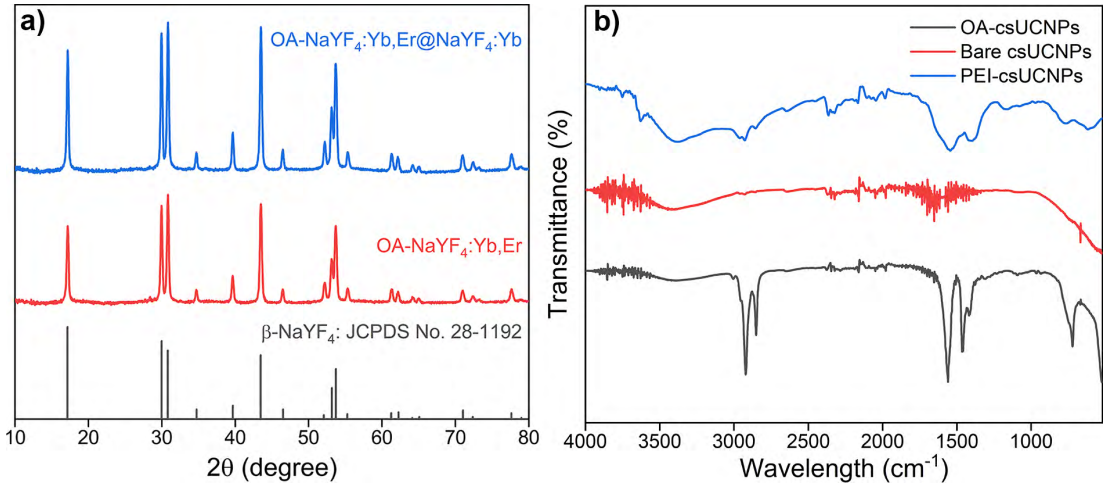

Fig. 4.4 (a) XRD patterns of OA-UCNPs, OA-csUCNPs, and the standard data of hexagonal $NaYF_4$ (JCPDS No. 28-1192). (b) FT-IR spectra of OA-, ligand-free, and PEI-csUCNPs.

The high-quality OA-csUCNPs obtained by the high-temperature coprecipitation method are prone to disperse in nonpolar solvents due to the presence of oleate ligand on the surface. However, the ligand can be efficiently removed by the vortexing method. Ligand removal *via* acid treatment and further PEI molecules functionalization *via* secondary surface modification are confirmed by FT-IR measurement (Fig. 4.4b). The transmission bands of as-synthesized OA-csUCNPs at 2923 and 2854 cm^{-1} are attributed to asymmetric and symmetric stretching vibrations of methylene ($-CH_2-$) groups in the long alkyl chain. A weak peak at 3008 cm^{-1}, assigned to the =C-H stretching vibration, can be clearly observed in the spectrum. Moreover, two peaks centered at 1561 and 1460 cm^{-1} can be assigned to the asymmetric and symmetric stretching vibrations of the carboxylate group. These characteristic peaks validate the

presence of oleate ligand on the surface of OA-csUCNPs. Nevertheless, all the characteristic peaks disappeared after the acid treatment, except the broad band centered at around 3420 cm^{-1}, assigning to the solvated water molecules, validate the success in ligand removal and the hydrophilic nature of the obtained ligand-free csUCNPs. After the modification of bare csUCNPs by PEI, two bands centered at 2930 and 2854 cm^{-1} are shown in the spectrum, which can be attributed to the asymmetric and symmetric stretching vibrations of the C-H bond, respectively. A weak peak at 1167 cm^{-1} is attributed to the stretching vibrations of the C-N bond, and a strong transition band centered at 1545 cm^{-1} is observed, which can be attributed to the N-H bending mode of the amino group. Accordingly, the FT-IR results verify the success in ligand removal of OA-csUCNPs and further attachment of PEI on bare csUCNPs.

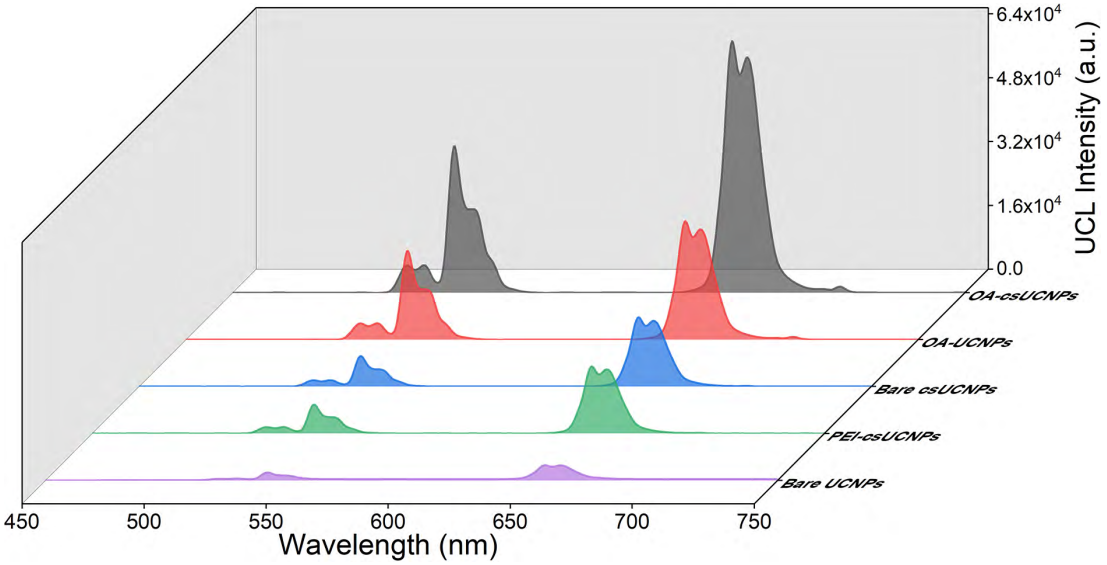

Fig. 4.5 UCL spectra of OA-UCNPS and OA-csUCNPs dispersed in cyclohexane, ligand-free UCNPs, ligand-free csUCNPs, and PEI-csUCNPs dispersed in water (the concentrations of UCNPs and csUCNPs are fixed at 1 mg/mL).

The UCL is the most significant feature of upconversion NPs, and the UCL emission spectra of hydrophobic OA- and ligand-free upconversion NPs under 980 nm laser excitation are shown in Fig. 4.5. OA-UCNPs present a relatively low UCL emission intensity due to the energy loss by large surface defects, and a remarkable loss of green and red emissions in intensity occurs in aqueous solution after the transition of OA-UCNPs to ligand-free ones *via* ligand exfoliation by FA, which is attenuated by water molecules[14, 15]. In order to enhance the UCL intensity of upconversion NPs, especially hydrophilic ones, core-shell-structured OA-csUCNPs are synthesized by coating a similar material on core OA-UCNPs, and bare csUCNPs are obtained by FA treatment *via* the vortexing method. The UCL intensity of OA-csUCNPs enhances by

a factor of two compared with the core-only OA-UCNPs in cyclohexane, while the UCL intensity of bare csUCNPs is about 4.5 times larger than ligand-free core-only UCNPs in aqueous solution, owing to the passivated surface defects by the shell layer. Moreover, nearly identical UCL intensity is observed in PEI-csUCNPs in the aqueous solution compared with bare csUCNPs.

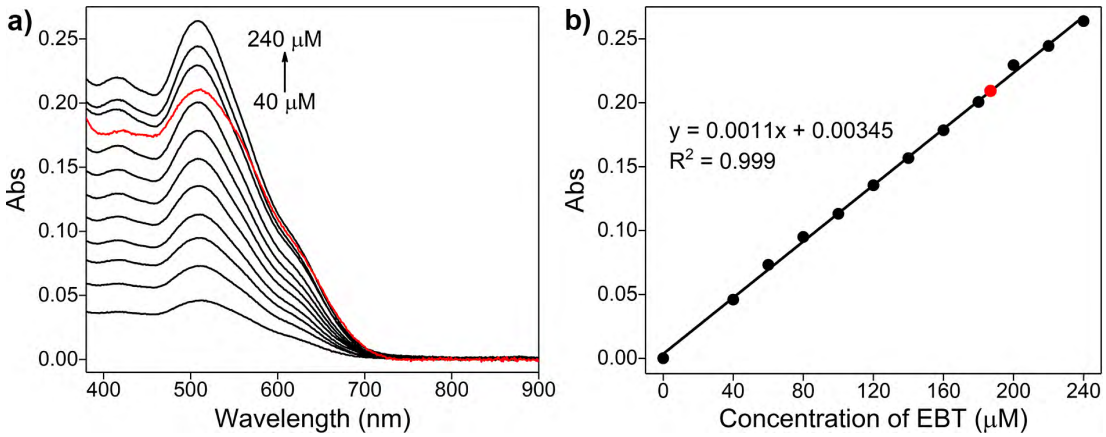

Fig. 4.6 (a) UV-vis absorption spectra of EBT with different concentrations in BRB solution (100 mM, pH 3). The red curve represents the absorption data of csUCNPs/EBT nanoprobes (0.5 mg/mL csUCNPs). (b) The plot of absorbance intensities at 508 nm as a function of EBT concentration. The red dot represents the absorption intensity of csUCNPs/EBT at 508 nm.

After the treatment of OA-csUCNPs with FA and further surface modification by PEI, positively charged PEI-csUCNPs are obtained, and the EBT dye can easily assemble on the surface *via* electrostatic interactions. The amount of EBT on the surface of csUCNPs/EBT nanocomposites is determined by detailed spectrophotometric titration spectra. The absorption spectrum of EBT shows a maximum absorption peak at 508 nm, and the absorption intensity increases with the increasing concentration of the EBT (Fig. 4.6a). A linear relationship is shown between the EBT concentrations and absorption intensities at 508 nm. The amount of EBT on the surface of 0.5 mg/mL csUCNPs/EBT is calculated to be about 187 μM (Fig. 4.6b).

4.3.3 Sensitive and Selective Detection of Cu^{2+}

The sensing ability of EBT-modified upconversion nanoprobes is investigated by UCL emission spectroscopy. The addition of Cu^{2+} to BRB solution (100 mM, pH 3) containing the csUCNPs/EBT nanocomposites leads to a minor decrease in green emission, but a significate reduction in red emission. As discussed above, the addition of Cu^{2+} induces enhanced spectral overlap between UCL emission of csUCNPs and

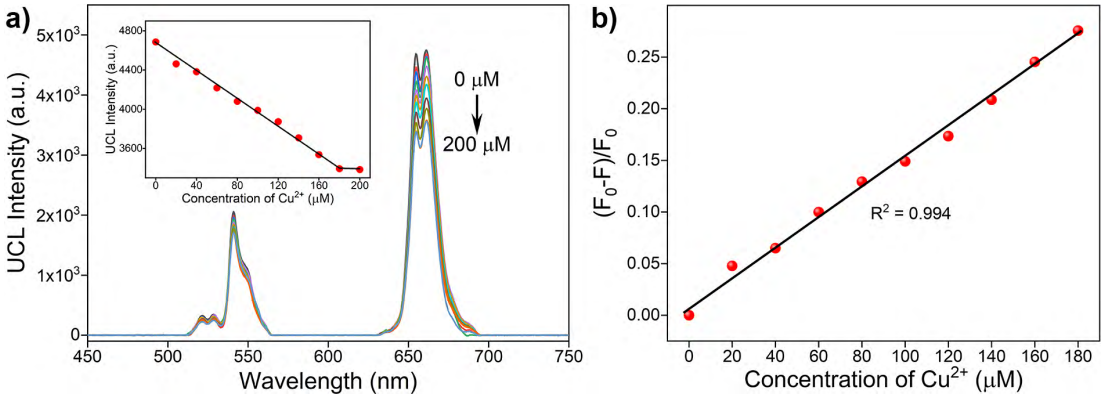

Fig. 4.7 (a) UCL spectra of 0.5 mg/mL csUCNPs/EBT (187 μM EBT) in BRB solution (100 mM, pH 3) upon addition of Cu^{2+} (0-200 μM). Inset: changes in UCL intensities at 654 nm upon the addition of different concentrations of Cu^{2+}. (b) Plot of luminescence intensity ($(F_0-F)/F_0$) at 654 nm against Cu^{2+} concentration (0-180 μM).

Table 4.1 Comparison of fluorescence sensing of Cu^{2+} by different probes

Materials	Linear range	LOD	Ref.
RB-FC-UCNPs	0-240 μM	5.95 μM	[16]
azurin-UCNPs system	0-60 μM	2 μM	[17]
RBH-modified csUCNPs@$mSiO_2$	0-400 μM	2.56 μM	[18]
UCNPs@SiO_2-TSPP NRs	0-160 μM	2.16 μM	[19]
N-(quinoline-8-yl) pyrazine-2 carboxamide	0-100 μM	14.8 μM	[20]
ZnS quantum dots	1-1000 μM	25 μM	[21]
benzene and pyridine-based chemosensor	0-20 μM	8 μM	[22]
benzimidazole-based chemosensor	0-48 μM	9.76 μM	[23]
csUCNPs/EBT nanocomposites	0-200 μM	9.42 μM	this work

absorption of the EBT-Cu adducts, and FRET from the visible UCL of csUCNPs to the absorption of EBT-Cu increases, thereby, leading to the reduction in UCL emission. The UCL intensity at 654 nm proportionally reduces when the Cu^{2+} concentration is lower than 180 μM, and at higher concentrations of Cu^{2+}, the UCL intensity reaches a plateau, which is mainly due to the saturation of chelating sites with Cu^{2+} binding (Fig. 4.7a). The variation of UCL ratio $(F_0-F)/F_0$ at 654 nm increases linearly with the concentrations of Cu^{2+} from 0 to 180 μM (F_0 and F are the luminescence intensities of nanoprobes in the absence and presence of Cu^{2+}, respectively), which is shown in Fig. 4.7b. The LOD is given by the equation $LOD= 3S_0/S$, where 3 is the factor at the 99% confidence level, S_0 the standard deviation of the blank measurements (n = 10), and

S is the slope of the calibration curve, and the LOD for Cu^{2+} is approximately 9.42 μM, exhibiting the excellent sensitivity for Cu^{2+}. The here proposed method exhibits a comparable sensitivity with previously reported fluorescent probes (Table 4.1).

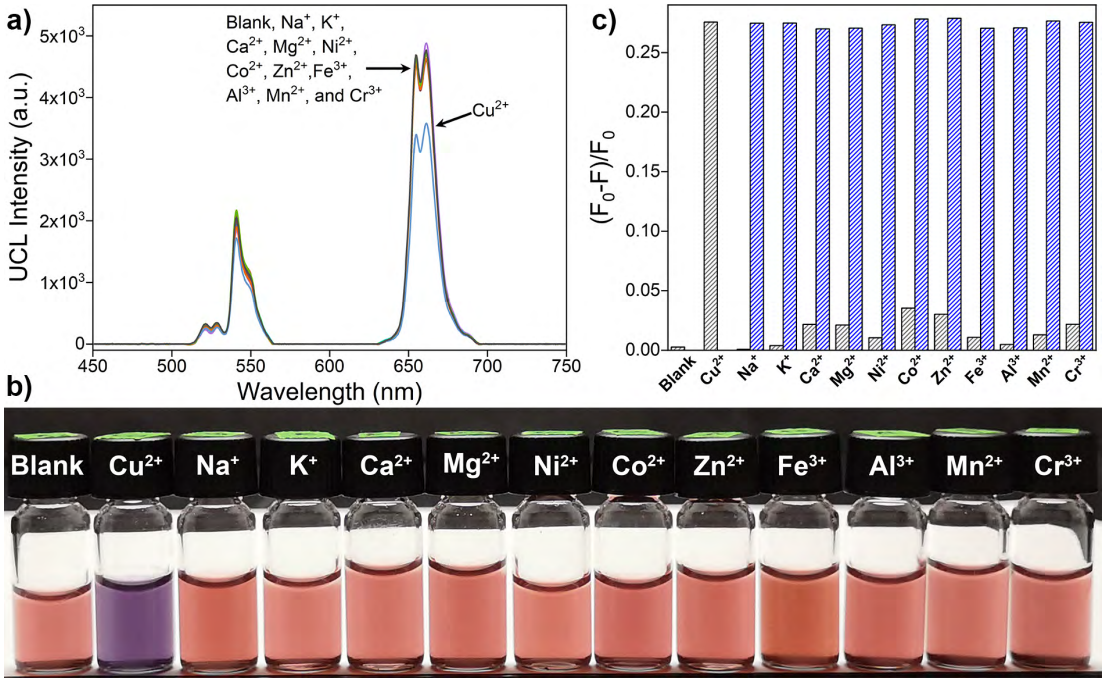

Fig. 4.8 (a) UCL spectra and (b) color changes of 0.5 mg/mL csUCNPs/EBT (187 μM EBT) in the presence of different cations (200 μM). c) Changes in UCL intensity ($(F_0-F)/F_0$) of 0.5 mg/mL csUCNPs/EBT (187 μM EBT) at 654 nm upon addition of 200 μM Cu^{2+}, 500 μM other metal cations. Grey bars represent the UCL changes upon addition of various cations, blue bars represent the subsequent addition of 200 μM Cu^{2+} to the above solution.

High selectivity is necessary for chemosensors, and to investigate the specificity of the csUCNPs/EBT nanocomposites, the UCL emission and color response of csUCNPs/EBT to different cations in aqueous solutions including Na^{+}, K^{+}, Ca^{2+}, Mg^{2+}, Ni^{2+}, Co^{2+}, Zn^{2+}, Fe^{3+}, Al^{3+}, Mn^{2+}, and Cr^{3+} are investigated. As shown in Fig. 4.8a, only the addition of Cu^{2+} leads to a significant reduction in UCL emission, whereas the addition of other cations with large excesses shows no apparent change in UCL intensity. Furthermore, the csUCNPs/EBT solution exhibits significant color change (from crimson to purple) upon the addition of Cu^{2+}, while the color remains with the addition of other metal ions (Fig. 4.8b). Moreover, competition experiments are carried out by the addition of Cu^{2+} to csUCNPs/EBT solutions containing other metal ions. Significant enhancements in the UCL ratio $(F_0-F)/F_0$ at 654 nm are observed (Fig. 4.8c), indicating the sensing of Cu^{2+} by csUCNPs/EBT is hardly interfered by the presence of other common metal ions. Therefore, csUCNPs/EBT nanocomposites can act as highly selective luminescence nanoprobes for Cu^{2+}.

4.3.4 Design Principle of Upconversion-Based Nanoprobes for CN^-

The design strategy of csUCNPs/Au nanosystem for selective cyanide anion sensing relies on the FRET process as well, where core-shell-structured csUCNPs are used as the energy donor and Au NPs are employed as the energy acceptor, as depicted in Fig. 4.9a. Without modifications, csUCNPs give rise to green and red luminescent emissions deriving from the $^2H_{11/2} \rightarrow {}^4I_{15/2}$, $^4S_{3/2} \rightarrow {}^4I_{15/2}$, and $^4F_{9/2} \rightarrow {}^4I_{15/2}$ transitions of Er^{3+} under 980 nm laser excitation. Ultrasmall Au NPs (*ca.* 1.7 nm) with a broad absorption in the whole visible region exhibit quenching rather than plasmonic effects. When the csUCNPs couple with Au NPs, an efficient FRET process occurs, resulting in the weakening of green and red emissions in the UCL intensity. However, the energy transfer from csUCNPs to Au NPs is suppressed in the presence of cyanide ion, owing to the etching property of cyanide ion for Au NPs. As a consequence, the UCL of csUCNPs is recovered caused by the consumption of Au NPs upon the addition of cyanide ion (Fig. 4.9b), and the variation of UCL intensity of csUCNPs allows the quantitative detection of cyanide ion.

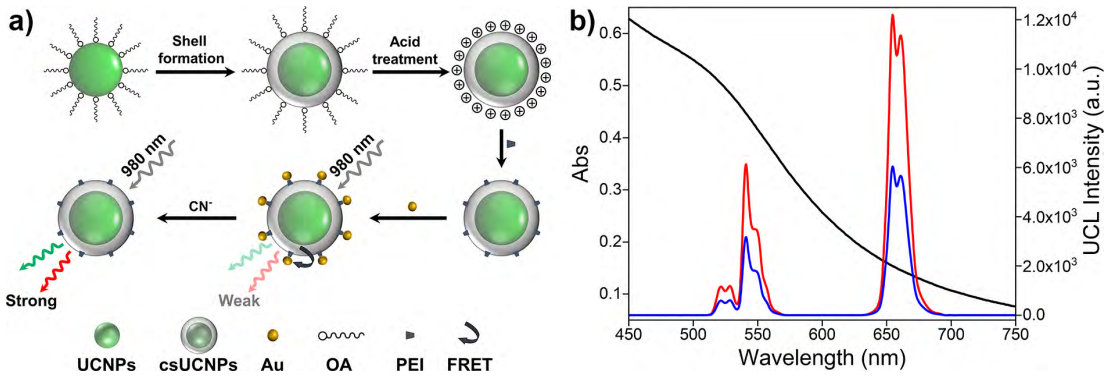

Fig. 4.9 (a) Schematic illustration of the synthesis of csUCNPs/Au nanoassemblies and their response to cyanide ion. (b) UV-vis spectrum of Au NPs (black). UCL spectra of csUCNPs/Au in the absence (blue) and presence (red) of cyanide ion.

4.3.5 Characterization of csUCNPs/Au Nanoassemblies

Ligand-free csUCNPs obtained *via* the vortexing method can be well-dispersed in water to form a stable colloidal solution, and the zeta potential is determined to be 36.8 mV (pH ~5.5). Furthermore, the positively charged bare csUCNPs favor the attachment of PEI on their surface. The size and morphology remain unchanged after the modification of bare csUCNPs by PEI, which is revealed by the TEM image (Fig. 4.3d, e). Meanwhile, nearly identical UCL intensity is observed in PEI-csUCNPs in the

aqueous solution compared with bare csUCNPs (Fig. 4.5).

To obtain csUCNPs/Au nanoassemblies, ultrasmall Au NPs with a mean diameter of about 1.7 nm are prepared (Fig. 4.10a), and the nanocomposites can then be easily achieved by assembling negatively charged Au NPs (-2.7 mV) on positively charged PEI-csUCNPs (34.3 mV) through electrostatic interaction. As presented in the TEM image (Fig. 4.10b), small Au NPs can be clearly seen on the csUCNPs. For the addition of 0.10 mM Au NPs, we can estimate that ~140 Au NPs are decorating one csUCNP. As the connection between csUCNP and Au relies on electrostatic interaction, the nonuniform distribution of Au NPs is likely caused by the drying process during the sample preparation for the TEM measurement, as during drying the concentration of the Au NPs increases and therefore their tendency for clustering. Moreover, the compositional analysis of hybrid NPs by EDX shows the existence of Na, F, Y, Yb, and Au elements (Fig. 4.10c), evidencing the presence of Au NPs.

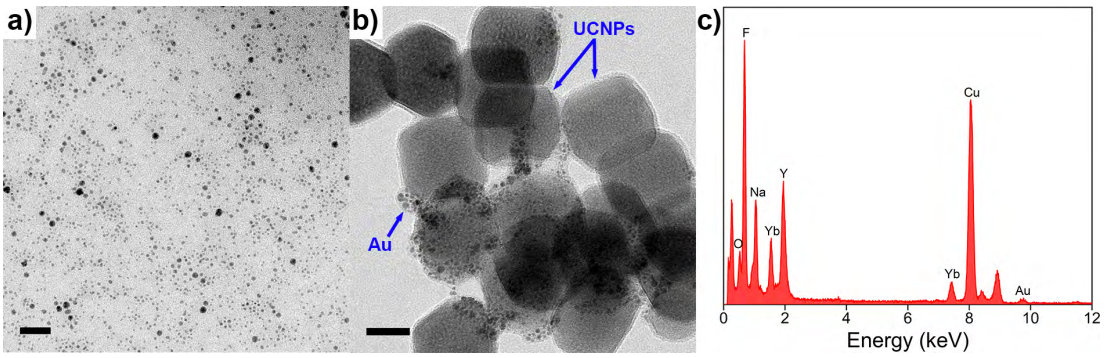

Fig. 4.10 TEM images of (a) Au NPs and (b) csUCNPs/Au nanoassemblies. Scale bars: 20 nm. (c) EDX analysis of csUCNPs/Au nanoassemblies.

Optical properties of csUCNPs/Au nanoassemblies are assessed by UV-vis absorption and UCL emission spectroscopies. Au NPs show a broad band absorption in the visible region, and the broad spectral absorbance of Au NPs overlaps well with the UCL of csUCNPs in the green and red regions, as shown in Fig. 4.9b, enabling the FRET between csUCNPs and Au NPs. Furthermore, the FRET process is verified by the phenomenon of the UCL reduction in csUCNPs upon the 980 nm laser activation.

To optimize the nanosystem, different contents of Au NPs are used to modify PEI-csUCNPs. The performance of different amounts of Au NPs on PEI-UCNPs is evaluated by UCL spectra, which are shown in Fig. 4.11a. The UCL intensity experiences a significant decrease at the beginning, and the UCL intensity reaches the minimum when 0.1 mM Au NPs is added. However, at higher Au content this trend

suddenly stops and an increase in UCL intensity takes place when the content of Au NPs goes beyond 0.1 mM. Subsequently, a gradual uptrend in UCL intensity occurs upon further increasing the Au NPs content. In addition, the energy transfer efficiency between csUCNPs and Au NPs (i.e., quenching efficiency) is calculated from the UCL emission intensities in the red region (600-700 nm) by the following equation:

$$\eta = 1 - \frac{rUCL}{rUCL_0} \tag{13}$$

Where η denotes the quenching efficiency in the red region, rUCL and $rUCL_0$ are the integrated red emission intensities in 600-700 nm of csUCNPs/Au and csUCNPs, respectively.

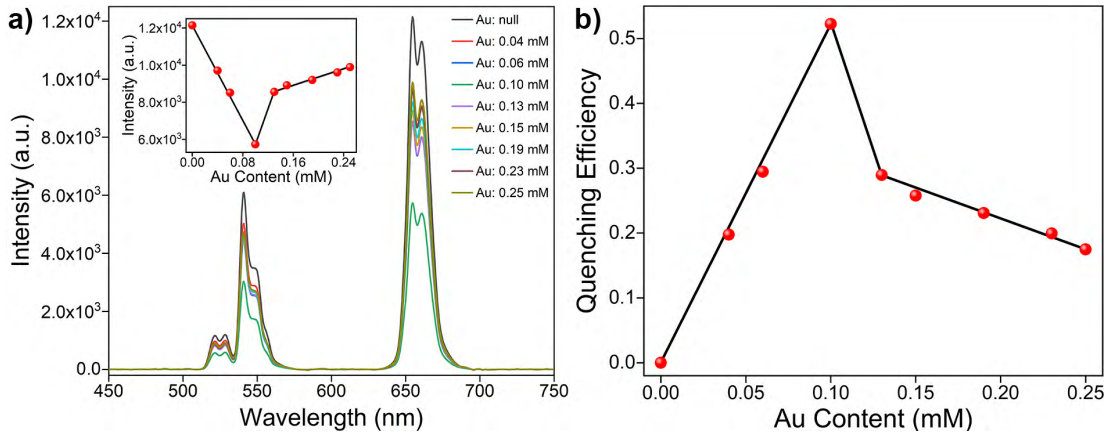

Fig. 4.11 (a) UCL spectra of csUCNPs upon addition of different contents of Au NPs. Inset: variations of UCL intensity at 655 nm upon addition of Au NPs. (b) Quenching efficiency of csUCNP/Au with different Au contents in 600-700 nm. (csUCNPs content: 0.5 mg/mL)

As shown in Fig. 4.11b, the UCL quenching efficiency in the wavelength range of 600-700 nm experiences a substantial increase for a low loading amount of Au NPs, and the greatest quenching efficiency of about 52% is reached for the addition of 0.1 mM Au NPs. For higher Au content, the quenching efficiency decreases with the increasing content of Au NPs. This abnormal phenomenon with the high loading amount of Au NPs may be attributed to partial aggregation of Au NPs on csUCNPs, leading to the plasmonic enhancement effect.

In order to verify the aforementioned conjecture, TEM and UV-vis absorption measurements of csUCNPs/Au nanocomposites are performed. Obviously, TEM images show that no apparent aggregation of Au NPs takes place with low amounts of added Au NPs (Fig. 4.12a-c). In contrast, small agglomerates appear when 0.13 mM

Au NPs are added, and agglomerates become larger with increasing loading amount of Au NPs (Fig. 4.12d-h). Moreover, no obvious absorption peak is observed when the added amount of Au NPs is less than or equal to 0.1 mM. However, an absorption peak at about 535 nm appears when the added amount of Au NPs is greater than 0.1 mM, and the absorption intensity at 535 increases with the growing addition of Au NPs to PEI-csUCNPs solutions, indicating the increasing amount of Au aggregates (Fig. 4.12i). As a consequence, the competition of Au aggregation-induced plasmonic enhancement effect[24] and single ultrasmall Au NPs-induced quenching effect results in the uptrend of the UCL intensity in csUCNPs/Au nanoassemblies with a high content of Au NPs.

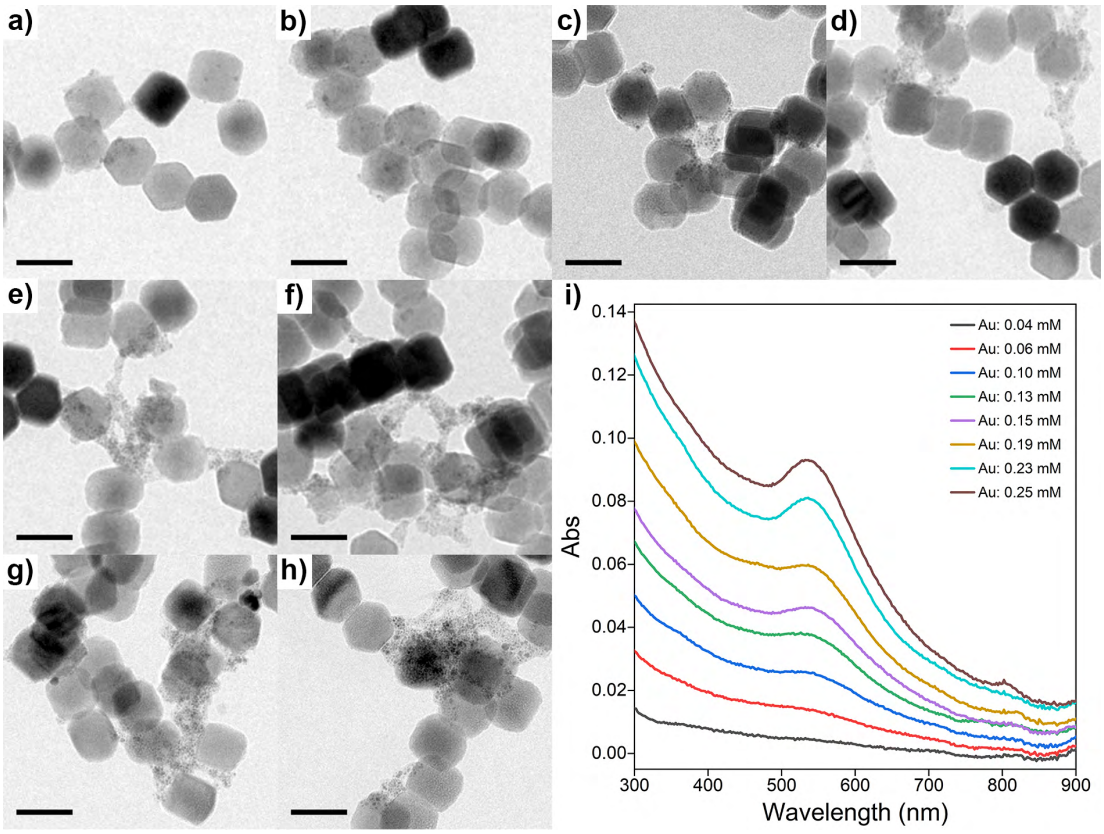

Fig. 4.12 TEM images of csUCNPs/Au nanoassemblies with different contents of Au NPs. (a) 0.04 mM, (b) 0.06 mM, (c) 0.10 mM, (d) 0.13 mM, (e) 0.15 mM, (f) 0.19 mM, (g) 0.23 mM, (h) 0.25 mM. (i) UV-vis absorption spectra of csUCNPs/Au with different contents of Au NPs.

4.3.6 Sensitive and Selective Detection of CN^-

The sensing ability of csUCNPs/Au nanoassemblies is based on the recovery of UCL emissions *via* the consumption of Au NPs by the addition of cyanide ion, attributed to the cyanide-mediated oxidation reaction of Au to $[Au(CN)_2]^-$, as described by the

following equation:

$$4Au + 8CN^- + O_2 + 2H_2O \rightarrow 4[Au(CN)_2]^- + 4OH^- \quad (14)$$

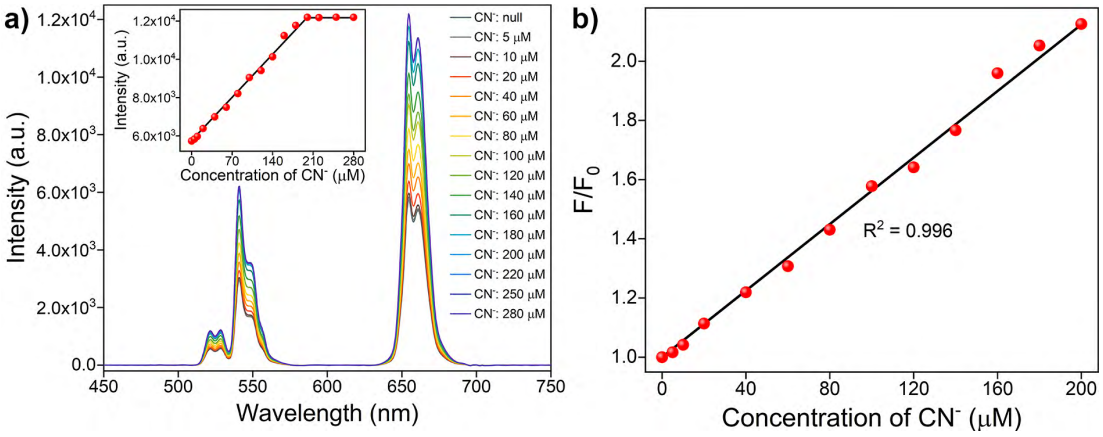

Fig. 4.13 (a) UCL spectra of csUCNPs/Au upon addition of different concentrations of cyanide ion. Inset: UCL intensity at 655nm as a function of cyanide concentration. (b) Linear relationship between UCL intensity at 655 nm and concentrations of cyanide ion.

Table 4.2 Comparison of various methods for cyanide ion sensing

Materials	Methods	Linear range	LOD	Ref.
gold nanocluster	fluorometry	0-10 μM	0.2 μM	[25]
iridium complex-modified UCNPs	fluorometry	0-1.8 mM	62.6 μM	[26]
phenothiazine-cyanine-modified UCNPs	colorimetry	0-50 μM	9.85 μM	[27]
	fluorometry	0-300 uM	0.84 μM	[27]
bicinchoninic acid-Cu(II) complex	colorimetry	0-50 mM	1.25 μM	[28]
Co(II)Pc modified carbon paste electrode	voltammetry	24-270 μM	3.6 μM	[29]
chitosan-gold NPs	colorimetry	0-38 μM	2.31 μM	[30]
hexaazatriphenylene	electrochemical assay	0-200 μM	0.87 μM	[31]
csUCNPs/Au nanocomposites	fluorometry	0-200 μM	1.53 μM	this work

The csUCNPs/Au nanoassemblies formed by the addition of 0.1 mM Au NPs are applied for the sensing due to their sufficient luminescence quenching efficiency. As discussed above, the consumption of Au NPs occurs upon the addition of cyanide ion, resulting in the suppression of the FRET process and corresponding to a gradual

increase of UCL in all emissions, which is shown in Fig. 4.13a. No further variation of UCL intensity is measured after the addition of 2 equiv of cyanide ion, which is in agreement with the reaction equation. The variations of the fluorescence enhancement factor at 655 nm (F/F_0, where F_0 and F refer to the luminescence intensities of nanoprobes at 655 nm in the absence and presence of cyanide ion, respectively) versus the addition of cyanide ion are shown in Fig. 4.13b, The calibration curve exhibits a linear relationship between F/F_0 and the concentration of cyanide ion in the range from 0 to 200 μM, and the linear correlation coefficient of the calibration curve is 0.996, and the LOD for cyanide ion is approximately 1.53 μM according to the 3σ rule. Compared to the developed methods for cyanide ion sensing (Table 4.2), the sensitivity of the UCNPs/Au nanocomposites is well competitive.

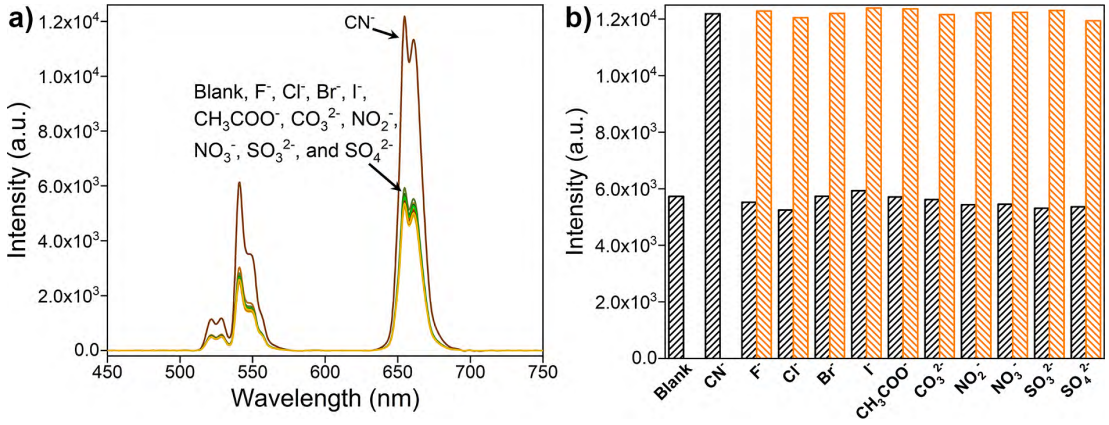

Fig. 4.14 (a) UCL spectra of 0.5 mg/mL csUCNPs/Au nanocomposites in the presence of various anions. (b) Changes in UCL intensity of 0.5 mg/mL csUCNPs/Au at 655 nm upon addition of 200 μM CN^- and 2 mM other ions. Black bars represent the UCL changes upon the addition of various anions, orange bars represent the subsequent addition of 200 μM CN^- to the above solution.

To further assess the selectivity of the nanosystem for cyanide ion, a series of control experiments is performed to investigate the response of csUCNPs/Au towards other potentially interfering anions. As shown in Fig. 4.14a, only the addition of cyanide ion leads to a noticeable variation in UCL emission intensity, and no obvious UCL changes are observed upon the addition of other anions, such as F^-, Cl^-, Br^-, I^-, CH_3COO^-, CO_3^{2-}, NO_2^-, NO_3^-, SO_3^{2-}, and SO_4^{2-}. In addition, competition experiments are carried out by adding cyanide anion to solutions of csUCNPs/Au in the presence of other anions. Significant reductions of the UCL are observed upon the addition of cyanide ion, which is presented in Fig. 4.14b. Therefore, it can be stated that csUCNPs/Au nanoassemblies can act as highly sensitive and selective luminescence nanoprobes for cyanide ion.

4.4 Conclusion

In summary, by assembling the EBT dye onto the surface of csUCNPs *via* electrostatic interactions, csUCNPs/EBT nanocomposites have been prepared. Owing to the strong chelating ability of EBT to Cu^{2+} at pH 3, the csUCNPs/EBT composites can be applied as the nanoprobes for Cu^{2+} sensing based on the FRET process, where csUCNPs serve as the energy donor and the EBT-Cu complex act as the energy acceptor. Upon addition of Cu^{2+}, the maximum absorption of nanocomposites exhibits a redshift, resulting in the enhanced spectral overlap between the absorption of the metal-dye complex and red UCL emission of csUCNPs, enabling an enhanced FRET process between csUCNPs and the EBT-Cu complex, and the nanocomposites display a detection limit of 9.42 μM for Cu^{2+}. Control experiments show that only the addition of Cu^{2+} leads to the variation in color and reduction in fluorescence intensity. Moreover, competition experiments show that the response of csUCNPs/EBT nanocomposites toward Cu^{2+} is hardly affected by the presence of commonly coexistent cations, indicating the selectivity of such nanocomposites to Cu^{2+}.

Based on the same mechanism, csUCNPs/Au nanoassemblies have been constructed for cyanide ion sensing by assembling Au NPs with csUCNPs, where csUCNPs act as the energy donor and Au NPs act as the energy acceptor. Additionally, the optimum Au NPs loading content was determined with the aim of achieving the highest fluorescence quenching efficiency. Au NPs are exclusively etched by cyanide but are inert to other anions, thus cyanide-induced Au consumption favors the inhibition of the FRET process, leading to the recovery of the UCL emissions, enabling the sensing of cyanide ion over other anions with high sensitivity (1.53 μM). Furthermore, competition experiments show that the response of csUCNPs/Au nanoassemblies toward cyanide ion remains undisturbed by the presence of other interfering anions, proving their selectivity to cyanide ion.

4.5 References

[1] S.-H. Park, N. Kwon, J.-H. Lee, J. Yoon, and I. Shin, Synthetic ratiometric fluorescent probes for detection of ions, *Chem. Soc. Rev.*, **2020**, 49, 143-179.

[2] Y.-H. Chan, J. Chen, Q. Liu, S.E. Wark, D.H. Son, and J.D. Batteas, Ultrasensitive copper(II) detection using plasmon-enhanced and photo-brightened luminescence of CdSe quantum dots, *Anal. Chem.*, **2010**, 82, 3671-3678.

[3] L. Chen, X. Tian, C. Yang, Y. Li, Z. Zhou, Y. Wang, and F. Xiang, Highly selective and

sensitive determination of copper ion based on a visual fluorescence method, *Sens. Actuators B Chem.*, **2017**, 240, 66-75.

[4] C. Lei, Z. Wang, Z. Nie, H. Deng, H. Hu, Y. Huang, and S. Yao, Resurfaced fluorescent protein as a sensing platform for label-free detection of copper(II) ion and acetylcholinesterase activity, *Anal. Chem.*, **2015**, 87, 1974-1980.

[5] C. Liu, R. Bai, and Q. San Ly, Selective removal of copper and lead ions by diethylenetriamine-functionalized adsorbent: Behaviors and mechanisms, *Water Res.*, **2008**, 42, 1511-1522.

[6] Q. Gao, L. Ji, Q. Wang, K. Yin, J. Li, and L. Chen, Colorimetric sensor for highly sensitive and selective detection of copper ion, *Anal. Methods*, **2017**, 9, 5094-5100.

[7] Y. Zhou, S. Wang, K. Zhang, and X. Jiang, Visual detection of copper(II) by azide- and alkyne-functionalized gold nanoparticles using click chemistry, *Angew. Chem. Int. Ed.*, **2008**, 47, 7454-7456.

[8] Z.-Z. Dong, C. Yang, K. Vellaisamy, G. Li, C.-H. Leung, and D.-L. Ma, Construction of a nano biosensor for cyanide anion detection and its application in environmental and biological systems, *ACS Sens.*, **2017**, 2, 1517-1522.

[9] K. Deng, L. Wang, Q. Xia, R. Liu, and J. Qu, A turn-on fluorescent chemosensor based on aggregation-induced emission for cyanide detection and its bioimaging applications, *Sens. Actuators B Chem.*, **2019**, 296, 126645.

[10] J. Ma, and P.K. Dasgupta, Recent developments in cyanide detection: A review, *Anal. Chim. Acta*, **2010**, 673, 117-125.

[11] F. Wang, R. Deng, J. Wang, Q. Wang, Y. Han, H. Zhu, X. Chen, and X. Liu, Tuning upconversion through energy migration in core-shell nanoparticles, *Nat. Mater.*, **2011**, 10, 968-973.

[12] D.G. Duff, A. Baiker, and P.P. Edwards, A new hydrosol of gold clusters. 1. Formation and particle size variation, *Langmuir*, **1993**, 9, 2301-2309.

[13] Z. Li, and Y. Zhang, An efficient and user-friendly method for the synthesis of hexagonal-phase $NaYF_4$:Yb,Er/Tm nanocrystals with controllable shape and upconversion fluorescence, *Nanotechnology*, **2008**, 19, 345606.

[14] R. Arppe, I. Hyppanen, N. Perala, R. Peltomaa, M. Kaiser, C. Wurth, S. Christ, U. Resch-Genger, M. Schaferling, and T. Soukka, Quenching of the upconversion luminescence of $NaYF_4:Yb^{3+},Er^{3+}$ and $NaYF_4:Yb^{3+},Tm^{3+}$ nanophosphors by water: the role of the sensitizer Yb^{3+} in non-radiative relaxation, *Nanoscale*, **2015**, 7, 11746-11757.

[15] F.T. Rabouw, P.T. Prins, P. Villanueva-Delgado, M. Castelijns, R.G. Geitenbeek, and A. Meijerink, Quenching pathways in $NaYF_4:Er^{3+},Yb^{3+}$ upconversion nanocrystals, *ACS Nano*, **2018**, 12, 4812-4823.

[16] B. Gu, M. Ye, L. Nie, Y. Fang, Z. Wang, X. Zhang, H. Zhang, Y. Zhou, and Q. Zhang, Organic-dye-modified upconversion nanoparticle as a multichannel probe to detect Cu^{2+} in living cells, *ACS Appl. Mater. Interfaces*, **2018**, 10, 1028-1032.

[17] C. Liu, Y. Yu, D. Chen, J. Zhao, Y. Yu, L. Li, and Y. Lu, Cupredoxin engineered

upconversion nanoparticles for ratiometric luminescence sensing of Cu^{2+}, *Nanoscale Adv.*, **2019**, 1, 2580-2585.

[18] Y. Xu, H. Li, X. Meng, J. Liu, L. Sun, X. Fan, and L. Shi, Rhodamine-modified upconversion nanoprobe for distinguishing Cu^{2+} from Hg^{2+} and live cell imaging, *New J. Chem.*, **2016**, 40, 3543-3551.

[19] X. Huang, L. Wang, X. Zhang, X. Yin, N. Bin, F. Zhong, Y. Liu, and Q. Cai, Dye-assembled nanocomposites for rapid upconversion luminescence sensing of Cu^{2+}, *Sens. Actuators B Chem.*, **2017**, 248, 1-8.

[20] M. Sohrabi, M. Amirnasr, H. Farrokhpour, and S. Meghdadi, A single chemosensor with combined ionophore/fluorophore moieties acting as a fluorescent “Off-On” Zn^{2+} sensor and a colorimetric sensor for Cu^{2+}: experimental, logic gate behavior and TD-DFT calculations, *Sens. Actuators B Chem.*, **2017**, 250, 647-658.

[21] M.L. Desai, B. Deshmukh, N. Lenka, V. Haran, S. Jha, H. Basu, R.K. Singhal, P.K. Sharma, S.K. Kailasa, and K.-H. Kim, Influence of doping ion, capping agent and pH on the fluorescence properties of zinc sulfide quantum dots: sensing of Cu^{2+} and Hg^{2+} ions and their biocompatibility with cancer and fungal cells, *Spectrochim. Acta, Part A*, **2019**, 210, 212-221.

[22] Z. Li, L. Zhang, L. Wang, Y. Guo, L. Cai, M. Yu, and L. Wei, Highly sensitive and selective fluorescent sensor for Zn^{2+}/Cu^{2+} and new approach for sensing Cu^{2+} by central metal displacement, *Chem. Commun.*, **2011**, 47, 5798-5800.

[23] H. Goh, Y.G. Ko, T.K. Nam, A. Singh, N. Singh, and D.O. Jang, A benzimidazole-based fluorescent chemosensor for Cu^{2+} recognition and its complex for sensing $H_2PO_4^-$ by a Cu^{2+} displacement approach in aqueous media, *Tetrahedron Lett.*, **2016**, 57, 4435-4439.

[24] L. Polavarapu, J. Pérez-Juste, Q.-H. Xu, and L.M. Liz-Marzán, Optical sensing of biological, chemical and ionic species through aggregation of plasmonic nanoparticles, *J. Mater. Chem. C*, **2014**, 2, 7460-7476.

[25] Y. Liu, K. Ai, X. Cheng, L. Huo, and L. Lu, Gold-nanocluster-based fluorescent sensors for highly sensitive and selective detection of cyanide in water, *Adv. Funct. Mater.*, **2010**, 20, 951-956.

[26] L. Yao, J. Zhou, J. Liu, W. Feng, and F. Li, Iridium-complex-modified upconversion nanophosphors for effective LRET detection of cyanide anions in pure water, *Adv. Funct. Mater.*, **2012**, 22, 2667-2672.

[27] S. Zhao, F. Wu, Y. Zhao, Y. Liu, and L. Zhu, Phenothiazine-cyanine-functionalized upconversion nanoparticles for LRET and colorimetric sensing of cyanide ions in water samples, *J. Photochem. Photobiol. A*, **2016**, 319-320, 53-61.

[28] A.A. Biradar, A.V. Biradar, T. Sun, Y. Chan, X. Huang, and T. Asefa, Bicinchoninic acid-based colorimetric chemosensor for detection of low concentrations of cyanide, *Sens. Actuators B Chem.*, **2016**, 222, 112-119.

[29] E.C. Figueira, L.C.S. Neres, M.R.S. Ruy, G.F. Troiano, and M.D.P.T. Sotomayor,

Development of a biomimetic sensor for selective identification of cyanide, *Anal. Methods*, **2016**, 8, 6353-6360.

[30] C. Radhakumary, and K. Sreenivasan, Rapid and highly selective dipchecking for cyanide ions in aqueous media, *Analyst*, **2012**, 137, 5387-5391.

[31] G. Men, W. Han, C. Chen, C. Liang, and S. Jiang, A cyanide-sensing detector in aqueous solution based on anion-π interaction-driven electron transfer, *Analyst*, **2019**, 144, 2226-2230.

Chapter 5: Upconversion-Based Nanosystems for Fluorescence Sensing of pH and Small Molecule

Chapter 5 is based on the following article

> Chunning Sun, Michael Gradzielski, "Upconversion-based nanosystems for fluorescence sensing of pH and H_2O_2", *Nanoscale Adv.*, **2021**, 3, 2538-2546 (DOI: 10.1039/D0NA01045F).

C. Sun and M. Gradzielski conceived and designed the experiments. C. Sun performed the experiments and analyzed the data. Both authors discussed the results and jointly wrote the manuscript.

5.1 Introduction

Hydrogen peroxide (H_2O_2), an important bioactive molecule in living systems, plays an essential role in the physiological process including signal transduction, cell proliferation, differentiation, and maintenance[1, 2]. Abnormal production or accumulation of H_2O_2 will lead to severe damage to DNA and proteins, causing a series of serious diseases[3-7], such as Diabetes, Alzheimer's, and Parkinson's disease, cardiovascular disorders, and even cancer. Additionally, H_2O_2 is widely used as a bleaching agent and sterilant in industrial and environmental fields[8, 9], such as food processing, drinking water treatment, packaging, and organic pollutant degradation. However, exposure to high concentrations of H_2O_2 would be a great threat to organisms[10, 11]. Therefore, quantitative detection of H_2O_2 is of great importance for monitoring its potential risk.

Optical methods *via* fluorescence changes have attracted considerable attention, as the fluorometric approach is a non-destructive method that can be simply and rapidly performed with high sensitivity and selectivity[12]. In contrast to conventional fluorescence probes (such as organic dyes, carbon nanomaterials, and semiconductor quantum dots), upconversion NPs featuring large anti-Stokes shifts, excellent chemical- and photo-stability, sharp multicolor emissions, and low toxicity have been

regarded as a promising class of luminophores[13].

Up to now, a variety of functional materials including organic dyes[14-16], noble metals[17-19], quantum dots[20-22], carbon nanomaterials[23-25], and two-dimensional materials[26-28] has been employed to couple with upconversion NPs to construct fluorescence probes, realizing the quantitative detection of inorganic ions[29-31], pH[32-34], small molecules[35-38], and nucleic acids[39-42]. Most of the upconversion-based probes rely on the FRET process, in which a very short distance (typically <10 nm) between the upconversion NPs and absorbers is required. Moreover, in order to obtain high-sensitivity detection, high-quality upconversion NPs with strong emission and high upconversion efficiency are employed, which are commonly prepared by applying OA as the ligand. The oleate-capped upconversion NPs are hydrophobic and prone to disperse in nonpolar solvents. However, prior to sensing applications, hydrophilic upconversion NPs are required and the hydrophobic-to-hydrophilic transition of NPs is essential[43].

Herein, different upconversion nanosystems for H_2O_2 sensing were proposed using MoO_{3-x} NSs as the energy acceptor based on either the EEA effect or the joint effect of the EEA and FRET, owing to the strong absorbance of MoO_{3-x} NSs in both visible and NIR regions. By the alignment of MoO_{3-x} NSs solution and OA-UCNPs solution, a EEA-based upconversion nanosystem for sensing of H_2O_2 in the non-contact mode is developed, where MoO_{3-x} NSs act as the energy acceptor of the incident light for the activation of UCNPs. Additionally, this system can be used for pH sensing as well. Benefiting from the non-contact method, hydrophobic OA-UCNPs can be used directly for the sensing and ultrahigh quenching efficiency (99.8%) can be reached. Meanwhile, by the integration of hydrophilic UCNPs and MoO_{3-x} NSs, we are able to prepare conventional upconversion-based nanocomposites for H_2O_2 sensing *via* the joint effect of the EEA and FRET, where MoO_{3-x} NSs act as the energy acceptor of not only the 980 nm exciting light for UCNPs but also fluorescence emissions of UCNPs. To the best of our knowledge, this is the first upconversion-based nanoprobes toward the sensing of one analyte by two different systems while using the same material as an energy acceptor.

5.2 Materials and Methods

5.2.1 Reagents

Yttrium(III) acetate tetrahydrate (99.9%), ytterbium(III) acetate hydrate (99.9%), erbium(III) acetate hydrate (99.9%), MoO_3 (99.95%) were purchased from Alfa Aesar, OA (90%), ODE (90%), NH_4F (≥98%), NaOH (≥98%), MeOH (99.8%), ethanol (≥99.8%), cyclohexane (99.5%), FA (≥98%), PEI (branched, Mw ~25,000), $NaNO_3$ (≥99.0%), KNO_3 (≥99.0%), $Ca(NO_3)_2{\cdot}4H_2O$ (≥99.0%), $Mg(NO_3)_2{\cdot}6H_2O$ (99%), $Zn(NO_3)_2{\cdot}6H_2O$ (≥99%), NaF (≥99%), NaCl (≥99.5%), Na_2CO_3 (≥99%), Na_2SO_4 (≥99%) L-cysteine (≥97%), L-glutamine (≥99%), glycine (≥99%), L-leucine (≥98%), L-proline (≥99%), L-serine (≥99%), L-threonine (≥98%), and L-valine (≥98%) were obtained from Sigma-Aldrich. Milli-Q water (18.2 MΩ·cm at 25 °C) was used in all experiments.

5.2.2 Instruments

FT-IR spectra were acquired on a Thermo Scientific Nicolet iS5 FT-IR spectrometer using the KBr method. The spectra were recorded in transmission mode with the wavenumber range from 4000-500 cm^{-1}. UV-Vis absorption spectra were obtained by using a CARY 50 spectrophotometer. TEM, HR-TEM, and EDS were performed by FEI Tecnai G^2 20 S-TWIN with a LaB_6 cathode operating at 200 kV. XRD spectra were obtained by using Philips X'Pert MPD Pro X-ray diffractometer at a scanning rate of 4°/min in the 2θ range from 10° to 90° with Cu Kα radiation (λ = 0.15406 nm). ζ-potential measurements were carried out with an Anton Paar Litesizer™ 500. X-ray photoelectron spectroscopy (XPS) was measured with a Thermo Fisher Scientific ESCALAB 250Xi instrument. UCL emission spectra were collected at room temperature with a fiber-coupled spectrometer (Ocean HDX, Ocean Optics) equipped with an external 980 nm CW laser (Roithner Lasertechnik GmbH) with tunable power from 0 to 5 W. Quartz cuvettes (0.7 mL, 10 mm × 2 mm light path) were used for UV-vis absorption and UCL measurements.

5.2.3 Synthesis of MoO_{3-x} NSs

MoO_{3-x} NSs were prepared according to previous publications with minor modifications[44, 45]. In a typical process, 1.5 g bulk MoO_3 powder was ground with 0.3 mL of ACN for 30 min and then added to a water/ethanol solution (25 mL, v/v=1/1). The dispersion was then probe-sonicated for 2 h at 100 W (Branson Digital Sonifier W-250D) at a 5 sec ON and 2 sec OFF pulse. To avoid overheating of the solvent, the beaker filled with MoO_3 dispersion was immersed in an ice bath during sonication. The light blue supernatant containing a high concentration of MoO_3 NSs (denoted as S-

MoO3 NSs) was collected *via* centrifugation at 8000 r.p.m for 30 min. For the preparation of MoO_{3-x} NSs, the supernatant dispersion was filled into a quartz glass vial and irradiated with a UV lamp (254 & 365 nm, 15 W) for 5 h, dark blue MoO_{3-x} NSs solution was finally obtained, and the MoO_{3-x} NSs solution was then diluted to 2 mg/mL by water and ethanol (v/v=1/1) solution, and stored at 4 ºC for further use.

5.2.4 Synthesis of OA-UCNPs

OA-UCNPs were prepared as described in Chapter 3. Typically, 3.12 mL $Y(CH_3COO)_3$ (0.2 M), 0.8 mL $Yb(CH_3COO)_3$ (0.2 M) and 0.8 mL $Er(CH_3COO)_3$ (0.02 M) were added to a three-neck flask containing 6 mL OA and 14 mL ODE at room temperature. The mixed solution was heated to 110 ºC for 30 min to remove the water, followed by heating to 160 ºC for 40 min to form Ln-oleate complexes and then cooled down to 50 ºC. A MeOH solution (10 mL) containing NH_4F (3.2 mmol) and NaOH (2.0 mmol) was added afterward and stirred at 50 ºC for 30 min. After evaporating the MeOH, the solution was heated to 305 ºC at a ramp rate of 10 °C/min and maintained at this temperature for 40 min under N_2 atmosphere. After cooling down to room temperature, the NPs were precipitated out by adding excess ethanol, collected by centrifugation at 6000 r.p.m for 5 min, repeatedly washed with ethanol, and finally redispersed in cyclohexane for further use.

5.2.5 Synthesis of Ligand-Free UCNPs

Ligand-free UCNPs were prepared *via* the aforementioned vortexing method. Typically, FA (5 mmol) was added to 2 mL cyclohexane solution containing OA-UCNPs (10 mg/mL) directly, the mixture was then shaken for 10 s (3000 r.p.m) on a vortex mixer, ligand-free UCNPs were precipitated out. The resultant NPs were obtained by centrifugation at 6000 r.p.m for 20 min, washed one time with ethanol and three times with water, and finally redispersed in water.

5.2.6 Preparation of UCNPs/MoO_{3-x} Nanocomposites

To synthesize UCNPs/MoO_{3-x} nanocomposites, PEI-capped UCNPs (abbreviated as PEI-UCNPs) were first prepared. Typically, 4 mL ligand-free UCNPs solution (5 mg/ mL) were added to a vial containing 4 mL PEI solution (10 mg/mL), followed by overnight stirring. PEI-UCNPs were collected after centrifugation at 12000 r.p.m for 30

min and washing three times with water, and finally dispersed in water with a concentration of 1 mg/mL. UCNPs/MoO_{3-x} nanocomposites were prepared by mixing 0.5 mL PEI-UCNPs solution with an appropriate amount of MoO_{3-x} NSs solution, the mixture was first shaken for 3 min (3000 r.p.m) on a vortex mixer and then ultrasonicated for 5 min. UCNPs/MoO_{3-x} nanocomposites were then collected by centrifugation at 8000 r.p.m for 30 min, washed three times with water, and redispersion in water.

5.2.7 Non-Contact Fluorescence Sensing of pH

To detect pH in the non-contact mode, OA-UCNPs dispersed in cyclohexane with a concentration of 1 mg/mL were sealed in a quartz cuvette, the cuvette was then aligned with the other cuvette containing 1 mg/mL MoO_{3-x} NSs solution with different pH. The pH was adjusted by either 50 mM NaOH or 50 mM HCl ethanol/H_2O (v/v=1/1) solution. The cuvette containing MoO_{3-x} NSs was put in front of the other one containing OA-UCNPs solution, and the UCL spectra were collected under the excitation of a 4 W 980 nm CW laser.

5.2.8 Non-Contact Fluorescence Sensing of H_2O_2

The non-contact sensing procedure for the H_2O_2 was similar to that of the non-contact pH sensing, except that MoO_{3-x} NSs were dissolved in acetate buffer (50 mM, pH 4.5, ethanol/H_2O, v/v=1/1) with different concentrations of H_2O_2.

5.2.9 Fluorescence Sensing of H_2O_2 by UCNPs/MoO_{3-x} Nanoassemblies

To detect H_2O_2, 0.5 mg/mL of UCNPs/MoO_{3-x} aqueous solution (0.35 mg/mL MoO_{3-x} NSs) and different concentrations of H_2O_2 (0.4 mL) were added to 0.1 mL acetate buffer (50 mM, pH 4.5, DMF/H_2O, v/v=1/1), The mixture was then incubated at RT for 2 h, and the UCL spectra were measured under excitation of a 4 W 980 nm CW laser.

5.3 Results and Discussion

5.3.1 Design Strategy of Upconversion-Based Nanosystems for pH and H_2O_2 Sensing

The design strategy of UCNPs/MoO_{3-x} nanocomposites for fluorescence sensing of H_2O_2 is based on the modulation of MoO_{3-x} NSs-induced reduction in UCL emissions by H_2O_2 through the joint effect of EEA and FRET. In contrast, the pH and H_2O_2 dual-responsive upconversion-based nanosystem is realized by the direct adjustment of the excitation energy for UCNPs in the non-contact mode (Fig. 5.1a).

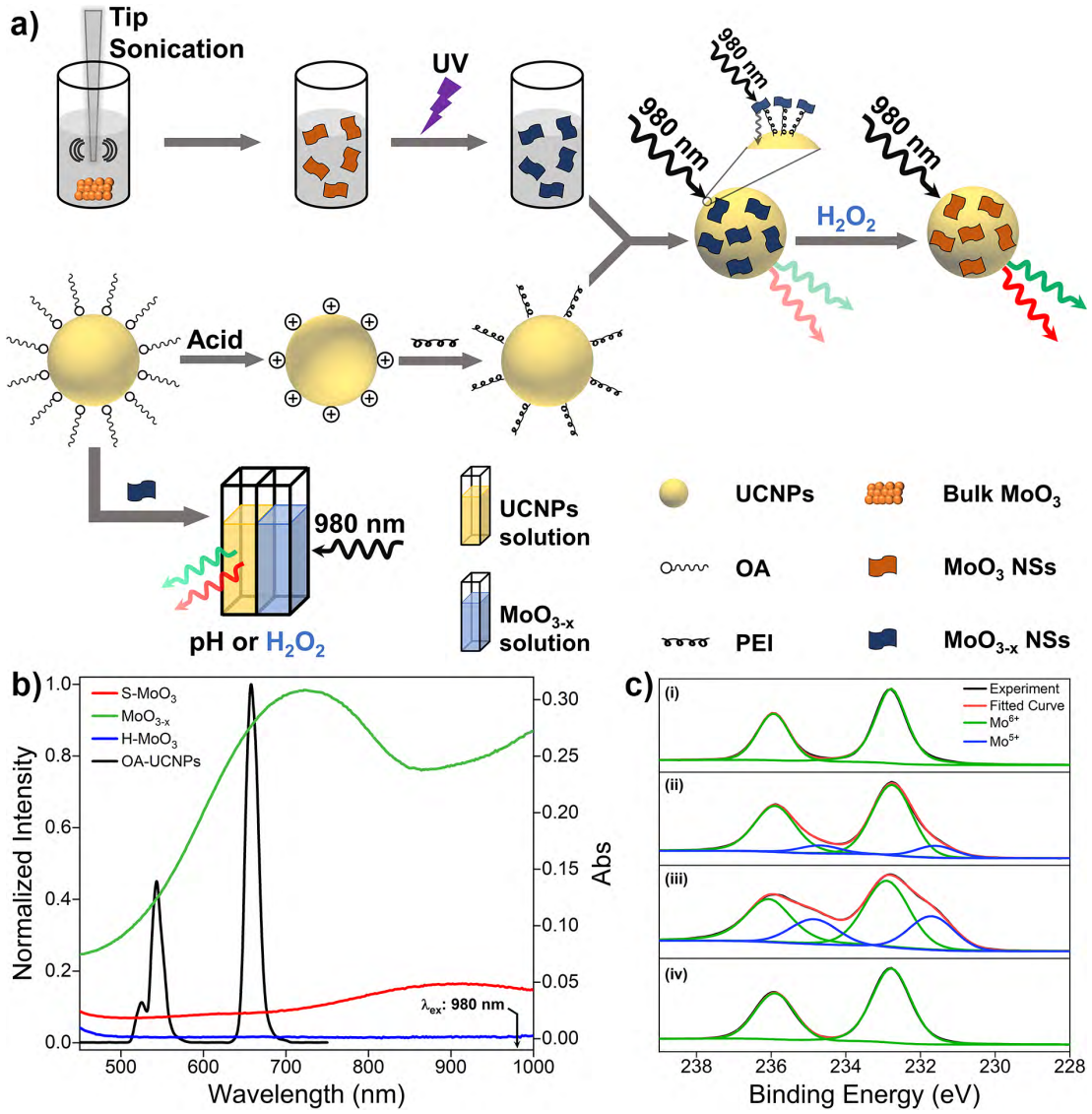

Fig. 5.1 (a) Schematic illustration of the design principle of upconversion-based nanosystems for pH and H_2O_2. (b) UCL spectrum of OA-UCNPs under 4 W 980nm CW laser excitation and UV-vis spectra of S-MoO_3, MoO_{3-x}, and H-MoO_3. c) The Mo 3d XPS spectra of (i) pristine MoO_3, (ii) S-MoO_3 NSs, (iii) MoO_{3-x} NSs, and (iv) H-MoO_3 NSs.

Without modifications, UCNPs give rise to green and red luminescence emissions under 980 nm excitation. After the reduction of MoO_3 by UV light, the oxygen-deficient MoO_{3-x} NSs exhibit strong absorption in both visible and NIR regions, overlapping well with the UCL emissions of UCNPs and the excitation wavelength for UCNPs of 980

nm (Fig. 5.1b). Owing to the strong NIR absorption of MoO_{3-x} NSs attached on the UCNPs, the EEA will first take place in the UCNPs/MoO_{3-x} system when activated by the 980 nm light, resulting in a lowered intensity of excitation light arriving at the UCNPs, thus weakening the resulting luminescence emissions. Moreover, the efficient FRET process occurs through the spectral overlap between the absorption of MoO_{3-x} NSs and the UCL of UCNPs in the visible region, leading to a further decrease in the intensity of luminescence emissions. Thus, the quenching in UCL of UCNPs is efficiently achieved by the joint effect of the EEA and FRET. However, upon the addition of H_2O_2, the oxygen-deficient MoO_{3-x} NSs can be oxidized back to MoO_3 (denoted as H-MoO_3), leading to the decrease of absorption in the visible and NIR regions (Fig. 5.1b), resulting in the recovery of UCL emissions *via* the reduction in EEA and FRET. Additionally, XPS was performed to evaluate the valence state of Mo in these nanosheets. As shown in Fig. 5.1c, the doublet peaks (235.9 eV and 232.8 eV) in the pristine MoO_3 sample are assigned to the binding energies of the $^3d_{3/2}$ and $^3d_{5/2}$ orbital electrons of Mo^{6+}. After treatment by tip-sonication, two new peaks at lower binding energies (234.7 eV and 231.6 eV) appear in the obtained S-MoO_3 NSs, which can be assigned to the Mo^{5+} oxidation state, and the integral area ratio of Mo^{5+}/Mo^{6+} is calculated to be 17.1% from the XPS spectrum. This phenomenon indicates that the MoO_3 is slightly reduced during the exfoliation process, showing weak absorption ability of S-MoO_3 NSs in visible and NIR regions (Fig. 5.1b). Furthermore, the peak area ratio of Mo^{5+}/Mo^{6+} increases to 47.9%, suggesting that oxygen-deficient MoO_{3-x} NSs are formed, where one-third of the Mo^{6+} is reduced upon UV irritation. However, the peaks at lower binding energies disappear after the addition of H_2O_2, confirming that MoO_{3-x} NSs have been oxidized. Thus, H_2O_2-involved oxidation of MoO_{3-x} enables the ability of UCNPs/MoO_{3-x} nanoprobes for H_2O_2 sensing with high sensitivity. Additionally, the adjustment of pH or addition of H_2O_2 in the acidic environment will lead to the variation of MoO_{3-x} NSs in NIR absorption, and thus fluorescence sensing of pH and H_2O_2 can be achieved through the direct modulation of MoO_{3-x} absorption-induced EEA in the non-contact mode.

5.3.2 Characterization of UCNPs, MoO_{3-x} NSs, and UCNPs/MoO_{3-x} Nanocomposites

Hydrophobic OA-UCNPs were synthesized by employing OA as the ligand *via* the high-temperature coprecipitation method[46]. As revealed by the TEM image (Fig. 5.2a), OA-UCNPs present uniform hexagonal shape with a mean diameter of about 28 nm. The

XRD pattern of the obtained OA-UCNPs with well-defined diffraction peaks agrees well with the standard data of hexagonal-phase $NaYF_4$ (JCPDS no. 28-1192), demonstrating their high crystallinity (Fig. 5.3a). In addition, the lattice fringes on the individual NP are clearly distinguished in the HR-TEM image (Fig. 5.2d), confirming the high crystallinity of the prepared NPs. The distance between the lattice fringes is measured to be about 0.32 nm, corresponding to the d-spacing for the (111) lattice planes of the hexagonal $NaYF_4$ structure.

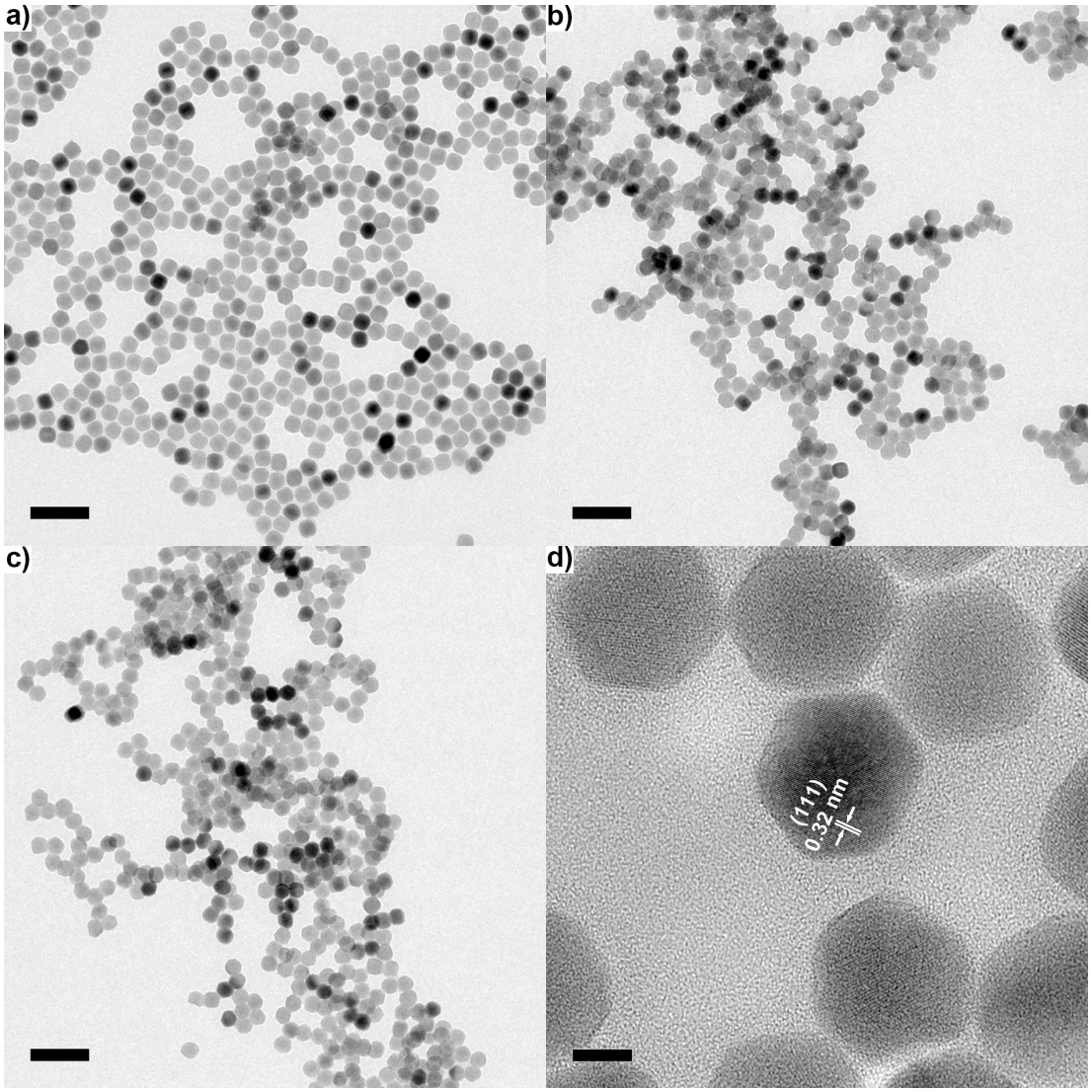

Fig. 5.2 TEM image of (a) OA-UCNPs, (b) bare UCNPs, and (c) PEI-UCNPs. Scale bars: 100 nm. (d) HR-TEM image of OA-UCNPs. Scale bar: 10 nm.

Ligand-free UCNPs are prepared by direct addition of FA to the cyclohexane solution containing OA-UCNPs through the vortexing method and sequential modification with PEI to obtain PEI-UCNPs. TEM images demonstrate unchanged morphology and size after ligand removal and polymer functionalization (Fig. 5.2b, c). The transition of OA-

UCNPs to ligand-free UNCPs and further to PEI-UCNPs are confirmed by FT-IR (Fig. 5.3b). Transmission bands of as-synthesized OA-csUCNPs at 2926 and 2852 cm^{-1} are attributed to asymmetric and symmetric stretching vibrations of methylene (-CH_2-) groups in the long alkyl chain. A weak peak at 3008 cm^{-1}, assigned to the =C-H stretching vibration, can be clearly observed in the spectrum. Moreover, two peaks centered at 1561 and 1460 cm^{-1} can be assigned to the asymmetric and symmetric stretching vibrations of the carboxylate group. These characteristic peaks validate the presence of oleate ligand on the surface of OA-UCNPs. Nevertheless, all the characteristic peaks disappeared after the acid treatment, except the broad band centered at around 3420 cm^{-1}, assigning to the solvated water molecules, validate the success in ligand removal and the hydrophilic nature of the obtained ligand-free UCNPs. After the modification of bare UCNPs by PEI, two bands centered at 2930 and 2854 cm^{-1} are shown in the spectrum, which can be attributed to the asymmetric and symmetric stretching vibrations of the C-H bond, respectively. A weak peak at 1167 cm^{-1} is attributed to the stretching vibrations of the C-N bond, and a strong transition band centered at 1545 cm^{-1} is observed, which can be attributed to the N-H bending mode of the amino group. Accordingly, the FT-IR results verify the success in ligand removal of OA-UCNPs and further attachment of PEI on bare UCNPs. After ligand exfoliation and polymer modification, positively charged ligand-free UCNPs (+35.7 mV) and PEI-UCNPs (+32.8 mV) are obtained (Fig. 5.3b), and can be easily dispersed in water, indicating stable colloidal solutions are obtained.

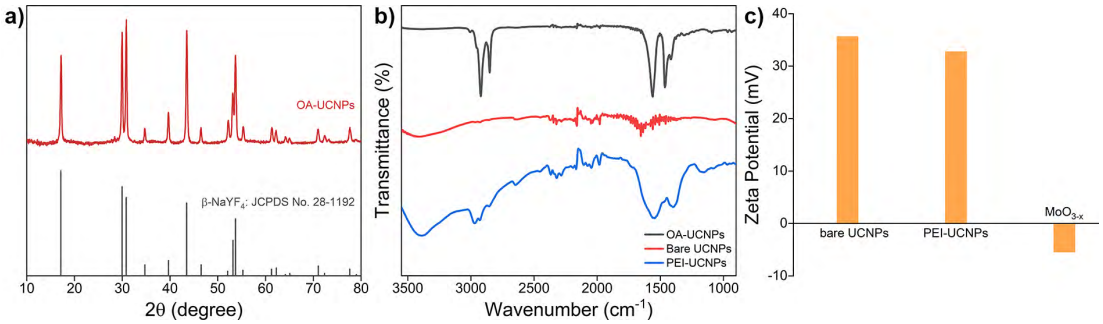

Fig. 5.3 (a) XRD patterns of OA-UCNPs and the standard data of hexagonal $NaYF_4$ (JCPDS No. 28-1192). (b) FT-IR spectra of OA-, ligand-free, and PEI-UCNPs. (c) Zeta potential of bare UCNPs, PEI-UCNPs, and MoO_{3-x} NSs (pH ~4.5).

To prepare UCNPs/MoO_{3-x} nanoassemblies, MoO_3 NSs are firstly prepared by tip sonication of bulk MoO_3, and oxygen-deficient MoO_{3-x} NSs are easily obtained by UV irradiation. As shown in Fig. 5.4a, the nanostructure of the MoO_{3-x} sample is comprised of NSs with lateral diameters in the range of 20-300 nm. UCNPs/MoO_{3-x}

nanoassemblies are then constructed by the assembly of positively charged PEI-UCNPs and negatively charged MoO_{3-x} (Fig. 5.3c) *via* electrostatic interactions, as characterized by TEM (Fig. 5.4b). In addition, the EDS spectrum of UCNPs/MoO_{3-x} nanocomposites implies the existence of Na, F, Y, Yb, Er, Mo, and O elements. These results prove the successful assembling of UCNPs and MoO_{3-x} NSs (Fig. 5.4d). Moreover, the morphology remains after the oxidation of MoO_{3-x} by the addition of H_2O_2 (Fig. 5.4c).

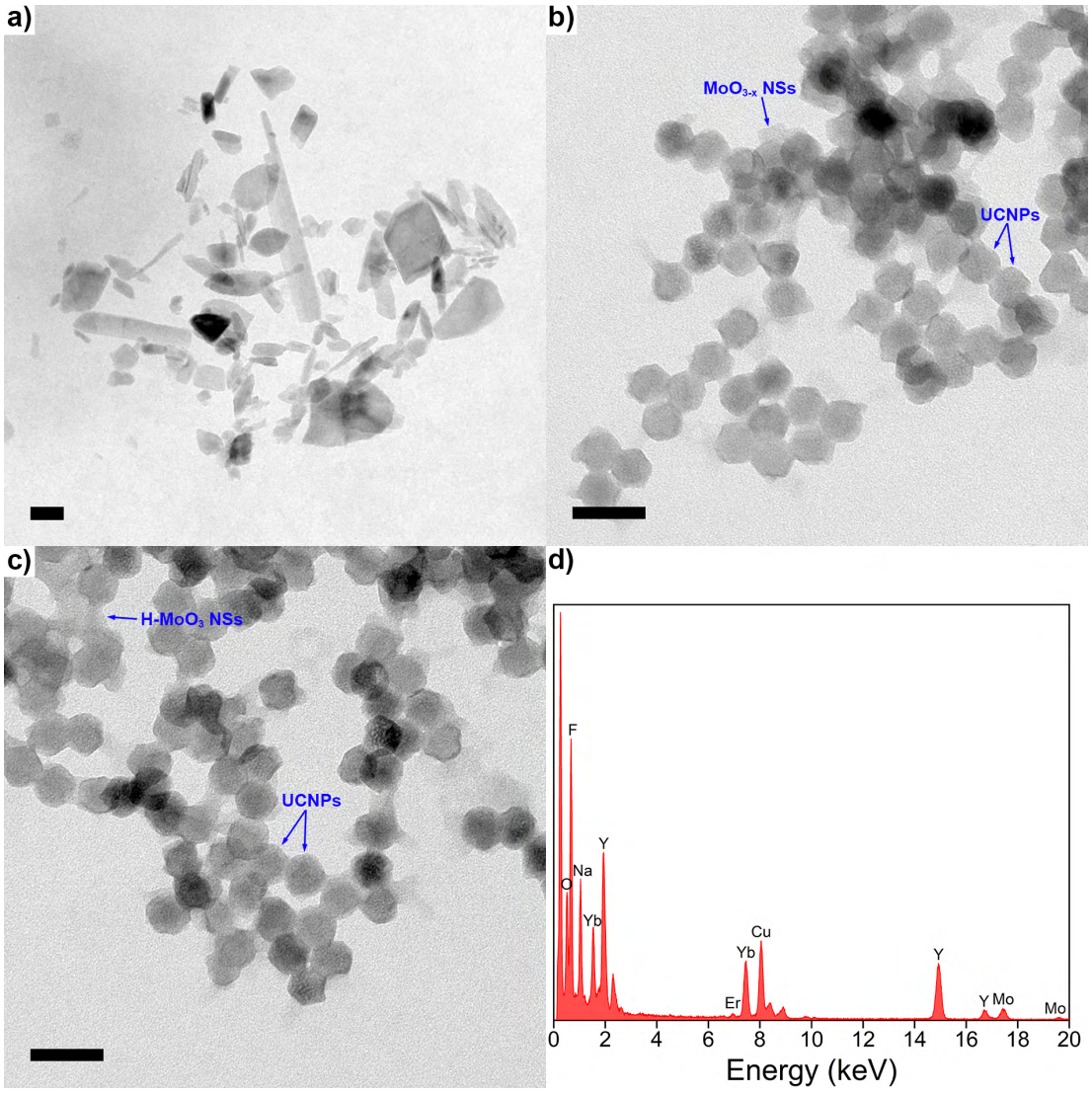

Fig. 5.4 TEM images of (a) MoO_{3-x} NSs, (b) UCNPs/MoO_{3-x} nanocomposites, and (c) UCNPs/MoO_{3-x} nanocomposites after the addition of H_2O_2. Scale bars: 50 nm. (d) EDS spectrum of UCNPs/MoO_{3-x} nanocomposites.

Next, the optical properties of UCNPs, MoO_{3-x} NSs, and UCNPs/MoO_{3-x} nanocomposites are investigated. OA-UCNPs dissolved in cyclohexane produce green (525 nm and 545 nm) and red (565 nm) UCL emissions originating from the

$^2H_{11/2} \rightarrow {}^4I_{15/2}$, $^4S_{3/2} \rightarrow {}^4I_{15/2}$, and $^4F_{9/2} \rightarrow {}^4I_{15/2}$ transitions of Er^{3+} ion under 980 nm CW laser excitation. The UV-vis spectroscopy of MoO_3 NSs shows only slight absorption in visible and NIR regions. In contrast, MoO_{3-x} NSs strongly absorb in visible and NIR regions, ascribed to the enhancement of the free electron concentration and the increased oxygen vacancies in the MoO_{3-x} NSs after exposure to UV light. The absorption of MoO_{3-x} NSs overlaps well with not only UCL emissions of UCNPs but also the excitation wavelength for UCNPs, namely 980 nm. Additionally, the absorption in the visible and NIR regions disappears after the addition of H_2O_2, as shown in Fig. 5.1b. The loss in the absorption intensity is due to the oxidative effect of H_2O_2 in an acidic medium, filling up the oxygen vacancies of MoO_{3-x} NSs[47].

5.3.3 Non-Contact Fluorescence Sensing of pH

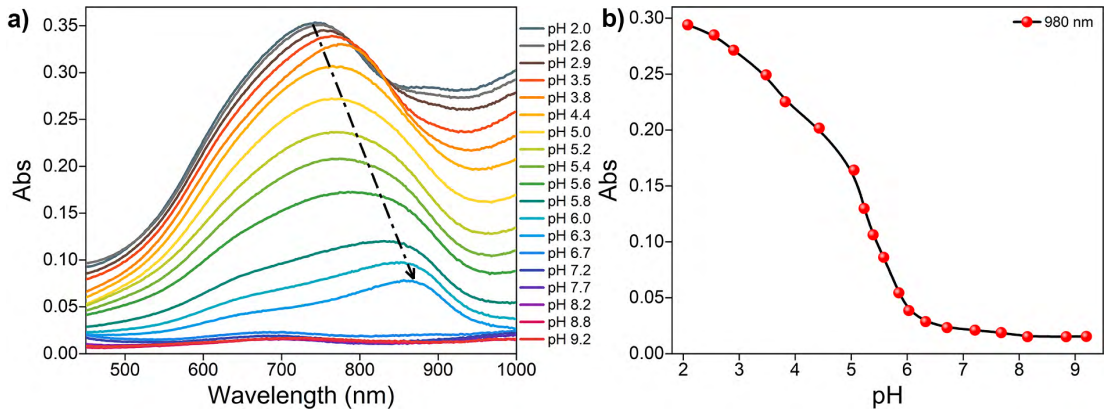

Fig. 5.5 (a) UV-vis absorption spectra of MoO_{3-x} NSs solution (1 mg/mL) at different pH values. (b) The absorbance of MoO_{3-x} NSs solution at 980 nm as a function of pH. The black line serves as a guide to the eye.

The optical properties of MoO_{3-x} NSs solutions (1 mg/mL) at different pH are first investigated by UV-vis spectroscopy. As represented in Fig. 5.5a, the absorption intensity in the visible and NIR regions shows a reducing trend with increasing pH, and the maximum absorption peak gradually redshifts from 744 to 866 nm. However, no obvious absorption peak in the visible and NIR regions is found after pH >7. Moreover, the absorption at 980 nm shows the same decreasing trend as well (Fig. 5.5b). This phenomenon arises from the generation of more Mo^{6+} cations by the addition of OH^- to the MoO_{3-x} NSs solution, leading to the reduction of free carrier concentration, and thus reducing the absorption in visible and NIR regions[47, 48].

Next, the luminescence properties are investigated by placing MoO_{3-x} NSs solutions (1 mg/mL) with different pH in front of the OA-UCNPs solution (1 mg/mL), and illuminate

it with the light of 980 nm wavelength at room temperature, where the 980 nm light first passes through the MoO_{3-x} NSs solution and then reaches OA-UCNPs. The overall trend in luminescence intensity enhances with increasing pH and remains constant above pH 8.2, as is presented in Fig. 5.6a. As shown in the inset of Fig. 5.6b, the intensity at 658 nm grows slowly when pH <4.4, then increases remarkably in the range of 5.0 to 8.2, and the UCL intensity at 658 shows no significant change afterward. However, the UCL intensity at 658 nm shows a nonlinear relationship with pH, which is different from typical upconversion sensors based on the FRET process[32-34]. Notably, we find that the logarithm of luminescence intensity at 658 nm exhibits three-separated linearity with the pH, and the linear correlation coefficient of each calibration curve is calculated to be 0.992 (pH 2.6-4.4), 0.988 (pH 5-6), and 0.998 (6.3-8.2), respectively (Fig. 5.6b). Thus, this upconversion-based nanosystem shows broad pH responsiveness in the range of 2.6 to 8.2.

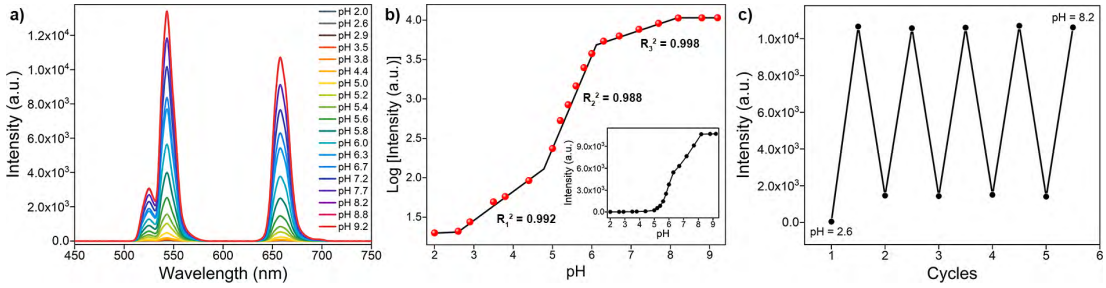

Fig. 5.6 (a) UCL spectra of OA-UCNPs in the presence of MoO_{3-x} NSs solutions with different pH in the non-contact mode under 4 W 980 nm CW laser excitation. (b) Relationship between the logarithm of luminescence intensity of OA-UCNPs at 658 nm and pH. Inset: corresponding luminescence intensities of OA-UCNPs at 658 nm, and the black line serves as a guide to the eye. (c) Fluorescence intensity of OA-UCNPs at 658 nm in the presence of MoO_{3-x} NSs solution by altering the pH value in the non-contact mode.

To investigate the reversibility of this pH sensor, the pH value of MoO_{3-x} NSs was adjusted from 8.2 to 2.6 and back to 8.2 by NaOH and HCl solutions for 5 cycles. As shown in Fig. 5.6c, the fluorescence intensity shows good reversibility of the two-way switching processes after the second cycle of pH adjustment. A slight increase in the fluorescence intensity at pH 2.6 was noticed after the first pH adjustment from 8.2, which may result from a lower reduction degree of Mo(VI) in the acidic environment than under exposure to the UV light.

5.3.4 Non-Contact Fluorescence Sensing of H_2O_2

The sensing ability of the upconversion-based nanosystem for H_2O_2 in the non-contact

mode is evaluated by the UV-vis absorption and UCL spectroscopy. As can be seen in the absorption spectrum (Fig. 5.7a), the MoO_{3-x} NSs solution shows a broad absorption in both visible and NIR regions, and the overall absorption intensity of MoO_{3-x} NSs solution decreases with the increasing amount of H_2O_2, and the absorbance is barely observed after the addition of 0.8 mM H_2O_2. Notably, the maximum absorbance of MoO_{3-x} NSs at 722 nm decreases substantially when a low amount of H_2O_2 is added (<0.3 mM), then the absorption intensity reduces gradually, and no further variation in absorption is found after the addition of 0.8 mM H_2O_2 (Fig. 5.7b), indicating the completion in the conversion of MoO_{3-x} to H-MoO_3. The change in absorption intensity at 722 nm (denoted as $(A_0 – A)/A_0$, where A_0 and A refer to the MoO_{3-x} NSs solution in the absence and presence of H_2O_2, respectively) shows a linear relationship with the H_2O_2 concentration in two-separated regions (Fig. 5.7c). Moreover, the linear correlation coefficients of these two calibration curves are larger than 0.99, and the LOD (in terms of the 3σ rule) is calculated to be 0.75 μM.

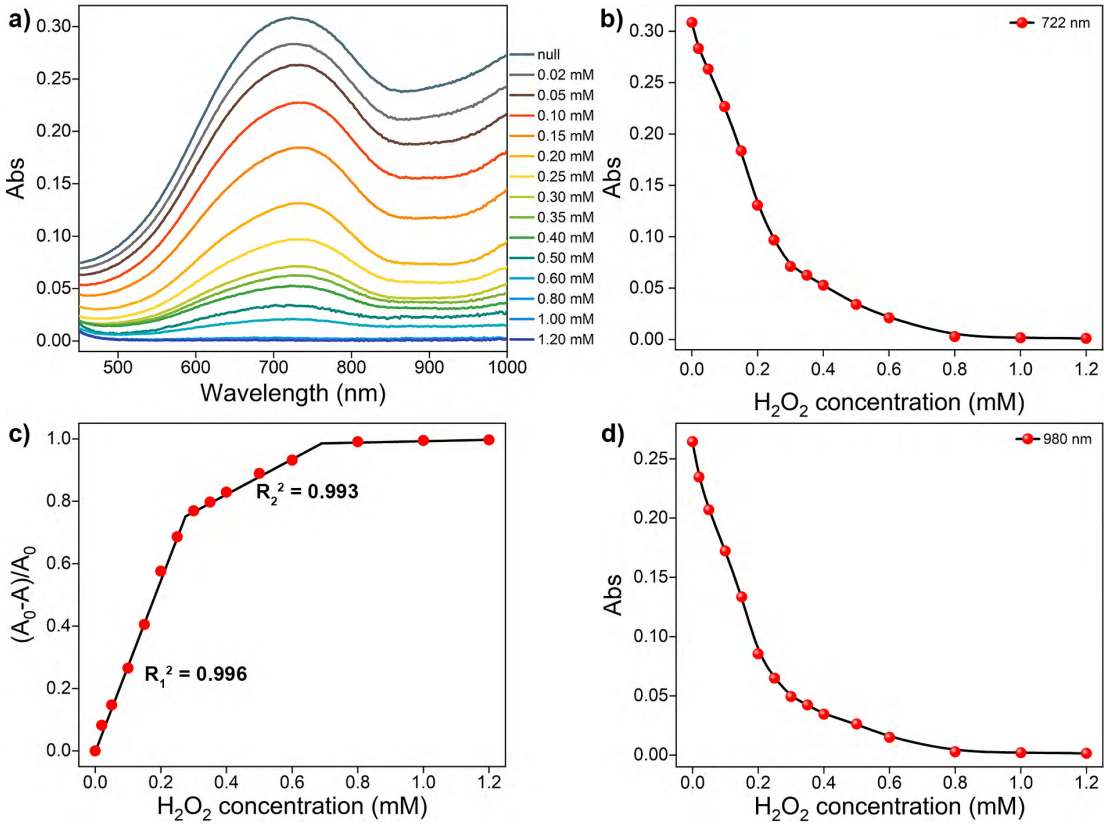

Fig. 5.7 (a) UV-vis spectra of MoO_{3-x} NSs (1 mg/mL) upon addition of different H_2O_2 concentrations. (b) The absorbance of MoO_{3-x} NSs solution at 722 nm as a function of H_2O_2 concentration. (c) Relationship between the change in absorbance of MoO_{3-x} NSs at 722 nm and H_2O_2 concentration. (d) The absorbance of MoO_{3-x} NSs solution at 980 nm with the addition of different H_2O_2 concentrations at pH 4.5.

The luminescence properties are then studied using similar procedures as the above-

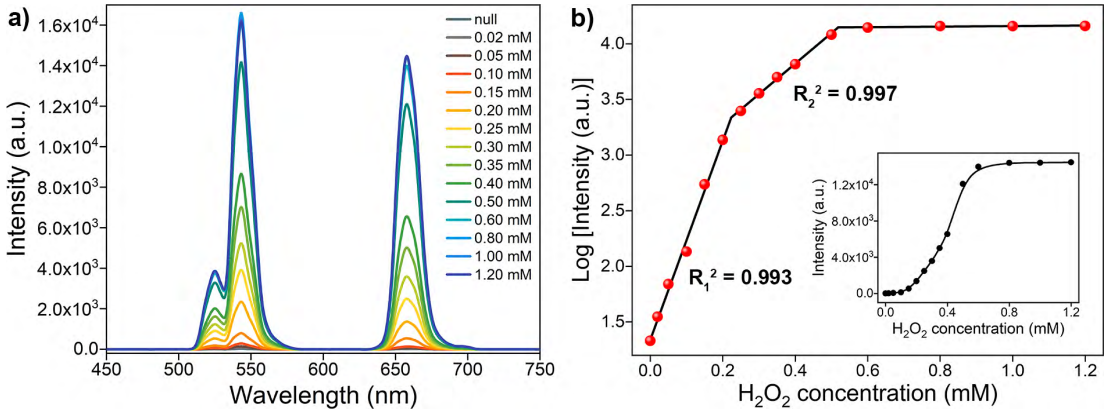

Fig. 5.8 (a) UCL spectra of OA-UCNPs (1 mg/mL) in the presence of MoO_{3-x} NSs solutions (1 mg/mL, pH 4.5) containing different H_2O_2 concentrations under 4 W 980 nm CW laser excitation. (b) Relationship between the logarithm of luminescence intensity of OA-UCNPs at 658 nm and the H_2O_2 concentration. Inset: corresponding luminescence intensities of OA-UCNPs at 658 nm.

Table 5.1 Comparison of various upconversion-based nanoprobes for H_2O_2 sensing

Sensors	Mechanisms	LOD	Ref.
benzopyrylium-coumarin-functionalized UCNPs	FRET	4.37 μM	14
DNA-Ag/UCNPs nanocomposites	FRET	1.08 μM	17
MnO_2-NSs-modified UCNPs	FRET	0.9 μM	26
squaric acid-Fe(III) & UCNPs	inner filter effect	2.3 μM	49
UCNPs & MoO_{3-x} (non-contact mode)	EEA	0.63 μM	this work
UCNPs/MoO_{3-x} nanoassemblies	EEA & FRET	9.61 μM	this work

mentioned pH sensing, except that MoO_{3-x} solutions (1 mg/mL in acetate buffer, pH 4.5) with different added H_2O_2 concentrations are placed in front of the OA-UCNPs solution. The quenching efficiency (denoted as $(F_0 - F)/F_0$, where F and F_0 represent the luminescence intensity in the presence and absence of MoO_{3-x} NSs, respectively) at 658 nm reaches 99.8% when 1 mg/mL MoO_{3-x} NSs solution is aligned in front of 1 mg/mL OA-UCNPs solution. When H_2O_2 is added in the range from 0 to 0.8 mM, the absorption intensity of MoO_{3-x} NSs solution at 980 nm shows a continuous decrease (Fig. 5.7d). As a result, the UCL intensity of OA-UCNPs experiences a gradual uptrend in both red and green regions upon 980 nm excitation with the increasing addition of H_2O_2 (Fig. 5.8a). This can be ascribed to the oxidation of MoO_{3-x} to MoO_3 by H_2O_2, leading to the reduction in excitation energy depletion by MoO_{3-x} NSs at 980 nm, and resulting in more excitation energy reached to OA-UCNPs. Similarly, like the above-discussed pH sensing in the non-contact mode, the fluorescent intensity exhibits a nonlinear relationship with the H_2O_2 concentration as well (inset of Fig. 5.8b). In

addition, the logarithm of luminescence intensity at 658 nm is linearly correlated with the H_2O_2 concentration in the range of 0-200 μM (R_1^2 = 0.993) and 250-500 μM (R_2^2 = 0.997), respectively (Fig. 5.8b). According to the 3σ rule, the detection of H_2O_2 can be down to 0.63 μM, providing a lower detection limit than those reported by other upconversion-based nanoprobes (Table 5.1).

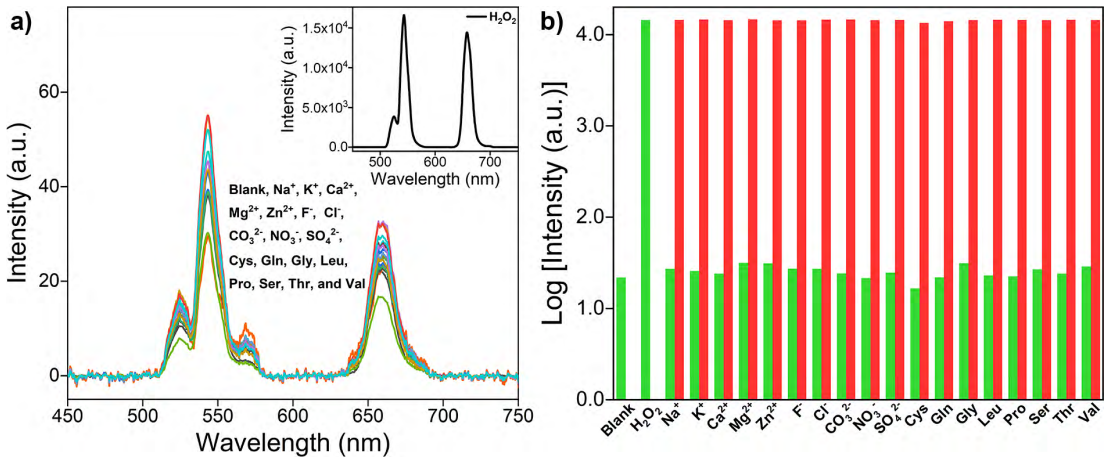

Fig. 5.9 (a) UCL spectra of OA-UCNPs in the presence of MoO_{3-x} NSs solutions containing 3 mM various interfering species at pH 4.5 under 4 W 980 nm CW laser excitation. Inset: UCL spectrum of OA-UCNPs in the presence of MoO_{3-x} NSs solutions containing 0.6 mM H_2O_2 at pH 4.5. (b) Changes in the logarithm of luminescence intensity of OA-UCNPs at 658 nm upon addition of 0.6 mM H_2O_2 and 3 mM other interfering species to MoO_{3-x} NSs solution at pH 4.5. Green bars represent changes in the logarithm of luminescence intensity at 658 nm upon addition of various species in MoO_{3-x} NSs solution, red bars represent the subsequent addition of 0.6 mM H_2O_2 to the above MoO_{3-x} NSs solution.

To further estimate the selectivity for H_2O_2 in the non-contact mode, the fluorescence responses of the nanosystem toward various interfering species including cations, anions, and amino acids are investigated. As shown in Fig. 5.9a, only the addition of H_2O_2 results in the recovery of the UCL emission, whereas no obvious change in luminescence intensity is observed after the addition of large excesses of the other interfering species, such as Na^+, K^+, Ca^{2+}, Mg^{2+}, Zn^{2+}, F^-, Cl^-, CO_3^{2-}, NO^{3-}, SO_4^{2-}, Cys, Gln, Gly, Leu, Pro, Ser, Thr, and Val. Furthermore, competition experiments exhibit the recovery in UCL intensities at 658 nm, performed by adding H_2O_2 to MoO_{3-x} NSs solutions containing other interfering species (Fig. 5.9b). The results indicate that the sensing of H_2O_2 is barely affected by these coexistent species. Therefore, this nanosystem can serve as an upconversion fluorescence nanoprobe for H_2O_2 with high selectivity in the non-contact mode.

For a practical application of the non-contact upconversion-based sensor, we studied the detection of H_2O_2 residue in contact lens solution, as H_2O_2 is usually applied in the

contact lens disinfection processes and is harmful to human eyes. The results are summarized in Table 5.2. The recoveries of H_2O_2 in contact lens solutions range from 96.56% to 102.04% and the relative standard deviation (RSD, n = 3) values are lower than 4.45%, suggesting the efficient practical applicability of the proposed sensor.

Table 5.2 Detection of H_2O_2 in contact lens solution

Contact lens solution	Detected (μM)	Added (μM)	Found (μM)	Recovery (%)	RSD (%)
1	ND	50	48.64	97.28	1.47
2	ND	100	102.04	102.04	4.45
3	ND	200	193.11	96.56	3.32

ND = no detection

5.3.5 Conventional Fluorescence Sensing of H_2O_2

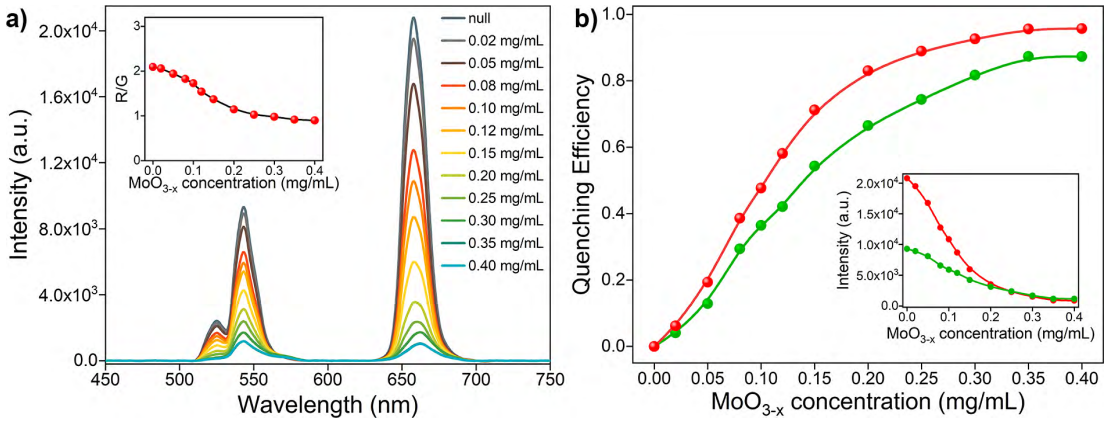

Fig. 5.10 (a) UCL spectra of 0.5 mg/mL UCNPs upon the addition of different contents of MoO_{3-x} NSs at pH 4.5 under 4 W 980 nm CW laser excitation. Inset: R/G values of UCNPs/MoO_{3-x} nanocomposites with different MoO_{3-x} NSs contents. The black line in the inset serves as a guide to the eye. (b) Fluorescence quenching efficiency of UCNPs/MoO_{3-x} nanocomposites at 658 nm (red) and 543 nm (green) upon the addition of different MoO_{3-x} NSs concentrations at pH 4.5. Inset: corresponding luminescence intensities of OA-UCNPs at 658 nm and 543 nm. The red and green lines serve as a guide to the eye.

To quantitatively analyze the quenching ability of MoO_{3-x} NSs on UCNPs, a series of MoO_{3-x} NSs modified PEI-UCNPs nanocomposites (the concentration of PEI-UCNPs is fixed at 0.5 mg/mL) is prepared by changing the MoO_{3-x} NSs content (from 0 to 0.4 mg/mL). The effect of different MoO_{3-x} NSs loading on PEI-UCNPs is then evaluated by UCL spectra. As shown in Fig. 5.10a, the overall UCL emission intensity experiences a decreasing trend with the increasing loading content of MoO_{3-x} NSs. As shown in the inset of Fig. 5.10b, the red emission intensity of UCNPs/MoO_{3-x}

nanoassemblies shows a significant decrease with the increasing content of MoO_{3-x} NSs. Additionally, the green emission intensity of upconversion-based nanoassemblies with different loading of MoO_{3-x} NSs shows a similar tendency, but with a slower downward trend. The fluorescence quenching efficiency is shown in Fig. 5.10b. The quenching efficiency enhances rapidly with the increasing addition of MoO_{3-x} NSs, and shows no obvious changes at 543 and 658 nm after adding 0.35 mg/mL MoO_{3-x} NSs. Compared with unmodified PEI-UCNPs, the highest fluorescence quenching efficiency at 658 nm reaches 95.6% with the addition of 0.35 mg/mL MoO_{3-x} NSs. Moreover, the quenching efficiency at 543 nm shows the same trend, but with a maximum value of 87.3%. Correspondingly, 0.5 mg/mL UCNPs/MoO_{3-x} nanocomposites with the addition of 0.35 mg/mL MoO_{3-x} NSs are selected for the subsequent sensing experiments.

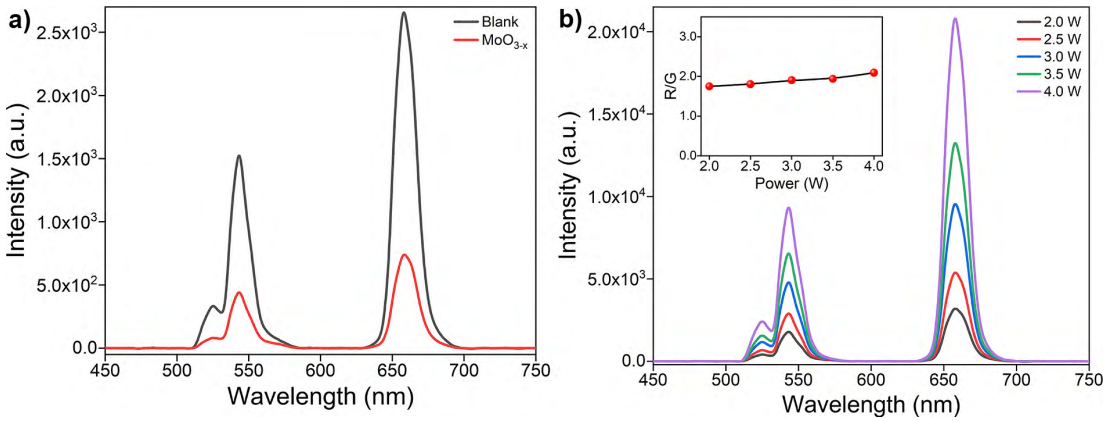

Fig. 5.11 (a) UCL spectra of 0.5 mg/mL PEI-UCNPs in the absence (black) and presence(red) of 0.35 mg/mL MoO_{3-x} NSs solution under 4 W 980 laser excitation in the non-contact mode. (b) UCL spectra of 0.5 mg/mL PEI-UCNPs under excitation with different power. Inset: the relationship between the R/G ratio and laser power. The black line in the inset serves as a guide to the eye.

To elucidate the effect of EEA-induced reduction in the UCL of UCNPs by MoO_{3-x} NSs, a non-contact mode is designed. The MoO_{3-x} NSs solution (0.35 mg/mL) is sealed in the quartz cuvette, aligning in front of another quartz cuvette containing 0.5 mg/mL PEI-UCNPs solution, and the UCL spectra are depicted in Fig. 5.11a. Upon the excitation by a 980 nm CW laser, the incident light first passes through the MoO_{3-x} NSs solution, and the energy-reduced light then reaches the UCNPs, resulting in the loss of intensity in UCL emissions. Ideally, the UCL intensity at 658 nm reduces by 72.3% when compared with the control experiment.

Notably, the EEA effect will only affect the intensity in all emissions, while the red-to-green emission ratio (R/G, where the red emission is integrated from 600-700 nm and

the green emission is integrated from 500-600 nm) keeps its stability, which is confirmed by the activation of PEI-UCNPs (0.5 mg/mL) with different power of the 980 nm laser. As presented in Fig. 5.11b, the red and green emission intensities increase with increasing laser power, while the R/G remains constant (inset of Fig. 5.11b). However, a gradual decrease in the R/G values is observed for the UCNPs/MoO_{3-x} nanocomposites with the increasing loading content of MoO_{3-x} NSs (inset of Fig. 5.10a). This phenomenon can be attributed to the FRET-induced fluorescence quenching by MoO_{3-x} NSs, where the quenching ability by MoO_{3-x} NSs in red emission is more pronounced than in the green region. As discussed above, the fluorescence quenching of UCNPs by MoO_{3-x} NSs is achieved by the joint effect of EEA and FRET, owing to the strong absorbance ability of MoO_{3-x} NSs in both visible and NIR regions.

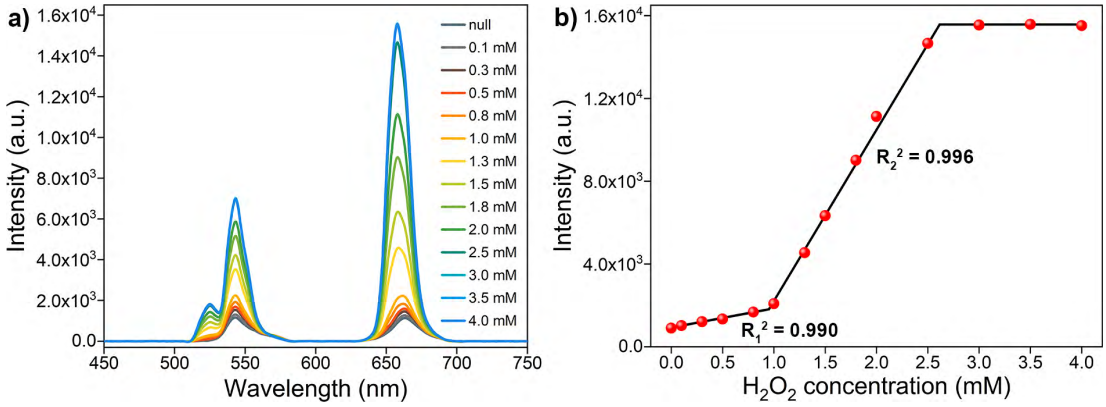

Fig. 5.12 (a) UCL spectra of 0.5 mg/mL UCNPs/MoO_{3-x} nanocomposites (0.35 mg/mL MoO_{3-x} NSs) upon the addition of different H_2O_2 concentrations at pH 4.5 under 4 W 980 nm CW laser excitation. (b) Relationship between the fluorescence intensity of UCNPs/MoO_{3-x} nanocomposites at 658 nm and the H_2O_2 concentration.

The sensing performance of UCNPs/MoO_{3-x} nanoassemblies toward H_2O_2 is investigated by UCL emission spectroscopy. As shown in Fig. 5.12a, the UCL emission intensity in red and green regions increases with the increasing addition of H_2O_2. As discussed above, the addition of H_2O_2 leads to the oxidation of MoO_{3-x}, resulting in the reduction in the absorption in both visible and NIR regions, and thus inhibiting the EEA effect at 980 nm and FRET process from the UCL of UCNPs to absorption of MoO_{3-x} in the visible region, corresponding to the enhancement of UCL emission intensity. However, the fluorescence intensity shows no obvious changes if more than 3.0 mM H_2O_2 are added. The fluorescence intensity at 658 nm exhibits a linear correlation to the H_2O_2 concentration in the range of 0-0.8 mM (R_1^2 = 0.990) and 1.0-2.5 mM (R_2^2 = 0.996), respectively (Fig. 5.12b). The detection limit of H_2O_2 is calculated to be 9.61 μM according to the 3σ rule. Intriguingly, the addition of a low concentration of H_2O_2

only leads to slight UCL recovery, while significant UCL recovery takes place with the addition of a large amount of H_2O_2, showing an opposite trend when compared to the sensing of H_2O_2 in the non-contact mode (Fig. 5.8b). Moreover, much more H_2O_2 is required for the full recovery of UCL in the conventional UCNPs/MoO_{3-x} system. This phenomenon may be attributed to the structure of the stacked MoO_{3-x} NSs on UCNPs, slowing H_2O_2 to fill up the oxygen vacancies in MoO_{3-x} NSs, and thus more H_2O_2 is consumed for complete oxidation of MoO_{3-x}.

5.4 Conclusion

In summary, we have developed two different methods (i.e. a non-contact method and a conventional method) for upconversion fluorescence sensing of H_2O_2. The non-contact method relies on MoO_{3-x} NSs absorption-induced EEA effect and operates by placing the MoO_{3-x} NSs solution in front of the UCNPs solution, whereas the conventional upconversion-based fluorescence nanoprobe, based on the joint effect of EEA and FRET, was constructed by the integration of hydrophilic PEI-UCNPs and MoO_{3-x} NSs *via* electrostatic interactions. An advantage of the non-contact method is that the valuable sensor particles do not become consumed or contaminated during the measurement and can be reused for a long time. The MoO_{3-x} NSs act as the quencher in both methods, owing to the strong absorptive capacity of MoO_{3-x} in both visible and NIR regions. However, the addition of H_2O_2 leads to the oxidation of MoO_{3-x}, resulting in the recovery of UCL emissions, and thus enabling the quantitative detection of H_2O_2 by both methods. Benefiting from the non-contact method, hydrophobic OA-UCNPs can be applied as the luminophore directly and ultrahigh fluorescence quenching (99.8%) is obtained. Moreover, the non-contact method exhibits high sensitivity toward H_2O_2 down to 0.63 μM, which is lower than that determined by spectrophotometry (0.75 μM) and conventional UCNPs/MoO_{3-x} nanocomposites (9.61 μM). Additionally, pH sensing can be achieved by employing the non-contact mode as well, which has shown a broad pH-responsive range from 2.6 to 8.2. We believe that these results could provide new insights into the design of upconversion-based nanosystems for fluorescence sensing of other analytes.

5.5 References

[1] M. Giorgio, M. Trinei, E. Migliaccio, and P.G. Pelicci, Hydrogen peroxide: a metabolic by-product or a common mediator of ageing signals?, *Nat. Rev. Mol. Cell Biol.*, **2007**, 8, 722-728.

[2] E.A. Veal, A.M. Day, and B.A. Morgan, Hydrogen peroxide sensing and signaling, *Mol. Cell*, **2007**, 26, 1-14.

[3] R.S. Balaban, S. Nemoto, and T. Finkel, Mitochondria, oxidants, and aging, *Cell*, **2005**, 120, 483-495.

[4] M.P. Mattson, Pathways towards and away from Alzheimer's disease, *Nature*, **2004**, 430, 631-639.

[5] R. Pop-Busui, A. Sima, and M. Stevens, Diabetic neuropathy and oxidative stress, *Diabetes Metab. Res. Rev.*, **2006**, 22, 257-273.

[6] M.T. Lin, and M.F. Beal, Mitochondrial dysfunction and oxidative stress in neurodegenerative diseases, *Nature*, **2006**, 443, 787-795.

[7] K. Ishikawa, K. Takenaga, M. Akimoto, N. Koshikawa, A. Yamaguchi, H. Imanishi, K. Nakada, Y. Honma, and J.-I. Hayashi, ROS-generating Mitochondrial DNA mutations can regulate tumor cell metastasis, *Science*, **2008**, 320, 661.

[8] X. Xiong, C. You, X. Cao, L. Pang, R. Kong, and X. Sun, Ni_2P nanosheets array as a novel electrochemical catalyst electrode for non-enzymatic H_2O_2 sensing, *Electrochim. Acta*, **2017**, 253, 517-521.

[9] W. Chen, S. Cai, Q.-Q. Ren, W. Wen, and Y.-D. Zhao, Recent advances in electrochemical sensing for hydrogen peroxide: a review, *Analyst*, **2012**, 137, 49-58.

[10] L. Yu, C. He, Q. Zheng, L. Feng, L. Xiong, and Y. Xiao, Dual Eu-MOFs based logic device and ratiometric fluorescence paper microchip for visual H_2O_2 assay, *J. Mater. Chem. C*, **2020**, 8, 3562-3570.

[11] A.R. Lippert, G.C. Van de Bittner, and C.J. Chang, Boronate oxidation as a bioorthogonal reaction approach for studying the chemistry of hydrogen peroxide in living systems, *Acc. Chem. Res.*, **2011**, 44, 793-804.

[12] D. Wu, A.C. Sedgwick, T. Gunnlaugsson, E.U. Akkaya, J. Yoon, and T.D. James, Fluorescent chemosensors: the past, present and future, *Chem. Soc. Rev.*, **2017**, 46, 7105-7123.

[13] X. Zhu, Q. Su, W. Feng, and F. Li, Anti-Stokes shift luminescent materials for bio-applications, *Chem. Soc. Rev.*, **2017**, 46, 1025-1039.

[14] J. Zheng, Y. Wu, D. Xing, and T. Zhang, Synchronous detection of glutathione/hydrogen peroxide for monitoring redox status in vivo with a ratiometric upconverting nanoprobe, *Nano Res.*, **2019**, 12, 931-938.

[15] N. Wang, X. Yu, K. Zhang, C.A. Mirkin, and J. Li, Upconversion nanoprobes for the ratiometric luminescent sensing of nitric oxide, *J. Am. Chem. Soc.*, **2017**, 139, 12354-12357.

[16] T. Liang, Z. Li, P. Wang, F. Zhao, J. Liu, and Z. Liu, Breaking through the signal-to-background limit of upconversion nanoprobes using a target-modulated sensitizing switch, *J. Am. Chem. Soc.*, **2018**, 140, 14696-14703.

[17] S. Wu, X.-J. Kong, Y. Cen, J. Yuan, X. Chu, and R. Yu, Fabrication of a LRET-based upconverting hybrid nanocomposite for turn-on sensing of H_2O_2 and glucose, *Nanoscale*,

2016, 8, 8939-8946.

[18] Y. Yang, Y. Cong, X. Lin, B. Cao, D. Dong, K. Liu, Y. Xiao, J. Shang, Y. Bao, Y. Liu, G. Fang, Y. Wang, Y. Chen, J. Zhang, and B. Dong, Dual LSPR of Au/$W_{18}O_{49}$ heterostructures for upconversion enhancement and application of molecular detection, *J. Mater. Chem. A*, **2020**, 8, 4040-4048.

[19] X. Chen, J. Wang, C. Yang, Z. Ge, and H. Yang, Fluorescence resonance energy transfer from $NaYF_4$:Yb,Er to nano gold and its application for glucose determination, *Sens. Actuators B Chem.*, **2017**, 255, 1316-1324.

[20] L. Ling, L. Ruiyi, W. Guangli, G. Zhiguo, and L. Zaijun, Graphene quantum dots-$NaYF_4$:Yb,Er hybrid with significant enhancement of upconversion emission for fluorescent detection of carcinoembryonic antigen with exonuclease III-aided target recycling amplification, *Sens. Actuators B Chem.*, **2019**, 285, 453-461.

[21] Y. Zhou, X. Shao, Y. Han, and H. Zhang, Detection of procalcitonin (PCT) using the double antibody sandwich method based on fluorescence resonant energy transfer between upconversion nanoparticles and quantum dots, *Anal. Methods*, **2018**, 10, 1015-1022.

[22] H. Kurt, M. Yüce, B. Hussain, and H. Budak, Dual-excitation upconverting nanoparticle and quantum dot aptasensor for multiplexed food pathogen detection, *Biosens. Bioelectron.*, **2016**, 81, 280-286.

[23] C. Zhang, Y. Yuan, S. Zhang, Y. Wang, and Z. Liu, Biosensing platform based on fluorescence resonance energy transfer from upconverting nanocrystals to graphene oxide, *Angew. Chem. Int. Ed.*, **2011**, 50, 6851-6854.

[24] M. Laurenti, M. Paez-Perez, M. Algarra, P. Alonso-Cristobal, E. Lopez-Cabarcos, D. Mendez-Gonzalez, and J. Rubio-Retama, Enhancement of the upconversion emission by visible-to-near-infrared fluorescent graphene quantum dots for miRNA detection, *ACS Appl. Mater. Interfaces*, **2016**, 8, 12644-12651.

[25] D. Giust, M.I. Lucío, A.H. El-Sagheer, T. Brown, L.E. Williams, O.L. Muskens, and A.G. Kanaras, Graphene oxide-upconversion nanoparticle based portable sensors for assessing nutritional deficiencies in crops, *ACS Nano*, **2018**, 12, 6273-6279.

[26] J. Yuan, Y. Cen, X.-J. Kong, S. Wu, C.-L. Liu, R.-Q. Yu, and X. Chu, MnO_2-nanosheet-modified upconversion nanosystem for sensitive turn-on fluorescence detection of H_2O_2 and glucose in blood, *ACS Appl. Mater. Interfaces*, **2015**, 7, 10548-10555.

[27] Y. Cen, J. Tang, X.-J. Kong, S. Wu, J. Yuan, R. Yu, and X. Chu, Cobalt oxyhydroxide-modified upconversion nanosystem for sensitive fluorescence sensing of ascorbic acid in human plasma, *Nanoscale*, **2015**, 7, 13951-13957.

[28] P. Wang, A. Wang, M.M. Hassan, Q. Ouyang, H. Li, T. Jiao, and Q. Chen, A highly sensitive upconversion nanoparticles-WS_2 nanosheet sensing platform for Escherichia coli detection, *Sens. Actuators B Chem.*, **2020**, 320, 128434.

[29] C. Liu, Y. Yu, D. Chen, J. Zhao, Y. Yu, L. Li, and Y. Lu, Cupredoxin engineered upconversion nanoparticles for ratiometric luminescence sensing of Cu^{2+}, *Nanoscale*

Adv., **2019**, 1, 2580-2585.

[30] Y. Liu, Q. Ouyang, H. Li, Z. Zhang, and Q. Chen, Development of an inner filter effects-based upconversion nanoparticles-curcumin nanosystem for the sensitive sensing of fluoride ion, *ACS Appl. Mater. Interfaces*, **2017**, 9, 18314-18321.

[31] J. Wang, Y. Zhu, C.A. Grimes, Z. Nie, and Q. Cai, Eu,Sm,Mn-Doped CaS nanoparticles with 59.3% upconversion-luminescence quantum yield: enabling ultrasensitive and facile smartphone-based sulfite detection, *Anal. Chem.*, **2018**, 90, 8658-8664.

[32] S. Ghosh, Y.-F. Chang, D.-M. Yang, and S. Chattopadhyay, Upconversion nanoparticle-mOrange protein FRET nanoprobes for self-ratiometric/ratiometric determination of intracellular pH, and single cell pH imaging, *Biosens. Bioelectron.*, **2020**, 15, 112115.

[33] C. Ding, S. Cheng, C. Zhang, Y. Xiong, M. Ye, and Y. Xian, Ratiometric upconversion luminescence nanoprobe with near-infrared Ag_2S nanodots as the energy acceptor for sensing and imaging of pH in vivo, *Anal. Chem.*, **2019**, 91, 7181-7188.

[34] R. Arppe, T. Näreoja, S. Nylund, L. Mattsson, S. Koho, J. M. Rosenholm, T. Soukka, and M. Schäferling, Photon upconversion sensitized nanoprobes for sensing and imaging of pH, *Nanoscale*, **2014**, 6, 6837-6843.

[35] M. Xu, J. Zhuang, X. Jiang, X. Liu, and D. Tang, A three-dimensional DNA walker amplified FRET sensor for detection of telomerase activity based on the MnO_2 nanosheet-upconversion nanoparticle sensing platform, *Chem. Comm.*, **2019**, 55, 9857-9860.

[36] W. Wang, H. Li, M. Yin, K. Wang, Q. Deng, S. Wang, and Y. Zhang, Highly selective and sensitive sensing of 2,4,6-trinitrophenol in beverages based on guanidine functionalized upconversion fluorescent nanoparticles, *Sens. Actuators B Chem.*, **2018**, 255, 1422-1429.

[37] X. Liu, X. Li, X. Qin, X. Xie, L. Huang, and X. Liu, Hedgehog-like upconversion crystals: controlled growth and molecular sensing at single-particle level, *Adv. Mater.*, **2017**, 29, 1702315.

[38] L.M. Wiesholler, C. Genslein, A. Schroter, and T. Hirsch, Plasmonic enhancement of NIR to UV upconversion by a nanoengineered interface consisting of $NaYF_4$:Yb,Tm nanoparticles and a gold nanotriangle array for optical detection of vitamin B12 in serum, *Anal. Chem.*, **2018**, 90, 14247-14254.

[39] F. Zhang, Q. Shi, Y. Zhang, Y. Shi, K. Ding, D. Zhao, and G.D. Stucky, Fluorescence upconversion microbarcodes for multiplexed biological detection: nucleic acid encoding, *Adv. Mater.*, **2011**, 23, 3775-3779.

[40] S. Li, L. Xu, W. Ma, X. Wu, M. Sun, H. Kuang, L. Wang, N.A. Kotov, and C. Xu, Dual-mode ultrasensitive quantification of microRNA in living cells by chiroplasmonic nanopyramids self-assembled from gold and upconversion nanoparticles, *J. Am. Chem. Soc.*, **2016**, 138, 306-312.

[41] K. Zhang, F. Lu, Z. Cai, S. Song, L. Jiang, Q. Min, X. Wu, and J.-J. Zhu, Plasmonic modulation of the upconversion luminescence based on gold nanorods for designing a

new strategy of sensing microRNAs, *Anal. Chem.*, **2020**, 92, 11795-11801.

[42] P. Vilela, A. El-Sagheer, T.M. Millar, T. Brown, O.L. Muskens, and A.G. Kanaras, Graphene oxide-upconversion nanoparticle based optical sensors for targeted detection of mRNA biomarkers present in Alzheimer's disease and prostate cancer, *ACS Sens.*, **2016**, 2, 52-56.

[43] B. Gu, and Q. Zhang, Recent advances on functionalized upconversion nanoparticles for detection of small molecules and ions in biosystems, *Adv. Sci.*, **2018**, 5, 1700609.

[44] F. Ji, X. Ren, X. Zheng, Y. Liu, L. Pang, J. Jiang, and S. Liu, 2D-MoO_3 nanosheets for superior gas sensors, *Nanoscale*, **2016**, 8, 8696-8703.

[45] M.M.Y.A. Alsaif, K. Latham, M.R. Field, D.D. Yao, N.V. Medehkar, G.A. Beane, R.B. Kaner, S.P. Russo, J.Z. Ou, and K. Kalantar-zadeh, Tunable plasmon resonances in two-dimensional molybdenum oxide nanoflakes, *Adv. Mater.*, **2014**, 26, 3931-3937.

[46] Z. Li, and Y. Zhang, An efficient and user-friendly method for the synthesis of hexagonal-phase $NaYF_4$:Yb,Er/Tm nanocrystals with controllable shape and upconversion fluorescence, *Nanotechnology*, **2008**, 19, 345606.

[47] H. Cao, X. Hu, W. Shi, S. Li, and Y. Huang, pH-regulated reversible photoluminescence and localized surface plasmon resonances arising from molybdenum oxide quantum dot, *Appl. Mater. Today*, **2020**, 18, 100516.

[48] R. Li, H. An, W. Huang, and Y. He, Molybdenum oxide nanosheets meet ascorbic acid: tunable surface plasmon resonance and visual colorimetric detection at room temperature, *Sens. Actuators B Chem.*, **2018**, 259, 59-63.

[49] H. Chen, A. Fang, L. He, Y. Zhang, and S. Yao, Sensitive fluorescent detection of H_2O_2 and glucose in human serum based on inner filter effect of squaric acid-iron(III) on the fluorescence of upconversion nanoparticle, *Talanta*, **2017**, 164, 580-587

Chapter 6: Conclusions and Perspectives

6.1 Conclusions

In this dissertation, Ln-doped upconversion nano-/microcrystals with various sizes and morphologies were prepared *via* solvothermal and high-temperature coprecipitation methods. Next, we developed an easy-to-process approach to produce ligand-free UCNPs, realizing the fast and efficient hydrophobic-to-hydrophilic transition of UCNPs. Finally, we designed upconversion-based nanosystems for sensing applications.

In Chapter 2, a facile solvothermal approach was applied to prepare Ln-doped $NaYF_4$ upconversion nano-/microcrystals using DSNTA as the ligand. Thereby, the influence of volume ratios of EG/H_2O, molar ratios of NH_4F/RE^{3+}, Gd^{3+} ion contents, types of activator dopant ions, and different organic co-solvents on the crystal phase, size, and morphology of the resulting particles were studied systematically. A possible formation mechanism for the growth of crystals of different morphology is discussed. The results showed that the transition from the α- to the β-phase mainly depends on the volume ratio of EG/H_2O and the molar ratio of NH_4F/RE^{3+}, while the morphology and size could be controlled by the type of organic co-solvent and Gd^{3+} dopant ions. Furthermore, the reaction time has to be long enough to convert α-$NaYF_4$ into β-$NaYF_4$ during the growth process to optimize the UCL. The formation of larger β-$NaYF_4$ crystals, which possess a higher UCL than smaller particles, proceeds via intermediates of smaller crystals of cubic structure.

In Chapter 3, an easy-to-process approach was developed to remove the surface ligand from oleate-stabilized UCNPs using short-chain acids as stripping agents by a simple vortexing method on a time scale of 10 seconds. This method allows for the fast and efficient hydrophobic-to-hydrophilic transition in either biphasic solvent systems or single hydrophobic media. A wide range of polar solvents can be applied to form biphasic interfaces with cyclohexane, facilitating in-solution ligand exfoliation and allowing the transfer of bare UCNPs from the hydrophobic phase to the polar phase. Moreover, short-chain acids can be added directly as well to remove the surface ligand when cyclohexane, chloroform, or toluene is adopted as the dispersant for OA-UCNPs. This method is simply performed at ambient conditions on the second time scales without affecting the size, shape, and phase of the crystals. Furthermore, the obtained ligand-free UCNPs can be readily transferred to the aqueous solution and

further modified with water-soluble capping molecules by sequential surface functionalization. More importantly, our developed method can be applied to small-sized UCNPs and HCl-sensitive materials.

In Chapter 4, two different upconversion-based nanocomposites were constructed by assembling PEI-csUCNPs with organic dye molecules (EBT) or Au NPs via electrostatic interactions. With the addition of the Cu^{2+}, a significant reduction in the red UCL intensity of csUCNPs/EBT nanocomposites was observed, owing to the redshift absorption of the EBT-Cu complex and thus leading to an enhanced FRET process from the csUCNPs to the metal-dye complex. In the csUCNPs/EBT nanosystem, csUCNPs sever as the energy donor and the EBT-Cu adducts sever as the energy acceptor. Meanwhile, in the csUCNPs/Au nanosystem, csUCNPs act as the energy donor and Au NPs act as the energy acceptor. The Au content was optimized in order to have a large quenching efficiency in UCL. The cyanide-mediated redox reaction leads to the consumption of Au NPs, resulting in the UCL recovery by the inhibition of the FRET process. Therefore, the UCNPs/EBT and UCNPs/Au nanocomposites were used for fluorescence turn-off sensing of Cu^{2+} and fluorescence turn-on sensing of CN^{-}, respectively.

In Chapter 5, a non-contact upconversion nanosystem based on the EEA effect and a conventional upconversion nanosystem based on the joint effect of EEA and FRET were developed for the fluorescence sensing of H_2O_2. We showed that the UCL was quenched by MoO_{3-x} NSs in both systems due to the strong absorbance of MoO_{3-x} NSs in the visible and NIR regions. The recovery in UCL emissions upon the addition of H_2O_2 enabled the quantitative monitoring of H_2O_2. Benefiting from the non-contact method, hydrophobic OA-UCNPs can be used as the luminophore directly and ultrahigh quenching efficiency (99.8%) was obtained. Moreover, the non-contact method exhibited high sensitivity toward H_2O_2 with a detection limit of 0.63 μM, which is lower than that determined by simple spectrophotometry (0.75 μM) and conventional upconversion-based nanocomposites (9.61 μM). As an added benefit, the same strategy can be applied to the sensing of pH, showing a broad pH-responsive property over a range of 2.6 to 8.2.

In summary, hydrophilic Ln-doped upconversion materials were prepared via one-step and two-step methods, *i.e.*, the solvothermal method using water-soluble ligand and surface modification of as-prepared hydrophobic ones. By coupling hydrophilic

upconversion NPs with small molecules and noble metal NPs, conventional upconversion-based nanocomposites were developed for fluorescence sensing of Cu^{2+} and CN^-. Moreover, a novel upconversion-based nanosystem was designed for non-contact fluorescence sensing of pH and H_2O_2.

6.2 Perspectives

Ln-doped upconversion materials have attracted considerable attention in the past decades, owing to their capability of converting NIR excitation to visible or UV light when co-doped with appropriate activator ions. They feature large anti-Stokes shifts, sharp and narrow multicolor emissions, high chemical stability, and relatively low toxicity. With the significant progress made in material synthesis, upconversion crystals with high quality and monodispersity can be prepared. Despite these merits and achievements, some limitations should be overcome prior to their applications in the practical field.

(1) The major limitation of upconversion NPs, especially the small-sized ones (<10 nm), is their low upconversion efficiency (usually <1%), particularly under low power density excitation, owing to low absorption cross-section of Ln ions and the energy losses *via* nonradiative transitions. Some efforts have been made to enhance the luminescence of upconversion NPs, including core-shell construction, host selection, surface plasmon resonance, symmetry tuning, and excitation light source optimization. However, the upconversion efficiency is still far from satisfactory. Thus, the preparation of small upconversion NPs with high upconversion efficiency remains a great challenge.

(2) Thermal decomposition and high-temperature coprecipitation methods have been widely applied to synthesize upconversion NPs with precisely tuned size, composition, shape, and well-designed architecture using OA as the ligand. However, microgram-scale and hydrophobic upconversion NPs are usually obtained. The Hydro/solvothermal method, another reliable approach, holds the potential for scalable production of hydrophilic upconversion materials with high crystallinity and uniform size. However, in the existing systems, either hexagonal microcrystals or cubic nanocrystals are obtained via the hydro/solvothermal method. Therefore, the large-scale synthesis of hydrophilic hexagonal upconversion NPs is of great importance.

(3) The most widely used Ln-doped upconversion NPs are the ones sensitized by Yb^{3+}, which are excited at 980 nm. Nevertheless, the excitation wavelength of upconversion NPs at 980 nm strongly overlaps with the absorption of water molecules, leading to the overheating of water. To resolve the overheating problem, neodymium (Nd^{3+}) sensitized upconversion NPs under excitation of 800 nm have been explored. However, the upconversion efficiency of Nd^{3+} sensitized upconversion NPs under excitation at 800 nm is much lower than that of Yb^{3+} sensitized ones upon excitation at 980 nm. How to improve the Nd^{3+} sensitized upconversion NPs with high upconversion efficiency under 800 nm needs to be addressed.

(4) With the advances of the development of Ln-doped upconversion NPs, numerous results on the upconversion efficiency have been reported recently. However, it is difficult to compare these reported data, because the optical properties of upconversion NPs are highly dependent on the characterization conditions, such as excitation laser power and integration time. Moreover, the quantum yield of upconversion NPs relies on the excitation power density. Therefore, standard characterization procedures or reference materials are of great importance to be built to enable the direct comparison of results from laboratories worldwide, which is extremely challenging.

Appendix

Publications

The results of this thesis are already published:

C. Sun, M. Schäferling, U. Resch-Genger, M. Gradzielski, Solvothermal synthesis of lanthanide-doped $NaYF_4$ upconversion crystals with size and shape control: particle properties and growth mechanism, *ChemNanoMat*, **2021**, 7, 174-183 (DOI: 10.1002/cnma.202000564). The results have been described in Chapter 2.

C. Sun, J. Simke, M. Gradzielski, An efficient synthetic strategy for ligand-free upconversion nanoparticles, *Mater. Adv.*, **2020**, 1, 1602-1607 (DOI: 10.1039/D0MA00411A). The results have been described in Chapter 3 & 4.

C. Sun, M. Gradzielski, Fluorescence sensing of cyanide anions based on Au-modified upconversion nanoassemblies, *Analyst*, **2021**, 146, 2152-2159 (DOI: 10.1039/D0AN01954B). The results have been described Chapter 4.

C. Sun, M. Gradzielski, Upconversion-based nanosystems for fluorescence sensing of pH and H_2O_2. *Nanoscale Adv.*, **2021**, 3, 2538-2546 (DOI: 10.1039/D0NA01045F). The results have been described Chapter 5.